Bulk Properties and Evolution of Jupiter-Family Comet Nuclei

Thesis

The Open University

Bulk Properties and Evolution of Jupiter-Family Comet Nuclei

Submitted for the degree of Doctor of Philosophy

in Planetary & Space Sciences

Rosita Dimitrova Kokotanekova

The Open University

and

International Max Planck Research School
for Solar System Science

October 2018

Abstract

This thesis presents the results from photometric time-series observations of Jupiter-family comets (JFCs). A method was developed that allows mutual absolute photometric calibration of data taken at different epochs with different instruments and results in absolute-calibration uncertainty of ∼0.02 mag. The method was applied to various datasets with the goal of studying the rotation rates and surface properties of ten comets.

Previously published properties of JFCs were collected and complemented by new results. The resulting comprehensive sample was used to study the ensemble properties of JFC nuclei. It confirmed the cut-off in bulk density at ∼0.6 g cm^{-3} and provided evidence for a lower limit on the bulk tensile strength of 10-25 Pa.

New lightcurves of three JFCs were used to look for spin changes over their last orbits. None of the observed comets had detectable period changes, and strict conservative upper limits were set. Comparing these results with all eight other JFCs with measured rotational changes suggests that large JFCs are less likely to undergo rotationally-driven mass-loss, and are therefore more likely to survive more perihelion passages than smaller nuclei. This conclusion is supported by evidence from the cumulative size distributions of JFCs and dormant comets, as well as from recent dynamical simulations.

This work almost doubled the sample of JFCs with both albedos and phase-function slopes known. The extended sample shows a possible correlation of increasing phase-function slopes for larger geometric albedos, which can be interpreted as an evolutionary trend for JFCs. According to this hypothesis, newly activated JFCs have higher albedos and steeper phase functions, which gradually decrease due to sublimation-driven erosion. If confirmed, this correlation could be used to analyse surface erosion from the ground and to distinguish between dormant comets and asteroids.

Acknowledgements

First and foremost I would like to express gratitude towards my supervisors Colin Snodgrass, Pedro Lacerda and Simon Green for their trust, patience and constant support. I am deeply thankful that they provided me with the opportunity to have such an incredible PhD experience, full of exciting science, observations, travels and many meetings.

I would like to thank Pedro for showing me the beauty in every aspect of science we ever discussed, for motivating me to think clearly and creatively and for inspiring me to always look for ways to improve myself, my life and my work. I owe my deepest gratitude to Colin for his continuous help, encouragement and dedication. I am very grateful for everything he has taught me about comets and observations, for the long hours he has spent proofreading my proposals, papers and thesis chapters, for his enthusiasm to find travel and observing opportunities for me, for tirelessly replying to my emails and for showing me all of the good sides of being an observational astronomer. Last, but not least, I thank Simon for always carefully reviewing my work, for helping me with all administrative hurdles, and for providing invaluable insight on ways to greatly improve my work.

This thesis would not have been possible without the financial support of the Max Planck Institute for Solar System Research and the International Max Planck Research School for Solar System Science. I would especially like to thank the IMPRS coordinator Sonja Schuh, who works tirelessly to improve the research school even further. Sonja has provided me with enormous support whenever any administrative issues had to be solved and has always patiently answered all of my plentiful questions. I would also like to express my gratitude to Ulrich Christensen for providing guidance and support.

The journey to this PhD started before I could remember. My parents Joanna and Dimitar took me out stargazing when I could barely walk, and helped me take my first images of comets when I was a child. They showed me the beauty of astronomy, but also taught me that there is so much more in life one needs to enjoy. I am immensely grateful to have such a supportive family who have taught me to have big dreams and to work hard to achieve them.

I feel blessed to have had the support of my husband Frank, who has been there giving me courage at every step of the eventful journey this PhD has come to be. Thank you for empowering me when I felt weak; for calming me down when I felt helpless on the other side of the globe, and then for not stopping me when I made plans to go back; for giving me energy and making me confident that I could achieve more than I think and for making me smile every single day.

I would like to thank Georgi for being the greatest brother I could imagine, even after missing the Leonid meteor shower in 1997 for the sake of equality. He knows best how to cheer me up and to show me that there is always something to laugh about. I am also grateful that Zlatina endures all of the long train rides to Göttingen and around Europe alongside with him, so that we could share so many unforgettable moments together.

During my PhD, I have made many new friends. I am very grateful for having met "my conference buddy" Katya and for sharing the joys and sorrows of PhD life with her over cheesecake, coffee, balsam or wine. I am also very grateful for the long motivational conversations with Chris, who always makes me believe that there is so much beauty in everything around, and for the entertaining chats with Djordje, who makes me believe in myself.

I have found many good friends at MPS, too. They have filled my time at the institute with funny memories, especially during the coffee-chocolate meetings. In particular, I am very grateful to Gesa, Kok Leng, David, Abbey, Hans, Chi-Ju, Robin, Felix, Miha and Mayukh for the fun get-togethers during the past few months when I was tied to my desk, writing this thesis and recovering from a broken foot. Even though I spent much less time at the OU, I enjoyed my short stays in Milton Keynes and was always looking forward to meeting up with George, Candice and Jack even just for a cup of coffee.

I want to thank everyone who made the long cloudy nights at La Silla and La Palma worth the long trips even when no data were collected. I am especially grateful for all of the pool, table tennis, volleyball and Werewolf games at La Silla, as well as for the delicious Italian coffee and food Hristo made for me in the TNG kitchen.

These past few years have kept me busy and I have had to miss countless opportunities to spend time with friends. I would like to thank Anastas, Yanitsa, Vesela, Georgi and Tsvetan for not giving up on our friendships, and for being so understanding whenever I was too busy to catch up. I am also very grateful that the past years have brought me to visit other friends around the globe, who often had to host me on their couches to let me save up my travel budget for even more trips.

I owe my gratitude to Alan Fitzsimmons, Yanga Fernández, Stephen Lowry, Henry Hsieh, and Cecilia Tubiana who shared the data from their observing programmes with me, making this thesis possible. I am also indebted to Plamen Nikolov, who performed observations for this thesis even when the pipes at Rozhen Observatory were frozen and limited his access to warm water for days.

Finally, I would like to express my deepest gratitude to all of my previous teachers, supervisors and mentors who have helped me through the years. I am especially grateful for Elke Roediger's and Ralph Kraft's encouragement and support very early on during my studies. Without their help and the opportunities they have created for me, I would not have gained all of the knowledge and skills needed to complete this project.

To my parents and first astronomy teachers,

Joanna and Dimitar Kokotanekovi

Contents

Publications

A list of publications resulting from the work presented in this thesis is provided below.

Refereed publications

1. **Kokotanekova, R.**, Snodgrass, C., Lacerda, P., Green, S. F. , Nikolov, P., Bonev, T., 2018, "Implications of the Small Spin Changes Measured for Large Jupiter-family Comet Nuclei", MNRAS, 479, 4, 4665.

2. **Kokotanekova, R.**, Snodgrass, C., Lacerda, P., Green, S. F., et al., 2017, "Rotation of Cometary Nuclei: New Lightcurves and an Update of the Ensemble Properties of Jupiter-Family Comets", MNRAS, 471, 3, 2974.

3. Holman, M. J. Payne, M. J., Fraser, W., ... **Kokotanekova, R.**, ... et al. 2018, "A dwarf planet class object in the 21:5 resonance with Neptune", ApJL, 885, 1, L6.

4. Evans, D. F., Southworth, J., Smalley B., ... **Kokotanekova, R.**, ... et al. 2018, "High-resolution Imaging of Transiting Extrasolar Planetary systems (HITEP). II. Lucky Imaging results from 2015 and 2016", A&A, 610, A20.

5. Ryu, Y.-H., Yee, J. C., Udalski, A., ... **Kokotanekova, R.**, ... et al. 2017, "OGLE-2016-BLG-1190Lb: First Spitzer Bulge Planet Lies Near the Planet/Brown-Dwarf Boundary", AJ, 155, 1, 40.

6. Snodgrass, C., A'Hearn, M. F., ... **Kokotanekova, R.**, ... et al. 2017, "The 67P/Churyumov-Gerasimenko observation campaign in support of the

Rosetta mission", Philosophical Transactions of the Royal Society A, Volume 375, Issue 2097.

7. Hsieh, H. H., Hainaut, O., Novaković, B.... **Kokotanekova, R.**, ... et al. 2015, "Sublimation-Driven Activity in Main-Belt Comet 313P/Gibbs", ApJ, 800, L16.

Selected non-refereed publications

1. **Kokotanekova, R.**, "Jupiter-family comet evolution from photometric time series", ISSI Workshop "Comets: Post 67P Perspectives" 15–19 January, 2018, Bern, Switzerland

2. **Kokotanekova, R.**, Snodgrass, C., Lacerda, P., Green, S. F. "Physical properties of Jupiter-family comets and KBOs from ground-based lightcurve observations", American Astronomical Society, DPS meeting #49, 15–20 October 2017, id.403.03.

3. **Kokotanekova, R.**, Snodgrass, C., Lacerda, P., Lowry, S. C., et al., "Evidence for low tensile strength in comet nuclei", European Planetary Science Congress 2017, 17–22 September, 2017, Riga Latvia, id. EPSC2017-569.

4. **Kokotanekova, R.**, Snodgrass, C., Lacerda, P., Green, S. F., "Rotation of Jupiter Family Comet Nuclei: New Optical Lightcurves, Rotation Rate Changes and an Update on the Population Properties" Asteroids, Comets, Meteors, Montevideo, 9–14 April, Montevideo, Uruguay

5. **Kokotanekova, R.**, Snodgrass, C., Lacerda, P., Green, S. F., "Rotation Rates and Spin Changes of Jupiter Family Comet Nuclei: New optical lightcurves and an update on the population properties", American Astronomical Society, DPS #48/EPSC, 16–21 October 2016, id.219.04

Chapter 1

Introduction

With their magnificent beauty and intricate nature, comets are among the most fascinating objects in the sky. From historical records found all around the world, it is evident that humans have been captivated by their spectacular appearances for millennia. It was believed, across cultures, that comets are a window to the future and they were often assigned astrological significance.

Even though these ideas pervaded for centuries, they gradually subsided and were replaced by a thorough scientific understanding. The second half of the twentieth century was marked by important milestones in cometary science which unveiled the origin and nature of these phenomena. It was established that comets consist of small solid nuclei of dust and ice, typically a few kilometres in size. When the nuclei are exposed to solar radiation they begin to sublimate and release tails of dust and gas which can span millions of kilometres. It is now widely accepted that comets can be used to provide insights about the formation of the Solar System, the details of its dynamical past and even about the beginnings of life on Earth. Thus, comet nuclei turned out to be windows to the past.

Comets are divided into different dynamical classes which reflect the parameters of their orbits. In this thesis, I focus on Jupiter-family comets, or JFCs. They have orbits with small inclinations and periods of less than 20 years. Even though their activity is not as strong as that of other comets with longer orbital periods,

JFCs provide a much better opportunity for detailed studies. Having relatively short orbital periods, JFCs allow repeated observations over multiple perihelion passages, which can be used to monitor their changing characteristics. Moreover, the relatively low eccentricity and inclination of JFCs as well as their relative proximity to Earth has made them accessible to several space missions, which have improved the understanding of cometary physics substantially over the past few decades.

So far, space missions have successfully imaged the nuclei of six comets. These detailed in situ measurements have significantly advanced the understanding of JFCs. The greatest achievement of the space exploration of comets so far is the Rosetta mission. Rosetta followed comet 67P/Churyumov-Gerasimenko along its closest approach to the Sun between 2014 and 2016 and successfully landed a probe on the comet nucleus. Rosetta had a large suite of instruments which performed an unprecedented variety of observations, mainly aiming to reveal how comets were formed and how their activity takes place.

Even after the tremendous success of Rosetta, many questions about the complex physics of comets have remained unresolved. Among others, the exact formation processes, the migration path after formation, the structure of the nuclei, the surface characteristics, the processes that lead to their ageing and the properties that determine their level of activity still need to be understood better. The ongoing analysis of the data from Rosetta will certainly provide further insight into these topics. However, it is necessary to combine the findings for 67P with the knowledge about other comets in order to understand the Rosetta outcomes in the context of the JFC population as a whole, and to explain comets within the paradigm of the Solar System history.

The enormous cost and complexity of space missions limit the number of comets that can be explored by spacecraft. At the time of writing this thesis, there are no future missions scheduled to encounter a comet, although NASA is considering a sample return mission from comet 67P. It is therefore necessary to use ground-

and space-based telescopes in order to expand the number of characterised JFCs. Despite their limitations, telescope observations of comets can provide valuable information about the composition, the activity, the properties of the nuclei (sizes, shapes and rotation rates) as well as the surfaces by measuring the reflectance properties, such as albedos, phase darkening and colours. Importantly, they can in principle be carried out for a large number of comets.

This thesis is motivated by the need to expand the number of JFC nuclei observed from ground. In the chapters below I analysed the optical photometry of ten JFCs. Typically, telescope observations of cometary nuclei pose many technical difficulties, mainly due to activity which obscures the nuclei close to the Sun or the faintness of the nuclei themselves when they are inactive. Consequently, the observations of the rotational and surface properties of comets require the allocation of many observing hours on relatively large telescopes. These obstacles have prevented the direct characterisation of many comet nuclei, and therefore the new results provide a significant increase of the number of JFC nuclei characterised with telescope observations.

The data reduction, analysis and interpretation presented in this thesis is my own work. I was the PI of three of the observing runs (in January 2016, July 2016 and February 2017) and I performed the awarded observations with the help of Pedro Lacerda and Colin Snodgrass. Simon Green contributed to refining the observing proposals that secured the telescope time. A large portion of the observations were part of the SEPPCoN (Survey of Ensemble Physical Properties of Cometary Nuclei), and were provided to me by the observers: Colin Snodgrass, Yanga Fernández, Alan Fitzsimmons, Stephen Lowry and Henry Hsieh. Another set of observations was part of an observing campaign led by Cecilia Tubiana and Colin Snodgrass who shared the raw data with me. Colin Snodgrass also observed one of the comets as a backup target for a large observing program at La Silla Observatory with principal investigator: Pedro Lacerda. Finally, Plamen Nikolov and Tanyu Bonev performed observations in Rozhen Observatory during three

observing runs for me.

In order to analyse the data, I developed a technique which successfully combines observations taken during different observing runs executed with various instruments. Using this technique relaxes the constraints of the observation scheduling and reduces the observing time necessary to characterise the rotation and the surfaces of the comets. This method relies on the precise absolute photometric calibration of the frame magnitudes of comets using star magnitudes from the Pan-STARRS catalogue (see Chapter 3). The availability of comparison stars in each telescope frame provides a significant improvement of the photometric techniques used for the analysis of moving objects. The method developed for this thesis demonstrates the great capabilities of the new-generation absolute calibration techniques.

One main goal of the thesis is to add the newly characterised nuclei to all other studied JFCs in order to study the ensemble properties of the population. I therefore collected an up-to-date sample of all 37 JFCs with known rotation properties (Chapter 4). This sample allowed me to study the shapes and rotations of JFCs. Two further outcomes of this work were the lower limits on the density and tensile strength of JFCs nuclei (Chapter 6). These are important physical characteristics that could be used to better constrain the formation scenarios of comets. Moreover, they determine how prone comet nuclei are to destruction and can be used to study the mechanisms responsible for ending the lives of comets.

In particular one of the mechanisms which is thought to be responsible for comet disruption is spin-up of the nucleus. It is caused by the torques exerted on the nucleus from the sublimation-driven outgassing. If the nucleus spins too fast, its gravity and material strength are no longer sufficient to hold it together, and it begins to lose mass. To better understand the mechanisms of rotational changes of comets I studied the rotation rates of 3 comets (Chapter 7). All of the selected comets were relatively large (with radii > 3 km). The findings from this analysis have been used to formulate a hypothesis for an enhanced survivability

of large comets which is critically discussed in Chapter 8.

The time-series observations analysed in this work were also used to study the surface properties of JFCs. I determined the albedos and phase functions of the studied comets. Thus, I increased the number of comets for which both parameters are known by a factor of two. The expanded sample was used to search for a correlation between albedo and phase function that could be used to investigate the physical evolution of cometary nuclei.

This thesis demonstrates the capabilities of the currently available instrumentation and data analysis techniques for photometric characterisation of comet nuclei from ground-based telescopes. The results presented below, combined with the most recent findings from the Rosetta mission, advance the understanding of the physical parameters and the surface properties of JFCs. The observational results inspired a hypothesis for the activity-driven evolution of JFC nuclei, which can be validated by future observations. This work has therefore provided an inspiring perspective to find the links between comet nuclei and their related small-bodies populations (Kuiper Belt objects, Centaurs and Near-Earth asteroids) in terms of cost-effective and easy to execute ground-based optical observations.

Chapter 2

Towards a better understanding of comets

2.1 Milestones in cometary science

2.1.1 Early work

Comets are among the most remarkable phenomena on the night sky. They can become visible to the unaided eye and may span tens of degrees on the sky. Such objects did not remain unnoticed, and their seemingly irregular appearances caused strong feelings of fear and awe throughout history. In records found all over Europe, for centuries, comets were considered to be bad omens predicting upcoming disasters (Fig. 2.1).

The historical evidence of comet observations go back millennia. Continual records of the positions and appearance of comets from around 1000 BC until the nineteenth century have been found in China. They were collected because of the astrological importance that was assigned to comet sightings.

Ideas about the true nature of comets developed gradually, starting in Ancient Greece. Around 330 BC, Aristotle described comets as a meteorological phenomenon occurring in the atmosphere. This view remained popular until the precise observations of Danish astronomer Tycho Brahe enabled him to determine

Figure 2.1: Illustration of a comet observed in 1506 from the "Augsburg Book of Miraculous Signs", 1552. The appearance of the comet was interpreted as an omen for the crops in the same year as well as a destructive earthquake in southern Europe in the following years.

the parallax of comet C/1577 V1 in 1578, proving that the comet was further away from Earth than the Moon. This opened a new chapter in cometary science with a main focus on understanding the orbits of comets (see Festou et al., 2004, and references therein).

This effort was enabled by the publication of Newton's 'Principia' (Newton, 1687), which provided the necessary tools to derive the orbital parameters of comets. The periodic nature of comet apparitions was conclusively proved when the reappearances of comets 1P/Halley and 2P/Encke were accurately predicted by the calculations of Halley (1705) and Encke (1822), respectively.

Over the course of the nineteenth century an increasing number of comets were observed with polarimetry and spectroscopy. The connection between comets and meteors was established and the basic understanding that comets have nuclei which lose material when illuminated by the Sun, gradually developed (see Festou et al., 2004, for a detailed review).

These findings led to the icy-conglomerate, or "dirty-snowball" model proposed by Whipple (1951, 1950), which set the foundations of modern understanding of comet nuclei. It described the nucleus as a solid mixture of ice and dust, which produces increasing quantities of gas as it approaches the Sun and its surface temperature rises.

The icy-conglomerate model suggested very high material strengths that enable the comets to survive close perihelion passages close to the Sun. According to the current understanding, however, comets have very low tensile strengths (see Section 2.3.6). Thus the two later 'rubble-pile' models – the 'fluffy aggregate' model (Donn et al., 1985; Donn & Hughes, 1986) and the 'primordial rubble pile model' by Weissman (1986) are currently favoured. These models describe the nuclei as aggregates of small icy planetesimals which are held together by gravity or weak cohesive forces.

2.1.2 Basic structure of comets

Nowadays, the large-scale structure of comets is well-understood (Fig. 2.2). They consist of a nucleus composed of dust particles, ice and complex molecules of the most abundant elements (H, C, N and O). When comets are observed at a large distance from the Sun, only the nucleus is present. Closer to perihelion, however, sublimation of the surface layers of the nucleus (driven mostly by H_2O, CO_2 and CO ices) causes the release of gas and dust. The released material expands in the surrounding vacuum and forms an envelope around the nucleus known as coma. Even though comet nuclei are typically only up to a few tens of kilometres in diameter, their comae can stretch up to thousands, or even millions of kilometres.

Solar radiation pressure and the solar wind act on the coma to form a tail pointing away from the Sun. Comet tails can have two components. The dust particles form a dust tail, which is left behind tracing the cometary orbit and curving due to the different pressure exerted on particles with different sizes. The

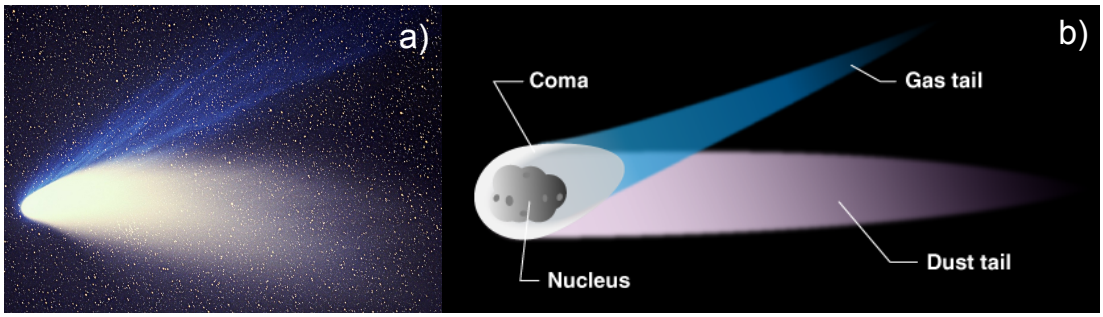

Figure 2.2: Basic structure of a comet: a) Image of comet C/1995 O1 (Hale-Bopp), from 1997 April 04 Credits: E. Kolmhofer, H. Raab; Johannes-Kepler-Observatory, Linz, Austria; b) Schematic overview of the structure of comets (nucleus not to scale).

gas molecules, on the other hand, are ionized by the UV radiation coming from the Sun and are strongly affected by the solar wind. They form the gas tail which follows the magnetic field lines of the solar wind in anti-solar direction.

2.1.3 Spacecraft exploration of comet nuclei

Even though, with the increase of knowledge over the past few centuries, comets have become less mysterious, they still remain equally fascinating to scientists and the public. While there have been no spectacular comet appearances in the past decade, the recent spacecraft visits to comet nuclei, and in particular the Rosetta mission, have brought a lot of attention to comets.

Rosetta's rendezvous with comet 67P/Churyumov-Gerasimenko between 2014 and 2016 was the culmination of a thirty-year long quest for in situ space exploration of comet nuclei. The space era of cometary science began with the NASA spacecraft International Cometary Explorer (*ICE*). Its main goal was to study the interaction of comets with the solar wind. *ICE* flew through the tail of comet 21P/Giacobini-Zinner at 7860 km from the nucleus at its closest approach. Later, it passed through the tail of comet Halley about 31 million kilometres away from the nucleus on 11 September 1985.

ICE was part of the so called Halley 'Armada' - a suite of space missions aiming to explore comet Halley during its apparition in 1986. The 'Armada'

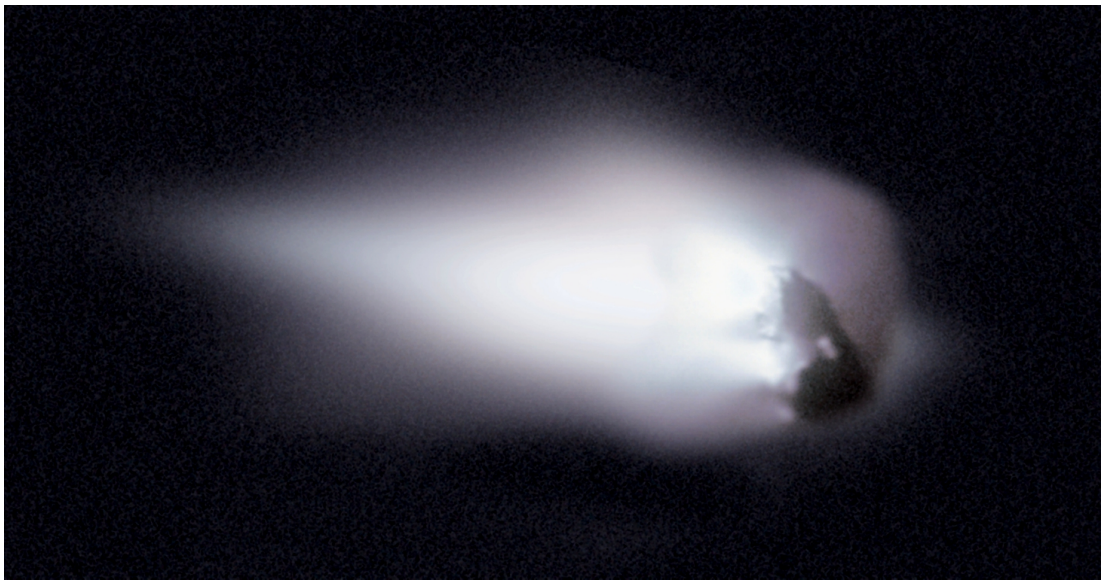

Figure 2.3: Nucleus of comet 1P/Halley observed by the Multicolour Camera on *Giotto* during the fly-by in 1986.

included also the Japanese twin spacecraft *Sakigake* and *Suisei*; the Soviet/French probes *Vega-1* and *Vega-2*, and ESA's *Giotto* mission. *Vega* and *Giotto* returned the first images of a comet nucleus (Fig. 2.3, Keller et al., 1986; Sagdeev et al., 1986). Furthermore, these two missions were able to derive some fundamental properties of comet nuclei for the first time. They showed that Halley's nucleus is small and elongated ($15 \times 7 \times 7$ km); it has a dark reddish surface with an albedo of ~ 0.04; it is porous and has low density of 550 ± 250 kg/m^3; it has a complex state of rotation with a period of 2.84 days; its surface has a complex topography of ridges and terraces; its activity comes from jets concentrated in areas of enhanced activity (Keller & Thomas, 1997).

Since the extensive study of comet Halley, the number of comets with spacecraft images of resolved nuclei has increased to five (Fig. 2.4). On 22 September 2001 NASA's *Deep Space 1* spacecraft had an approach to comet 19P/Borrelly and returned detailed images of its surface (Britt et al., 2004). Following this success, on 2 January 2004 NASA's *Stardust* mission had a closest approach within 240 km of the nucleus of comet 81P/Wild 2 (Brownlee, 2014). *Stardust*'s primary mission was to collect dust particles from the coma of 81P. The dust particles

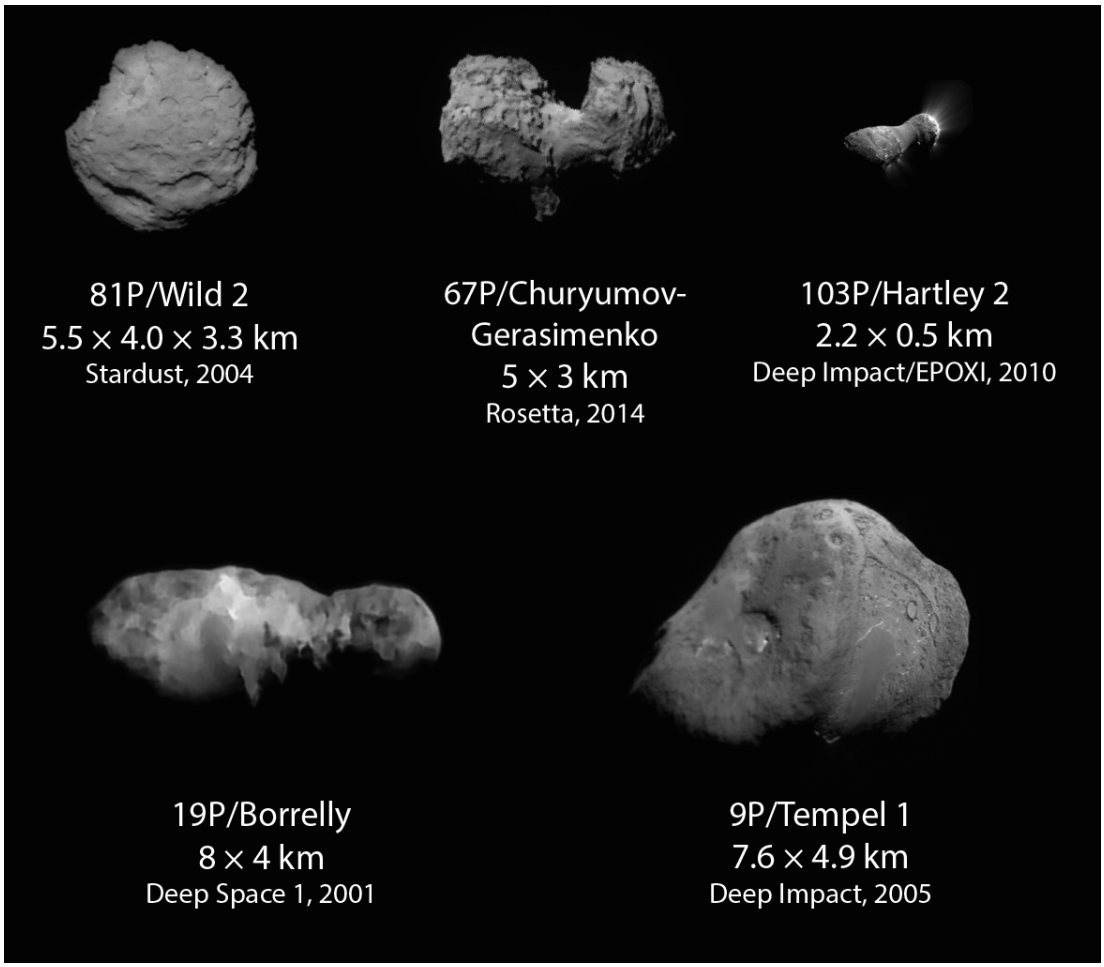

Figure 2.4: Nuclei of the Jupiter-family comets visited by spacecraft. Modified version of a montage by Emily Lakdawalla, The Planetary Society. Image credits: Borrelly: NASA / JPL / Ted Stryk. Tempel 1 and Hartley 2: NASA / JPL / UMD. Churyumov-Gerasimenko: ESA / Rosetta / NavCam / Emily Lakdawalla. Wild 2: NASA / JPL. Montage by Emily Lakdawalla.

were collected in a sample-return capsule, which was delivered to Earth in 2006.

Stardust was extended to *Stardust-NExT* (New Exploration of Tempel 1). The goal of *Stardust-NExT* was to visit comet 9P/Tempel 1 in 2011 (Veverka et al., 2013). This was decided because Tempel 1 had been the target of another mission - NASA's *Deep Impact* (A'Hearn et al., 2005). *Deep Impact* was designed to release an impactor onto the comet in order to study its interior composition. The impactor successfully reached the comet on 4 July 2005, returning close up images of the surface up to a few seconds before touchdown. However, the impact released a bright dust cloud which obscured the observations of the crater. Therefore,

to study the results of the impact, on February 15, 2011 *Stardust-NExT* was redirected to perform a close fly-by 200 km from the nucleus to study the impact crater as well as the activity-driven changes on the surface during 9P's perihelion passage.

After the flyby to 9P, *Deep Impact* was directed toward comet 103P/Hartley 2 as part of the extension mission *EPOXI* (A'Hearn et al., 2011). In November 2010 *EPOXI* approached 103P within 700 km of the nucleus, providing high-resolution images of its surface, activity jets and inner coma.

2.1.4 The Rosetta mission

The Rosetta space probe was developed by ESA and launched on 2 March 2004. Rosetta had two parts - an orbiter with 12 science instruments on board and the Philae lander with ten instruments (Glassmeier et al., 2007). With this suite of instruments, Rosetta was the most ambitious comet mission to date. The extensive scientific program of Rosetta included studying of the nucleus composition, the interior of the nucleus, the surface, the inner coma and the plasma environment. The mission intended to provide a comprehensive characterisation of the nucleus and the mechanisms which drive its activity in order to improve the understanding of the origin of comets (Glassmeier et al., 2007).

After fly-bys of asteroids 21 Lutetia and 2867 Steins, and a total of ten years in space, Rosetta reached comet 67P in the summer of 2014. It performed a series of manoeuvres and entered an orbit around the comet nucleus on 6 August 2014, when the comet was 3.7 au from the Sun (Taylor et al., 2015).

During the first month, Rosetta characterised the nucleus and selected a landing site for Philae. The lander was delivered to the comet nucleus on 12 November 2014 when 67P was about 3 au from the Sun (for a detailed overview of the Philae landing, see Boehnhardt et al., 2017). The lander reached the chosen landing site, but due to failure of its anchoring mechanisms it bounced off the surface and

after two more possible surface contacts it eventually landed at another region of the comet. Starting from the first touchdown the lander performed the planned scientific sequence of experiments for 56 h and 28 min until the battery power was exhausted. Even though some of the measurements were compromised because of landing complications, the lander delivered unprecedented measurements from the comet surface.

Rosetta continued orbiting the comet for over two years, accompanying it during its most active phase around the perihelion passage on 13 August 2015. The continuous monitoring of the nucleus, the volatiles and dust released throughout this period allowed the seasonal effects on a comet to be monitored continuously for the first time.

The mission was terminated on 30 September 2016 when the orbiter was crash-landed on the comet surface and the signal transmission to Earth was interrupted. During the whole mission, the instruments on board Rosetta collected a huge volume of scientific data, which already provided answers to long-standing questions in cometary science and will serve as the foundation of future studies on comets (see A'Hearn, 2017).

2.2 Comet life cycles

It has been widely accepted that comets formed in the early Solar System and have remained mostly unaltered since then (e.g. Davidsson et al., 2016). There is, however, growing evidence suggesting that comet nuclei might not be primordial. Instead, it is possible that they have formed later from re-accretion of material ejected from planetesimal collisions (Jutzi et al., 2017; Schwartz et al., 2018) or from repeated fission and reconfiguration cycles (Hirabayashi et al., 2016). Moreover, once sublimation sets in and the comets become active, they are also expected to undergo dramatic changes. Understanding better the different stages of cometary evolution and their signatures on the nuclei is therefore key for

discerning the primordial nucleus properties and relating them to the early Solar System history. The following sections presents the current understanding of the different stages of the life cycle of comets.

2.2.1 Comets and related populations

This section presents the different classes of small bodies related to JFCs. Defining the different populations currently observed in the Solar System and recognising the relationships between them is a necessary step for understanding the different stages of comet evolution.

Historically, comets have been defined as objects which show signs of activity (coma, dust/gas tails). They were first divided into two groups: long-period comets (LPCs, with periods $P > 200$ years), and short-period comets ($P \leq 200$ years). Later, short-period comets were divided into Halley-type comets ($20 \leq P \leq 200$ years) and Jupiter-family comets ($P < 20$ years).

The formal distinction between comets and the various small body populations in the Solar System is often based on the Tisserand parameter with respect to Jupiter:

$$T_J = \frac{a_J}{a} + 2\sqrt{\frac{a(1-e^2)}{a_J}}\cos(i), \tag{2.1}$$

where e, i, and a are the eccentricity, inclination and semi-major axis of the orbit of the object, and a_J is the semi-major axis of Jupiter's orbit (a_J is approximately 5.2 au). The Tisserand parameter is a useful characteristic of the orbits of minor planets since it remains approximately constant for any object even after perturbations by Jupiter. (Levison, 1996).

For the purposes of this paper, I consider JFCs to be objects with $2 \leq T_\mathrm{J} \leq 3$ that have been observed as active during more than one apparition (and therefore have periodic comet designations, e.g. 9P/Tempel 1). According to Levison (1996), Halley-type and long-period comets have $T_\mathrm{J} \leq 2$, and all active objects with T_J

> 2 are classified as ecliptic comets. Thus, the class of ecliptic comets includes active asteroids and active Centaurs. These objects have been observed as active during multiple orbits, and therefore have been given periodic-comet designations. However, since they are believed to have different physical properties from JFCs, I focus the analysis below only on objects with $2 \leq T_{\rm J} \leq 3$.

Centaurs have orbits with semi-major axes between those of Jupiter and Neptune and Jovian Tisserand parameters above 3.05. Their orbits are unstable because they cross the orbits of the giant planets. The list of Centaurs with known activity includes 29P/Schwassmann-Wachmann 1, 39P/Oterma, 95P/Chiron, 165P/Linear, and 174P/Echeclus (see Jewitt, 2009). JFCs are likely to have originally been Centaurs as both are believed to have evolved from the Scattered disc (SD) and the Kuiper belt (KB, also known as the Edgeworth-Kuiper Belt) inwards towards the inner Solar System (see Section 2.2.3). However, the known active Centaurs are larger than JFCs and show mass loss at heliocentric distances larger than 5 au where water sublimation cannot be the major driving mechanism for the observed activity. This suggests that the known Centaurs are shaped by different processes and must be studied as a separate population.

Active asteroids have semi-major axes $a < a_J$ and $T_J > 3.08$ (see Jewitt et al., 2015). Despite showing evidence for mass loss, these objects have typical asteroid-like values for characteristics such as orbital dynamics, colours, and albedos (for a review, see Jewitt et al., 2015). Active asteroids must therefore also be considered as a separate population from JFCs.

The median dynamical lifetime of JFCs (the time before they undergo ejection from the Solar System or ultimate destruction by collision with a planet or the Sun) is approximately 3×10^5 years (Duncan et al., 2004). This implies that the JFC population needs to be resupplied with newly incoming comets from reservoirs away from the Sun, where their volatile content could remain preserved.

The reservoirs supplying JFCs are believed to be the SD and the KB. The SD consists of objects with perihelia greater than 30 astronomical units with

orbital eccentricities up to 0.8 and inclinations reaching 40°. The Kuiper belt is a population of objects with moderate eccentricities and inclinations, situated between the orbit of Neptune (at heliocentric distance of 30 au) up to $\sim$ 50 au from the Sun. Often, the objects from the SD and the KB together are referred to as Trans-Neptunian Objects, or TNOs.

The reservoir supplying long-period comets is believed to be the Oort cloud. The Oort cloud is a theoretically predicted population of icy planetesimals at distances ranging between $\sim$1,000 and 50,000-200,000 au from the Sun. The existence of the Oort cloud was conjectured by Oort (1950) to explain the large semi-major axes and the random inclination of the orbits of long-period comets (see Festou et al., 2004, and references therein).

The final class of objects that needs to be mentioned in relation to comets are the so called asteroids on cometary orbits (ACOs). According to the definition in Fernández et al. (2005a), these are Near-Earth objects (with perihelion distance $<$ 1.3 au) or "unusual" asteroids (UAs; inner Solar System objects with perihelion distance $>$ 1.3 au and with large eccentricities and/or inclinations) which have $T_{\rm J} \leq 3$. These objects do not show signs of activity and could be either inactive comet nuclei or asteroids from the main belt which have been placed in cometary-like orbits.

2.2.2 Comet formation

According to the most widely accepted models, JFCs were formed beyond the snowline in the early Solar System about 4.6 Gyr ago through a process of very gentle accretion. Formation from low-velocity collisions of planetesimals is necessary to explain the low bulk density and high porosity (Section 2.3.5), as well as the low strength (Section 2.3.6) of comet nuclei. On the other hand, the presence of supervolatiles (e.g. CO, CO_2, N_2 and Ar), the possible presence of amorphous

water ice and the lack of metasomatism[1] and aqueous-alteration signatures suggest that comets have not undergone significant thermal processing due to collisions during the accretion phase or due to internal radiogenic heating from short-lived radionuclides such as ^{26}Al (see Davidsson et al., 2016; Guilbert-Lepoutre et al., 2016, and references therein).

According to the well-established Nice model for the early evolution of the Solar System (see Section 2.2.3), comets were formed in the transplanetary disc (e.g. Tsiganis et al., 2005). This was a region consisting of dust and ice particles with a total mass of 20-50 Earth masses. It extended out to a heliocentric distance of 30 au, beyond the orbits of the giant planets, which were closer to the Sun at that point (Levison et al., 2011).

The details of the processes in the transplanetary disc that led to the formation of the planetesimals which eventually became today's comets are still subject to debates (Johansen et al., 2014). It is believed that initially, the μm-sized particles collided with very low speeds, which led to sticking and the growth of porous pebbles. The growth continued until the aggregates became $\sim$ 1 cm in size and reached the bouncing barrier (Zsom et al., 2010). There are two possible mechanisms which led to forming planetesimals from the pebbles. The planetesimals could be formed via hierarchical agglomeration (e.g., Weidenschilling et al., 1997; Windmark et al., 2012) and/or gravitational collapse of pebble clouds formed in streaming instabilities (e.g., Youdin & Goodman, 2005; Johansen et al., 2007; Jansson & Johansen, 2014; Blum et al., 2017; Lorek et al., 2016, 2018)

These processes are able to produce planetesimals which have the characteristics of today's comet nuclei. The outcomes of these scenarios are 'primordial rubble-pile' nuclei (Weissman, 1986). The term rubble-pile is usually used to describe the structure of asteroids larger than $\sim$100 m. They are believed to have undergone multiple collisions which left them as aggregates of rocks bound together only by

[1]Metasomatism is defined as the change in the composition of a rock due to introduction or removal of chemical compounds as a result of interactions with fluids.

gravity (e.g. Pravec et al., 2002). In contrast, the 'rubble-pile' structure of comet nuclei is considered to be primordial and not the result of subsequent collisional evolution as for asteroids (see Weissman et al., 2004).

One problem with this formalism for comet formation is that recent dynamical studies indicate that JFC nuclei of the size of comet 67P must have undergone multiple collisions in the past (e.g., Morbidelli & Rickman, 2015; Rickman et al., 2015). It is important to keep in mind that the calculated collision rates depend on the details of the models used for the dynamical simulations, and in alternative models (e.g., Davidsson et al., 2016) it is possible to avoid significant collisional processing. Even though it is not certain whether comets are collisionally processed, the possibility that they have undergone collisions either in the transplanetary disc or the SD and KB, have inspired a number of interesting studies. In particular, the recent works by Jutzi et al. (2017) and Schwartz et al. (2018) suggest that even after a number of shape-changing collisions, it is possible to produce bodies with the physical characteristics of comet 67P.

These works propose an interesting shift in the common perception that the structure of comets is primordial. If the nuclei of JFCs observed today are collisional remnants of larger planetesimals, they must be collisional rubble-piles formed recently instead of being primordial rubble-piles. If this is the case, the cometary parameters derived from observations and spacecraft visits probe the collisional environment in the transplanetary disc, the SD and the KB, as well as the processes of collisional disruption and subsequent gravitational re-assembly, rather than the conditions in the solar nebula and the protoplanetary disc. Understanding whether comet nuclei are primordial, is therefore one of the most important tasks of cometary science after Rosetta, since this question determines to what extent the observations from spacecraft instruments can be used to interpret the history of the early Solar System

2.2.3 From planetesimal to JFC

The fate of the planetesimals formed in the outer Solar System is currently best understood in the framework of the Nice model, which was first proposed by Tsiganis et al. (2005) and Gomes et al. (2005), and later revised by Levison et al. (2011); Nesvorný (2011); Batygin et al. (2012); Nesvorný & Morbidelli (2012). The Nice model explains a number of characteristics of the Solar System structure and reproduces the Late Heavy Bombardment (LHB) of the terrestrial planets from 3.8 Gyr ago (Gomes et al., 2005). The LHB is well-constrained from lunar crater records to about 400 Myr after the formation of the primordial disc, and therefore can be used to set the time frame of the Nice model to that period.

According to the original version of the Nice model, the giant planets formed within 15 au of the Sun on orbits with low eccentricities and inclinations. Gravitational interactions of planetesimals from the transplanetary disc with the outer planets led to slow migration of the giant planets, until after 700 Myr Jupiter and Saturn reached a mutual 1:2 mean motion resonance. This event destabilised the outer Solar System and lead to the dispersal of the transplanetary disc. The majority of the planetesimals were scattered throughout the Solar System and were lost due to collisions with the planets and the Sun, or left the Solar System. A small fraction of them, however, was trapped in the Oort cloud, the SD and the KB (see Levison et al., 2011), as well as in the asteroid belt, as Jupiter Trojans, and as irregular satellites (see Nesvorný et al., 2017, and references therein). Thus, in the framework of the Nice model, the Oort cloud and the scattered disc were formed from the same original population (Brasser & Morbidelli, 2013). Even though the details of the Nice model have evolved since the original idea (e.g. Nesvorný, 2011; Batygin et al., 2012; Nesvorný & Morbidelli, 2012), the link between planetary migration and the formation of the Oort cloud, the SD and the KB is common to all scenarios.

Since the focus of this thesis is on Jupiter-family comets, only the subsequent

dynamical evolution of objects from the SD and the KB is discussed further. Levison & Duncan (1997) and Duncan & Levison (1997) performed dynamical simulation to study the origin and evolution of JFCs and Centaurs. They discovered that some objects can leak from the two populations (SD and KB) and can get scattered towards the inner Solar System to become Centaurs. When encountering a planet, these objects get scattered inwards and outwards in a random walk, getting passed to the next planet interior or exterior to it (Duncan et al., 2004). If the orbits of Centaurs evolve to cross Jupiter's orbit, they become dynamically dominated by Jupiter, and are therefore considered to be part of the JFC population. These objects encounter increasing energy input from the Sun along their path towards the inner Solar System and are expected to begin sublimating. This marks the beginning of their phase as active JFCs.

2.2.4 Final stages

Dynamical simulations have determined that the median dynamical lifetime of JFCs is 3.25 $\times 10^5$ years (Duncan et al., 2004). This is defined as the time from entering a JFC orbit until the comet is ejected from the Solar System or is destroyed by encounters with planets or the Sun. A spectacular illustration of one of these scenarios was the encounter of comet Shoemaker-Levy 9 with Jupiter which led to fragmentation in 1992 and subsequent collision of the fragments with Jupiter in 1994.

In addition to the dynamical pathways to comet destruction or ejection, there are a few other possibilities for the final fates of comets. These mechanisms determine the physical lifetime of comets. Most nuclei are believed to either gradually lose their activity until they become dormant or dead comets, or, alternatively, to experience catastrophic comet-splitting events (see Jewitt, 2004; Boehnhardt, 2004).

One of the possible mechanisms leading to comet splitting is activity-driven

spin-up (see Section 2.3.3). This mechanism takes place when outgassing produces torques which bring the rotation periods of the nuclei down to a critical limit. Below this limit, the centrifugal force exceeds the gravity and the material forces, and the comet nucleus starts to shed mass and disintegrates (e.g. Davidsson, 1999, 2001).

If the nuclei do not undergo significant mass-loss and disruption events during the prime of their activity as JFCs, they are expected to gradually decay in activity until they become dormant (nuclei for which the available volatiles are shielded from solar insolation) or dead (totally devolatilised) comets (Weissman et al., 1999; Jewitt, 2004). Due to the lack of detectable activity of these objects it is difficult to distinguish dormant/dead comets from asteroids that have been placed on comet-like orbits (Fernández et al., 2001, 2005a).

2.3 Physical properties of JFCs

2.3.1 Direct observations of comet nuclei

Spacecraft visits provide the only opportunity to observe comet nuclei directly and to characterise them in detail. However, in situ observations are limited only to very few objects and cannot be used to derive the ensemble properties of the whole population. It is therefore necessary to employ other techniques in order to extract the properties of an extended sample of JFCs. The list of possible methods includes ground- and space-based photometric telescope observations in visible wavelength, visible and near-infrared (near-IR) spectroscopy, infrared (IR) observations of the comet's thermal emission and radar observations.

Visible-wavelength photometry can be used to detect comet nuclei by observing the sunlight reflected by the nucleus. These observations are based on observing techniques developed for asteroids and can be used to determine the colours as well as the apparent magnitudes of the nuclei (which is equivalent to the product

of the albedo and the object cross-section). Photometric observations of comet nuclei are, however, more challenging than those of asteroids because of cometary activity. When the comet is active, it is hard to distinguish the nucleus because it is faint with respect to the light scattered from the dust grains in the surrounding coma.

There are two ways to avoid this complication: either to observe the 'bare' nuclei at large heliocentric distances (>3 au) when they are expected to be inactive, or to observe comets with low levels of activity, which remain inactive even close to the Sun. Since the latter approach is only possible for very few JFCs, most photometric observations are done for comet nuclei at large heliocentric distances. Due to the small nucleus sizes and low albedos, however, comet nuclei are faint in these configurations and typically require at least 2-4 metre diameter telescopes (Figure 2.5). An additional complication of these observations is that they have the risk of containing hidden coma contribution, which may remain unresolved if the comet is active even at large heliocentric distances (for more details, see Section 3.5).

In certain favourable configurations, when comets pass at small geocentric distances, it is possible to benefit from the high spatial resolution of the Hubble Space Telescope (HST) in order to derive the nucleus properties even in the presence of a surrounding coma (Lamy & Toth, 1995). In order to extract the signal of the nucleus from such observations, the combined surface brightness distribution of the nucleus and the coma are modelled and compared to the images. This technique has been successfully used to derive the properties of many JFCs (Lamy et al., 2011) and has been verified from comparison with measurements obtained with other techniques.

The sizes and surface properties of comet nuclei can also be characterised by observing the comets' thermal emission in mid-IR wavelengths, typically between 5-20 μm (for a detailed overview of this technique, see Lamy et al., 2004). In order to extract information from the measured thermal continuum flux density,

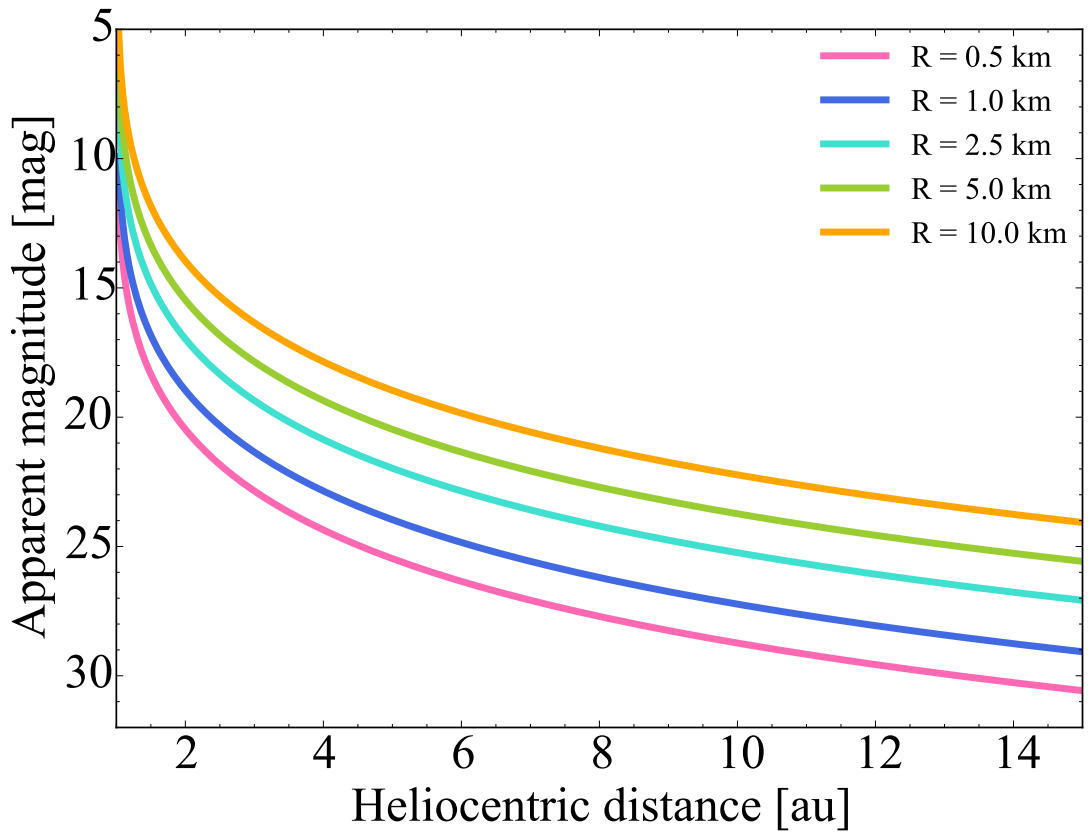

Figure 2.5: Apparent magnitude in r-band of inactive cometary nuclei of different effective radii at opposition. The magnitude estimates assume an albedo A_r = 0.04 and apparent magnitude of the Sun m_r = -26.91 mag.

a surface temperature map needs to be calculated. This can be done using a thermophysical model, which incorporates the size, shape, rotation period, spin axis orientation, thermal inertia (equal to the square root of the product of the bulk density, conductivity and heat capacity of the surface layer of the comet) and surface roughness to predict the surface temperature and hence the thermally emitted flux to fit to the observed flux. In most cases, shape and spin are unknown, so simple models that represent extreme cases are commonly used. These are the 'standard thermal model' and the 'isothermal latitude model'. The isothermal latitude model is used when the objects spin fast or have high thermal inertia, which does not allow every point on the surface to cool once it is no longer sunlit. The standard thermal model applies to objects with slow rotation or low thermal inertia. For such bodies, each surface element instantaneously achieves equilibrium

with the incident solar radiation. Therefore, the maximum temperature is reached at the subsolar point and drops to zero at the terminator, while the dark side does not contribute to the thermal emission. It has been found that comet nuclei behave as slow rotators, and therefore, the Near-Earth Asteroid Thermal Model (Harris, 1998), based on the standard thermal model, is used to interpret their IR observations.

A crucial parameter in thermal modelling is the beaming parameter, η. It is used to describe how much infrared 'beaming' a body has, which is determined by the thermal inertia and the surface roughness. For instance an object with no topographical features and zero thermal inertia has $\eta = 1$. The presence of some night-side emission lowers the surface temperature and raises η to above 1. The beaming parameter can be lowered if prominent features such as craters and pits are present on the surface. If the thermal emission is measured in at least two wavelengths, fitting the thermal model can be used to derive both the radius of the comet nucleus and η. If only measurements in a single wavelength exist, an assumption of the beaming parameter needs to be made in order to derive the nucleus radius (e.g. Fernández et al., 2013).

This technique can be used to find the sizes of comet nuclei even in the presence of weak to moderate activity. This can be done by modelling the surface brightness of the coma and/or the tail away from the nucleus and extrapolating the dust contribution close to the centre. Thus the dust contribution can be removed in order to extract the point-source corresponding to the nucleus (see Lamy et al., 2004; Fernández et al., 2013).

At even longer wavelengths, JFC nuclei can be studied using radar observations. In this technique, bursts of microwaves of a certain power are sent towards a nucleus in order to measure the returned echo. These observations are only available for the few comets that pass close to Earth, since the radar detectability decreases with Δ^{-4}, where Δ is the geocentric distance. Radar data can be used to reveal the radar-albedo and the bulk density of the top surface layers. For a

detailed overview of radar observations of comets, see Harmon et al. (2004).

The final technique which can be used to study comet nuclei from ground- and space-based telescopes is spectroscopy. The spectra of bare nuclei in visible and IR can be obtained in order to study their surfaces. More details about the outcomes of this technique can be found in Section 2.4.2.

2.3.2 Size distribution

The size distributions of small-body populations in the Solar System can put constraints on their formation and evolution. Deriving the size distribution of JFCs can be used to address some of the most important questions in cometary science, e.g. whether comet nuclei are primordial or shaped by collisions, or what processes dominate the final stages of the cometary life cycle.

The sizes of comet nuclei are more accessible to observers than most other nucleus parameters. The easiest way to estimate the size of a comet nucleus is to convert its apparent magnitude in visible wavelengths to size using an assumption of the albedo (see equation 3.9 in Section 3.6.3). Typically an albedo of 4% is assumed for all nuclei (see Section 2.4.4). The brightness can be determined either by observations at large heliocentric distance when the comet is inactive, or by modelling the coma in high-resolution images. Alternatively, as described in Section 2.3.1, comet radii can be derived by thermal modelling of IR observations, or by radar observations. These techniques are technically more difficult than visible-wavelength photometry but are expected to produce more accurate results, since they do not rely on assumptions about the albedo, and are less influenced by the effects of cometary activity.

The cumulative size distributions (CSD) of small-body populations are usually expressed as:

$$N(> r_N) \propto r_N^{-q}, \tag{2.2}$$

where N is the number of comet nuclei with radius larger than r_N. The slope of the power law, q, is used to characterise and to compare the different small-body populations.

If the objects in a certain population experience a lot of collisions, some objects get destroyed and the number of smaller objects increases over time in a process known as collisional cascade. Analytical models show that collisionally relaxed populations consisting of self-similar bodies that have identical collisional response parameters (e.g. strength per unit mass) have a power-law distribution with q = 2.5. (Dohnanyi, 1969). The power-law index q = 2.5 is therefore expected to characterise collisionally evolved populations, such as the asteroid belt. In comparison, collisional populations of strengthless bodies (bodies held together just by gravity) are expected to have a shallower slope, q = 2.04 (O'Brien & Greenberg, 2003).

There have been numerous attempts to determine the CSD of JFCs (e.g. Lowry et al., 2003; Lamy et al., 2004; Meech et al., 2004; Tancredi et al., 2006; Snodgrass et al., 2011; Weiler et al., 2011; Bauer et al., 2017). The shapes of these distributions are very similar. However, the slopes derived in each work are somewhat different, partially because the power laws were derived for a different range of nucleus sizes. All of these studies are based mostly on sizes determined from snapshot photometry of distant nuclei. These results are therefore expected to be influenced by the assumptions made while converting the photometry to sizes (e.g. assumed albedo, phase function and shape of the nucleus, as well as photometric uncertainty). In order to assess the uncertainty of the CSD slope, Snodgrass et al. (2011) performed Monte Carlo simulations accounting for all of these effects and determined $q = 1.92 \pm 0.20$ (for nuclei with radius $r_N \geq 1.25$ km).

The largest sample of JFCs sizes was collected within the SEPPCoN program (Fernández et al., 2013). The survey combined mid-infrared measurements from the Spitzer Space Telescope with quasi-simultaneous ground-based visible light

photometry from 2-8m telescopes. The infrared observations were used to derive the sizes, while the ground-based visible photometry was collected to study the albedos, colours and lightcurves of the comet nuclei. Since the SEPPCoN sizes were derived from thermal IR data, they are expected to be more accurate than those from previous studies that were derived mainly from snapshots of bare comet nuclei. Nevertheless, the shape of the CSD from Fernández et al. (2013) was found to be very similar to the CSDs from the previous studies. The power law slope of the CSD determined from the 89 comets included in Fernández et al. (2013) was found to be around 1.9 (depending on the radius range chosen for the fit). Thus, the derived CSD of JFC nuclei is consistent with the expected value for collisionally relaxed population of strengthless bodies from (O'Brien & Greenberg, 2003).

However, it is important to consider that JFCs are not expected to match the collisional CSD completely, even if comet nuclei are collisional fragments. With every apparition, the nuclei of active comets lose mass due to sublimation, which leads to a progressive size decrease. Additionally, comet nuclei can undergo fragmentation or fatal disruptions (e.g. Boehnhardt, 2004; Fernández, 2009, and references therein).

If these processes are more efficient at destroying small comets, they can be used to explain the shallower CSD measured for small radii (Meech et al., 2004; Fernández et al., 2013). While the paucity of sub-kilometre JFCs can be attributed to a bias against the discovery and observations of small objects, the analysis of Meech et al. (2004) determined that the discovery bias only partially contributes to the shallow CSD. Meech et al. (2004) therefore concluded that the lack of small comets must be a real feature of the population.

Using data from the NEOWISE project, which utilises the Wide-field Infrared Survey Explorer (WISE) infrared telescope, Bauer et al. (2017) derived the size distributions of JFCs and LPCs and debiased the samples of observed comets in order to remove the effects of the systematic observational biases. They did not

find evidence for a turnover at small sizes in either population, however, due to the small-number statistics at those size ranges its presence could not be ruled out. The comparison of the two populations indicated that the average size for JFCs is smaller by a factor of 1.6 than for LPCs. Bauer et al. (2017) also found slightly different debiased size distributions for the two populations, which they attributed to the evolutionary mass loss of JFCs that decreases the sizes of all comets and possibly destroys the smaller ones.

An alternative explanation for the shallow CSD at small radii is the hypothesis that it reflects the CSD of the source populations of JFCs in the KB and the SD. Interestingly, recent evidence from the Pluto flyby of the New Horizons mission adds new evidence to this debate. The size distribution of impact craters on Pluto and Charon shows a shallower slope for craters below 10 km in diameter suggesting that the "hot" population of the KB (consisting of objects with high inclination) also has a lack of small objects (Singer et al., 2016).

Another interesting feature of the CSD of JFCs was noticed by Fernández et al. (2013). They spotted a small bump in the CSD for radii from 3 to 6 km. Fernández et al. (2013) note that this feature could be an artefact of the low number of comets in this size range, but proceed to interpret it as a remnant from the primordial size distribution of the JFCs' parent population. However, the evidence collected in this thesis suggests that it possibly reflects the evolution of JFCs (see Chapter 8).

2.3.3 Rotation

Spin state

The rotational dynamics of comet nuclei is described through rigid-body dynamics. Comet nuclei are usually represented as rotating triaxial ellipsoids with principal axes $a \geq b \geq c$. The most stable spin state of such a body is the constant angular velocity rotation around the short principal axis (PA). Other PA rotations are

possible around the two longer PA axes.

Rigid bodies can also have non-principal-axis (NPA) rotational states, also known as complex rotational states, or tumbling. The excited states of rotation can be caused by sporadic events such as collisions or recurring excitation from activity. NPA rotation is associated with frictional loss of mechanical energy, which is eventually expected to bring the object back to the least-energetic state of PA rotation around the shortest axis (e.g Jewitt, 1998).

Given sufficiently detailed observations, NPA spin states can be distinguished from PA rotation since NPA rotation states have two independent periods. Only a few comets have been observed to be in an NPA state: e.g. comets 1P, 2P and 29P (e.g. Samarasinha et al., 2004, and references therein) and 103P (A'Hearn et al., 2011). Comet 67P was found to have PA rotation with a small precession of the pole (Jorda et al., 2016). It is important to keep in mind that NPA rotation can remain hidden for observers on ground, depending on the rotational parameters of the nucleus and the observing geometry (Samarasinha et al., 2004). I did not find evidence for NPA rotation for any of the comets analysed in this thesis, and therefore all comets were assumed to be rotating around their shortest principal axes.

PA rotators are characterised by the sidereal rotational period, or the time it takes to make one complete rotation around the rotational axis with respect to distant stars (i.e. in an inertial frame). The periods measured from ground- and space-based telescopes depend on the changes in the Sun-comet-Earth geometry during the observations. Thus these observations measure the synodic periods of comets, and cannot be converted to sidereal periods without knowledge of the rotational axis orientation of the nucleus (e.g. see Samarasinha et al., 2004). However, the difference between the synodic and sidereal rotation periods is expected to be very small when the objects are observed close to opposition (Harris et al., 1984), which is the typical configuration for observing bare comet nuclei. It has been found that the difference between the synodic and sidereal

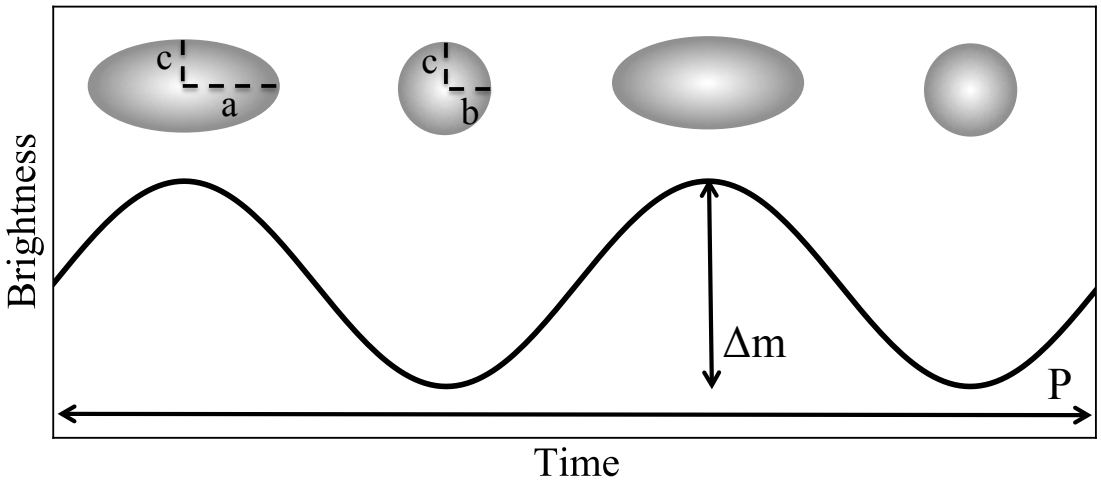

Figure 2.6: The lightcurve of a triaxial ellipsoid with axes a, b, and c, The observed cross-sections and the corresponding lightcurve with period P and peak-to-peak variation Δm are presented for a full rotation of the body.

rotation periods is usually very small (< 0.001 hours) even for near-Earth asteroids (e.g. Pravec et al., 1996), so the synodic rotation periods are good approximations for the spin rates of JFCs, which are typically observed at larger distances.

Rotational lightcurves

A rotating triaxial ellipsoid with uniform albedo will exhibit a periodic change in brightness caused by the modulation of the cross section facing the observer (see Fig. 2.6). One full rotation of the ellipsoid corresponds to two peaks and two minima since each of the four semi-axes will be seen during one period. In this set-up, the period of the lightcurve corresponds to the spin rate of the comet nucleus. The peak-to-peak brightness variation (Δm) gives a lower limit to the axis ratio of the ellipsoid, and therefore constrains the shape of the nucleus. However, we can only consider this result as a lower limit on the elongation of the body, since we do not know the exact inclination of the rotation axis (c) with respect to the line of sight. If we look at the elongated ellipsoid equatorially (aspect angle $\theta = 90°$), we will see maximum variation, while a polar orientation ($\theta = 0°$) will produce a flat lightcurve.

The fact that the orientation with respect to the observer changes the appear-

ance of the observed brightness variation suggests that lightcurves do not directly lead to determinations of the nuclei shapes. The typical approximately sinusoidal shape of the lightcurves can be produced also by surface features with different albedos and scattering functions or even by a binary system. The ambiguity of lightcurve interpretation has been identified for asteroids long ago by Russell (1906) and the limitations of this method remain valid to date. Yet, although the observed lightcurves cannot be uniquely interpreted as signatures of the object's shape, there is a growing body of evidence suggesting that the other possibilities are less likely. This is justified by the data from spacecraft observations, which demonstrate that the albedo non-uniformities of comet nuclei are generally too small to account for the lightcurve variations (e.g. Li et al., 2009, 2013; Fornasier et al., 2015).

There are two main techniques to derive rotational lightcurves from telescope observations: (1) photometric time-series of bare nuclei and (2) periodic variability of coma structures of active comets (for an overview see Samarasinha et al., 2004). The former relies on the direct detection of the nucleus signal, and is expected to produce more precise results (Samarasinha et al., 2004). In order to detect the nucleus brightness variation directly, the comets need to be observed at large heliocentric distances when they are inactive. Observing the comets when they are weakly active can also allow reliable lightcurve derivations, but only in the cases when the nucleus signal dominates over the coma contribution. It is also possible to derive the rotation rates of active comet nuclei, provided that they are observed with sufficient spatial resolution to distinguish the nucleus signal from that of the coma (see Lamy et al., 2004).

Additionally, comet rotations can be studied during spacecraft flybys. Such missions have allowed the rotational properties of three comets to be studied in greater detail: 9P (Chesley et al., 2013, and references therein), 103P (Belton et al., 2013, and references therein), and 67P (Jorda et al., 2016).

This thesis aims to use the known rotational characteristics of JFCs to constrain

the bulk properties of the population. In order to enable this, I have reviewed the known JFCs rotations in Chapter 4.

Rotation changes

Repeated observations of eight JFCs during different apparitions have shown clear indications for spin changes on orbital timescales (see Samarasinha & Mueller, 2013; Eisner et al., 2017; Bodewits et al., 2018, and references therein). Moreover, the direct measurements of the rotation changes of comet 67P/Churyumov–Gerasimenko during the Rosetta mission were successfully reproduced by the numerical model of Keller et al. (2015a). This study confirmed the widely accepted hypothesis that rotation-period changes are controlled by outgassing torques and depend on the shape and orientation of the cometary nuclei (Keller et al., 2015a).

The sublimation-induced jets from the cometary surface generate a net torque which causes the spin state of the nucleus to change (Fig. 2.7). The resulting spin changes of outgassing comets can be described by simple theoretical considerations (e.g. Samarasinha et al., 2004; Samarasinha & Mueller, 2013). In particular, Samarasinha & Mueller (2013) derived that for comets of identical bulk densities, shapes, active-region distributions, and activity mechanisms, the period change per orbit, ΔP is:

$$|\Delta P| \propto \frac{P^2 f \zeta}{R_n^2}. \tag{2.3}$$

In this expression P is the rotation period of the comet, R_n is the radius of the nucleus, f is the effective active fraction (for a definition, see A'Hearn et al., 1995), and ζ is the water production rate per unit surface area at the subsolar point, integrated over the whole active phase during the orbit. This expression shows that the smaller the nuclei and the longer their periods are, the larger the period changes they experience.

The rotation changes of small cometary nuclei were studied by numerical

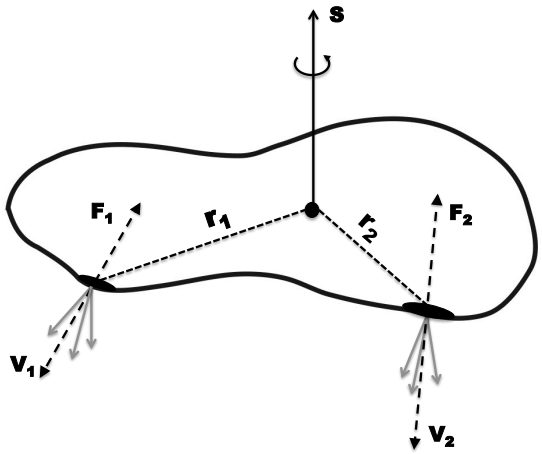

Figure 2.7: A comet nucleus losing mass from two active regions at distances $\mathbf{r_1}$ and $\mathbf{r_2}$ from the centre of mass. The mass is ejected perpendicularly to the surface and exerts recoil forces $\mathbf{F_1}$ and $\mathbf{F_2}$, which result in torques on the nucleus. The net torque, which is a sum of the torques at all individual activity areas, is responsible for changing the spin vector of the comet ($\mathbf{S}$).

models using realistic shape models and activity distributions (Gutiérrez et al., 2005). These authors confirmed that small active nuclei experience typical changes of 0.01–10 hours per orbit. However, to the extent of my knowledge, the spin changes of larger nuclei have not been directly modelled in published works. This is why the observational evidence for small rotation changes of large JFCs presented in this thesis is relevant for understanding the activity-induced rotation changes of JFCs.

Rotation changes are particularly interesting because they can cause comet disruption. If the net torque from outgassing leads to a comet spin up, the rotation period can reach a critical limit beyond which the comet nucleus becomes unstable and starts losing mass and eventually splits (e.g. Boehnhardt, 2004). This happens if the centrifugal force exceeds the self-gravity and the material strength of the nucleus. Comet spin-up can therefore significantly contribute to the erosion of comet nuclei and possibly to the flattening of the CSD of the population.

2.3.4 Shapes

As discussed above in Section 2.3.3, the peak-to-peak amplitude of rotational lightcurves can be used to derive lower limits to the axis ratios of the observed nuclei. If the comet nucleus is represented as a prolate ellipsoid seen equator-on (see Fig. 2.6) the ratio of the maximum and the minimum flux ($F_{\max}/F_{\min}$) corresponds to the ratio of the maximum and minimum cross-section of the comet nucleus ($A_{\max}/A_{\min}$), which is equal to the ratio between the axes (a/b):

$$\frac{F_{\max}}{F_{\min}} = \frac{A_{\max}}{A_{\min}} = \frac{\pi ab}{\pi b^2} = \frac{a}{b}. \tag{2.4}$$

The flux ratio can be calculated from the peak-to-peak magnitude amplitude Δm, and therefore the minimum axis ratio can be calculated as:

$$\frac{a}{b} = 10^{0.4\Delta m}. \tag{2.5}$$

Off-equator viewing geometries will result in smaller Δm and, consequently, a smaller inferred a/b. The median value of the axis ratios derived from telescope observations is ~ 1.5, and a few comets have a/b of up to 2.6 (Lamy et al., 2004). However, the in situ observations of all comets visited by spacecraft show axis ratios larger than 1.5 (See Chapter 4).

Spacecraft images have also revealed an interesting characteristic of comet nuclei shapes that is usually inaccessible for telescope observations. More than two thirds of the comets visited by spacecraft have bi-lobed nuclei (Keller et al., 2015b). The high occurrence of bi-lobed nuclei suggests that this is an important feature which needs to be explained by the formation or evolution models of comets (Massironi et al., 2015; Jutzi et al., 2017; Hirabayashi et al., 2016; Nesvorný et al., 2018).

Rosetta brought two lines of evidence pointing to the conclusion that the two lobes of comet 67P formed separately and subsequently merged during a

low-velocity collision. Firstly, Massironi et al. (2015) provided evidence that the nucleus is characterised by layers with thickness up to 650 m. These strata envelop each lobe individually, which indicates that they must have formed before the lobes merged. Secondly, thermophysical models of the nucleus indicate that the “neck" region of the comet which connects the two lobes has lower levels of energy input throughout the orbit as compared to other regions, and it is therefore unlikely that the neck cavity is a result of enhanced erosion (Sierks et al., 2015; Keller et al., 2015a; Davidsson et al., 2016).

2.3.5 Density

Determining the bulk density of comet nuclei has been among the most prioritised tasks in cometary science. Density depends on the composition and can set important constraints on whether the nuclei are more ice-like or rock-like. It can also provide a better understanding of the internal structure of comet nuclei (and therefore of comet formation mechanisms) because it partially depends on the porosity of the aggregates forming the nucleus. In particular, rubble-piles are expected to have low bulk densities and large porosities due to the macroscopic voids between their building blocks. Therefore, estimates of the density of comet nuclei were needed to confirm the rubble-pile models developed after the flybys to 1P/Halley (see Weissman et al., 2004). However, before Rosetta, the density of comet nuclei could only be measured indirectly.

The first method to derive the density of comets visited by spacecraft is based on the effects of the non-gravitational force (NGF) caused by outgassing of the nucleus while it passes through perihelion. The NGF has a measurable effect on the orbital parameters of the comet that can be used to estimate the nucleus mass. The density can then be calculated from the mass and the volume measured from the spacecraft images. These estimates were done for comets 1P/Halley, 19P/Borrelly, and 81P/Wild 2, and lie in the range between 100 and 1500 kg m^{-3}

(see Jorda et al., 2016, and references therein). NGF forces can also be used to derive the densities of comets not visited by spacecraft. In this case the volume of the nucleus is estimated from the comet radius derived from photometry and assuming a spherical shape (Sosa & Fernández, 2009).

Space missions have contributed significantly to finding the bulk density of comets. The ejecta plume resulting from the Deep Impact experiment on comet 9P/Tempel 1 was used to estimate a bulk density of 470 kg m^{-3} with a range of possible values between 240 and 1250 kg m^{-3} (Richardson et al., 2007; Thomas et al., 2013b). Using the characteristic shape of the nucleus of comet 103P/Hartley 2, and in particular the "waist" connecting the two lobes, A'Hearn et al. (2011) estimated a mean value for the density of 220 kg m^{-3} with possible values between 140 and 520 kg m^{-3} (Richardson & Bowling, 2014).

The close encounter of comet Schoemaker-Levy 9 with Jupiter provided a natural laboratory for investigating the physical parameters of comet nuclei. Solem (1995) used HST observations of the fragments produced by the tidal disruption to model the breakup and derived a density 550 ± 50 kg m^{-3}. Asphaug & Benz (1996) modelled the effects of the tidal force responsible for disrupting the nucleus and estimated the nucleus density to be approximately 600 kg m^{-3}.

Radar observations can be used to constrain the bulk density of comets. The bulk density of the surface layers can be estimated from the radar albedo if the nucleus surface is covered by a thick homogeneous layer (e.g. Harmon et al., 2004). The radar density estimates range between 500 and 1500 kg m^{-3} and generally match the bulk density estimates from the other methods (Harmon et al., 2004). However, it is important to be aware that the radar measurements are only sensitive to the top layer of the comets. The derived densities from this method are characteristic only of the surface layer down to the penetration depth of the radar wave ($\sim$ 10 wavelengths for packed soils).

Attempts to constrain the bulk density of JFC nuclei from ground observations have also been made. If the nuclei are modelled as strengthless prolate ellipsoids

that are held together only by gravity, a minimum density is required to balance the centrifugal force for the given rotation rate (see Section 3.6.3). Considering all JFCs with available rotation rates and minimum axis ratios Lowry & Weissman (2003) determined a cut-off in density at 600 kg m^{-3}, later confirmed by Snodgrass et al. (2006). The lack of objects which require larger minimum densities implies that these objects have been destroyed by the fast rotation. In analogy with interpreting the asteroid spin barrier (Harris, 1996; Pravec et al., 2002), 600 kg m^{-3} is therefore considered to correspond to the bulk density of JFCs. While this density estimate is indirect and relies on a simplified model based on assumptions about the material strength and the shape of JFCs, the derived result is in excellent agreement with the densities estimated from other methods.

Rosetta provided the first direct and precise measurement of a cometary density. The detailed shape model of the comet nucleus allowed its volume to be calculated with great precision (Preusker et al., 2015; Jorda et al., 2016). The mass of the comet was determined by the Radio Science Investigation instrument on board Rosetta. Combining the two parameters allowed Jorda et al. (2016) to determine that the bulk density of the nucleus of 67P is 532 $\pm$ 7 kg m^{-3}. This study also determined that the nucleus has high porosity of 70–75%.

2.3.6 Tensile strength

The ability of a given material to withstand mechanical stresses can be described by three types of strengths: the tensile strength σ_T, the shear strength σ_S, and the compressive strength σ_C, usually obeying $\sigma_T \leq \sigma_S \leq \sigma_C$. Tensile strength is an important property which quantifies the ability of a material to resist tensions which are pulling it apart. This property describes how resilient comets are to tidal interactions during close approaches to massive bodies or to rotational splitting. Ultimately, tensile strength determines how likely JFCs are to survive their journey toward the inner Solar System and to end their lives as dormant

comets.

The mechanical strengths of comet nuclei have been determined using a variety of methods, and a detailed summary of the findings can be found in Biele et al. (2009) and Groussin et al. (2015). The recent results from Rosetta point to very low values for the tensile strength of 3–15 Pa (Groussin et al., 2015), $\leq$ 20 Pa (Thomas et al., 2015a) or 50 Pa Vincent et al. (2015a), with an upper limit of 150 Pa (Groussin et al., 2015). The relatively large range of tensile strength values can be explained with the different methods and the different locations on the comet they probe. However, as a comparison, all of the derived values are much lower than the tensile strength of snow, which lies in the range 0.1–1000 kPa for densities of 100 to 600 kg m^{-3} (e.g. Schulson & Duval, 2009).

The low tensile strength of comet nuclei was measured in various works prior to the Rosetta mission. Asphaug & Benz (1996) modelled the breakup of comet Shoemaker-Levy 9 and concluded that its tensile strength is 5 Pa. From the catastrophic breakup of comet ISON in 2013, Steckloff et al. (2015) determined that the tensile strength of the nucleus and its resulting fragments is $\sim$ 0.5–9 Pa. In support of their low estimates, Steckloff et al. (2015) also noted that for reasonable cometary parameters, the calculations of Sekanina & Yeomans (1985) of the bulk tensile strength of comet Brooks 2 yield a value of $<$2 Pa. Using the rotation rates of JFCs, bulk tensile strength of $<$100 Pa (Toth & Lisse, 2006) or 1-53 Pa (Davidsson, 2001) was determined to be sufficient to keep them stable against rotational disruptions (see Chapter 6 for more details on this method).

These studies aimed to estimate the bulk tensile strength of the nuclei. Even though the bulk tensile strength can be very different from the tensile strength of the surface layers of comets, there is evidence that the surface tensile strength is also very low. In particular, theoretical and experimental work suggests that the surface layers of comets need to have "ultra-low" tensile strength of $\sim$ 1 Pa in order to allow water ice sublimation to lift-off dust particles (Skorov & Blum, 2011; Blum et al., 2014). Measuring the mechanical properties of the nucleus surface was

among the main goals of the Philae lander. However, the landing complications did not allow all measurements to be executed according to plan, and the lander experiments produced contradictory results which are still undergoing refinement. Modelling the lander data from the first touchdown at Agilkia region agrees with a tensile strength of 10 Pa, however, this number is noted to depend on assumptions about the landing mechanics (Roll & Witte, 2016).

One particularly interesting result from the lander studies comes from the MUPUS instrument which failed to penetrate the surface of the comet, suggesting a large compression strength of over 2 MPa at Abydos (Boehnhardt et al., 2017). The surface waves produced by the hammering of MUPUS were recorded by the accelerometers of the SESAME/CASSE instrument of Philae. Knapmeyer et al. (2018) analysed these measurements and concluded that the surface of the comet at the landing site consists of layers with different properties: a surface layer of depth up to a few centimetres which is strong enough to prevent the penetration of MUPUS; a rigid layer with thickness between 10 and 50 cm having shear modulus between 3.6 MPa and 346 MPa, and a Young's modulus between 7.2 MPa and 980 MPa; and a high-porosity low-density interior of the comet which forms the bulk of the nucleus. Laboratory experiments of comet-analogues show that such hard surface layers with thickness from a few centimetres to several metres can result from recondensation and/or sintering of water ice (Pommerol et al., 2015; Kossacki et al., 2015).

2.4 Comet surfaces

2.4.1 Topography

Spacecraft images enabled geological studies of comet surfaces and thus opened an entirely new chapter in cometary science. High-resolution images have enabled the topographies of the individual comets to be characterised and compared to

one another (Keller et al., 2004; Basilevsky & Keller, 2006). Moreover, Rosetta's continuous monitoring of the nucleus of comet 67P allowed the ongoing processes reshaping the surface to be observed and to be directly linked to sublimation activity (Vincent et al., 2015a,b, 2016; El-Maarry et al., 2017; Pajola et al., 2017, among others). The detailed observations of the nucleus of comet 67P showed that topography plays an important role in the long-term activity and erosion of the comet (Keller et al., 2015b).

The surface of comet 67P is characterised by a great morphological variety (Fig. 2.8), which led to the definition of 26 distinct regions (El-Maarry et al., 2015, 2016). The most prevalent type of region on 67P consists of consolidated material often forming sharp cliffs. These types of terrain are considered to be the sources of most of the dust and gas production (see Vincent et al., 2015b; Keller et al., 2015b). Very different from the consolidated regions are the smooth dust-covered terrains. They are found close to the neck, in the northern hemisphere of the comet and are absent in the southern hemisphere. The smooth terrains can be explained by the re-deposition of large particles which failed to escape the gravity of the comet (e.g. Thomas et al., 2015b).

Similar topographies are found on the other nuclei visited by spacecraft (e.g. Basilevsky & Keller, 2006; A'Hearn et al., 2011). It is therefore important to understand their origins, and to explain their formation either as primordial structures on the nuclei, or as results of erosion.

2.4.2 Spectra and colours of cometary surfaces

The dependence of the reflectivity of comet nuclei on wavelength can be used to infer information about their surface compositions. However, the spectra of comet surfaces are very difficult to obtain with telescope observations due to the faintness of the bare nuclei. The visible spectra of JFCs lack prominent absorption and emission features and have approximately constant gradients (Luu,

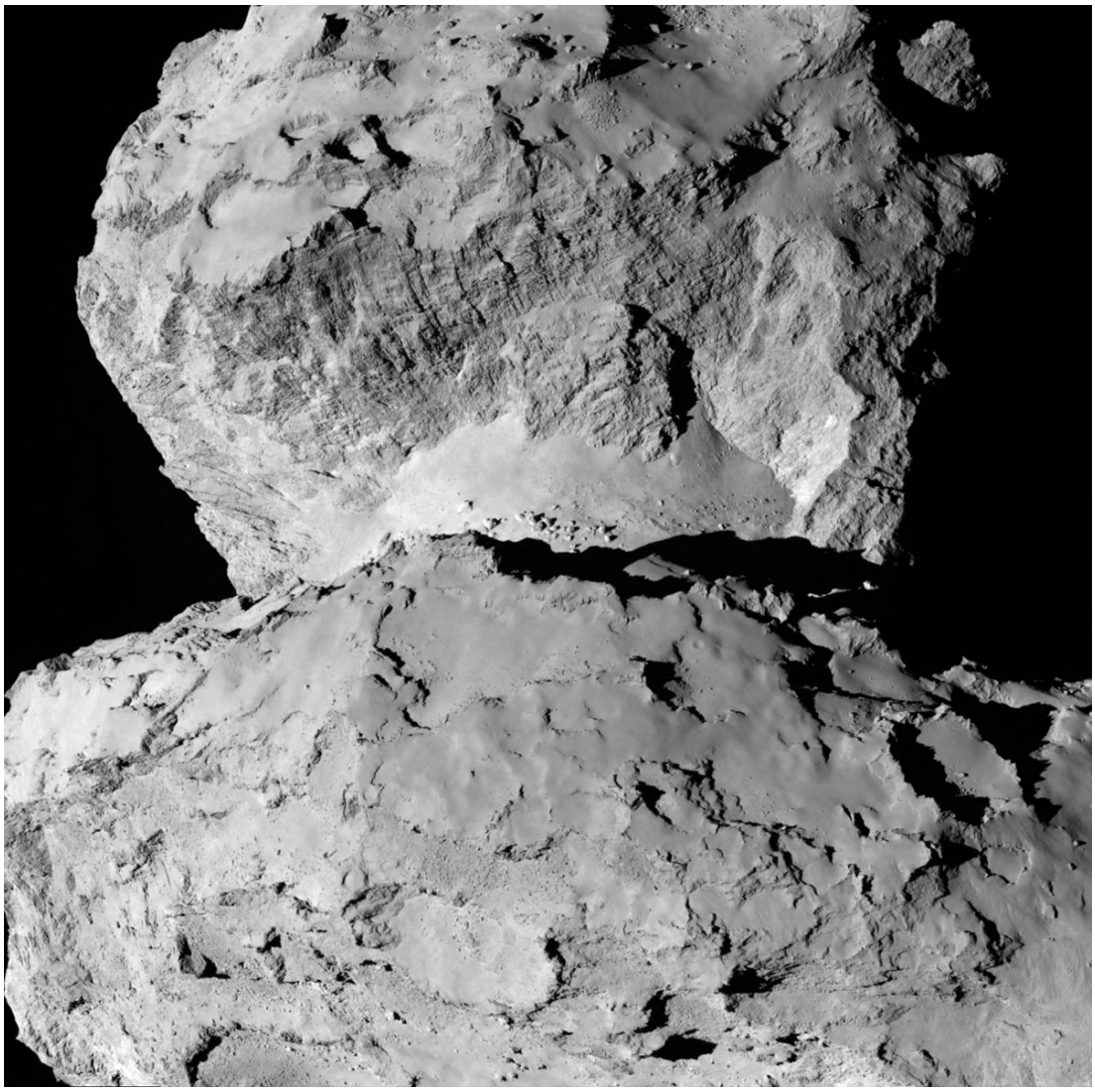

Figure 2.8: The northern hemisphere of comet 67P/C-G from Rosetta's OSIRIS narrow angle camera taken on 7 August 2014 from a distance of 104 km. Credits: ESA/Rosetta/MPS for OSIRIS Team MPS/UPD/LAM/IAA/SSO/INTA/UPM/DASP/IDA.

1993). Telescope observations of the near-IR spectra of JFC nuclei have also been observed as featureless within the noise level (Licandro et al., 2003; Soderblom et al., 2004; Campins et al., 2006).

Even though the spectra from ground- and space-based telescopes cannot reveal the composition of comet surfaces, they can be used to compare JFCs to other small-body populations, e.g. asteroids and Kuiper Belt objects (KBOs). The surface properties of different objects are usually compared in terms of the reflectivity gradient, which is measured in %/1000 Å.

Since the spectra of JFCs have approximately constant gradients in the visible, measuring the flux with different filters can also be used to derive the reflectivity gradient of the surfaces. Such observations measure the colour index, or the difference between the magnitudes of the object measured with two different filters ($m_{\lambda_1} - m_{\lambda_2}$). For spectra with constant gradients, colour indices provide the same information as very low-resolution spectra.

The reflectivity gradient S can be calculated as:

$$S(\lambda_1, \lambda_2) = 100 \times \frac{R(\lambda_2) - R(\lambda_1)}{(\lambda_1 - \lambda_2)/1000}, \tag{2.6}$$

where λ_1 and λ_2 are the central wavelengths of the two filters and the relative spectral reflectivity R is defined as:

$$R(\lambda) = 10^{-0.4[(m_\lambda - m_V)_{\rm comet} - (m_\lambda - m_V)_{\rm Sun}]}. \tag{2.7}$$

The median reflectivity gradient of JFC nuclei was found to be equal to 8.3 ± 2.8 %/1000 Å(Jewitt, 2002). The colour indices of JFCs have been collected and used to compare JFCs to other small-body populations in multiple works (e.g. Lamy et al., 2004; Snodgrass et al., 2006; Lamy & Toth, 2009; Jewitt, 2015). The most recent estimates of the mean colour indices of JFCs are $(B-V) = 0.87 \pm 0.05$, $(V - R) = 0.50 \pm 0.03$, $(R - I) = 0.46 \pm 0.03$ and $(B - R) = 1.37 \pm 0.08$ (Lamy & Toth, 2009; Jewitt, 2015).

Spacecraft studies of the surfaces of JFCs provide the opportunity to obtain near-IR spectra with higher resolution. Additionally, due to the proximity during flybys (or while orbiting the comet, in the case of Rosetta), the spectra of different areas on the surface can be derived and compared. Such observations by the high resolution imager spectrometer on board Deep Impact, and by the Visible InfraRed and Thermal Imaging Spectrometer (VIRTIS) instrument on Rosetta have shown that the dark surfaces of comet nuclei consist mainly of carbon-rich compounds (Capaccioni et al., 2015). Additionally, absorption features in the

near-IR spectra have revealed the presence of water ice on the surface of comets 9P and 67P (e.g. Sunshine et al., 2006; Filacchione et al., 2016).

2.4.3 Phase functions

The intensity of the reflected light from Solar System bodies is a function of phase angle (α, the angle between the Sun, the object and the observer). The resulting phase function, also known as phase darkening, is determined by the surface properties of the objects. Ground observations of JFCs are constrained by the large heliocentric distances when activity is low/negligible and therefore typically cover $\alpha < 15°$, while spacecraft images allow the phase function to be probed at large phase angles. For some objects, the phase function for α between 0° and ∼5° is characterised by a non-linear increase in brightness. This phenomenon is known as opposition surge, or opposition effect (OE). The phase functions of small bodies are usually characterised by a linear decrease between 10° and 60°.

The OE is particularly interesting because it can be described by models directly linked to physical properties of the surface material. The first mechanism proposed to explain the OE is shadow hiding. According to this model, the decrease of phase angle diminishes the size of the shadows that the surface particles cast on one another until the shadows completely disappear at $\alpha = 0°$. Alternatively, the OE can be explained by Coherent Backscattering. In this model, the light reflected by the surface particles is enhanced at small phase angles if the distance between the scatterers is greater than the wavelength of the reflected light and if the size of the particles is comparable to the wavelength. Since, the conditions for constructive interference are most favourable at small phase angles, the intensity of the reflected light increases close to $\alpha = 0°$.

Attempts have been made to link the OE to other surface properties. For instance a dependence between the phase function at small angles and the albedo of asteroids was found (Belskaya & Shevchenko, 2000). For a review on the

opposition effect for asteroids, refer to Li et al. (2015).

Prior to this thesis, the phase functions of less than a dozen JFC nuclei were determined from ground observations in visible wavelengths. They do not show indications for opposition effect and can be fit by linear functions with phase-function slopes β in the range 0.02-0.09 mag/deg (Snodgrass et al., 2011), although many of them are poorly sampled, especially at small phase angles, so the observations do not rule out OE. Phase functions from in situ observations are available for the five JFCs visited by spacecraft. They are in an excellent agreement with the linear phase functions determined from ground observations. Evidence for an opposition surge was found only for comet 67P (Masoumzadeh et al., 2017; Hasselmann et al., 2017). A more detailed review of the known phase functions of JFCs is presented in Chapter 9.

2.4.4 Albedos

The Vega spacecraft images of comet 1P/Halley demonstrated for the first time that comet nuclei have very dark surfaces with albedo of approximately 4% (Keller et al., 2004). Since then the albedos of 5 JFCs have been determined from spacecraft measurements and estimated for a handful of JFCs from telescope observations.

It is important to distinguish between the different definitions of albedo. In this work, I report values of the geometric albedos of comet nuclei. Geometric albedo is defined as the ratio between the zero-phase angle reflectance of an object and the reflectance of an idealised diffusing fully-reflecting disc with the same cross-section. Other works require the use of Bond albedo (A). The Bond albedo is defined as:

$$A = p\,q, \tag{2.8}$$

where p is the geometric albedo and q is the phase integral:

$$q = 2 \int \Phi(\alpha) \sin(\alpha) \mathrm{d}\alpha. \tag{2.9}$$

In this expression α is the phase angle and $\Phi(\alpha)$ is the disc-integrated normalised phase function.

It is important to note that both albedos are functions of wavelength. Since the spectral gradients of comet nuclei are shallow (see Section 2.4.2), the variation of the reflectance over the visible wavelength range is comparable to the uncertainty of the measured albedos, and it is often assumed that the bolometric Bond albedo (integrated Bond albedo over all wavelengths) is approximately equal to the Bond albedo.

For comets visited by spacecraft, the geometric albedo can be derived by comparing the disc-integrated brightness of the nucleus with the true surface area measured from resolved images or from the shape model of the nucleus. Radar observations can also provide information about the albedo of comet surfaces. From the limited number of radar observations, it was found that the radar albedo of comets is similar to the optical one (see Harmon et al., 2004).

The albedos can also be determined by simultaneously measuring the brightness of the nuclei in visible and IR. In the usual approach, thermal modelling of the IR data is used to derive the radius of the nucleus (see Section 2.3.1), and then equation 3.10 is applied to derive the albedo (see Section 3.6.3 and Lamy et al., 2004, for details).

Prior to this work, the albedos of less than a dozen JFCs were known (Snodgrass et al., 2011), ranging from 2% to 6% (Lamy et al., 2004). The average geometric albedo from these measurements for V- and R- bands were $p_V = 3.8 \pm 0.9$ % and $p_R = 4.2 \pm 1.7$ %, respectively (Lamy et al., 2004). The range of measured albedos was found to be very narrow, which motivated Lamy et al. (2004) to describe the possibility to look for trends in the albedo as "hopeless". However, using the SEPPCoN observations, Fernández et al. (2016) found a trend for a

decreasing albedo with increasing nucleus size. Additionally, in this thesis I found a possible correlation between albedos and phase-function slopes (see Chapter 9).

Chapter 3

Instrumentation and data analysis

3.1 Instruments

The photometric time-series analysed in this thesis were obtained from seven different instruments on six telescopes. The observations are summarised in Tables 5.1 and 7.1).

Comets 14P, 47P, 94P, 123P and 137P were observed using the red arm of the EMMI instrument (Dekker et al., 1986) which was mounted at the f/11 Nasmyth-B focus of the 3.6m New Technology Telescope (NTT) at the European Southern Observatory (ESO) La Silla site. The red arm of EMMI was equipped with a mosaic of two MIT/LL 2048 × 4096 CCDs. The observations were done in 2 × 2 binning mode which gave a pixel scale of 0.332 arcsec/pixel. The effective size of the field of view was 9.1 × 9.9 arcmin^2. All images presented here were taken with the Bessel R filter.

EFOSC2 replaced EMMI at the Nasmyth focus of the NTT in 2008 (Buzzoni et al., 1984; Snodgrass et al., 2008a). The effective field of view of EFOSC2 is 4.1 × 4.1 arcmin^2. It contains a LORAL 2048 × 2048 CCD which was used in a 2 × 2 binning mode with an effective pixel scale of 0.24 arcsec/pixel. The observations of comets 93P, 94P, 110P, 149P and 162P were taken through a Bessel R filter, while 47P was observed with an SDSS r' filter.

Some of the data for the lightcurves of 93P, 110P, 149P and 162P were obtained with the visual and near-UV FOcal Reducer and low-dispersion Spectrograph (FORS2) instrument at ESO's 8.2 m Very Large Telescope (VLT) on Cerro Paranal, Chile (Appenzeller et al., 1998). The detector of FORS2 consists of a mosaic of two 2k × 4k MIT CCDs. The pixel scale at the default readout mode used (2 × 2 pixel binning) is 0.25 arcsec/pixel. The field of view of the instrument is 6.8 × 6.8 arcmin^2.

Comets 14P, 93P, 149P and 162P were observed with the 4.2m William Herschel Telescope (WHT) at the Roque de Los Muchachos observatory on the island of La Palma, Spain. The observations were done using the Prime Focus Imaging Platform (PFIP) which contains an optical mosaic of two EEV 2k × 4k CCDs. The total field of view of the instrument is 16.2 × 16.2 arcmin^2 with a gap of 9 arcsec between the two chips. Both chips were used in an unbinned mode with a pixel scale of 0.24 arcsec/pixel. All observations were done using CCD2, as it has fewer bad pixels and defective columns than CCD1. The filter used for the observations was Harris R with a central wavelength 640.8 nm.

Some of the observations of 143P and 162P, as well as a re-analysed dataset from Snodgrass et al. (2006) used to obtain the lightcurve of 94P, were taken using the 2.5m Isaac Newton Telescope (INT) at the Roque de Los Muchachos observatory. The Wide Field Camera (WFC), mounted at the primary focus of INT, was used for the observations. The WFC is a mosaic of four thinned EEV 2048 × 4096 pixel CCDs. Each CCD has an effective field of view of 11.5 × 23 arcmin^2 and the pixel scale of the instrument is 0.33 arcsec/pixel. Only CCD3 was used for collecting the 94P time series, while 143P and 162P were observed only with CCD 4. All observations were done through an SDSS r' filter.

Comets 14P and 143P were observed using the Large Area Imager for Calar Alto (LAICA) installed at the prime focus of the 3.5m telescope of Calar Alto Observatory in Spain. LAICA has a mosaic of 4 CCDs each with 4000 × 4000 pixels. The total field of view of LAICA is 44.36 × 44.36 arcmin^2 and the pixel

scale is 0.225 arcsec/pixel. Throughout the observing run only CCD 1 was used.

Comets 143P and 162P were also observed with the 2-m Ritchey-Chrétien Coudé telescope of the National Astronomical Observatory Rozhen in Bulgaria. The observations were done using the VersArray 1300B CCD camera (1340 × 1300 pixels) which is attached to the two-channel focal reducer FoReRo-2, giving resolution of 0.74 arcsec/pixel and a field of view of about 15 arcmin in diameter.

3.2 Data reduction

Before the photometric frames can be analysed, the raw images need to be reduced. To ensure compatibility, the same reduction routine was followed consistently for each individual dataset. The data reduction was performed using standard `IRAF` tasks (Tody, 1986, 1993) implemented on `PyRAF`[1].

As a first step, the bias was subtracted from each frame in order to correct for the electronic noise of the detector. The bias frames were taken at the start and/or at the end of each observing night with the shortest possible exposure time and a closed shutter. A master bias frame for each night was created by using 9-19 individual bias frames. The median of all frames was taken so that the extreme pixel values of the individual exposures could be removed. Once the bias frame was produced, it was subtracted from all other frames.

The next step was the flat-field correction. Flat fields are necessary in order to correct for the non-uniform illumination of the CCD as well as for the possible difference in sensitivity of some pixels. Additionally, flat fields reveal the typically doughnut-shaped patterns produced by dust particles in the optical systems. Flat-field frames need to simulate uniform illumination conditions and should be taken nightly for each filter and configuration used during the observations. For most instruments the best flat-field correction is achieved by taking images of the sky during evening and/or morning twilight. Dome flats can be used in the cases

[1] http://www.stsci.edu/institute/software_hardware/pyraf

when sky flats are impossible to obtain due to cloud coverage that may produce non-uniform illumination conditions. Dome flat fields are taken by illuminating a bright surface inside the telescope dome (usually a special screen), and can be taken at any time. The disadvantage of dome flats is that the direction of the incoming light is different than that during the night.

For the data in this thesis, if at least five twilight sky flats were taken during the night, the normalised sky flats were median combined. Since all used instruments have demonstrated stable night-to-night flat fields, in some cases the same master flat field was used for more than one night. This was done only when there were no sky flats available for some of the nights within the same run. In the cases when no sky flats were obtained within 2 nights of the observations, dome flats were used. All science images were flat-field corrected by division to the median-combined flat field of the corresponding night.

Some of the images were affected by fringing. Fringing is a Newton's Rings type pattern which is caused by slight variations in the thickness of the CCD. It occurs because the thinned chip has the right thickness to allow the interference of light which has been multiply reflected in the layers of the CCD, or interference of long-wavelength light which passes through the array and gets reflected back into it.

In order to correct for this effect, the fringing pattern for the given instrument and filter combination has to be identified by combining many images of different pointings. Then the pattern can be scaled to the value of the fringing in each individual image and then subtracted from the image. The r'-band images from the instruments used in this thesis do not require fringing correction. The R-band images affected by fringing were corrected using the `IRAF` script provided by Snodgrass & Carry (2013).

3.3 Photometry

3.3.1 Seeing and point spread function

Point sources imaged on two-dimensional arrays produce surface brightness profiles known as a point-spread function, or PSF. The PSF of a given image is shaped by atmospheric and instrumental effects, such as atmospheric turbulence, diffraction, chromatic aberration, and geometric aberration.

Turbulent mixing causes variations of the optical properties of the layers in Earth's atmosphere as well as in the air inside the telescope domes. This effect, known as "astronomical seeing", deteriorates the image quality and produces blurred images of the observed point sources, also known as seeing discs. Seeing is commonly used to describe the quality of the collected data. It can be estimated from the shape of the PSF and the easiest way to obtain it is to measure the full width at half maximum (FWHM) of a Gaussian fit to the PSF.

3.3.2 Aperture photometry

The aim of the observations analysed in this thesis is to derive the brightness of comet nuclei as a function of time, in order to study their variability over short and intermediate timescales. There are two main effects which can produce an observable brightness change of an inactive comet nucleus. On short scales (of the order of hours) the brightness variation is driven by the rotation of the nucleus and produces a periodic lightcurve. If the object is observed over a few days or longer, its brightness will change due to geometric effects – change of its heliocentric and geocentric distances as well as changing phase angle. Typically, the largest lightcurve brightness variation of comet nuclei is ~ 1 mag, but most observed comets have lightcurves with Δm much smaller than this. Therefore, in order to detect the rotational lightcurves of JFC nuclei, it is necessary to have suitable techniques to detect subtle brightness variations as small as 0.01 mag.

Aperture photometry is one of the most commonly used photometric techniques. It estimates the brightness of a source from the sum of the counts observed within a defined aperture centred on the source. While the apertures can be defined to have various shapes (e.g. square, elliptical), most commonly, circular apertures are used to study inactive comet nuclei. Circular apertures are suitable because inactive nuclei should be point sources and their surface brightness profiles should be similar to the typically circular PSF of the instruments. An exception are the so called "trailed images". They are produced when sidereal tracking of the telescope is used, while, due to its fast apparent motion against the stars, the comet moves beyond the seeing disc during the exposure. For such images pill-shaped apertures (see Fraser et al., 2016) are found to be more suitable.

To calculate the flux of the objects from aperture photometry, first the sum of the CCD counts within the area A of the aperture is taken. Then, the sky background level is estimated, typically from an annulus concentric to the aperture used to measure the flux of the object. The background contribution within A is then subtracted from the total signal to arrive at the flux of the object.

When performing aperture photometry, it is important to place the centre of the aperture exactly at the centre of the object. An even more important step is to select a suitable aperture radius. Details on the effects of different aperture radii can be found in Howell (2006). In summary, it has been found that typically the total flux of a point source is contained within a circular aperture with radius $r = 3 \times$ FWHM of the PSF. However, the pixels further away from the centre of the point source contain an increasing background contribution. If they are included within the aperture, they will decrease the S/N ratio of the flux (Howell, 2006, and references therein). The optimal aperture radius which maximizes the S/N is found to be around $r = 1 \times$ FWHM, with fainter sources producing maximum S/N for smaller radii (e.g. Howell, 1989).

Aperture photometry is computationally easy since it requires no modelling of the PSF shape of the source. However, it is not suitable for analysing images of

densely populated areas of the sky. Such images require PSF-fitting techniques in order to separate the flux of the different objects.

The most precise way to find the brightness variation of a point source is by performing differential photometry (also known as relative photometry). This technique allows the brightness variation of an object to be derived from a comparison with neighbouring stars in the frame. It measures the relative magnitude change of the target with respect to other objects in the image. Differential photometry can reach extremely low photometric uncertainties down to 0.001 magnitude for bright sources (Howell, 2011). This can be achieved by averaging the difference in magnitude of the variable object to a large ensemble of comparison stars (20-50 and above) common to all frames (Howell, 2006).

For stationary objects, such as variable stars and exoplanetary transits, differential photometry is sufficient to study their variation. However, small Solar System bodies, and JFCs in particular, move relatively fast with respect to the background stars and have to be compared to a different set of stars for every observing night. Thus, differential photometry can be used to derive the nightly variation of the comets, while absolute photometry needs to be performed in order to combine observations taken during different nights.

Absolute photometry requires the observation of stars which have well determined magnitudes in one of the photometric systems. It allows an offset (zero-point) of the frame to be found from the difference between the instrumental and the catalogue magnitude of the comparison stars. If this offset is applied to the frames containing the object of interest, its absolute magnitude can be derived, which enables its direct comparison to other objects or to observations from other epochs.

3.3.3 Photometric systems

Photometric systems are sets of filters with well-defined passbands and known sensitivity to incident radiation. Having clear-cut photometric systems allow magnitudes measured with different light detectors and filters to be converted to a common system, which makes them comparable. Here, I briefly mention the most commonly used photometric system in the visible range of the spectrum. For a detailed overview on the development of photometric systems, see Bessell (2005).

The first standardized photoelectric photometric system was the Johnson-Morgan system (Johnson & Morgan, 1953), also referred to as the UBV photometric system. With the development of CCD cameras in the second half of the twentieth century, observations became more sensitive to red wavelengths. That motivated the development of the Johnson-Kron-Cousins photometric system (UBVRI, Cousins, 1973), which was an expansion of the UBV system. Later, Bessell (1990) re-analysed the UBVRI system using standard-star photometry and synthetic photometry from spectrophotometry of many stars. This established the Bessell photometric system, which has been widely used ever since. Since the data of the Sloan Digital Sky Survey (SDSS) were released (Abazajian et al., 2003), the SDSS u'g'r'i'z' filter system (Fukugita et al., 1996) has become more wide-spread because the survey provided a catalogue of photometric observations with an unprecedented size. Due to improvements in filter technology, the SDSS-type filters have a number of advantages over older UBVRI filters. They generally have a higher throughput and clear cut in wavelength, which results in a decreased overlap between the bands. The use of r'-filters also eliminates the fringing pattern typical for R-filters.

In this thesis, I have converted all observations to the Pan-STARRS photometric system (Tonry et al., 2012). I selected this system because the Pan-STARRS survey provides standard stars with well-measured magnitudes on each frame, allowing a very precise magnitude determination (see Section 3.3). The Pan-STARRS

PS1 Data Release 1[2] (DR1) archive was publicly released on 16 December 2016 (Kaiser et al., 2002, 2010; Chambers et al., 2016, and references therein). PS1 used a 1.4 Gigapixel camera mounted on a 1.8 metre telescope to complete a 3π steradian survey of the whole sky north of declination $-30°$ in five broadband filters (g_{P1}, r_{P1}, i_{P1}, z_{P1}, y_{P1}). The PS1 filter system is slightly different from SDSS (Fig. 3.1) but the magnitudes from the two systems can easily be converted using the equations presented in Tonry et al. (2012).

As described in Section 2.4.2 cometary surfaces are slightly redder than the Sun, and their brightness peaks in R-band. The red bands, centred at around 650 nm, are therefore most suitable for observations of faint bare comet nuclei at large distances. Most observations of comet nuclei in the literature are taken in R-filter (see Lamy et al., 2004; Snodgrass et al., 2006) because the UBVRI filters have been commonly available on most telescopes for decades. These filters also provided the opportunity for converting the instrument magnitudes to absolute magnitudes in the Johnson-Kron-Cousins photometric system using the Landolt catalogue of standard stars (Landolt, 1992, see Section 3.4.3).

In recent years all-sky catalogues such as SDSS (Abazajian et al., 2003), Pan-STARRS (Chambers et al., 2016) and GAIA (Brown et al., 2016) have released photometric measurements of stars spread all over the sky. Such large catalogues allow direct absolute calibration with stars on each science frame, thus improving the precision of the derived magnitudes (see Section 3.4.3). Since these surveys were equipped with SDSS-filters (or similar, i.e. g_{P1}, r_{P1}, i_{P1}, z_{P1}, y_{P1}), it is becoming more common to observe small bodies in the Solar System with u'g'r'i'z' filters.

All observations analysed in the following chapters were taken with various R- and r'-filters. Using the technique described in Section 3.4.3 those observations were calibrated to r_{P1} magnitudes in the PS1-system.

These calculations required the colour index $(g_{P1} - r_{P1})_{JFCs}$ to be determined

[2] http://panstarrs.stsci.edu

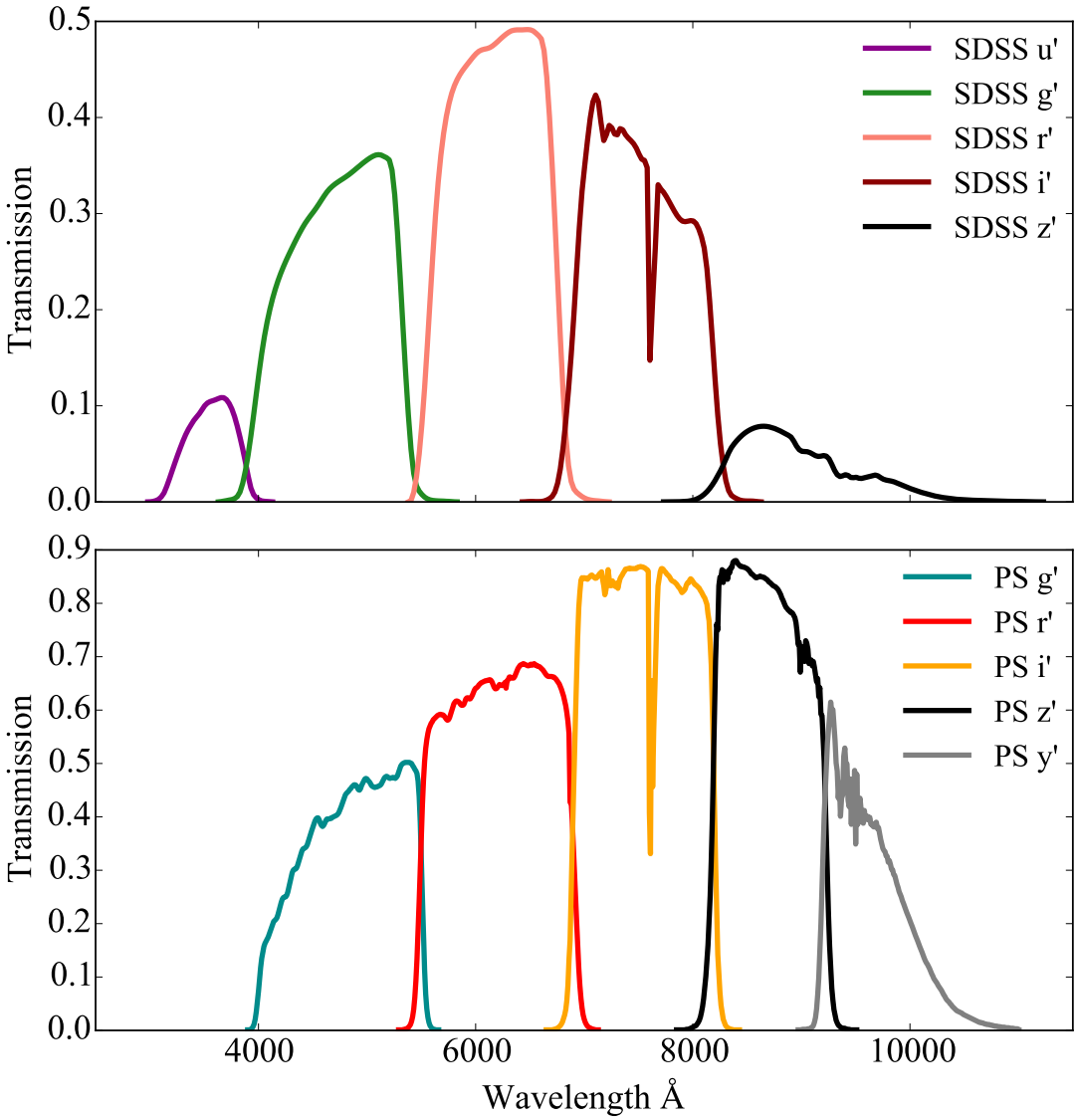

Figure 3.1: Comparison between the SDSS and Pan-STARRS filter systems. The response curves include atmospheric extinction through an airmass of 1.3 (SDSS) and 1.2 (Pan-STARRS). The filter transmission curves taken from the Space Virtual Observatory Filter Profile Service (`http://svo2.cab.inta-csic.es/theory/fps/`)

(see Section 3.4.3). The average JFC colour index $(B-V) = 0.87 \pm 0.05$ mag (Lamy & Toth, 2009) can be converted to $(g_{P1} - r_{P1})_{JFCs} = 0.60 \pm 0.06$ mag by combining the following two colour transformation equations from Tonry et al. (2012):

$$(g_{P1} - B) = -0.108 - 0.485(B-V) - 0.032(B-V)^2 \tag{3.1}$$

$$(r_{\mathrm{P1}} - V) = 0.082 + 0.462(B - V) + 0.041(B - V)^2. \quad (3.2)$$

In order to compare, or in some cases to combine, the newly derived r_{P1} magnitudes with previous measurements, the previously determined magnitudes in R-band had to be converted to r_{P1}-band. This conversion was done using the equation:

$$(r_{\mathrm{P1}} - R) = 0.117 + 0.128(B - V) - 0.019(B - V)^2 \quad (3.3)$$

from Tonry et al. (2012), where (B-V) is the colour index of the comet. In the cases when the colour index of the comet is unknown, the average value (B-V) = 0.87 ± 0.05 mag from Lamy & Toth (2009) was used.

As shown in Section 3.6.3 below, the magnitudes derived from photometric observations can be used to determine some physical properties of the nuclei (e.g. radius and albedo). These calculations use the apparent magnitude of the Sun in the same band as the observations. The apparent magnitude of the Sun is $V_\odot$ = -26.75 ± 0.02 mag (Cox, 2000). Using the colour index of the sun $(V_\odot - R_\odot)$ = 0.354 ± 0.010 mag (Holmberg et al., 2006), this converts to $R_\odot$ = -27.10 ± 0.02 mag. Using equation 3.3 and $(B_\odot - V_\odot)$ = 0.642 ± 0.016 mag (Holmberg et al., 2006) gives $(r_{\mathrm{P1}\odot} - R_\odot)$ = 0.191 ± 0.002 mag. Finally, the apparent magnitude of the Sun in r_{P1}-band becomes $r_{\mathrm{P1}\odot}$ = -26.91 ± 0.02 mag.

3.4 Technique for absolute photometric calibration

In this thesis I aimed to expand the sample of comets with known rotation rates. Since the available observations of JFC nuclei were very sparse I had to analyse archival data sets taken as part of different scientific programmes. This posed the challenge of combining data from different instruments and different observing geometries. In order to be able to reconcile all observations, I developed a robust

technique for absolute photometric calibration which uses the Pan-STARRS1 (PS1) survey (Chambers et al., 2016). The main advantage of this method is that on each frame the comet is compared to numerous neighbouring stars with precisely measured PS1 magnitudes. This provides the opportunity to calibrate absolutely the comet's magnitude even in non-photometric conditions, and allows absolute photometric calibration with uncertainties as low as 0.02 mag.

3.4.1 Selecting comparison stars

The first step of the photometric calibration procedure is to identify comparison stars on the science frames. For each observing night, the relative comet brightness variation was determined with respect to an ensemble of rigorously selected neighbouring stars. The selected stars had to be present on all comet frames for the corresponding night, so that the comet variation with respect to each of the comparison stars could be measured throughout the night. The selection criteria ensured that no stars located in bad sections of the CCDs were used. In order to avoid vignetting effects, all stars close to the edges of the frames were excluded, taking care that the specific limits of each instrument were respected.

All stars were selected from the Pan-STARRS PS1 Data Release 1[3] (DR1) archive which was publicly released on 16 December 2016 (Kaiser et al., 2002, 2010; Chambers et al., 2016, and references therein). The catalogue stars were matched to objects on the science frames using the sky coordinates from PS1. This was possible after `WCSTools`[4] was used to set the world coordinate systems (WCS) in the image headers. `WCSTools` is a set of programs that determine the conversion of the image pixels to sky coordinates by comparing the objects on the frames to positions on the real sky taken from star catalogues.

The PS1 survey provides positions and magnitudes of both stars and extended objects. To distinguish between them, I followed the PS1 DR1 guidelines for

[3] http://panstarrs.stsci.edu
[4] http://tdc-www.harvard.edu/wcstools/

star-galaxy separation[5]. According to the recommendations, the simplest way to identify the stars is to select objects with difference between the PSF magnitudes and the Kron magnitudes in i_{P1}-band (`iPSFMag−iKronMag`) < 0.05 mag.[6] These magnitudes are available for all objects in the catalogue but the criterion is expected to work well only for magnitudes i_{P1} in the range 14–21 mag.

A careful comparison of the PSF of the selected PS1 comparison stars identified on FORS2 images confirmed that indeed the selected catalogue objects corresponded to objects with stellar profiles on the frames. This study of the 8.2m VLT telescope data allowed definite identification of non-stellar profiles and indicated that very few galaxies should be contaminating the selected ensembles of comparison stars. Even if some galaxies are left in the list of selected catalogue objects, their influence would become negligible due to the large total number of comparison stars per frame (typically > 20).

To ensure that the photometric calibration is dominated by suitable comparison stars, I applied two additional criteria for selecting PS1 stars. I removed PS1 entries with uncertainties in the r_{P1} larger than 0.008 mag and only used stars with colours $g_{P1} - r_{P1} < 1.5$ mag.

3.4.2 Differential photometry

Once the positions of the comet and the comparison stars are defined on each frame, first the differential lightcurve of the comet with respect to the comparison stars for each night is measured. Then, the lightcurves from the individual nights are calibrated absolutely by shifting all points by a factor derived from the absolute calibration of just one reference frame for each night. Taking the differential magnitude of the comet rather than absolutely calibrating each frame is a better approach since the brightness variation within each night is independent of the

[5] https://outerspace.stsci.edu/display/PANSTARRS/

[6] The Pan-STARRS catalogue contains the magnitudes of each object, measured in a few different methods, e.g. circular apertures, PSF-fitting and Kron apertures (developed for better photometry of faint galaxies, Kron, 1980).

absolute calibration uncertainty.

To measure the frame magnitudes of the comet and the selected comparison stars, I performed circular aperture photometry. All measurements were done using the `IRAF` packages `DIGIPHOT` and `APPHOT` (Davis, 1999).

The observations were taken with sidereal tracking of the telescopes. Exposure times were generally short enough so that the apparent motion of the comet would be less than 0.5-0.6 arcsec and the comet would thus remain within the seeing disc. The few frames which did not fulfil this criterion were excluded from the analysis below. Having stellar profiles for both the comet and the background comparison stars guaranteed that the adopted circular aperture photometry procedures allowed direct comparison with the catalogue magnitudes of the stars.

The aperture radius used to measure the brightness of the comet nucleus was set equal (within the nearest integer pixel) to the FWHM of the stellar PSF for each frame. As discussed above in Section 3.3.2, this approach was previously found to be optimal for minimising the uncertainty of the relative photometry of faint targets (e.g. Howell, 1989). Using such relatively small apertures was also beneficial for slightly more crowded sky fields, as it decreased the probability that light from neighbouring stars influences the measured brightness.

To find the FWHM of the stellar PSF on each frame, I used the `IRAF` routine PSFMEASURE. The value for each frame was determined using the median of the measured FWHM of the best fit Gaussian profile to each of the selected comparison stars.

The motion of the comet on the sky over the course of the observing night can be non-linear. Therefore instead of using the position of the comet predicted from its ephemeris, I determined the centre of the comet on each frame interactively using the `IRAF` task IMEXAMINE.

Since INT/WFC has a large field of view, I corrected the instrument magnitudes for the specific distortions of the instrument. The image distortion can be identified as small position-dependent systematics in the aperture photometry of the field

stars and can be corrected by scaling the magnitudes with a small coefficient (see Hodgkin et al., 2008, for INT/WFC). The images taken with Rozhen2m/FoReRo also suffered from small distortions and I used larger apertures of 1.6 times the FWHM of the PSF to compensate for the positional dependence of the star magnitudes measured on the frame. This correction decreased the uncertainty of the absolute calibration. The larger aperture slightly decreased the S/N of the comet nuclei although it did not have a noticeable effect in the derived relative lightcurves.

Once the frame magnitudes of all objects were determined, the calculation of the relative magnitude of the comet could be computed. First, I determined the differences between the comet magnitude and each star, i ($\Delta m_{\mathrm{comet},i} = m_{\mathrm{comet}} - m_i$). I also computed the difference in brightness between each star and the brightest non-saturated star ($\Delta m_{*,i} = m_i - m_*$, averaged over all frames to get small uncertainty). The brightest star was selected because it had the highest S/N. Then, I scaled the difference of the comet and each star with $\Delta m_{*,i}$ ($\Delta m_{\mathrm{frame},i} = \Delta m_{\mathrm{comet},i} - \Delta m_{*,i}$). Finally, the differential photometry magnitude of the comet with respect to the brightest star, $m_{\mathrm{comet,diff}}$, was calculated as the median of $\Delta m_{\mathrm{frame},i}$. Its uncertainty was estimated from the median absolute deviation of $\Delta m_{\mathrm{frame},i}$.

3.4.3 Absolute calibration

A key aspect of the absolute calibration technique is the use of stars from the PS1 catalogue. This procedure allows the combination of data from different observing runs with significantly smaller systematic uncertainties than those from other works. Previous photometric studies of cometary nuclei have adopted the traditional method for absolute calibration which is based on observing standard star fields (e.g. Landolt stars, Landolt, 1992) a few times during the night, and solving for the zero-points, the extinctions and the colour terms for each filter (For a description of the method, see Warner, 2006a). It is difficult to determine the

uncertainty of the absolute calibration using Landolt star fields but a commonly cited value is 0.05 mag. Moreover, this method works only for photometric nights when the zero-point and the extinction remain stable throughout the night.

The technique which I have developed in this thesis, on the other hand, can be used to achieve precise absolute calibration even for nights with changing observing conditions. This is possible because each of the science frames contains a sufficient number of stars with well-determined magnitudes from the PS1 survey. Thus, if needed, the zero-point for each frame can be derived from a direct comparison with the catalogue. However, as was described above, differential photometry produces smaller uncertainties and is better for deriving the nightly variation of the comet nuclei. I therefore use absolute calibration to derive the absolute magnitude of one frame per object per night, while all other magnitudes are computed from the relative photometry with respect to that frame.

There are two main factors which need to be taken into account while deriving the conversion: 1) the colour term of the instrument set up (CCD chip and filter) with respect to the star catalogue (PS1), and 2) the zero-point for each night. The throughput of the filters and the sensitivity of the detectors of each instrument can be slightly different. Due to these differences, the shift between the instrumental and the catalogue magnitudes of the comparison stars depends on the colour of the stars. Figure 3.2 illustrates this effect with a frame used to calibrate the magnitude of comet 137P in an image taken with NTT-EMMI. The difference between the frame and the catalogue magnitudes on Figure 3.2 follows a linear function for the relatively narrow range of $(\mathrm{g_{P1}} - \mathrm{r_{P1}})$ colour indices.

The colour dependence of the frame magnitude offset can be expressed as:

$$R_{\mathrm{frame}} - r_{\mathrm{P1}} = \mathrm{ZP} + \mathrm{CT} \times (g_{\mathrm{P1}} - r_{\mathrm{P1}}), \tag{3.4}$$

where $\mathrm{R_{frame}}$ is the frame magnitude of the stars, while $\mathrm{r_{P1}}$ and $\mathrm{g_{P1}}$ are the PS1 magnitudes of the same stars. In this equation ZP is the zero-point of the frame

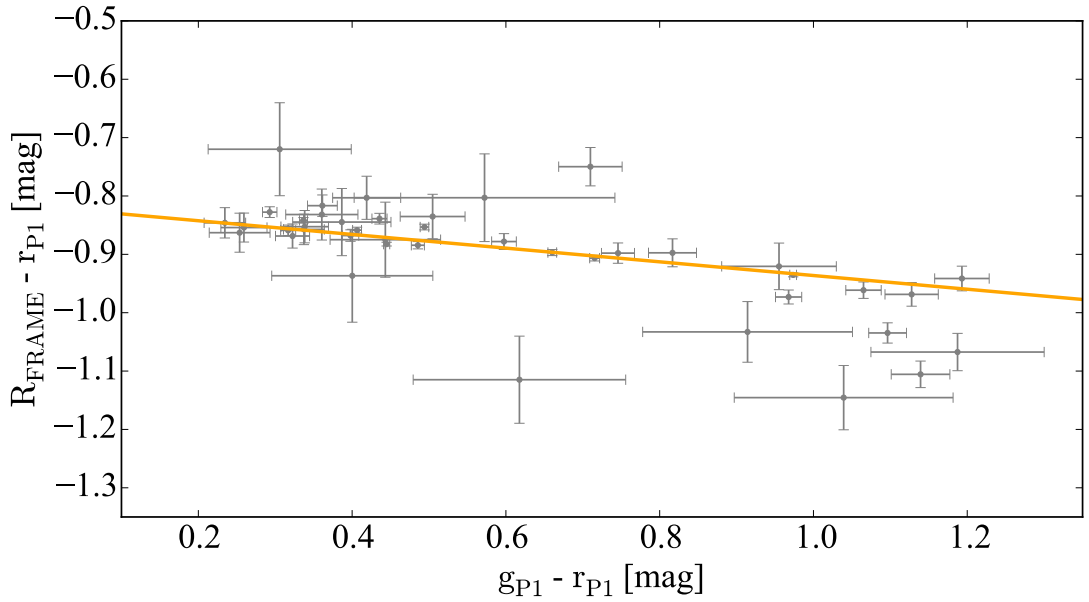

Figure 3.2: Colour term of the red arm of NTT-EMMI used with a Bessel R filter. The scaled difference of the measured R magnitudes and the PS1 r_{P1} magnitudes of the comparison stars are plotted against their PS1 $(g_{P1} - r_{P1})$ colour indices. The orange line has a slope equal to the colour term of the instrument and intercept equal to the zero-point of the frame.

and CT is the colour term. It is important to note the difference between the definition of ZP here and the zero-point term used in other absolute-calibration methods. Zero-point usually refers to the constant required to convert counts to magnitudes for a given instrument observing at zenith. Here, the zero-point (ZP) is defined as the offset from PS1 for a given frame and includes the extinction term.

In an ideal case, all stars with similar colour terms $(g_{P1} - r_{P1})$ should follow this linear dependence. However in reality some stars deviate from it slightly. The most likely reason for the differences is the faintness of the objects, which makes the photometry more uncertain. Additionally cosmic rays or readout from bad pixels on the CCD could lead to erroneous magnitude estimates. The zero-point is expected to vary slightly from frame to frame, while the colour term is determined by the instrument set-up (filter and CCD) and should be stable over long periods of time.

I determined the colour term for each of the instrumental set-ups used in this

thesis by comparing the frame magnitudes and the PS1 magnitudes of 500-1500 stars in each case. For each observing night, I chose the frame with the best seeing as a reference frame. The frame magnitudes of the comparison stars on the reference frame (R_{frame}) were then compared to the corresponding PS1 r_{P1} and g_{P1} magnitudes. After PS1 stars with extreme colour indices ($g_{P1} - r_{P1} > 1.5$ mag) were excluded, the differences $R_{frame} - r_{P1}$ were plotted versus the colour indices of the stars. All points were scaled so that the median of $R_{frame} - r_{P1}$ was brought to 0 mag. After this was done for all observed fields, all points were combined into a common plot such as the one in Fig. 3.3. The colour term of the instrument was determined by taking the slope of the best fitting linear function. The derived colour indices of each instrument and their uncertainties are presented in Table 3.1.

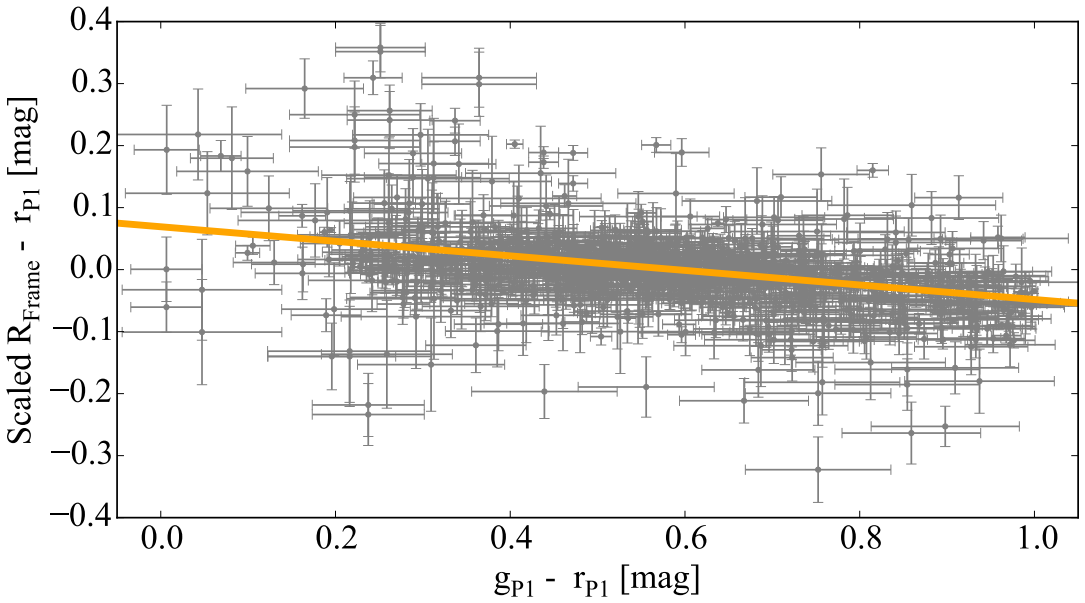

Figure 3.3: Magnitude transformation for a frame taken with the red arm of NTT-EMMI used with a Bessel R filter on 06/03/2005. The difference between the frame magnitude in R-band and the catalogue magnitude from Pan-STARRS r_{P1} is plotted against the colour index ($g_{P1} - r_{P1}$). The orange line has a slope equal to the colour term for the instruments and intercept equal to the zero-point of the current frame.

The next step was to find the zero-point of each reference frame from the difference between the colour-corrected frame magnitudes and the corresponding

Table 3.1: Derived colour terms for all instruments used in this work

Instrument	**Filter**	**CT**[a]	σ_{CT}[b]	$(g_{P1} - r_{P1})$ **range**[c]
NTT-EMMI	R	−0.117	0.005	0.0 - 1.0
NTT-EFOSC	R	−0.158	0.012	0.4 - 1.5*
NTT-EFOSC	r'	−0.194	0.005	0.0 - 1.5
VLT-FORS2	R**	−0.071	0.006	0.0 - 1.0
WHT-PFIP	R	−0.100	0.008	0.0 - 1.0
INT-WFC CCD 3	r'	−0.007	0.002	0.0 - 1.5
INT-WFC CCD 4	r'	0.008	0.004	0.0 - 1.5
CAHA-LAICA CCD 1	r'	−0.009	0.006	0.0 - 1.5
ROZHEN-FoReRo	r'	−0.030	0.010	0.0 - 1.5

[a] Colour term c derived from comparison with PS1 star magnitudes in r_{P1} and g_{P1}.
[b] Uncertainty in the colour term.
[c] Range of the PS1 $g_{P1} - r_{P1}$ colour indices of the used stars. Colour indices < 1 for Johnson-Cousins R filters and < 1.5 for SDSS r filters.
[*] This range was selected due to an insufficient number of stars with $g_{P1} - r_{P1} < 0.4$ in the observations used in this thesis.
[**] ESO R_SPECIAL+76 filter with effective wavelength 655 nm and FWHM 165.0 nm.

PS1 r_{P1} magnitudes. This was done by first correcting for the colour-term by taking the differences:

$$\Delta_i = (R_{frame,i} - r_{P1,i}) - CT \times (g_{P1,i} - r_{P1,i})$$

for each star i. The zero-point was then determined as the weighted average of Δ_i. The uncertainty of the zero-point was taken from the median absolute deviation of Δ_i.

With the colour term and the zero-point of the reference frame at hand, I converted the comet's magnitude to $r_{P1,JFC}$ in the PS1 system using the comet's colour index. Since for most comets no colour information was available, the average value $(g_{P1} - r_{P1}) = 0.60 \pm 0.06$ mag derived in Section 3.3.3 was used.

The magnitude of the comet nucleus in PS1 r_{P1}-band was computed from the following equation:

$$r_{P1,JFC} = R_{JFC} - ZP - CT \times (g_{P1} - r_{P1})_{JFC}, \quad (3.5)$$

where R_{JFC} is the frame magnitude of the comet nucleus, and $(g_{P1} - r_{P1})_{JFC}$ is its colour index. The total uncertainty of the calibrated absolute magnitude is then the quadratic sum of the relative-photometry uncertainty and the uncertainty of the term $ZP + CT \times (g_{P1,JFC} - r_{P1,JFC})$, which is referred to as the absolute-calibration uncertainty below.

The final step of the technique was to convert the relative photometry for all frames to absolute magnitudes. Once the comet magnitude on the reference frame was converted to PS1 r_{P1} magnitudes, I shifted all the relative magnitudes to produce an absolutely-calibrated lightcurve of the comet for each night.

3.4.4 Geometric corrections

In order to make the individual time-series dataset comparable, they had to be corrected for geometric effects. The first step was to bring all observations to the same time frame. Therefore, I corrected each time series for light-travel time, converting "observation times" to "times when the light left the nucleus". This was done by subtracting the time it takes photons to travel from the comet nucleus to Earth (the light-travel time) from the observing time of each frame.

The next step was to convert the absolutely calibrated frame magnitudes, m_r, to absolute magnitudes, $m_r(1, 1, 0)$. The apparent magnitude of the comet nucleus, m_r is related to the observing geometry with the following relation :

$$m_r = H_r + 5 \log(R_h \Delta) + \beta\alpha, \tag{3.6}$$

where $H_r = m_r(1, 1, 0)$ is the hypothetical absolute magnitude of the comet nucleus measured at an imaginary point at heliocentric distance $R_h = 1$ au; geocentric distance $\Delta = 1$ au and phase angle $\alpha = 0°$. This equation is valid for objects whose phase functions do not show an opposition surge and can be described by a linear fit with slope β. In the case of JFCs, a linear model with $\beta = 0.04$ mag/deg is generally accepted (e.g Lowry & Fitzsimmons, 2001; Lamy et al., 2004;

Snodgrass et al., 2005).

For most comets the datasets consisted of observations taken at different epochs that could be used to derive a phase function slope β independently. If the available observations covered narrow phase angle ranges smaller than $\sim 2°$, I used $\beta = 0.04$ mag/deg to find the absolute magnitude of the nucleus H_r. For such single-run observations, I used the frame magnitude m_r, rather than H_r, to derive the lightcurves.

3.5 Activity search

The photometric observations conducted in this thesis aimed to derive the photometric and physical properties of the nuclei of the observed comet. All JFCs were observed at heliocentric distance > 3 au, where water sublimation levels are expected to be very low. However, some comets are known to remain active even at heliocentric distances beyond 3 au (e.g Lowry et al., 2003).

If comet nuclei are observed while active, the nucleus signal is obscured by the surrounding coma. This has two main effects on the photometric observations - it makes the comet appear brighter and it reduces the observed lightcurve variation. If the activity remains unnoticed these effects would result in an overestimated nucleus radius and an underestimated elongation (axial ratio).

Fortunately, in most cases it is possible to spot the presence of activity by inspecting the brightness profile of the comet. If the comet has a tail, it is easy to spot that the nucleus appears elongated in one direction. Alternatively, if the comet is not resolved and no obvious tail can be distinguished, to reveal the presence of activity, the radial profile of the comet can be compared to the PSF in the frame. The radial profile of an active comet is different from that of a point source and does not match the stellar profiles on the frame. Instead, the surface brightness of the comet follows the PSF at small distances (< 1 FWHM of the PSF) but shows excess brightness further away from the comet centre.

The effects of the presence of weak activity on the brightness profile of comet 47P/Ashbrook-Jackson is illustrated in Fig. 3.4.

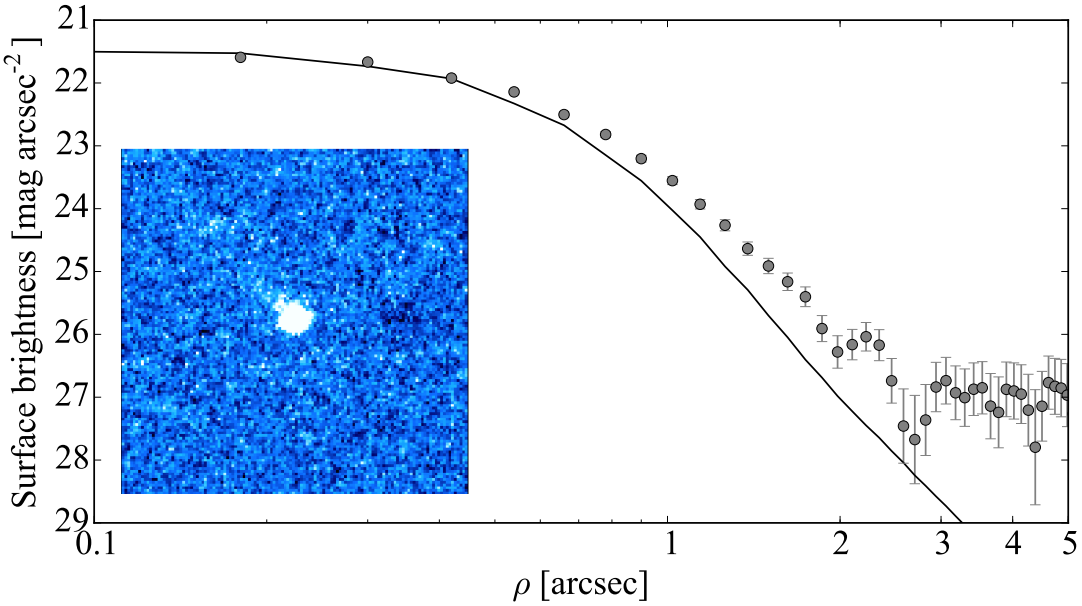

Figure 3.4: Comparison between the scaled surface brightness profile of a bright non-saturated star and of comet 47P from images taken on 24 April 2015 with NTT/EFOSC2. The co-added composite image of 47P in the lower left corner is made up of 26 × 80 s exposures. The surface brightness of the comet indicates an excess brightness at large distances ρ from the comet centre. The weak tail detected to the north-east of the nucleus in the composite image confirms that the comet was slightly active.

To check whether the comets analysed in this thesis were active at the time of the observations, I developed the following procedure to compare the average comet PSF profile to that of a star. The first step was to subtract the sky background, determined from the mode of each image. Then all sky-subtracted images for the night were median-combined, producing a composite image of the background stars without cosmic rays and the moving comet. The next step was to scale the resulting image using the difference in magnitude of a few selected stars and to subtract it from each comet frame, in order to remove the background stars. Next, each difference frame was centred on the comet. All aligned frames were then combined using a median filter, removing all cosmic rays. The surface brightness profile of the comet was measured for concentric annuli on the comet-composite

image, while the PSF of a bright star was measured from the combined star field image. Finally, the stellar PSF was scaled to match the surface brightness at the centre of the comet and the two profiles were compared as shown in Fig. 3.4.

This procedure is preferred over the direct comparison of the comet with the PSF of a field star on a selected frame. Creating a deep combined image of the comet increases the S/N ratio of the comet and makes the signatures of activity easier to detect. Measuring the surface brightness profile of the nucleus and the stellar PSF from combined images also eliminates the effects of the changes in seeing between the frames. Thus, the difference in the profiles should only be due to a presence of coma signal. However, it is possible that in certain cases the positional uncertainty of the centre of the comet on each frame produces a slight elongation of the comet profile in the combined image. To decrease this effect, it is important to define the comet centre manually on each frame instead of using interpolated ephemeris predictions, since the comet motion can be non-linear during the night.

Similar techniques for comparing the comet surface brightness profile to the stellar PSF have been widely used to identify the coma contribution since some of the very first CCD observations of JFC nuclei (e.g. Jewitt & Danielson, 1984). However it is important to keep in mind that recent results have provided clear evidence that a nucleus can be active and still maintain a stellar profile on photometric images from ground telescopes. In particular, the profile of comet 67P/C-G remained indistinguishable from the stellar PSF on VLT/FORS images from May 2014 (Snodgrass et al., 2016). During the same period, however, the Rosetta/OSIRIS observations already indicated resolved activity of the comet (Tubiana et al., 2015a).

It is therefore important to interpret all ground photometric observations with caution and to keep in mind that weak coma signal can remain undetected. This is particularly important for observations which capture comet nuclei at the detection limit of the telescope (either due to the faintness of the object or to

bad observing conditions). In such images the positional uncertainty and the low signal-to-noise ratio of the comet can make the surface brightness of the comet nucleus very uncertain away from the centre, which prevents deviations from the PSF to be spotted.

3.6 Deriving nucleus characteristics

3.6.1 Period search

Finding the periodicity of unevenly sampled time series is a challenging task. However, a number of possible period-finding techniques have been developed over the years. In this thesis I have used three methods: the Lomb-Scargle method (LS; Lomb, 1976; Scargle, 1982), phase dispersion minimization (PDM; Stellingwerf, 1978) and string-length minimization (SLM; Dworetsky, 1983).

LS is among the most widely used period-finding techniques in astrophysics. It uses a modified Fourier spectral analysis, which takes into account the fact that the time series are not evenly spaced. It therefore outputs a normalised spectral power, which weights the data "per point" instead of "per time interval". The best period according to the Lomb-Scargle technique is the one that maximises the normalised spectral power. A very thorough description of the principles and limitations of the LS technique can be found in VanderPlas (2017).

In the analysis of the comet lightcurves below, I used the python `gatspy`[7] `LombScargleFast` implementation of LS (VanderPlas & Ivezic, 2015). The LS implementation of VanderPlas & Ivezic (2015) is very computationally efficient and enabled the use of the Monte Carlo methods from Section 3.6.2, which required finding the best period of numerous data clones for each lightcurve. This implementation of LS includes the optimised algorithm `LombScargleFast`, which automatically determines the period grid depending on the most likely periods,

[7] http://www.astroml.org/gatspy/

and samples those regions better. This optimisation saved computing power and guaranteed that the longer periods are equally well-sampled as the shorter ones.

Typically, the period search was limited to the interval between 3 and 40 hours, based on the observed range for other JFCs (see Section 2.3). In the cases where the nightly brightness variations suggested slower rotation, I extended the range to cover larger periods. Everywhere in the analysis below, it is assumed that the brightness variation of the comets is a result of their shapes rather than surface albedo variations. The lightcurves of elongated bodies have two minima and two maxima per rotation cycle, therefore producing double-peaked lightcurves. The Lomb-Scargle periodogram identifies the periods of single-peaked lightcurves, and therefore the lightcurve periods are taken to be twice the LS periods.

The LS periods were cross-checked using the `PyAstronomy`[8] implementation of PDM. PDM phases the data with a trial period and aims to minimise the ratio (Θ) between the scatter of the phased data with that of the unphased data. The best-fitting period, then, produces the lightcurve with the smallest scatter.

Another phase-folding method, SLM, was also included in the analysis. SLM phases the data points with a test period and minimises the "length" of a hypothetical "string" which connects all points. The SLM string length is defined as:

$$L = [(m_1 - m_n)^2 + (\Phi_1 - \Phi_n)^2]^{1/2} + \sum_{i=1}^{n-1}[(m_i - m_{i-1})^2 + (\Phi_i - \Phi_{i-1})^2]^{1/2}. \quad (3.7)$$

In this expression, m_i are the magnitudes of each point, and Φ_i are the corresponding phases from the trial period.

For all comets below, the three methods detected the same set of possible periods and showed general agreement. Therefore, for simplicity, in most cases only the LS periodograms are presented.

[8] https://github.com/sczesla/PyAstronomy

The interpretation of the output of the period-fitting methods is often complicated by the existence of aliases. Since ground-based telescopes can only observe during the night and because objects are preferably observed close to their meridian passage, the observations are not randomly spaced in time. Other effects such as the camera read-out time and the exposure time create additional non-random gaps in the data. These frequencies in the data can interfere with the true period of the object and give rise to aliases. The main aliases arise from the night-to-night observing pattern at the following frequencies determined by the length of the sidereal day (1.0027^{-1} days):

$$\mathrm{P_{alias}}^{-1} = k \times 1.0027 \pm \mathrm{P_{true}}^{-1} \tag{3.8}$$

In LS periodograms, the aliases decrease in power with the increase of the integer k. Plotting the LS power as a function of frequency aids the identification of the aliases because of their spacing at approximately one cycle per day.

In some cases when the time series are very sparsely sampled it can be difficult to distinguish between the aliases and the true period, especially if the true period is close to 12 or 24 hours. This highlights the importance of visually inspecting the lightcurves corresponding to the periods identified on the periodograms. Thus, in the analysis below, before I confirm the periods suggested by the period-finding methods, I first refer to the corresponding lightcurve plots.

3.6.2 Monte Carlo methods

Determining the uncertainty in the lightcurve period is a challenging and often neglected task. In the analysis below, this problem is often additionally complicated by the large time span between the different observations, which leads to aliases in the periodograms. Additionally, as is shown for the individual comets below, sometimes more than one period seems to characterise the variation well, and it is not possible to decide on the most likely spin rate. In such cases, providing

an uncertainty in the determined period based just on the information on the periodogram (e.g. FWHM of the highest peak) can be misleading.

Moreover, it is not clear to what extent the detected periods are influenced by the intrinsic uncertainties of the comet magnitudes. Two main effects are at play when considering what might dominate the uncertainties of the available time series. Firstly, the data from the different nights are linked using absolute calibration. In some cases the sky area under consideration has few stars, which increases the absolute calibration uncertainty. Second, when the observations from two different observing runs are combined, the applied phase angle correction determines the relative difference between the comet magnitudes from the different epochs. This effect is hard to quantify, unless the influence of the different possible phase-function correction parameters is explored.

In an attempt to account for these effects, I developed two varieties of a Monte Carlo method to search for the lightcurve periods and phase-function slopes of the comets. These techniques result in good estimates of the phase-function coefficients and the rotation periods together with their corresponding uncertainties.

In Chapter 5 I used a Monte Carlo method to derive the phase-function slopes and the rotation periods of JFCs from sparsely sampled observations. Its main asset is that it provides uncertainty ranges of the derived phase-function slopes and periods. This Monte Carlo method, referred to as MC below, consists of the following steps:

1. Each magnitude from the time series of the comet is replaced by another randomly selected value. The new magnitude is selected from a normal distribution with mean equal to the original magnitude value and standard deviation equal to the uncertainty of the magnitude. The result is a clone i of the original time series, where the times and observing geometries are the same as the original time series, but the magnitudes were varied within the uncertainty space.

2. The clone magnitudes are used to find the best fitting linear phase function coefficient β_i.

3. The clone data set is corrected for the phase function by converting from $m(1, 1, \alpha)$ to $m(1, 1, 0)$ using the derived β_i.

4. The Lomb-Scargle period search routine is run on the clone magnitudes $m(1, 1, 0)$ to determine the best-fitting period P_i.

5. This procedure is repeated for $i = 1, 2, \ldots, 5000$.

6. To determine the phase function coefficient, I plot the histogram of the determined β_i and fit a gaussian probability density function to it. In the final results, I report the best fit for the phase function coefficient to be the mean of the distribution, while its uncertainty is taken to be equal to the central 3σ range of the distribution.

7. To determine the most likely rotation period, I plot the histogram of the derived P_i and fit a gaussian probability density function to it. As a final result I report the period of the comet as equal to the mean of the distribution, and an uncertainty equal to the central 3σ range of the fitted probability density function.

In all cases the distribution of the derived β_i can be described well by a normal distribution. However, for some comets the P_i distributions are more irregular. In the cases when the distribution is irregular, I take the highest peak as the most-likely period candidate, but I carefully explore the alternatives in the analysis.

The downside of the MC procedure is that it uses linear regression to fit a phase function to the data in each of the MC clones. I have confirmed that the linear fitting works very well when the whole range of the lightcurve variation and a broad range of phase angles are sampled. However, in certain cases when

the datasets probe the lightcurves just partially, a simple linear fit may produce erroneous results.

In Chapter 7 the main goal is to constrain the rotation periods with great accuracy in order to look for spin changes in comparison to previous epochs. To achieve this, I modified the MC procedure to consider the entire range of possible phase-function slopes, rather than using only the slopes derived from a linear regression fit to the points in each clone. This has the advantage that a broader range of possible phase-function slopes are tested and therefore the derived possible rotation period range is less dependent on the adopted phase function correction.

The modified MC2 procedure consists of the following steps:

1. At each iteration i, every magnitude point is replaced by a clone. The clone is a randomly selected value from a normal distribution with standard deviation equal to the photometric uncertainty and mean equal to the original magnitude.

2. Next, the clones are shifted to account for the uncertainty of the absolute photometric correction. All points belonging to the same calibration star field are shifted with a value randomly selected from a normal distribution with mean equal to 0, and standard deviation equal to the uncertainty of the absolute photometric correction of the given field.

3. Then, all points from the produced clone i are corrected for a linear phase function with slope β_i. The slope is randomly selected from a uniform distribution of phase-function slopes in the range 0.0 to 0.1 mag/deg. To account for the possibility of extreme phase functions, the selected phase-function slopes cover a slightly larger range than the total range of observed phase-function slopes of JFCs (0.02-0.08 mag/deg, see Chapter 9).

4. The best-fitting period to the clone, is found using the LS method. Ex-

perience has shown that the best periods from LS periodograms result in single-peaked lightcurves. Therefore, I double the LS output to get the rotation periods P_i.

5. For each clone I phase all points with the period P_i and compute the SLM total string length of the phased lightcurve. According to SLM, the lightcurves with shorter total string lengths are more confined and are therefore considered to be better.

6. After repeating this procedure for i=1,2,...,5000, I use the distribution of the selected best periods and the corresponding total string lengths for each clone to determine the most likely rotation period and its uncertainty.

3.6.3 Albedo, size, shape and density estimates

The rotational lightcurves derived in this work are used to set constraints on the sizes, shapes and albedos of the observed nuclei. The mean apparent magnitude of the comet ($\overline{m_{\rm r}}$) and the mean absolute magnitude ($\overline{H_{\rm r}}$) were calculated as the arithmetic mean of all magnitudes $m_{\rm r}$ and $H_{\rm r}$. The uncertainties are taken to be equal to the median of the uncertainties of all individual points. The mean absolute magnitude can be converted to an average radius for the nucleus in kilometres using:

$$r_{\rm N} = (k \,/\, \sqrt{A_{\rm r}}) \times 10^{0.2(m_\odot - \overline{H_{\rm r}})}, \tag{3.9}$$

where k = 1.496 $\times$ 10^8 km is the conversion factor between au and km; $A_{\rm r}$ is the geometric albedo of the comet and $m_\odot = -26.91$ mag is the apparent magnitude of the Sun, both in PS1 $r_{\rm P1}$-band. I used the commonly assumed geometric albedo value for comets, $A_{\rm r} = 0.04$.

The reported uncertainties on the radii are based only on the photometric uncertainty. They do not account for the uncertainties introduced by the albedo and the phase function slope. The albedos of JFCs are between 2-7 % (see Table

9.1), which is within a factor of 2 of the commonly assumed value of 4%. Therefore, the radius estimate can vary with maximum $\sqrt{2}$ from the reported value. Since all comets were observed in a narrow phase angle range (typically < 10 deg), the influence of the phase function uncertainty is also small. In the worst case, if the phase function slope varies with up to 0.08 mag/deg, the absolute magnitude of the comet will vary with 0.8 mag, and the estimated radius will be within a factor of 1.5 from the estimated value.

Nine of the comets have SEPPCoN thermal measurements of the radii. That allows the absolute magnitudes $H_{\rm r}$ and the SEPPCoN effective radii $R_{\rm eff}$ to be combined to derive the comets' geometric albedos using:

$$A_{\rm r} = (k^2 \,/\, R_{\rm eff}^2) \times 10^{0.4(m_\odot - \overline{H_{\rm r}})}. \tag{3.10}$$

The peak-to-peak variation $\Delta H_{\rm r}$ can also be used to set a lower limit on the elongation of the comet nucleus. I determined $\Delta H_{\rm r}$ by taking the observed range of magnitudes of the corresponding dataset. If the nucleus is modelled as a prolate ellipsoid with semi-axes a, b and c, where $b = c$ and $a > b$, the axis ratio a/b can be determined by

$$\frac{a}{b} \geq 10^{0.4\Delta H_{\rm r}}. \tag{3.11}$$

Since no knowledge on the orientation of the rotational axis of any of the considered nuclei is available, only the projection of the axis ratio onto the plane of the sky can be calculated. Therefore, Eq. 3.11 provides only a lower limit of the elongation.

The data were also used to place a lower limit on the bulk density of the comets by combining the derived rotation periods ($P_{\rm rot}$) in hours and axis ratios (a/b). For a fast-rotating strengthless body to remain stable, the gravitational acceleration at the surface must remain larger than the centrifugal acceleration at the equator. The balance of the two accelerations at play can be transformed to give a stability criterion depending only on the nucleus density ($D_{\rm N}$) and the

axis ration (Pravec & Harris, 2000). In units of g cm^{-3} this constraint can be approximated to:

$$D_{\mathrm{N}} \geq \frac{10.9}{P_{\mathrm{rot}}^2} \frac{a}{b}, \tag{3.12}$$

where the period is given in hours.

Chapter 4

Review of JFCs with studied rotation rates

One of the main goals of this thesis is to combine the newly obtained nuclei properties with those from previous works in order to analyse the bulk properties of the expanded sample of JFCs. Previously, the collective rotational properties of JFCs were studied by Lamy et al. (2004), Samarasinha et al. (2004) and Snodgrass et al. (2006). I expand their samples to include the cometary nuclei whose rotations were derived since then, and complement them with the newly obtained results from this work. Table 4.1 contains the properties of all considered comets together with the sources of all known parameters. However, the sections below focus in detail only on the comets with updates since the reviews in Lamy et al. (2004) and Snodgrass et al. (2006), including the unpublished HST results quoted in Lamy et al. (2004) that were revised by Lamy et al. (2011).

In addition to the rotational properties, I also review below the published size and shape estimates of the considered comets. While photometric lightcurves can be used to determine nucleus shapes, they do not provide absolute sizes. For those comets visited by spacecraft, the dimensions from the shape models are given. Radar and thermal infrared estimates of the effective radius are presented whenever available. For those objects with only photometric data in the visible,

the nucleus size was estimated by assuming a geometric albedo of typically 4%. The most recent reviews of comet sizes from visible photometry and thermal IR Spitzer photometry are given by Snodgrass et al. (2011) and Fernández et al. (2013) respectively.

4.1 JFCs with recently updated rotation rates

4.1.1 2P/Encke

Comet 2P/Encke has a Tisserand parameter T_J=3.025, which is slightly above the limit used to define JFCs (see Section 2.2.1). However, 2P is often classified as a JFC as it is possible for comets of JFC origin to achieve T_J of slightly above $T_J = 3$ following terrestrial planet interactions (e.g. Levison et al., 2006).

Comet 2P/Encke is among the comets with the shortest known orbital periods, 3.3 years, which has allowed different observers to study its properties over multiple apparitions. Its relatively small heliocentric distance at aphelion of 4.1 au allows the comet to stay mildly active at almost all times, which has hindered the direct observation of the comet's nucleus. Nevertheless, 2P is one of the best-studied JFCs, having well-constrained spin rate, rotation changes, colour, albedo and phase function. All of the earlier works leading to today's relatively good understanding of 2P are thoroughly described in Lamy et al. (2004) and Lowry & Weissman (2007). Newer papers have added spectroscopy of the nucleus (Tubiana et al., 2015b) and a study of the aphelion activity of this comet (Michael S. P. Kelley, private communication). Here, I provide an outline of the most important results on the nucleus shape and rotation rate.

The earliest attempts to determine the rotational lightcurve of 2P came from Jewitt & Meech (1987). Their time-series optical photometry suggested a most-likely period of 22.43 ± 0.08 hours. A later study by Luu & Jewitt (1990) led to a best-fit period of 15.08 ± 0.08 hours, although both studies note that alternative

periods were also consistent with their data. Fernández et al. (2000) used thermal infrared time series data to confirm the 15.08 hour period. A large data set of observations between July 2001 and September 2002 when 2P was close to perihelion was used by Fernández et al. (2005b) to determine that the comet's synodic period was either 11.079 ± 0.009 hours or 22.158 ± 0.012 hours. Fernández et al. (2005b) also discussed that these periods are not compatible with the spin rates found by Jewitt & Meech (1987) and Luu & Jewitt (1990).

Belton et al. (2005) compiled the available optical and infrared photometry and reached the conclusion that the nucleus of 2P is in a complex or excited rotation state. According to this analysis, the nucleus precesses about the total angular momentum vector with a period 11.1 hours and oscillates around the long axis with period 47.8 hours.

Lowry & Weissman (2007) added new optical data sets collected in October 2002, just a few weeks apart from some of the observations in Fernández et al. (2005b). This allowed Lowry & Weissman (2007) to combine data from the two studies and to derive an effective radius 3.95 ± 0.06 km, an axis ratio of 1.44 ± 0.06 and a rotation period of 11.083 ± 0.003 hours.

2P was later observed during the following aphelion, and the lightcurves obtained suggested that the spin period increases by ∼ 4 minutes per orbit (Mueller et al., 2008; Samarasinha & Mueller, 2013).

The early nucleus size estimates of ≤ 2.9 km (Campins, 1988, I use effective radius to characterise the nucleus size hereafter) and $2.8 \leq r_{eff} \leq 6.4$ km (Jewitt & Meech, 1987; Luu & Jewitt, 1990) were followed by a later estimate of 2.4 ± 0.3 km by Fernández et al. (2000) . Comet 2P was also observed with radar during two apparitions (Kamoun et al., 1982; Harmon & Nolan, 2005). The data from Harmon & Nolan (2005) confirmed a period of ∼ 11 hours and excluded the longer periods of ∼ 15 and ∼ 22 hours. Harmon & Nolan (2005) combined the radar data with previous infrared observations and obtained a solution for 2P's shape with an effective radius of 2.42 km and an axis ratio of 2.6.

Fernández et al. (2000) also managed to obtain the phase function of 2P with phase coefficient 0.06 mag degree^{-1} (in the range between 0 and 106 degrees) as well as a relatively high visual geometric albedo of 5 ± 2 %.

4.1.2 9P/Tempel 1

9P/Tempel 1 was the target for two NASA missions: Deep Impact and Stardust-NExT. It was also extensively observed from ground during the supporting campaigns (Meech et al., 2005, 2011a).

Multiple authors studied the size, shape and rotation rate of 9P before the Deep Impact flyby (e.g. Weissman et al., 1999; Lowry et al., 1999; Lowry & Fitzsimmons, 2001; Lamy et al., 2001; Fernández et al., 2003). A detailed overview of their contributions can be found in Lamy et al. (2004).

The two flybys provided sufficient information to determine the size of the nucleus with good precision. The mean radius of the shape model after the Deep Impact flyby was estimated as 3.0 ± 0.1 km, with axes of 7.6 and 4.9 km, and an axis ratio $a/b = 1.55$ (A'Hearn et al., 2005). Thomas et al. (2013a) combined the data sets from the two spacecraft and obtained a radius of 2.83 ± 0.1 km. They reported a shape model with radii between 2.10 and 3.97 km, which gives an axis ratio $a/b = 1.89$.

The two flybys combined with the ground observing campaigns gave an insight into the rotation of 9P. Belton et al. (2011) analysed multiple available data sets and determined that 9P had the following sidereal rotation periods: 41.335 ± 0.005 h before the 2000 perihelion passage; 41.055 ± 0.003 h between the perihelion passages in 2000 and 2005; 40.783 ± 0.006 h from the Deep Impact photometry slightly before the 2005 perihelion passage, and 40.827 ± 0.002 h in the period 2006-2010. Chesley et al. (2013) updated their work and concluded that 9P/Tempel 1 spun up by either 12 or 17 minutes during perihelion passage in 2000 and by 13.49 ± 0.01 minutes during the perihelion passage in 2005.

4.1.3 10P/Tempel 2

10P/Tempel 2 is one of the largest known JFCs. It is also known to be only weakly active at perihelion. The combination of these two factors has allowed its nucleus to be observed with very small coma contribution both at aphelion and perihelion, making 10P one of the best-studied comets.

A series of works have determined that 10P has a spheroidal shape with dimensions a=8-8.15 km and b=c=4-4.3 km (axis ratio of 1.9), albedo A_R = 2.4 ± 0.5% and rotation period about 9 hours (Sekanina, 1987; A'Hearn et al., 1989; Jewitt & Luu, 1989). A detailed summary of the works which have estimated the size of the nucleus of 10P can be found in Lamy et al. (2004). Lamy et al. (2009) used HST photometry to determine a nucleus radius of 5.98 ± 0.04 km.

10P was one of the first comets observed to change its spin rate on orbital timescales. It is progressively slowing down by ∼ 16 s per perihelion passage (Mueller & Ferrin, 1996; Knight et al., 2011, 2012). The most recent analysis by Schleicher et al. (2013) led to the conclusions that 10P has a prograde rotation with a period of 8.948 ± 0.001 hours, and that the rate of spin down has decreased over time, most likely in accordance with the known decrease in water production by the comet since 1988.

4.1.4 19P/Borrelly

The nucleus of comet 19P/Borelly was studied using HST images by Lamy et al. (1998b). Their analysis suggested a rotation rate of 25.0 ± 0.5 hours and dimensions of 4.4 ± 0.3 km × 1.8 ± 0.15 km, assuming an albedo of 4%. The comet was observed during five nights in July/August 2000 at the CTIO-1.5 m telescope (Mueller & Samarasinha, 2002). These data yielded a lightcurve with period 26.0 ± 1 hours and a large lightcurve variation - between 0.84 mag and 1.0 mag.

On September 22, 2001, just eight days after 19P passed perihelion, the NASA-

JPL Deep Space 1 Mission had a flyby of the comet (Soderblom et al., 2002). Using the encounter images, Buratti et al. (2004) determined that the nucleus has a radius of 2.5 ± 0.1 km and axes 4.0 ± 0.1 km and 1.58 ± 0.06 km. Dividing these two values yields an axis ratio $a/b = 2.53 \pm 0.12$.

HST/STIS observations were conducted in parallel to the Deep Space 1 encounter (Weaver et al., 2003). They could not be used to derive an independent measure of the nucleus rotation rate but were in agreement with the previous period measurement from Lamy et al. (1998b). Mueller & Samarasinha (2002) collected all available ground-based data from 2000 and the HST data from 2001 and improved the period by one order of magnitude. They narrowed down the possible periods to three values P = 1.088 ± 0.003 days, P = 1.108 ± 0.002 days, and P = 1.135 ± 0.003 days, which were consistent with the initial period of P = 1.08 ± 0.04 days from Mueller & Samarasinha (2002) (Mueller et al., 2010b). These authors continued studying the comet with observations from the SOAR telescope in Chile in September/October 2014 (Mueller & Samarasinha, 2015). These new data were used in an attempt to choose between the three possible rotation periods as well as to look for activity-induced spin changes of the nucleus during the two apparitions since the last observations. The most likely period was 1.209 days (29.016 hours) but 1.187 days (28.488 hours) could not be excluded (Mueller & Samarasinha, 2015). The newly derived period suggested that the rotation of 19P slows down by approximately 20 minutes per orbit (Mueller & Samarasinha, 2015).

4.1.5 61P/Shajn-Schaldach

Lowry et al. (2003) used snapshot observations of the nucleus of 61P (in non-photometric conditions) to determine a radius of 0.92 ± 0.24 km. Lamy et al. (2011) observed the comet at heliocentric distance 2.96 au (inbound) and determined a mean nucleus radius of 0.61 ± 0.03 km and axis ratio $a/b \geq 1.3$. Their partial

rotational lightcurve suggested a few possible periods, but the shortest one of them, 4.9 ± 0.2 hours was considered as most likely (Lamy et al., 2011).

4.1.6 67P/Churyumov-Gerasimenko

Comet 67P/Churyumov-Gerasimenko was selected as the backup target for the Rosetta mission after the 2003 launch of the mission had to be postponed due to a failure of the Ariane rocket (Glassmeier et al., 2007). The comet was observed in detail during only two apparitions before the rendezvous in August 2014.

The rotation period of 67P was first constrained to ∼12 hours by Hubble Space Telescope observations in March 2003, soon after its perihelion passage in September 2002 (Lamy et al., 2006). After the comet moved to greater heliocentric distances and its activity was quenched, it was possible to directly observe the nucleus from ground and to determine the spin rate with greater precision. Lowry et al. (2012) combined all available ground observations (Lowry et al., 2006; Tubiana et al., 2008, 2011) and determined the sidereal rotation period of the nucleus to be $P = 12.76137 \pm 0.00006$ hours. Mottola et al. (2014) revised the period before the second perihelion passage in 2009, and set it to $P = 12.76129 \pm 0.00005$ hours.

The next period determination was done with measurements from the Rosetta camera OSIRIS in March 2014 (Mottola et al., 2014). The new period of the comet was determined as $P = 12.4043 \pm 0.0007$ hours and suggested that the nucleus had spun up by 1285 s (∼ 21 minutes; Mottola et al., 2014).

OSIRIS continued monitoring the temporal evolution of the rotation rate of 67P throughout the extent of the mission (Jorda et al., 2016). The perihelion measurements of the orientation of the comet's rotational axis determined an excited rotational state with period of 11.5 ± 0.5 days and an amplitude of 0.15 ± 0.03° (Jorda et al., 2016). They determined a rotation period of 12.4041 ± 0.0001 h, which stayed constant from early July 2014 until the end of October

2014. After that, the rotation rate slowly increased to 12.4304 h until 19 May 2015, when it started dropping to reach 12.305 h just before perihelion on August 10, 2015 (Jorda et al., 2016).

According to the Rosetta measurements made available by ESA[1], the rotation rate continued decreasing until February 2016, and at the end of the mission, the sidereal period of 67P was 12.055 hours (ESA provided no uncertainty on this value). These measurements imply that 67P spun up by 1257 s ($\sim$ 21 minutes) during its latest perihelion passage (2014-2016). This period change is similar to the change of 1285 s measured by Mottola et al. (2014), which suggests that the comet spins up with a rate of approximately 21 minutes per orbit.

The overall spin evolution of 67P is in very close agreement with the activity model of Keller et al. (2015a). According to their analysis, the sign of the rotation period change is determined by the nucleus shape, while the magnitude of the change is controlled by the activity of the comet.

Rosetta measured the precise dimensions of the bilobate nucleus of 67P (Sierks et al., 2015). The overall dimensions along the principal axes are $(4.34 \pm 0.02) \times (2.60 \pm 0.02) \times (2.12 \pm 0.06)$ km, with the two lobes being $4.10 \times 3.52 \times 1.63$ km and $2.50 \times 2.14 \times 1.64$ km (Jorda et al., 2016). Using the longest and the shortest axes of the comet, I calculated an axis ratio $a/b = 2.05 \pm 0.06$.

The mean radius derived from the shape model of 67P is 1.743 ± 0.007 km. The area equivalent radius and the volume equivalent radius are 1.93 ± 0.05 km and 1.649 ± 0.007 km, respectively (Jorda et al., 2016).

4.1.7 73P/Schwassmann-Wachmann 3

Comet 73P/Schwassmann-Wachmann had a strong outburst in September 1995 (Crovisier et al., 1995) which was accompanied by a split-up into at least four pieces (Bohnhardt et al., 1995; Scotti et al., 1996). The remnants of the 73P nucleus were detected during the subsequent apparitions. The largest one of them

[1] http://sci.esa.int/rosetta/58367-comet-rotation-period/

is fragment C, which was estimated to have a radius of 0.5 km (Toth et al., 2005, 2006; Nolan et al., 2006).

In 2006, the comet approached Earth to less than 1 au and provided an excellent opportunity for different observers to study the lightcurve of fragment C. Toth et al. (2005) and Toth et al. (2006) used HST data to determine the dimensions of fragment C. Assuming an albedo of 0.04 and a linear phase coefficient of 0.04 mag deg^{-1} for the R-band, they obtained an effective radius of 0.41 $\pm$ 0.02 km. The derived lightcurve suggested an elongated body with axes 0.57 $\pm$ 0.08 km and 0.31 $\pm$ 0.02 km, which results in a minimum axis ratio $a/b \geq 1.8 \pm 0.3$ (Toth et al., 2006).

Drahus et al. (2010) collected all of the reported lightcurves (Farnham, 2001; Toth et al., 2006; Storm et al., 2006; Nolan et al., 2006), and added a further estimate of the spin rate using variations in the production rates of the HCN molecule from sub-mm observations. Their analysis showed that 73P-C had a stable rotation during the 21-day observing campaign in May 2006 and narrowed down the possible periods to 3.392 h, 3.349 h, or 3.019 h. Since none of these values could be excluded, Drahus et al. (2010) concluded that the rotation period of 73P-C was between 3.0 and 3.4 hours during the duration of their observing campaign. This is the fastest known rotation period of a JFC and its stability against rotational splitting suggests that 73P-C has a bulk tensile strength of at least 14-45 Pa (Drahus et al., 2010), or that it has a higher than expected density (see Section 6.3). Given that 73P has previously split, and continues to fragment (Williams, 2017), it is most likely at the very limit of stability.

4.1.8 76P/West-Kohoutek-Ikemura

Tancredi et al. (2000) observed the nucleus of 76P and estimated a radius of 1.3 km. However, the authors note that the collected photometric measurements of the nucleus brightness had a large scatter which makes the radius value uncertain.

Lamy et al. (2011) obtained a partial lightcurve of the comet with most likely period of 6.6 ± 1.0 hours and brightness variation of 0.56 mag which corresponds to an axis ratio $a/b \geq 1.45$. They estimated the nucleus radius to be 0.31 ± 0.01 km (Lamy et al., 2011).

4.1.9 81P/Wild 2

Comet 81P/Wild 2 was the primary target of the sample-return mission Stardust. The observations of 81P before 2004 provided an estimate of its size (summarised in Lamy et al., 2004). During the Stardust flyby in January 2004, the instruments on board revealed the shape of the nucleus as well as great details from the surface. Duxbury et al. (2004) used the obtained images to model the nucleus as a triaxial ellipsoid with radii 1.65 × 2.00 × 2.75 km ± 0.05 km, while the model of Sekanina et al. (2004) provided an effective radius of 1.98 km.

The rotation rate of the comet remained unknown until 81P was observed at perigee in March/April 2010 (Mueller et al., 2010a). Their narrow-band filter photometry revealed a periodic variation in the CN features of the coma with a period of 13.5 ± 0.1 hours.

4.1.10 82P/Gehrels 3

The radius of 82P was estimated to be $R_{\rm eff} < 3.0$ km (Licandro et al., 2000) or $R_{\rm eff} = 2.0$ km (Tancredi et al., 2000). However, 82P shows signs of activity all along its orbit (e.g. Licandro et al., 2000), and these values are therefore most likely influenced by the presence of coma.

Lamy et al. (2011) obtained a partial lightcurve with a rotation period P = 24 ± 5 hours. However, the lightcurve is poorly sampled and this result most likely corresponds to a lower limit of the comet's rotation period (Lamy et al., 2011). The authors used the same data set to derive a mean radius $R_{\rm eff} = 0.59 \pm 0.04$ km and axis ratio $a/b \geq 1.59$.

4.1.11 87P/Bus

The attempts to determine the size of the nucleus of 87P resulted in the following upper limits: $r_n \leq 0.8$ km (Lowry & Fitzsimmons, 2001), $r_n \leq 0.6$ km (Lowry et al., 2003) and $r_n < 3.14$-3.42 (Meech et al., 2004).

Lamy et al. (2011) analysed a partial HST lightcurve of 87P and determined a most likely period of 32 ± 9 hours, a mean radius of 0.26 ± 0.01 km and an axis ratio $a/b \geq 2.2$.

4.1.12 103P/Hartley 2

103P/Hartley 2 was extensively studied during the EPOXI flyby on 4 November 2010, and has been the target of multiple ground observations due to its favourable observing geometry during close approaches to Earth. The first determinations of its radius $r_n = 0.58$ km came from Jorda et al. (2000) but was later revised to $r_n = 0.71 \pm 0.13$ km (Groussin et al., 2004). This result was consistent with the upper limits set by Licandro et al. (2000), Lowry et al. (2003), Lowry & Fitzsimmons (2001) and Snodgrass et al. (2008b). In preparation for the EPOXI mission Lisse et al. (2009) used Spitzer to measure an effective radius of 0.57 ± 0.08 km. This value was practically the same as the mean radius of 0.580 ± 0.018 km measured with the in situ instruments of EPOXI (Thomas et al., 2013b). The shape model presented in Thomas et al. (2013b) results in an estimated diameter range for the nucleus of 0.69 - 2.33 km. I divided the two extreme diameter values to obtain an axis ratio $a/b = 3.38$.

The rotation period of 103P was studied in detail using the EPOXI data as well as the extensive support observations from ground. It was established that the spin rate of the nucleus decreased during the perihelion passage and that it is in a non-principal axis rotation (A'Hearn et al., 2011; Belton et al., 2013; Drahus et al., 2011; Harmon et al., 2011; Jehin et al., 2010; Knight et al., 2011, 2015; Meech et al., 2011b; Samarasinha et al., 2010, 2011, 2012). The EPOXI lightcurve

suggested several periodicities ranging from 17 to 90 hours (A'Hearn et al., 2011; Belton et al., 2013), which were used to understand the complex rotation of the nucleus (A'Hearn et al., 2011; Belton et al., 2013; Samarasinha et al., 2012). The ground observations between April 2009 and December 2010 monitored the change in the strongest periodicity of $\sim$ 18 hours, which corresponds to the precession of the long axis of the nucleus around the angular momentum vector (Meech et al., 2011b). Over the period covered by the campaign, the rotation rate increased by $\sim$ 2 hours, from 16.4 $\pm$ 0.1 hours (Meech et al., 2009, 2011b) to 18.4 $\pm$ 0.3 or 19 hours (Jehin et al., 2010).

4.1.13 147P/Kushida-Muramatsu

147P is among the smallest known JFC nuclei. Regarding the orbit class of this comet, Ohtsuka et al. (2008) showed that 147P is a quasi-Hilda comet, which underwent a temporary satellite capture by Jupiter between 1949 and 1961. Tancredi et al. (2000) reported a nucleus radius of 2.3 km but noted that the measurement is uncertain. Lowry et al. (2003) reported $r_n \leq 2.0$ km after a non-detection at heliocentric distance of 4.11 au. Lamy et al. (2011) derived a complete but poorly sampled lightcurve, which suggested that the rotation period of 147P was either 10.5 $\pm$ 1 hours or 4.8 $\pm$ 0.2 hours, where the former period is slightly favoured by the obtained periodogram. They estimate a radius of 0.21 $\pm$ 0.02 km and an axis ratio $a/b \geq 1.53$.

4.1.14 169P/NEAT

Comet 169P/NEAT was discovered as asteroid 2002 EX12 by the NEAT survey in 2002. Later it was designated as 169P/NEAT due to the detection of cometary activity (Warner & Fitzsimmons, 2005). Due to its albedo of 0.03 $\pm$ 0.01 (DeMeo & Binzel, 2008) and its weak activity level, 169P is considered to be a transition object on its way to becoming a dormant comet.

Warner (2006b) reported the first rotational lightcurve of 169P with a double-peaked period 8.369 ± 0.05 hours and peak-to-peak amplitude Δm = 0.60 ± 0.02 mag. Later, Kasuga et al. (2010) observed the comet with a much larger (1.85-m) telescope and separated the nucleus brightness from the slight coma contribution. Therefore their derived lightcurve period of 8.4096 ± 0.0012 hours, photometric range Δm = 0.29 ± 0.02 mag and consequent effective radius of 2.3 ± 0.4 km are more reliable measures of the nucleus properties. However, the presence of coma during the observations done by Warner (2006b) would suppress the lightcurve amplitude. Therefore the higher amplitude measured by Warner (2006b) must instead be the result of a more elongated shape, measured at a different aspect than Kasuga et al. (2010), unless the coma is highly variable on a timescale shorter than the spin period. However, due to the weak levels of activity present in this comet, this level of variability is unrealistic and I adopt the larger implied axis ratio limit from the Warner (2006b) data.

Fernández et al. (2013) determined an effective radius of $2.48^{+0.13}_{-0.14}$ km for 169P using Spitzer mid-infrared data.

4.1.15 209P/LINEAR

Hergenrother (2014) observed 209P and found its rotation rate to be either 10.93 or 21.86 hours. In May 2014, the comet had an exceptionally close approach to Earth (0.6 AU) which provided an opportunity for detailed studies of its intrinsically faint nucleus. Howell et al. (2014) used the Arecibo and Goldstone planetary radar systems to directly measure the nucleus to be 3.9 × 2.7 × 2.6 km in size, and calculated an effective radius of ∼ 1.53 km. These observations ruled out the longer period by Hergenrother (2014) since the measured rotational velocities were too fast for the longer period.

Schleicher & Knight (2016) also observed 209P during its perigee in May 2014. They used images obtained mainly with the 4.3 m Discovery Channel Telescope

to study the coma and the nucleus of the comet. They used a small aperture with fixed projected size of 312 km, minimising the coma contribution so that the estimated nucleus fraction of the obtained light was 52-69 percent (Schleicher & Knight, 2016). Their lightcurve was consistent with the two periods from Hergenrother (2014). However, Schleicher & Knight (2016) preferred the shorter value, 10.93 hours, since it also agreed with the radar observations. Schleicher & Knight (2016) reported that their lightcurve had a different shape than the one in Hergenrother (2014). Additionally, they measured variation of 0.6-0.7 mag, which is larger than the prediction of 0.4 mag based on the radar measurements. These differences can be explained by a possible interplay between shape and viewing geometry as well as albedo effects (Schleicher & Knight, 2016). Despite these discrepancies, all three investigations agree on the spin period of 10.93 hours.

4.1.16 260P/McNaught

260P was discovered in 2012, and the most reliable estimate of its effective radius to date is $1.54^{+0.09}_{-0.08}$ km (Fernández et al., 2013). Its rotational characteristics were studied by Manzini et al. (2014) with ground photometric observations while the comet was around perihelion in 2012 and 2013. Manzini et al. (2014) used coma structures to constrain the pole orientation of the comet, but they were unable to use the coma morphology to derive a rotational period. Instead, the comet's lightcurve was obtained by measuring the coma brightness with apertures larger than the seeing disc but small enough to include only contribution from the coma at a distance up to 2000 – 2500 km from the surface (Manzini et al., 2014). The resulting lightcurve had a variation of 0.07 mag and could be phased with a few possible periods, best summarised as 8.16 ± 0.24 hours.

While the method used in Manzini et al. (2014) has been used successfully to derive other rotations periods of comets with weak jet activity (e.g. Reyniers et al., 2009), I regard the results on 260P with caution. It is very likely that the

coma contribution in the selected apertures dilutes the received nucleus signal and dampens the possible variation caused by rotation. Therefore the limit on the nucleus elongation derived from the brightness variation is a weak constraint on the nucleus shape.

4.1.17 322P/SOHO 1

Comet 332P/SOHO 1 was discovered by *SOHO* as C/1999 R1, but after it was identified again in the *SOHO* fields during the following apparitions (Hoenig, 2005), it became the first *SOHO*-discovered comet with conclusive orbital periodicity. The observations of 322P during four consecutive apparitions displayed no clear signatures of a coma or tail and showed a nearly identical asymmetrical heliocentric lightcurve, implying repeated activity at similar levels each orbit (Lamy et al., 2013).

Despite its comet-like orbit with Tisserand parameter with respect to Jupiter of 2.3, the unusual properties of 322P suggest that it has asteroidal rather than cometary origin (Knight et al., 2016). Their optical lightcurve indicates a fast rotation rate of 2.8 ± 0.3 hr and photometric range of > 0.3 mag. These figures imply a density of > 1000 kg m^{-3}, which strengthens the argument for asteroidal origin (Knight et al., 2016). This density is significantly higher than the typical values of other known comets but is typical for asteroids (see Section 6.3). Additionally, the colour of 322P is indicative of V- and Q-type asteroids, and its albedo (estimated to be between 0.09 and 0.42) is higher than the albedos measured for any other comet (Knight et al., 2016). These, together with the very low activity of the nucleus, indicate the possibility that 322P is an asteroid which becomes active when very close to the Sun. However, since no other comet nucleus has been studied so close to the Sun, it is not excluded that it has a cometary origin, but proximity to the Sun has changed the properties of its surface (Knight et al., 2016).

4.2 Comets with new rotation rates derived in this work

4.2.1 14P/Wolf

The first attempt to find the size of the nucleus of comet 14P/Wolf resulted in an effective radius of 1.3 km (Tancredi et al., 2000). However, the authors classified the estimate as poor due to the large scatter in the data points. Lowry et al. (2003) determined a radius of 2.3 km using snapshots of the comet at large heliocentric distance (3.98 au). The most recent value for the comet's effective radius is 2.95 ± 0.19 km, obtained within the SEPPCoN survey (Fernández et al., 2013).

Snodgrass et al. (2005) obtained time-series of the bare nucleus of 14P on 20 and 21 January 2004 with the New Technology Telescope (NTT) in La Silla. The observations showed a clear brightness variation of the nucleus with a period of 7.53 ± 0.10 hours. The peak-to-peak variation of the lightcurve was 0.55 ± 0.05 mag, which corresponds to an axis ratio $a/b \geq 1.7 \pm 0.1$. The mean absolute magnitude of the time series was 22.281 ± 0.007 mag, which suggested an effective radius of 3.16 ± 0.01 km, assuming an albedo of 4% (Snodgrass et al., 2005).

In Section 5.2 I provide the results from a new lightcurve analysis. I combined the re-analysed data from 2004 with a SEPPCoN dataset from 2007 in order to improve the lightcurve of the comet and to derive its phase function. In addition to this, I added new observations of 14P taken one rotation later, in 2016. In Section 7.2 I present the results of the period-change search based on these data.

4.2.2 47P/Ashbrook-Jackson

The early estimates of the nucleus size of 47P from photometric observations close to aphelion determined an effective radius $R_{\rm eff} = 3.0$ km Licandro et al. (2000) and $R_{\rm eff} = 2.9$ km (Tancredi et al., 2000). Snodgrass et al. (2006) and Snodgrass et al.

(2008b) observed the nucleus in 2005 and 2006 at large heliocentric distance close to aphelion and estimated $R_{\rm eff} = 2.96 \pm 0.05$ km. However, their photometric comet profiles showed signatures of activity, and therefore this estimate was considered an upper limit of the nucleus size. Lamy et al. (2011) used HST observations of the active nucleus of 47P to determine a mean effective radius of 2.86 ± 0.08 km. The most recent effective radius measurement of $3.11^{+0.20}_{-0.21}$ km was obtained within the SEPPCoN survey (Fernández et al., 2013).

Lamy et al. (2011) derived a partial lightcurve with multiple possible periods. Analysing the periodogram, they suggested that the rotation period of the comet is $\geq 16 \pm 8$ hours. Both Snodgrass et al. (2008b) and Lamy et al. (2011) attempted to constrain the phase function of 47P by combining all mentioned photometric observations. While the analysis of Snodgrass et al. (2008b) clearly suggested a linear phase function with a slope $\beta = 0.083$ mag/deg , Lamy et al. (2011) showed that a less steep phase function similar to that of 19P/Borelly (0.072 ± 0.020 mag/deg; Li et al., 2007b) is also possible.

In Section 5.3, I show the result from my analysis of the data from Snodgrass et al. (2008b) complemented by a new data set obtained in 2015. I determined the lightcurve and the phase function of 47P, but the derived results need to be considered with caution since the comet was active during both observing runs.

4.2.3 93P/Lovas

Comet 93P/Lovas was one of the targets of the SEPPCoN survey. Its effective radius $R_{\rm eff} = 2.59 \pm 0.26$ km was derived from Spitzer thermal emission observations (Fernández et al., 2013).

New optical time-series observations are presented in Section 5.4. Despite the weak activity detected on the frames, I attempted to constrain the comet's rotation lightcurve.

4.2.4 94P/Russell 4

Tancredi et al. (2000) tried to estimate the effective radius of 94P. However, at the time of the observations, the comet exhibited slight activity and the absolute magnitude measurements of the nucleus had large scatter. Therefore Tancredi et al. (2000) considered their effective radius estimate of 1.9 km as uncertain and estimated the error bars of the measurement to be between ± 0.6 and ± 1 mag.

Snodgrass et al. (2008b) observed the comet during four nights in July 2005 at heliocentric distance 4.14 au, outbound. The analysis pointed to a nucleus with effective radius of 2.62 ± 0.02 km and a lightcurve with period ∼ 33 hours (Snodgrass et al., 2008b). The peak-to-peak variation of the lightcurve was 1.2 ± 0.2 mag, implying axis ratio $a/b \geq 3.0 \pm 0.5$. Their nucleus size estimate $R_{\rm eff}$ = 2.62 ± 0.02 km is in a good agreement with the SEPPCoN Spitzer data from Fernández et al. (2013), who reported an effective radius of $2.27^{+0.13}_{-0.15}$ km.

In Section 5.5, I present two additional data sets from 2007 and 2009 with time-series photometry of 94P. They allowed me to determine the rotational lightcurve and the phase function of the comet.

4.2.5 110P/Hartley 3

110P/Hartley 3 was observed with HST on November 24 2000 at heliocentric distance of 2.58 au, inbound (Lamy et al., 2011). The data yielded an estimate of the effective radius of the nucleus $R_{\rm eff}$ = 2.15 ± 0.04 km and a lightcurve with period 9.4 ± 1 hours. The peak-to-peak amplitude of the obtained lightcurve was 0.4 mag, which suggested an axis ratio $a/b \geq 1.30$.

In Section 5.6, I analyse a further data set from 2012 which was obtained in order to derive the comet's phase function. I used the data to derive a precise phase function of 110P as well as to constrain its lightcurve better.

4.2.6 123P/West-Hartley

Tancredi et al. (2000) estimated a radius of 2.2 km for the nucleus of comet 123P/West-Hartley. However, the authors consider this result as very uncertain since the individual photometric measurements of the comet nucleus displayed a large scatter. The SEPPCoN mid-infrared observations of 123P yielded an effective radius of 2.18 ± 0.23 km (Fernández et al., 2013).

In Section 5.7 I present the results from my analysis of a SEPPCoN data set from three observing nights in 2007. The comet was very faint (m_r = 23.3 ± 0.1 mag) and weakly active during the observations, which significantly obstructed the lightcurve analysis.

4.2.7 137P/Shoemaker-Levy 2

Licandro et al. (2000) observed 137P at heliocentric distance 4.24 AU and determined an effective radius of 4.2 km and a brightness variation of 0.4 mag. As described in Licandro et al. (2000), their observations suffered from different technical problems, and therefore this result is uncertain. Lowry et al. (2003) obtained a radius ≤ 3.4 km from observations of the still active nucleus of 137P at heliocentric distance 2.29 au. Tancredi et al. (2000) observed the comet at 5 au from the Sun and estimated the effective nucleus radius to be 2.9 km. Finally, Fernández et al. (2013) targeted the comet as part of SEPPCoN and measured an effective radius of $4.04^{+0.31}_{-0.32}$ km.

Snodgrass et al. (2006) obtained time-series photometry from one night on NTT/EMMI in La Silla. The data did not show brightness variation within the 3 hours of the observations and could not be used to determine the rotation rate of the nucleus. However, Snodgrass et al. (2006) used these frames to estimate the nucleus radius as 3.58 ± 0.05 km. I added 2 further nights of time-series obtained within SEPPCoN to the one night reported in Snodgrass et al. (2006) and I used the combined data set in an attempt to characterise the phase function and the

rotational properties of the comet (Section 5.8).

4.2.8 143P/Kowal-Mrkos

The nucleus of comet 143P/Kowal-Mrkos was observed during nine nights in 2001 by Jewitt et al. (2003). Using these observations, they derived a rotation period $P = 17.21 \pm 0.10$ hours, brightness variation $\Delta m = 0.45 \pm 0.05$ mag and phase-function slope $\beta = 0.043 \pm 0.014$ mag/deg in R-band. Assuming an albedo of 0.04, Jewitt et al. (2003) derived an effective radius of 5.7 ± 0.6 km. Fernández et al. (2013) used thermal infrared measurements to determine a radius $R_{\rm n} = 4.79^{+0.32}_{-0.33}$ km.

In Section 7.3, I add new observations from 2016 and 2017, which I used to look for period changes during the last perihelion passage. These observations, combined with the radius from Fernández et al. (2013), allowed me to determine the comet's albedo.

4.2.9 149P/Mueller 4

149P/Mueller was among the SEPPCoN targets. The Spitzer observations revealed a nucleus with an effective radius of $1.42^{+0.09}_{-0.10}$ km (Fernández et al., 2013). To my knowledge, no previous lightcurves of this comet are available.

In Section 5.9, I present an analysis of the optical observations taken as part of SEPPCoN. I use the data to derive the phase function of the comet and to place constraints on its shape and albedo.

4.2.10 162P/Siding Spring

Comet 162P was discovered as asteroid 2004 TU12 but was later identified as a comet since it shows weak intermittent activity (Campins et al., 2006, and references therein).

Fernández et al. (2006) analysed its thermal emission from NASA's Infrared Telescope Facility in December 2004 during the same apparition. Their measurements suggested a remarkably large nucleus with an effective radius of 6.0 ± 0.8 km (Fernández et al., 2006). 162P was also observed within SEPPCoN. The Spitzer mid-infrared observations from 2007 provided a more precise estimate of the effective radius, $R_{\rm eff} = 7.03^{+0.47}_{-0.48}$ km (Fernández et al., 2013).

There are no published rotational lightcurves of the nucleus of 162P to my knowledge. However, there is a well-sampled lightcurve with period $P_{\rm rot} \sim 33$ hours by the amateur observatory La Cañada[2]. Those data were taken in November 2004, just a month after the discovery of the comet.

In Section 5.10, I analyse two time-series data sets from 2007 and 2012. These data allow me to derive the phase function of 162P and to estimate its rotation period at two different epochs. I observed comet 162P again in 2017 in order to look for period changes during the last perihelion passage (Section 7.4).

[2] http://www.lacanada.es/Docs/162P.htm

Table 4.1: Summary of the properties of the comets with published rotation rates and the comets studied in this work

Comet	$R_{\rm eff}$ (km)	Ref. $R_{\rm eff}$	Δm	Ref. Δm	a/b	Ref. a/b	$P_{\rm rot}$ (hr)	Ref. $P_{\rm rot}$
2P	3.95 ± 0.06	(1)	0.4 ± 0.04	(1)	$\geq 1.44 \pm 0.06$	(1)	11.0830 ± 0.0030	(1)
6P	$2.23^{+0.13}_{-0.15}$	(2)	0.082 ± 0.016	(3)	≥ 1.08	(*)[a]	6.67 ± 0.03	(3)
7P	2.64 ± 0.17	(2)	0.30 ± 0.05	(4)	$\geq 1.3 \pm 0.1$	(4)	$7.9^{+1.6}_{-1.1}$	(4)
9P	2.83 ± 0.1	(5)	0.6 ± 0.2	(6)	1.89[b]	(5)	41.335 ± 0.005[c]	(7)
10P	5.98 ± 0.04	(8)	0.7	(9)	≥ 1.9	(9)	8.948 ± 0.001	(10)
14P	2.95 ± 0.19	(2)	0.37 ± 0.05	(*)	$\geq 1.41 \pm 0.06$	(*)	9.07 ± 0.01	(*)
17P	1.62 ± 0.01	(11)	0.30 ± 0.05	(11)	$\geq 1.3 \pm 0.1$	(11)	7.2/8.6/10.3/12.8	(11)
19P	2.5 ± 0.1	(12)	0.84-1.00	(13)	2.53 ± 0.12[b]	(12)	26.0 ± 1.0	(13)
21P	1.0	(14)	0.43	(15)	≥ 1.5	(15)	9.50 ± 0.2	(16)
22P	2.15 ± 0.17	(2)	0.55 ± 0.07	(17)	$\geq 1.66 \pm 0.11$	(17)	12.30 ± 0.8	(17)
28P	10.7 ± 0.7	(18)	0.45 ± 0.07	(19)	$\geq 1.51 \pm 0.07$	(19)	12.75 ± 0.03	(19)
31P	$1.65^{+0.11}_{-0.12}$	(2)	0.5 ± 0.1	(20)	$\geq 1.6 \pm 0.15$	(20)	5.58 ± 0.03	(20)
36P	2.55 ± 0.01	(21)	0.7 ± 0.1	(21)	$\geq 1.9 \pm 0.1$	(21)	~ 40	(21)
46P	0.56 ± 0.04	(22)	0.38	(22)	$\geq 1.4 \pm 0.1$	(22)	6.00 ± 0.3	(23)
47P	$3.11^{+0.20}_{-0.21}$	(2)	0.33 ± 0.06	(*)	$\geq 1.36 \pm 0.07$	(*)	15.6 ± 0.1	(*)

Table 4.1 continued

Comet	$R_{\rm eff}$ (km)	Ref. $R_{\rm eff}$	Δm	Ref. Δm	a/b	Ref. a/b	$P_{\rm rot}$ (hr)	Ref. $P_{\rm rot}$
48P	$2.97^{+0.19}_{-0.20}$	(2)	0.32 ± 0.05	(24)	≥ 1.34 ± 0.06	(24)	29.00 ± 0.04	(24)
49P	4.24 ± 0.2	(18,25,26)	0.5	(25)	≥ 1.63 ± 0.07	(25)	13.47 ± 0.017	(25)
61P	0.61 ± 0.03	(27)	0.26	(27)	≥ 1.3	(27)	4.9 ± 0.2	(27)
67P	1.649 ± 0.007	(28)	0.4 ± 0.07	(29)	2.05 ± 0.06[b]	(28)	12.055 ± 0.001	ESA/Rosetta
73P	0.41 ± 0.02	(30)	-	-	≥ 1.8 ± 0.3	(30)	3.0 - 3.4	(31)
76P	0.31 ± 0.01	(27)	0.56	(27)	≥ 1.45	(27)	6.6 ± 1.0	(27)
81P	1.98 ± 0.05	(32)	-	-	1.67 ± 0.04	(33)	13.5 ± 0.1	(34)
82P	0.59 ± 0.04	(27)	0.58	(27)	≥ 1.59	(27)	≥ 24 ± 5	(27)
87P	0.26 ± 0.01	(27)	0.94	(27)	≥ 2.2	(27)	32 ± 9	(27)
92P	2.08 ± 0.01	(4)	0.6 ± 0.05	(4)	≥ 1.7 ± 0.1	(4)	6.22 ± 0.05	(4)
93P	2.59 ± 0.26	(2)	0.21 ± 0.05	(*)	≥ 1.21 ± 0.06	(*)	$18.2^{+1.5}_{-15}$	(*)
94P	$2.27^{+0.13}_{-0.15}$	(2)	1.11 ± 0.09	(*)	≥ 2.8 ± 0.2	(*)	20.70 ± 0.07	(*)
103P	0.58 ± 0.018	(35)	–	–	3.38[b]	(35)	16.4 ± 0.1	(36)
110P	2.50 ± 0.04	(*)	0.20 ± 0.03	(*)	≥ 1.20 ± 0.03	(*)	10.153 ± 0.001	(*)
121P	$3.87^{+0.26}_{-0.21}$	(2)	0.15 ± 0.03	(21)	≥ 1.15 ± 0.03	(21)	10^{+8}_{-2}	(21)

Table 4.1 continued

Comet	R_{eff} (km)	Ref. R_{eff}	Δm	Ref. Δm	a/b	Ref. a/b	P_{rot} (hr)	Ref. P_{rot}
123P	2.18 ± 0.23	(2)	0.5 ± 0.1	(*)	1.6 ± 0.1	(*)	–	–
137P	$4.04^{+0.31}_{-0.32}$	(2)	0.18 ± 0.05	(*)	1.18 ± 0.05	(*)	–	
143P	$4.79^{+0.32}_{-0.33}$	(2)	0.45 ± 0.05	(37)	$\geq 1.49 \pm 0.05$	(18)	7.1966/17.2121/17.1812	(37)
147P	0.21 ± 0.02	(27)	0.40	(27)	≥ 1.53	(27)	10.5 ± 1 / 4.8 ± 0.2	(27)
149P	$1.42^{+0.09}_{-0.10}$	(2)	0.11 ± 0.04	(*)	1.11 ± 0.04	(*)	–	–
162P	$7.03^{+0.47}_{-0.48}$	(2)	0.59 ± 0.04	(*)	$\geq 1.72 \pm 0.06$	(*)	32.9 ± 0.2	(*)
169P	$2.48^{+0.13}_{-0.14}$	(2)	0.60 ± 0.02	(38)	$\geq 1.74 \pm 0.03$	(*)[a]	8.4096 ± 0.0012	(39)
209P	~ 1.53	(40)	0.4 - 0.7	(40,41)	≥ 1.55	(40)	10.93 ± 0.020	(40,41)
260P	$1.54^{+0.09}_{-0.08}$	(2)	0.07	(42)	≥ 1.07	(*)[a]	8.16 ± 0.24	(42)
322P	0.150 - 0.320	(43)	≥ 0.3	(43)	≥ 1.3	(43)	2.8 ± 0.3	(43)

[a] Calculated with Eq. 3.11 using the brightness variation Δm.

[b] The exact shape model was derived by spacecraft observations in the cited paper. The provided axis ratio is obtained by dividing the highest shape model radius to the lowest one.

[c] The comet is known to increase its period and this is the minimum known value measured with sufficient precision.

* Results derived in this thesis.

References: (1) Lowry & Weissman (2007); (2) Fernández et al. (2013); (3) Gutierrez et al. (2003); (4) Snodgrass et al. (2005); (5) Thomas et al. (2013a); (6) Fernández et al. (2003); (7) Belton et al. (2011); (8) Lamy et al. (2009); (9) Jewitt & Luu (1989); (10) Schleicher et al. (2013); (11) Snodgrass et al. (2006); (12) Buratti et al. (2004); (13) Mueller & Samarasinha (2002); (14) Tancredi et al. (2000); (15) Mueller (Mueller); (16) Leibowitz & Brosch (1986); (17) Lowry & Weissman (2003); (18) Lamy et al. (2004); (19) Delahodde et al. (2001); (20) Luu & Jewitt (1992); (21) Snodgrass et al. (2008b); (22) Boehnhardt et al. (2002); (23) Lamy et al. (1998a); (24) Jewitt & Sheppard (2004); (25) Millis et al. (1988); (26) Campins et al. (1995); (27) Lamy et al. (2011); (28) Jorda et al. (2016); (29) Tubiana et al. (2008); (30) Toth et al. (2006); (31) Drahus et al. (2010); (32) Sekanina et al. (2004); (33) Duxbury et al. (2004); (34) Mueller et al. (2010a); (35) Thomas et al. (2013b); (36) Meech et al. (2009); (37) Jewitt et al. (2003); (38) Warner (2006b); (39) Kasuga et al. (2010); (40) Howell et al. (2014); (41) Schleicher & Knight (2016); (42) Manzini et al. (2014); (43) Knight et al. (2016)

Chapter 5

Rotational and surface properties of JFCs from sparse photometry

5.1 Overview of observations

The main goal of this chapter is to expand the sample of JFCs with known rotational properties, as a step towards defining better constraints on the bulk properties of comets. Below I present the optical lightcurves of nine JFC nuclei which were observed in the period 2004–2015 (Table 5.1).

Most of the data come from SEPPCoN. Here, I present the lightcurves of eight of those comets. The remaining comets had time series which were not sufficient to measure reliable brightness variations. They will be included in a publication by the SEPPCoN team which will focus on the sizes, albedos and phase curves of all observed comets.

For some of the SEPPCoN comets presented below, I was also able to retrieve archival time-series from other programmes. For 14P and 94P, this included already published data from previous studies (Snodgrass et al., 2005, 2006). These archival datasets could be consolidated with the newly obtained data, since all observations were from the same aphelion passages. All observations were analysed with the newly developed method which ensured that the combined time series from all different epochs were consistent. Combining all available data allowed

me to derive more accurate lightcurves and phase functions for these two comets.

Comet 47P was also part of SEPPCoN although it was at an unfavourable orbital configuration during the ground observing campaign. Comet 47P was observed as a backup target of the ESO large program 194.C-0207 in 2015. These data were combined with an archival dataset from 2005 (Snodgrass et al., 2008b).

Another major source of time-series data were the ESO observing programmes P87.C-107 and P89.C-0372. Those campaigns aimed to follow the same comets over an extended period in order to provide a good phase-function sampling. Despite having a different observing strategy, those datasets were suitable for the extraction of rotational lightcurves. They provided short-time series of comets 110P and 162P over the course of a few months. Although the data came from different epochs and geometries, they could be linked together owing to the specially-developed procedure for absolute photometric calibration described in section 3.3.

5.2 14P/Wolf

The lightcurve of comet 14P/Wolf was first determined from 2 observing nights close to aphelion in 2004 by Snodgrass et al. (2005). The SEPPCoN team observed 14P once more in 2007 during the same aphelion passage. I analysed both datasets with the new method for absolute photometric calibration and combined them in order to constrain better the comet's rotational period.

I used the procedure described in Section 3.5 to check whether 14P was active during the observations in 2004. The comet appears stellar in the co-added comet composite image and its surface brightness profile is indistinguishable from that of the comparison star (Fig. 5.1). This confirms the conclusion of Snodgrass et al. (2005) that 14P was not active during the observations in 2004.

Figure 5.2 shows the Lomb-Scargle periodogram for the 2004 observations of 14P. The highest peak is at $P_{\rm fit} = 4.46$ h, corresponding to a rotation period

Table 5.1: Summary of all observations analysed in this chapter.

Comet	UT date	R_h [au][a]	Δ [au]	α [deg.]	Filter	Number	Exposure time (s)	Instrument	Proposal ID
14P	2004-01-20	5.51^{O}	4.96	8.96	R	29	220	NTT-EMMI	072.C-0233(A)
	2004-01-21	5.51^{O}	4.95	8.87	R	29	220	NTT-EMMI	072.C-0233(A)
	2007-05-14	4.36^{I}	3.43	6.05	R	6	60	NTT-EMMI	079.C-0297(A)
	2007-05-18	4.35^{I}	3.41	5.79	R	18	70	WHT-PFIP	W/2007A/20
	2007-05-19	4.34^{I}	3.41	5.75	R	29	70	WHT-PFIP	W/2007A/20
47P	2005-03-05	5.42^{I}	4.47	3.49	R	20	85	NTT-EMMI	074.C-0125(A)
	2005-03-06	5.42^{I}	4.47	3.30	R	34	85	NTT-EMMI	074.C-0125(A)
	2006-06-01	4.96^{I}	4.23	8.87	R*	4	300	VLT-FORS2	077.C-0609(B)
	2015-04-19	4.55^{I}	3.64	5.77	r'	5	100	NTT-EFOSC2	194.C-0207(C)
	2015-04-21	4.55^{I}	3.62	5.40	r'	7	150	NTT-EFOSC2	194.C-0207(C)
	2015-04-22	4.55^{I}	3.61	5.22	r'	19	17x80 , 2x100	NTT-EFOSC2	194.C-0207(C)
	2015-04-23	4.54^{I}	3.60	5.04	r'	21	20x80 , 1x120	NTT-EFOSC2	194.C-0207(C)
	2015-04-24	4.54^{I}	3.60	4.86	r'	29	26x80 , 3x120	NTT-EFOSC2	194.C-0207(C)
93P	2009-01-21	3.79^{O}	3.25	13.40	R	4	150	WHT-PFIP	W/2008B/23
	2009-01-22	3.80^{O}	3.24	13.30	R	2	250	VLT-FORS2	082.C-0517(B)

Table 5.1 continued

Comet	UT date	R_h [au][a]	Δ [au]	α [deg.]	Filter	Number	Exposure time (s)	Instrument	Proposal ID
	2009-01-24	3.81^{O}	3.22	13.00	R	8	250	VLT-FORS2	082.C-0517(B)
	2009-01-27	3.83^{O}	3.20	12.50	R	18	120	NTT-EFOSC2	082.C-0517(A)
	2009-01-28	3.83^{O}	3.19	12.30	R	29	120	NTT-EFOSC2	082.C-0517(A)
	2009-01-29	3.84^{O}	3.19	12.20	R	16	120	NTT-EFOSC2	082.C-0517(A)
94P	2005-07-04	4.14^{O}	3.19	5.62	r'	7	75	INT-WFC	I/2005A/11
	2005-07-05	4.14^{O}	3.18	5.37	r'	17	75	INT-WFC	I/2005A/11
	2005-07-06	4.14^{O}	3.18	5.13	r'	17	75	INT-WFC	I/2005A/11
	2005-07-07	4.15^{O}	3.18	4.88	r'	15	75	INT-WFC	I/2005A/11
	2007-07-17	4.68^{I}	4.38	12.30	R	1	750	NTT-EMMI	079.C-0297(B)
	2007-07-18	4.68^{I}	4.36	12.30	R	4	340	NTT-EMMI	079.C-0297(B)
	2007-07-19	4.68^{I}	4.35	12.20	R	6	360	NTT-EMMI	079.C-0297(B)
	2007-07-20	4.68^{I}	4.33	12.20	R	8	400	NTT-EMMI	079.C-0297(B)
	2009-01-22	3.41^{I}	3.12	16.60	R	6	120	WHT-PFIP	W/2008B/23
	2009-01-27	3.39^{I}	3.18	16.80	R	6	100	NTT-EFOSC2	082.C-0517(A)
	2009-01-28	3.39^{I}	3.19	16.90	R	8	100	NTT-EFOSC2	082.C-0517(A)

Table 5.1 continued

Comet	UT date	R_h [au][a]	Δ [au]	α [deg.]	Filter	Number	Exposure time (s)	Instrument	Proposal ID
	2009-01-29	3.39^{I}	3.21	16.90	R	8	100	NTT-EFOSC2	082.C-0517(A)
110P	2012-06-17	4.51^{I}	3.73	9.22	R	26	160	NTT-EFOSC2	089.C-0372(A)
	2012-06-18	4.51^{I}	3.72	9.06	R	42	10x250, 32x180	NTT-EFOSC2	089.C-0372(A)
	2012-06-22	4.50^{I}	3.67	8.37	R*	22	21x70, 1x40	VLT-FORS2	089.C-0372(B)
	2012-06-24	4.50^{I}	3.65	8.01	R*	28	70	VLT-FORS2	089.C-0372(B)
	2012-07-12	4.47^{I}	3.50	4.23	R*	25	70	VLT-FORS2	089.C-0372(B)
	2012-07-15	4.47^{I}	3.48	3.54	R*	18	70	VLT-FORS2	089.C-0372(B)
	2012-07-26	4.45^{I}	3.44	1.28	R*	13	70	VLT-FORS2	089.C-0372(B)
	2012-08-19	4.41^{I}	3.47	5.49	R*	11	70	VLT-FORS2	089.C-0372(B)
123P	2007-07-17	5.57^{O}	4.77	6.92	R	14	150	NTT-EMMI	079.C-0297(B)
	2007-07-18	5.57^{O}	4.76	6.79	R	23	110	NTT-EMMI	079.C-0297(B)
	2007-07-20	5.57^{O}	4.74	6.53	R	18	200	NTT-EMMI	079.C-0297(B)
137P	2005-03-06	6.95^{I}	6.17	5.36	R	18	140	NTT-EMMI	074.C-0125(A)
	2007-05-13	5.26^{I}	4.25	0.83	R	26	1x14, 1x30, 24x75	NTT-EMMI	079.C-0297(A)
	2007-05-14	5.25^{I}	4.24	0.62	R	31	1x15, 30x75	NTT-EMMI	079.C-0297(A)

Table 5.1 continued

Comet	UT date	R_h [au][a]	Δ [au]	α [deg.]	Filter	Number	Exposure time (s)	Instrument	Proposal ID
149P	2009-01-21	3.56^{I}	2.69	8.41	R	8	60	WHT-PFIP	W/2008B/23
	2009-01-22	3.56^{I}	2.69	8.57	R*	21	3x130, 18x80	VLT-FORS2	082.C-0517(B)
	2009-01-23	3.56^{I}	2.69	8.73	R*	19	4x110, 15x80	VLT-FORS2	082.C-0517(B)
	2009-01-24	3.55^{I}	2.69	8.90	R*	34	80	VLT-FORS2	082.C-0517(B)
	2009-01-27	3.54^{I}	2.70	9.42	R	16	60	NTT-EFOSC2	082.C-0517(A)
	2009-01-28	3.54^{I}	2.70	9.61	R	14	60	NTT-EFOSC2	082.C-0517(A)
	2009-01-29	3.54^{I}	2.70	9.79	R	36	60	NTT-EFOSC2	082.C-0517(A)
162P	2007-05-17	4.86^{O}	4.03	7.51	R	13	90	WHT-PFIP	W/2007A/20
	2007-05-18	4.86^{O}	4.04	7.69	R	13	3x90, 10x110	WHT-PFIP	W/2007A/20
	2007-05-19	4.86^{O}	4.05	7.86	R	12	90	WHT-PFIP	W/2007A/20
	2012-04-23	4.73^{O}	3.79	4.68	R*	30	60	VLT-FORS2	089.C-0372(B)
	2012-05-24	4.77^{O}	4.12	10.02	R*	5	60	VLT-FORS2	089.C-0372(B)
	2012-06-14	4.80^{O}	4.44	11.84	R	18	180	NTT-EFOSC2	089.C-0372(A)
	2012-06-17	4.80^{O}	4.49	11.97	R	13	300	NTT-EFOSC2	089.C-0372(A)

Table 5.1 continued

Comet	UT date	R_h [au][a]	Δ [au]	α [deg.]	Filter	Number	Exposure time (s)	Instrument	Proposal ID
	2012-06-23	4.81^O	4.59	12.14	R*	29	60	VLT-FORS2	089.C-0372(B)

[a] Superscripts I and O indicate whether the comet was inbound (pre-perihelion) or outbound (post-perihelion).

* ESO R_SPECIAL+76 filter with effective wavelength 655 nm and FWHM 165.0 nm.

$P_{\rm rot}$ = 8.93 h (Fig. 5.3). Using the Monte Carlo method without phase function correction, I determined that the best-fitting rotation period is $P_{\rm rot}$ = 8.93 ± 0.04 h (Fig. 5.4).

Using the same dataset, Snodgrass et al. (2005) identified 7.53 ± 0.10 h as the most likely rotation period of 14P. That period corresponds to the third highest peak in the current periodogram and results in an unusual asymmetric lightcurve. The difference in the periods likely originates from the different methods for night-to-night calibration adopted in the two works. While Snodgrass et al. (2011) used Landolt star calibration, here I applied the newly developed method for absolute calibration with PS1, which allows precise absolute calibration independent of the changing observing conditions during the night. Thus, by re-analysing the data from 2004 with my method, I improved the period determination of 14P.

The lightcurve of 14P in 2004 phased with $P_{\rm rot}$ = 8.93 ± 0.04 h has a peak-to-peak brightness variation of $\Delta m_{\rm r}$ = 0.36 ± 0.05 mag, which corresponds to axis ratio $a/b \geq 1.39 \pm 0.06$. From Eq. 3.12 I estimated a minimum nucleus density of 0.19 ± 0.04 g cm^{-3}.

Next, I analysed the observations from 2007. The comet appears stellar in the composite images and its surface brightness profile does not deviate from that of the comparison star (Fig. 5.5). I therefore assumed that 14P was inactive at the time of the observations.

The highest peak of the Lomb-Scargle periodogram for the 2007 observations is at $P_{\rm fit}$ = 4.51 h corresponding to a rotation period $P_{\rm rot}$ = 9.02 h. (Fig. 5.6). I used the Monte Carlo approach without geometric corrections to determine a rotation rate $P_{\rm rot}$ = 9.02 ± 0.04 h (right panel on Fig. 5.4). The lightcurve phased with the identified period (Fig. 5.7) has a peak-to-peak variation $\Delta m_{\rm r}$ = 0.39 ± 0.05 mag corresponding to $a/b \geq 1.43 \pm 0.07$ and $D_{\rm N} \geq 0.19 \pm 0.04$ g cm^{-3}.

The periods from 2004 and 2007, around the same aphelion passage, are very similar. Furthermore, the fact that the comet was inactive at both epochs suggests that 14P probably remained inactive around aphelion and a period change due

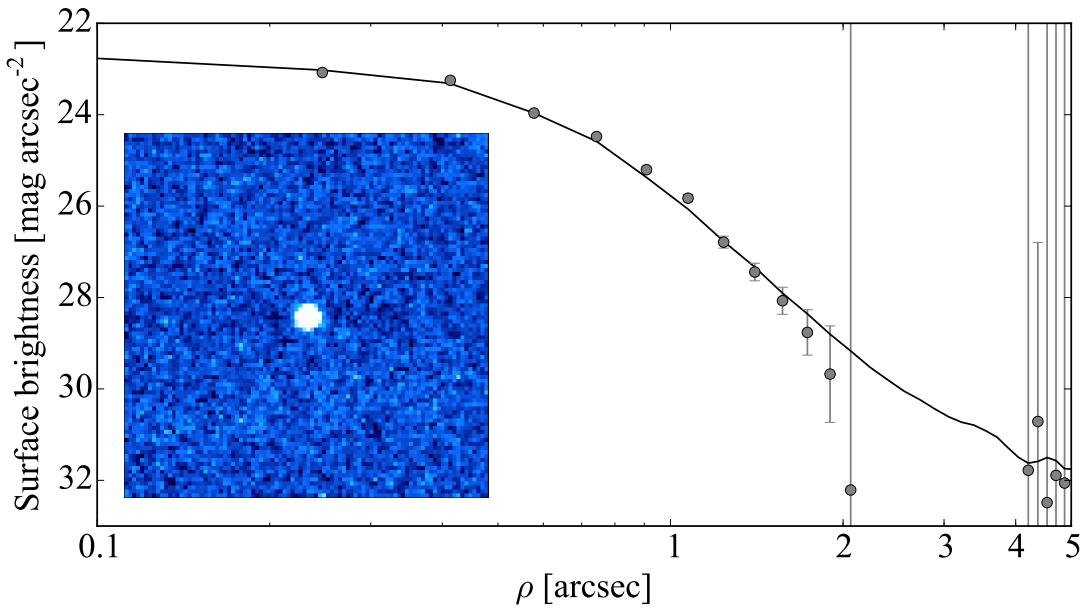

Figure 5.1: Surface brightness profile of 14P from the 2004 dataset. The lower panel shows a 30 × 30 arcseconds composite image of 14P made up of 29 × 220 s exposures taken on 21 January 2004. The frames are added using a method which removes cosmic rays, the background sky and fixed objects. The comet appears stellar and no signatures of activity can be recognised. The surface brightness of the comet is plotted as a function of radius ρ from the centre of the comet. The profile matches the scaled stellar PSF (solid line), indicating that the comet appears as a point source and is therefore considered to be inactive.

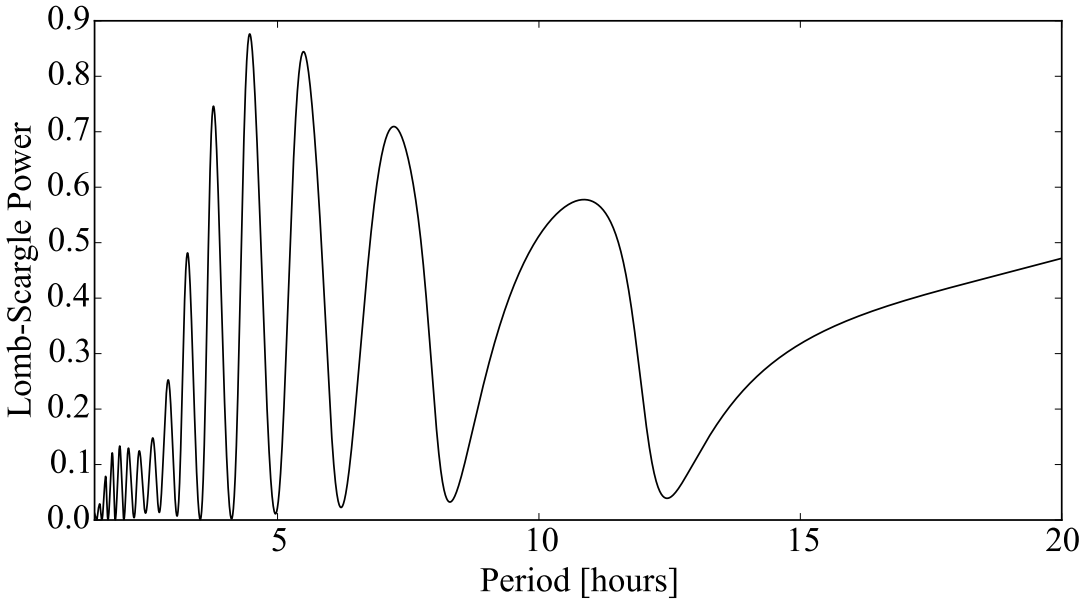

Figure 5.2: Lomb-Scargle periodogram for 14P from the dataset collected in 2004. The plot shows the LS power versus period. The highest peak occurs at 4.46 h, which corresponds to the most likely period $P_{\rm rot}$ = 8.93 h.

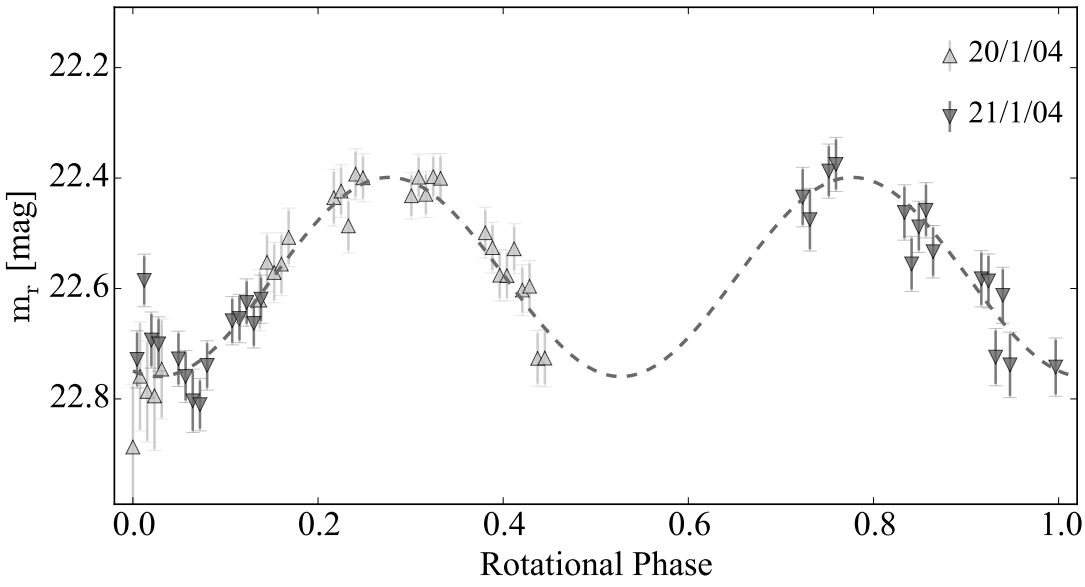

Figure 5.3: Rotational lightcurve of 14P with the data from 2004. The lightcurve is folded with the LS best period of 8.93 h.

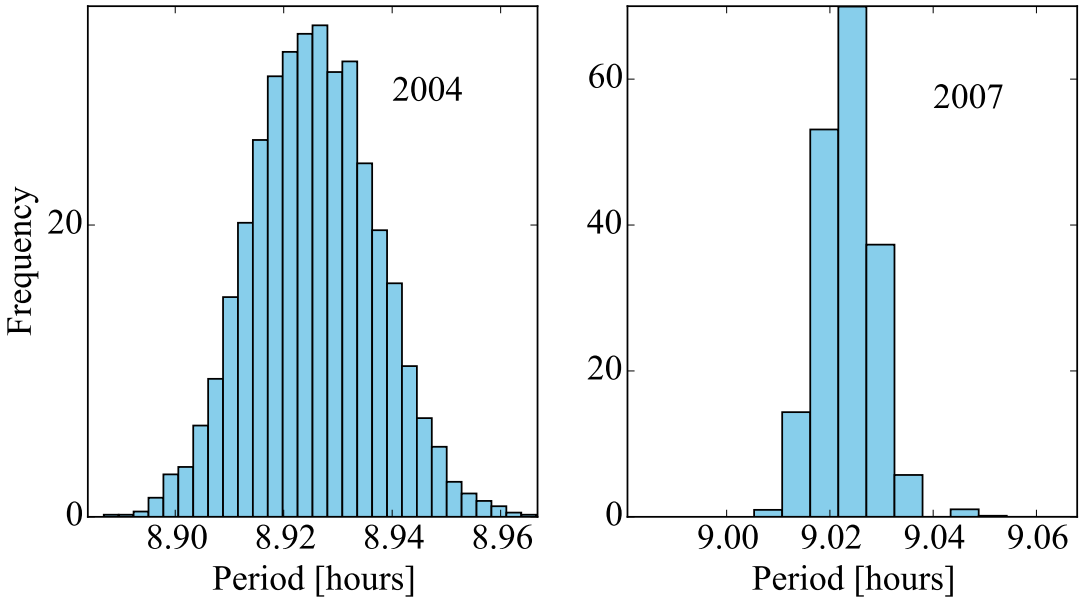

Figure 5.4: Results from the Monte Carlo simulations used to determine the rotation period of 14P from the datasets in 2004 (left) and 2007 (right). The resulting rotation periods for 2004 and 2007 are 8.93 ± 0.04 h and 9.02 ± 0.04 h respectively.

to outgassing is unlikely to have occurred. The solar elongation of the comet during the observations in January 2004 was ∼170°, while it was ∼ 240° in May 2007, and since there is no knowledge on the comet spin axis orientation, it is not possible to exclude the possibility that the viewing geometry changed between

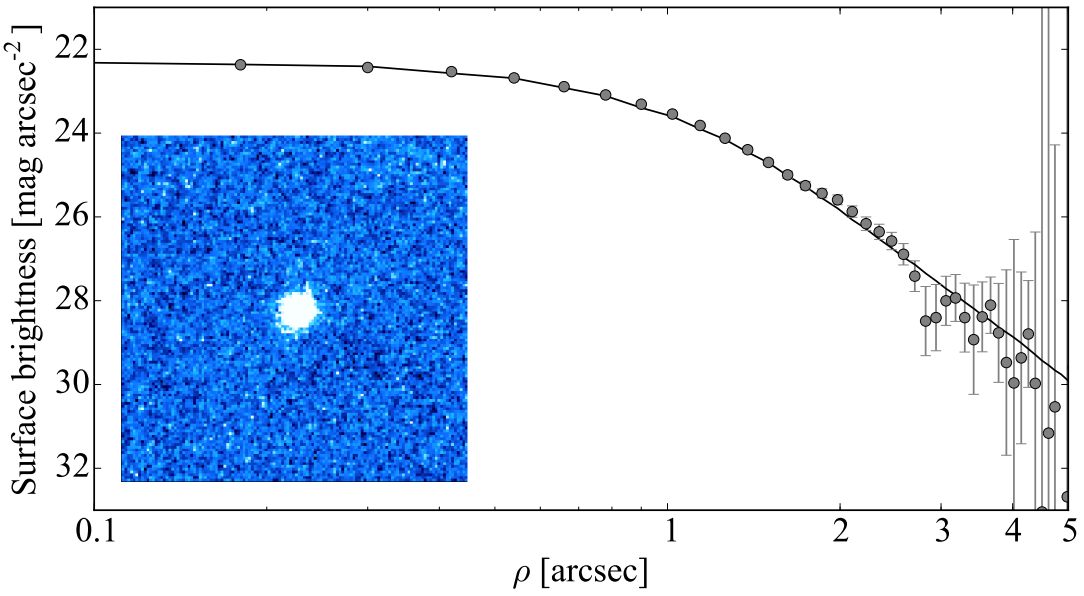

Figure 5.5: Same as Fig. 5.1, for 14P on 18 May 2007. The co-added composite image of 14P was made up of 18 × 70 s exposures. The stellar appearance on the composite image and the surface brightness profile of the comet suggest that 14P was inactive during the observations in 2007.

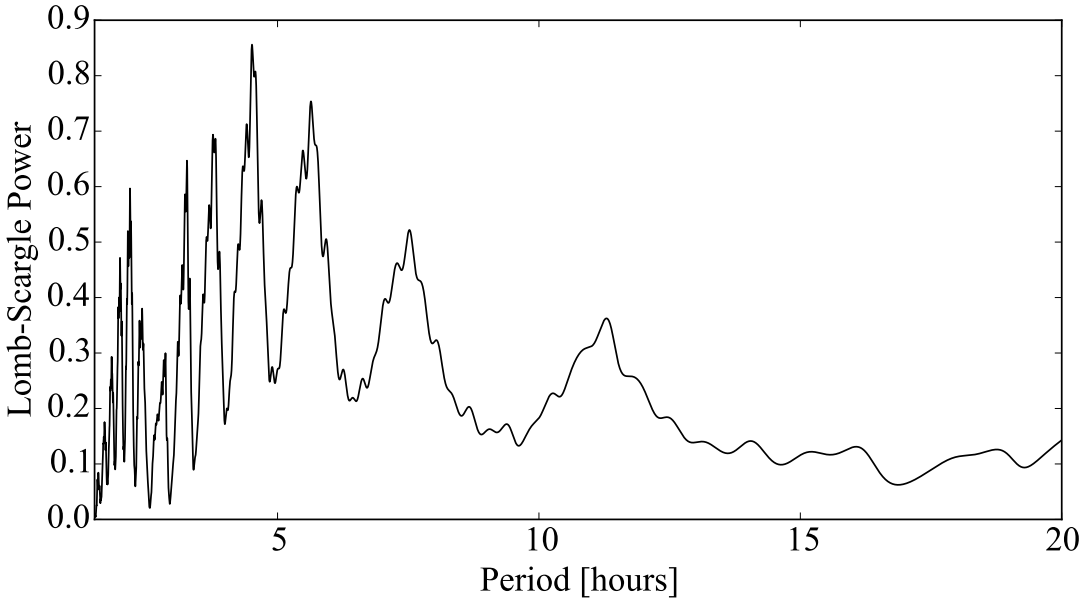

Figure 5.6: Lomb-Scargle periodogram for 14P with the dataset from 2007. The highest peak corresponds to a period $P_{\rm rot}$ = 9.02 h.

the two epochs. However, both individual lightcurves have the same peak-to-peak brightness variation (within the corresponding uncertainties), and therefore I assumed that the change in geometry did not influence the observed lightcurve. With these assumptions at hand, I proceeded to combine the two datasets in order

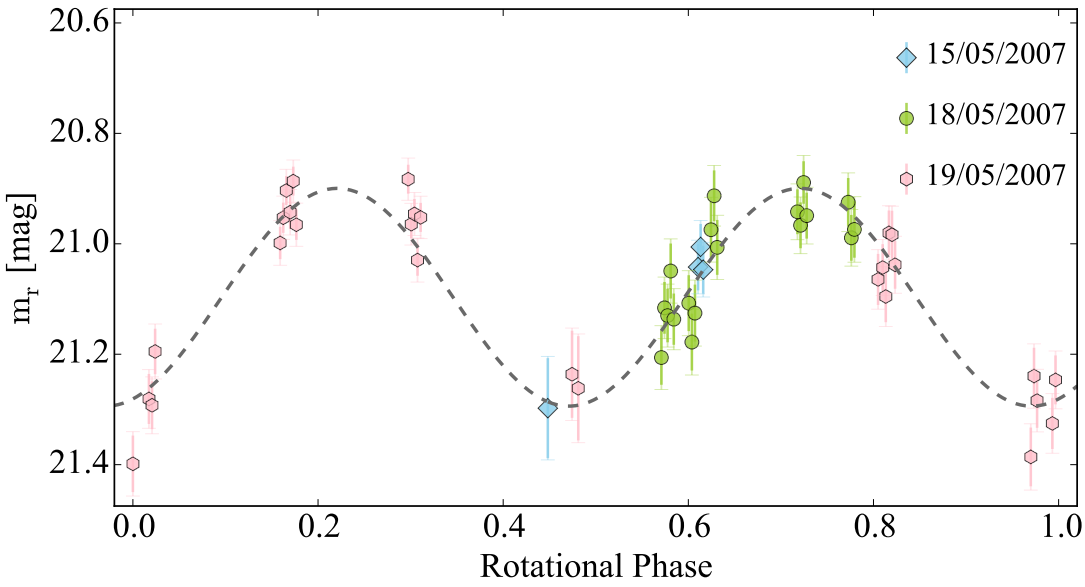

Figure 5.7: Rotational lightcurve of 14P with the data from 2007. The lightcurve is folded with period 9.02 h.

to determine a phase function and a common rotation period.

I ran the Monte Carlo simulation on the combined dataset and determined a phase function slope $\beta = 0.060 \pm 0.005$ mag/deg and period $P_{\rm rot} = 9.02 \pm 0.01$ h (Fig. 5.8, 5.9). The Lomb-Scargle periodogram of the combined datasets (Fig. 5.10) has a pronounced peak at $P_{\rm fit} = 4.51$ h which corresponds to the best period from the Monte Carlo simulation.

The lightcurve phased with the best period $P_{\rm rot} = 9.02$ (Fig. 5.11) has a range $\Delta H_{\rm r} = 0.37 \pm 0.05$ mag corresponding to $a/b \geq 1.41 \pm 0.06$ and $D_{\rm N} \geq 0.19 \pm 0.03$ g cm^{-3}. The mean absolute magnitude was $H_{\rm r}(1,1,0) = 14.87 \pm 0.05$ mag. Using eq. 3.10 and the radius from Fernández et al. (2013), I estimated the comet's albedo to be $A_{\rm r} = 5.0 \pm 0.7\%$.

5.3 47P/Ashbrook-Jackson

The first attempt to determine the rotation rate of 47P was made by Snodgrass et al. (2006) using data from two observing nights in 2005. However, the resulting time series were not sufficient to choose between four possible periods: 11.2, 15.5,

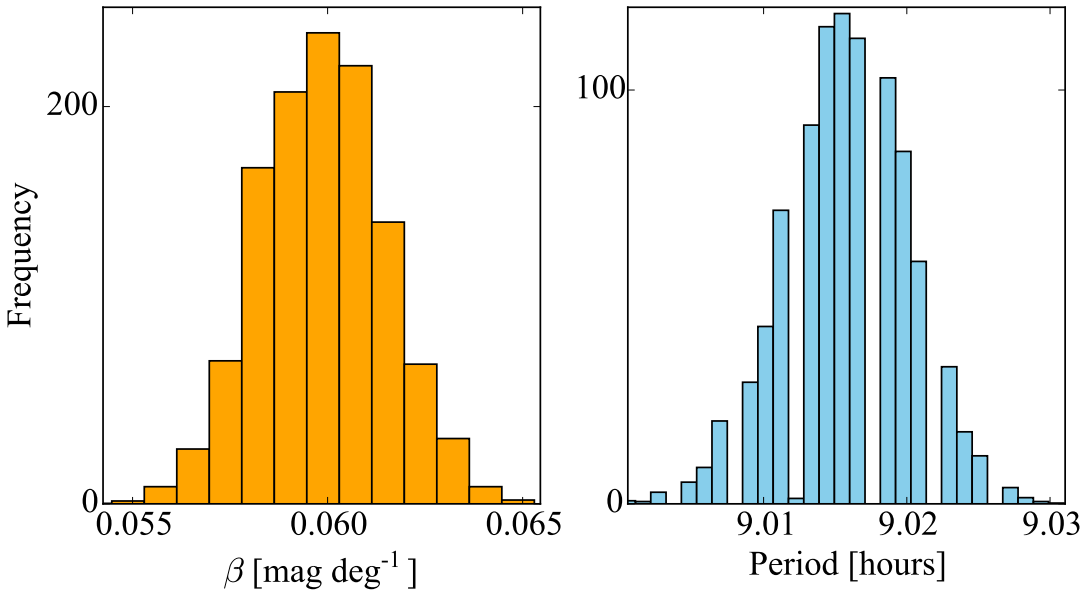

Figure 5.8: Monte Carlo simulation results for the phase function and the rotation period of 14P for the combined dataset from 2004 and 2007. The determined linear phase function slope is $\beta = 0.060 \pm 0.005$ (left) and the rotation period is $P_{\rm rot} = 9.02 \pm 0.01$ h (right).

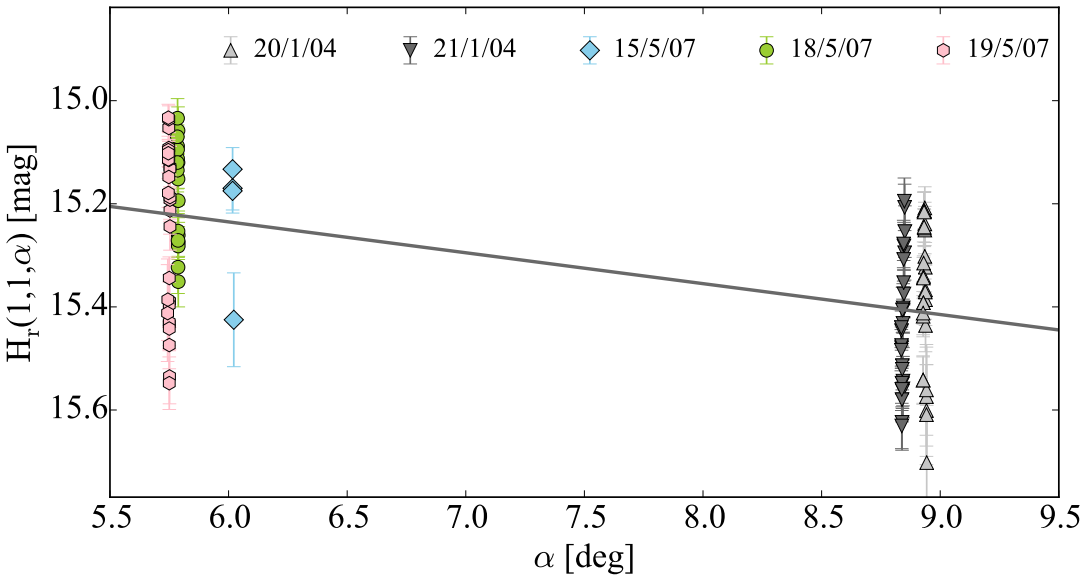

Figure 5.9: Phase function of comet 14P. The absolutely calibrated comet magnitudes corrected for heliocentric and geocentric distance are plotted versus phase angle α. The linear phase function with the best-fitting slope $\beta = 0.060 \pm 0.005$ mag/deg is plotted as a solid line.

21.6 and 44 h. Moreover, as discussed in Section 4.2.2, the attempts to determine the comet's phase function have also remained unconsolidated (Snodgrass et al., 2008b; Lamy et al., 2011).

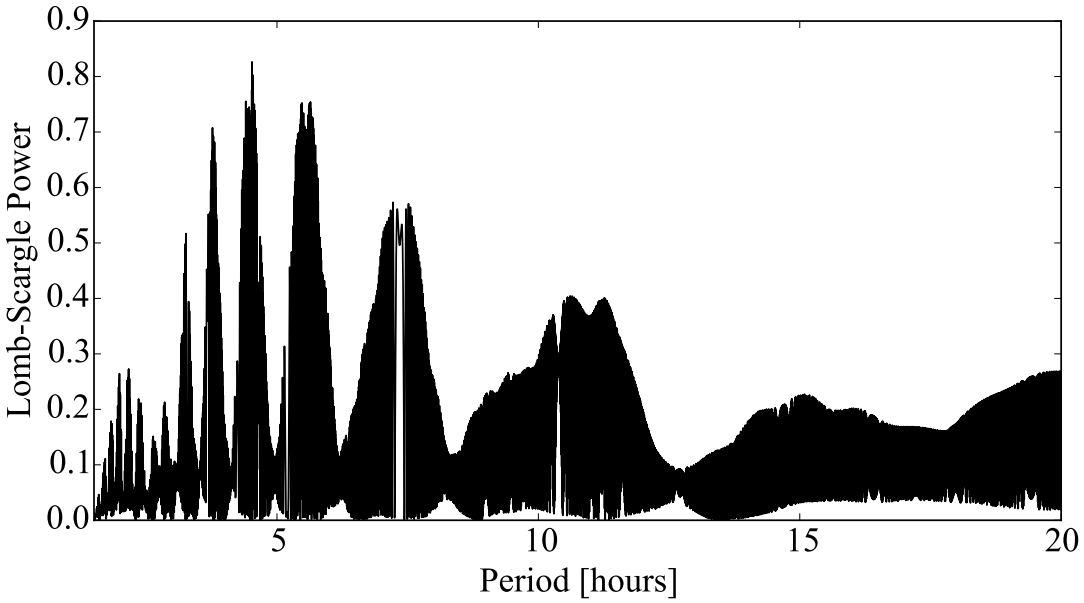

Figure 5.10: Lomb-Scargle periodogram of 14P with the combined datasets from 2004 and 2007. The highest peak corresponds to the most likely period $P_{\mathrm{rot}} = 9.02$ h. The periodogram is very densely populated with peaks from the aliases which are present due to the large time span between the two observing runs.

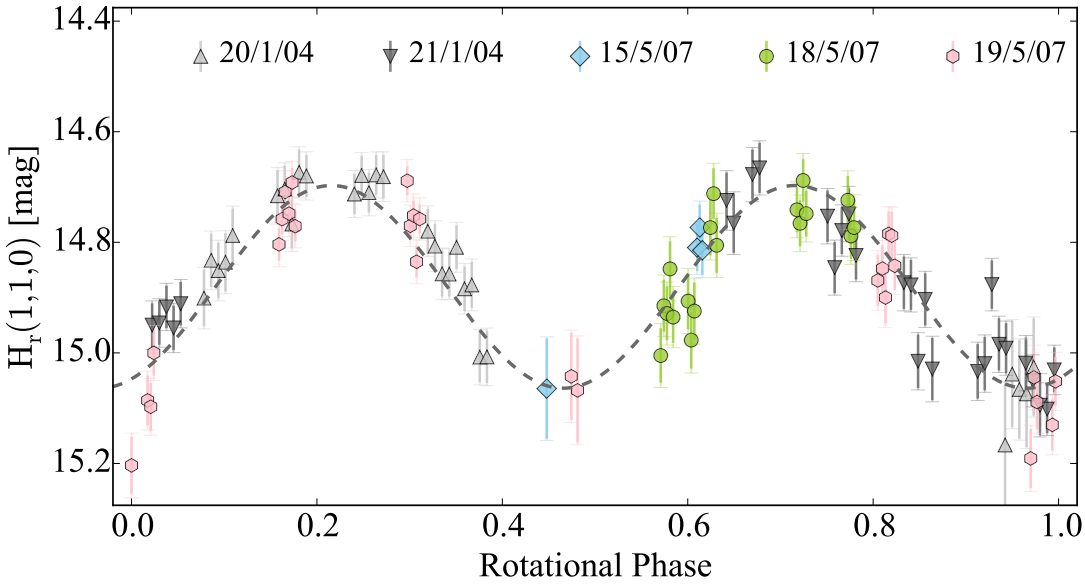

Figure 5.11: Rotational lightcurve of 14P/Wolf with the data from 2004 and 2007. The lightcurve is folded with period 9.02 h.

In order to address these inconsistencies, new time-series observations of the comet were obtained in April 2015. The new data were taken at a different apparition than those from 2005, and could not be used to look for a common period without introducing further uncertainties. Nevertheless, the two datasets

could still be combined for an attempt to derive the phase function of the nucleus.

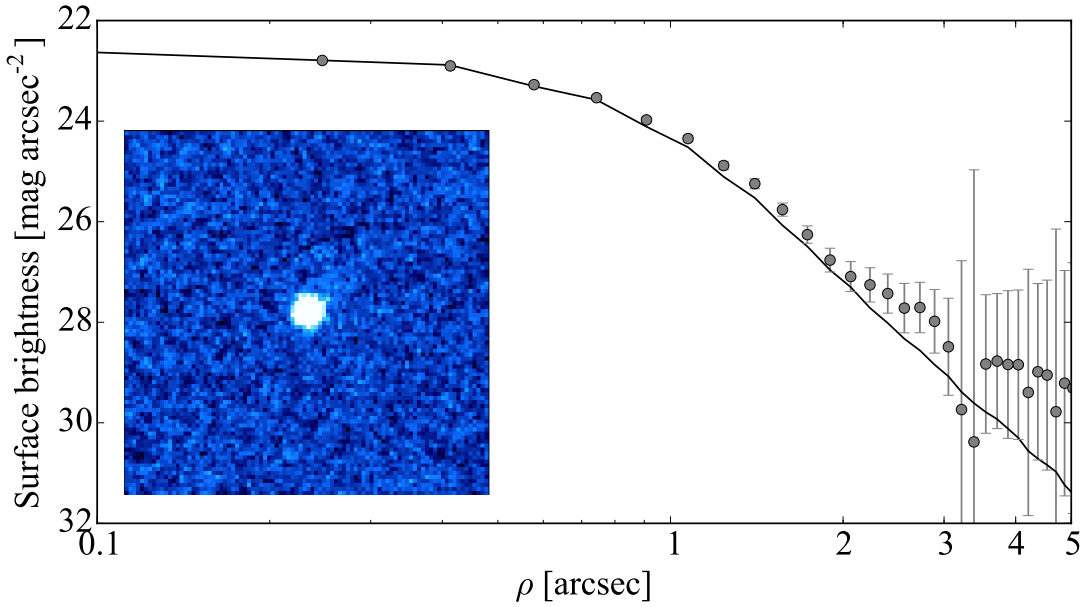

Figure 5.12: Same as Fig. 5.1, for 47P on 6 March 2005. The co-added composite image of 47P is made up of 27 × 85 s exposures. The surface brightness profile of the comet slightly deviates from the stellar one beyond 2 arcseconds, which suggests that the comet was weakly active during the time of the observations.

Upon re-analysing the 2005 dataset, I found that 47P was faintly active during the observing run. However, the inner surface brightness profile of the coma matched that of the comparison star well, suggesting that the activity was clearly weak (Fig. 5.12).

I re-analysed the data from 2005 using the new absolute-photometry calibration method. The PS1 night-to-night calibration led to the identification of a smaller brightness variation and different possible periods than those in Snodgrass et al. (2006). The two strongest peaks of the LS periodogram were at $P_{\rm rot,1} = 10.8$ and $P_{\rm rot,2} = 14.1$ h (Fig. 5.13), and it is impossible to choose between them unambiguously (Fig. 5.14). The brightness variation of the resulting lightcurve was $\Delta m_{\rm r} = 0.33 \pm 0.06$ mag suggesting axis ratio of $a/b \geq 1.36 \pm 0.07$.

When 47P was observed again in 2015, it appeared to be slightly active (Fig. 5.15). Nevertheless, the new time series showed sufficient brightness variation to enable a rotation period determination. The two highest peaks on the LS

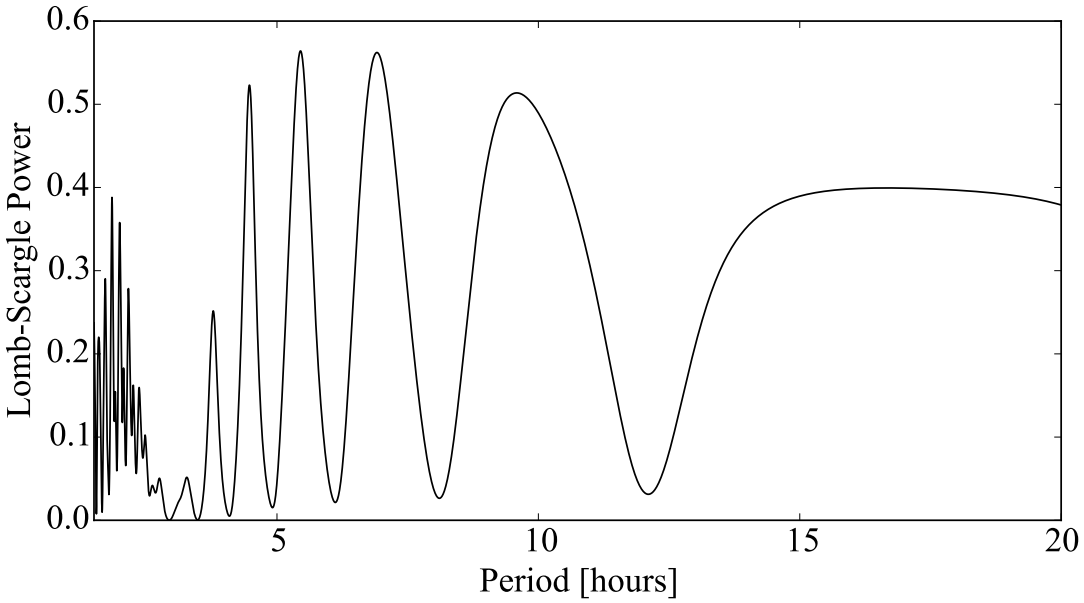

Figure 5.13: Lomb-Scargle periodogram of 47P with the data from 2005. The two highest peaks correspond to $P_{\mathrm{rot},1} = 10.8$ h and $P_{\mathrm{rot},2} = 14.1$ h.

periodogram of the 2015 dataset suggested $P_{\mathrm{rot},1} = 15.6$ h or $P_{\mathrm{rot},2} = 23.7$ h (Fig. 5.16). However, I consider that $P_{\mathrm{rot},2} = 23.7$ h is an alias due to the nightly sampling of the observations. Phasing the lightcurve of the comet with 23.7 h produced a non-realistic noisy lightcurve, and confirmed that this period does not correspond to the rotation rate of 47P.

I ran the Monte Carlo simulation for periods between 3 and 23 h (to avoid the 24-hour alias) and determined $P_{\mathrm{rot}} = 15.6 \pm 0.1$ h. The resulting plots of the MC simulation here and for most objects below are not shown since they are similar to Fig. 5.8, and do not provide additional information on the simulation outcomes. The brightness variation of the lightcurve (Fig. 5.17) was $\Delta m_{\mathrm{r}} = 0.24 \pm 0.06$ mag, suggesting $a/b \geq 1.25 \pm 0.07$ and $D_{\mathrm{N}} \geq 0.06 \pm 0.02$ g cm^{-3}.

Besides deriving the lightcurve of the comet, one of the main aims of the new observations from 2015 was to constrain the phase function of 47P. To address this, I first considered the previous brightness measurements from Licandro et al. (2000), Lamy et al. (2011) and Snodgrass et al. (2008b). Their magnitude measurements were converted to PS1 magnitudes using the colour indices of 47P (B-V) = 0.78 ± 0.08 and (V-R) = 0.40 ± 0.08 (Lamy et al., 2011), and the conversions from

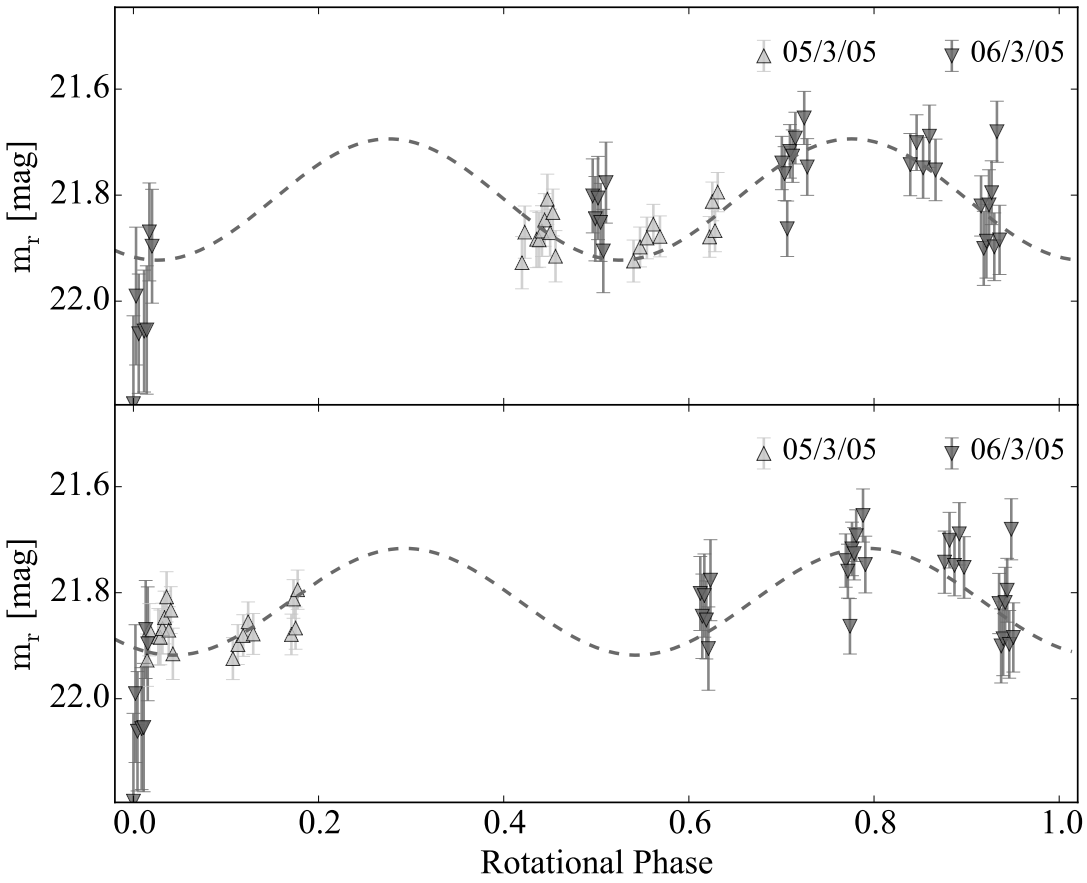

Figure 5.14: Rotational lightcurve of 47P with the data from 2005, folded with periods 10.8 h (top) and 14.1 h (bottom). It is impossible to select between these two periods.

Tonry et al. (2012).

Additionally, I attempted to add an archival VLT dataset from June 2006 when the comet was close to aphelion. However, these observations could not be used since the comet was clearly active on the frames (Fig. 5.18). Instead, these data complemented the dataset from March 2006 (Snodgrass et al., 2008b), and confirmed that the comet had an outburst around aphelion.

To derive the phase function coefficient β, I used the Monte Carlo approach considering only the long time-series from 2005 and 2015. I did not include the other observations where the comet was active, or where the photometric calibration had been done using different methods. The Monte Carlo method resulted in a coefficient $\beta = 0.096 \pm 0.004$ mag/deg. The derived phase function appears to be in good agreement with all previous observations (Fig. 5.19),

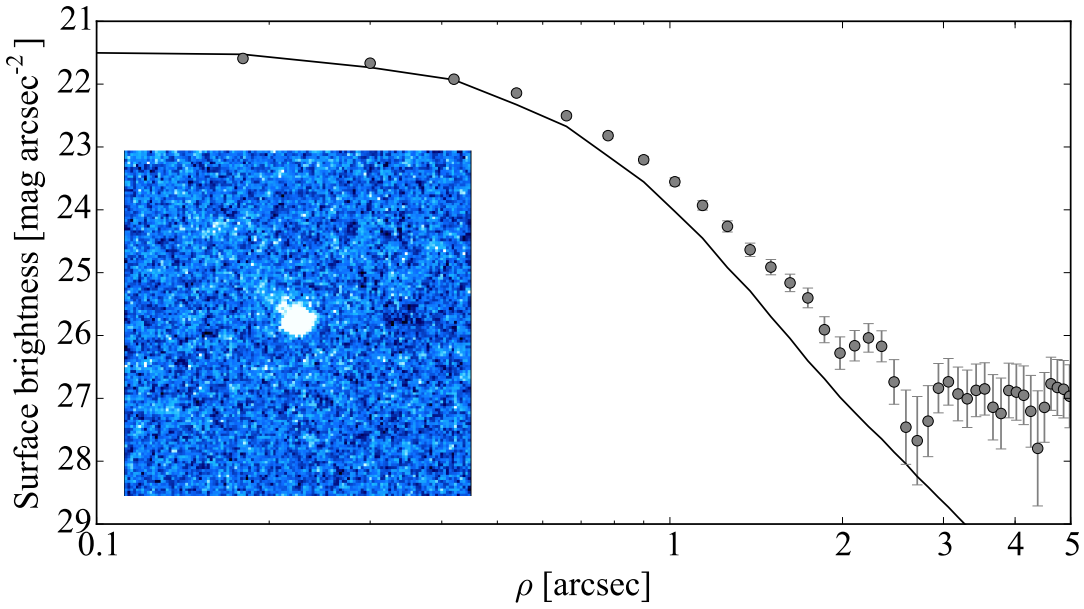

Figure 5.15: Same as Fig. 5.1, for 47P on 24 April 2015. The co-added composite image of 47P is made up of 26 × 80 s exposures. The comet appears to be slightly active with a tail detected to the north east.

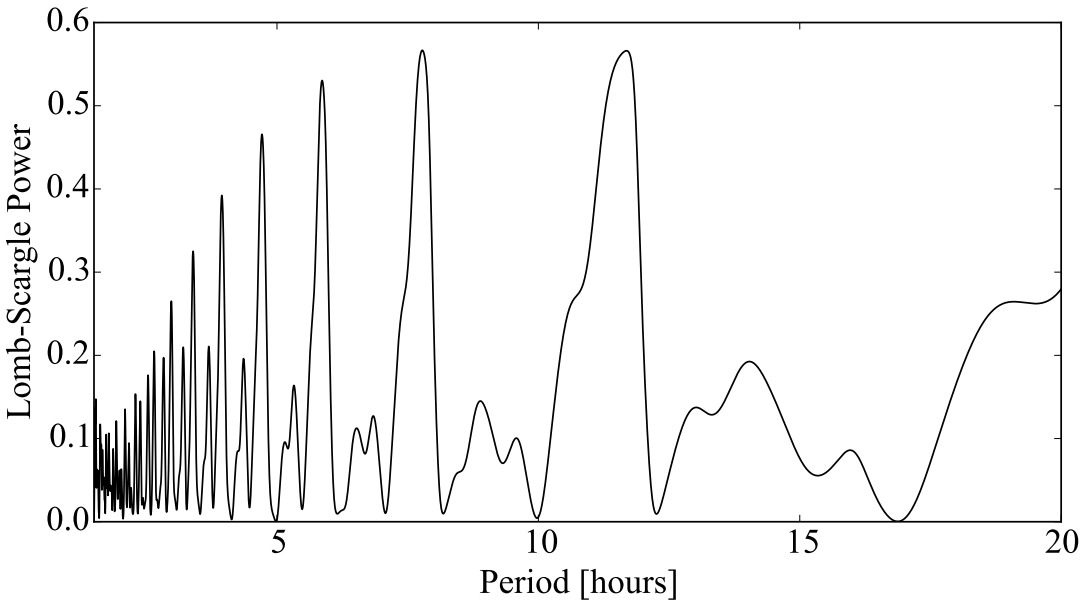

Figure 5.16: Lomb-Scargle periodogram of 47P with the data from 2015. The two highest peaks correspond to $P_{\rm rot}$ = 23.7 h and $P_{\rm rot}$ = 15.6 h, although the period of 23.7 is most likely a 24-hour alias.

although it is unusually steep compared to the typical phase function for JFCs (see Table 9.1).

Using that value for β to convert the observed magnitude, I calculated $H_{\rm r}(1,1,0)$

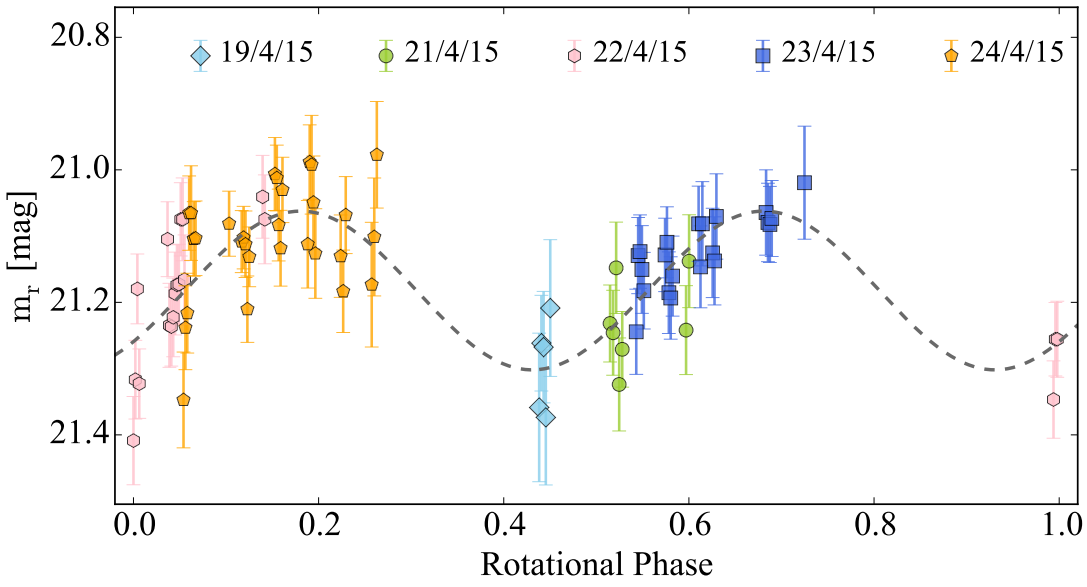

Figure 5.17: Rotational lightcurve of 47P with the data from 2015. The lightcurve is folded with the period of 15.6 h derived from the MC method.

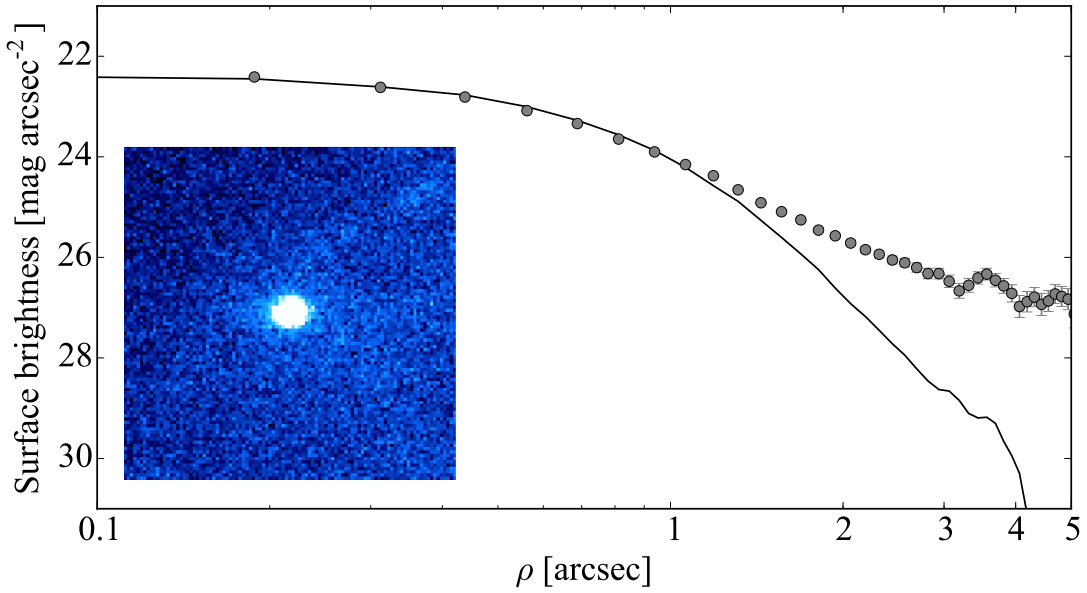

Figure 5.18: Same as Fig. 5.1, for 47P on 1 June 2006. The co-added composite image is made up of 4 × 300 s exposures. Due to the small number of frames, the composite image was made without subtraction of the average stellar background in order to avoid artefacts from the comet's slow position change. The comet appears active on the image, and its surface brightness profile deviates from the stellar PSF.

= 14.59 ± 0.06 mag. Using the radius from SEPPCoN and Eq. 3.10, I derived an albedo A_r = 5.8±0.9 %.

I interpret these results with caution because of the slight activity detected

on the stacked frames from 2005 and 2015, as well as the unusually steep phase function. If the coma contribution was large and/or the actual nucleus phase function slope was shallower, the absolute magnitude of 47P should be fainter. In that case, the comet must also have a smaller albedo ($A_r \leq 5.0$ %).

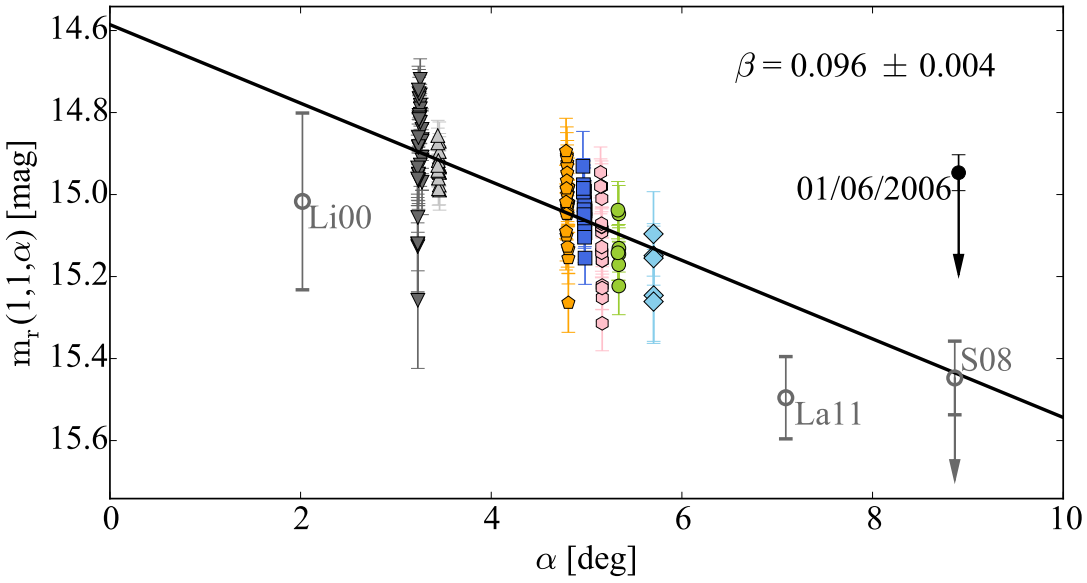

Figure 5.19: Phase function of comet 47P derived from the observing runs in 2005 and 2015. The symbols from 2005 and 2015 correspond to these used on Figs. 5.14 and 5.17. The linear phase function slope β determined with the MC method is 0.096 ± 0.004 mag/deg. Despite being unusually steep, the phase function is consistent with the previous observations of the comet from Licandro et al. (2000); Snodgrass et al. (2008b); Lamy et al. (2011). However, since the comet was probably active in 2005 and 2015, the derived phase function slope is not conclusive.

Similarly, the derived period $P_{rot} = 15.6 \pm 0.1$ h must also be regarded as uncertain. The comet was found to be active at the time of the observations and therefore the nucleus signal was likely dampened by the present coma, which would make the brightness variation more difficult to detect. Since the periods from both epochs were uncertain due to the limited sampling and the potential activity, I did not attempt to look for period changes occurring between 2005 and 2015.

5.4 93P/Lovas

93P/Lovas was observed with three different instruments during six nights in January 2009 as part of SEPPCoN. The observations were taken at heliocentric distance of 3.8 au when 93P was outbound. The composite images of the comet from each night contained traces of activity, and a tail to the west could clearly be resolved on the VLT frames (Fig. 5.20).

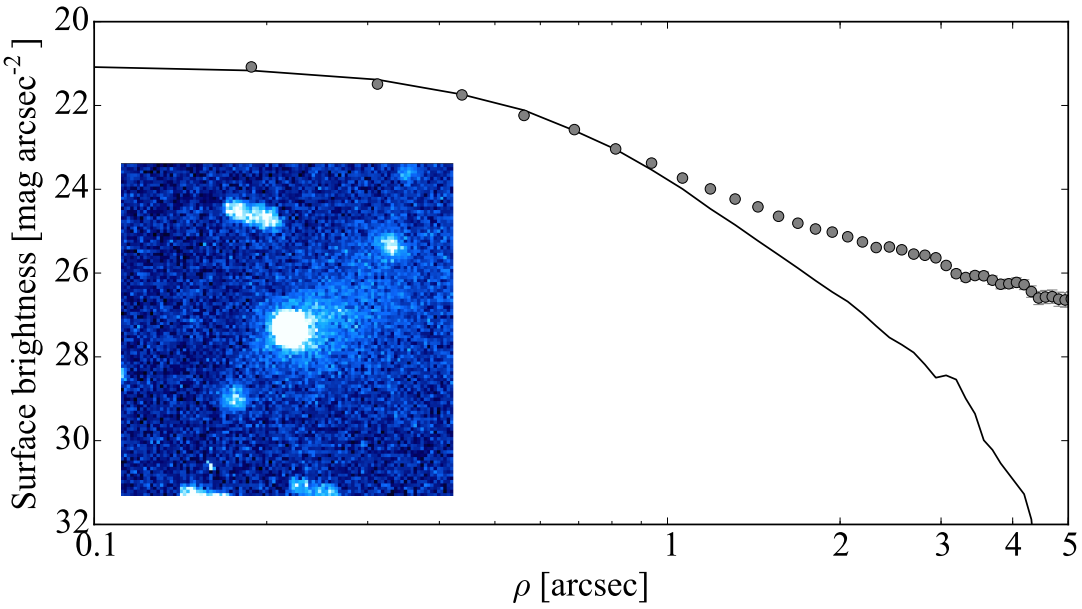

Figure 5.20: Same as Fig. 5.1, for the VLT observations of 93P on 24 January 2009. Due to the small number of frames, the composite image was made without subtraction of the average stellar background in order to avoid artefacts from the comet's slow position change. The co-added composite image is made up of 8 × 250 s exposures. A tail to the west can be clearly distinguished. The comet profile appears stellar close to the centre but deviates from that of the comparison star at larger radii.

Despite the weak activity, the brightness variation in the time series from each night suggested that the nucleus signal could still be detected. The LS periodogram of the combined dataset can be seen in Fig. 5.21. The strongest peak at $\sim$ 24 h does not produce a typical lightcurve and corresponds to a 24-hour alias. From the remaining peaks, those at $P_{\rm rot}$ = 18.2 h and $P_{\rm rot}$ = 13.2 h result in possible lightcurves (Fig. 5.22).

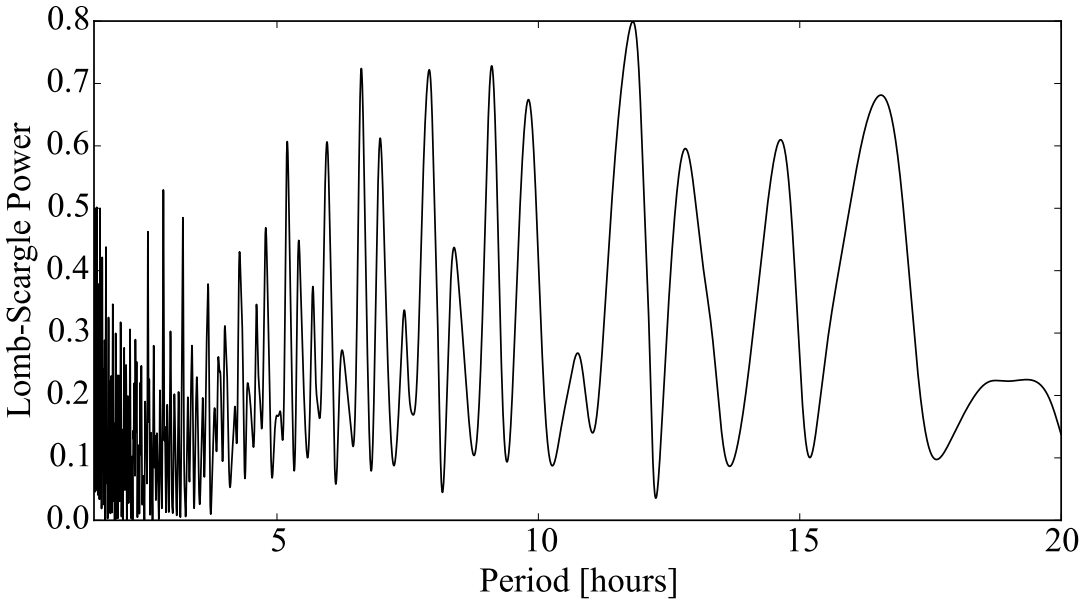

Figure 5.21: Lomb-Scargle periodogram of 93P showing the LS power versus period. The highest peak corresponds to a 24-hour alias. The next three peaks correspond to $P_{\rm rot}$ = 18.2, 13.2 and 15.8 h.

I used the MC method to look for the best period between 3 and 23 h (to avoid the aliasing at 24 h). The simulation resulted in possible periods between 13.1 and 19.7 with the most frequently preferred period of 18.2 h (29% of the iterations, Fig. 5.23). It is impossible to deduce the precise spin rate of 93P from these data, but the period can be constrained to the range $P_{\rm rot} = 18.2^{+1.5}_{-5}$ h.

The brightness variation of 93P is $\Delta m_{\rm r} = 0.21 \pm 0.05$ mag and suggests an axis ratio $a/b \geq 1.21 \pm 0.06$. The mean magnitude of the comet is $m_{\rm r} = 21.09 \pm 0.05$ mag which corresponds to $H_{\rm r}(1,1,0) = 15.17 \pm 0.05$ mag, for a typical phase function $\beta = 0.04$ mag/deg. Using Eq. 3.10 and the SEPPCoN radius from Fernández et al. (2013), I estimated that the albedo of 93P is $A_{\rm r} = 4.9 \pm 1.0$ %.

Since the comet showed signatures of activity during the time of the observations, the brightness and albedo values I have derived need to be treated as upper limits. If the coma contribution of the frames is significant, the absolute magnitude of the nucleus must be larger, and therefore the resulting albedo must be smaller. In order to derive more certain estimates of the nucleus parameters, the comet needs to be observed at higher heliocentric distances where it is more

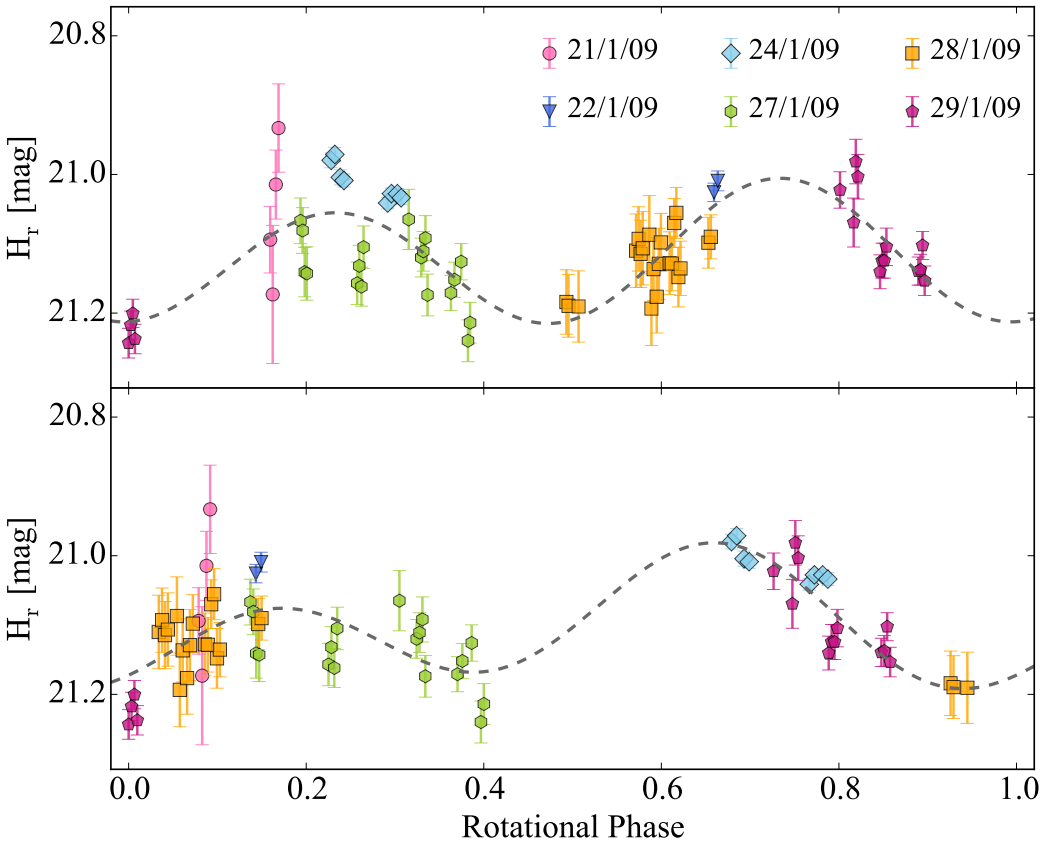

Figure 5.22: Rotational lightcurve of 93P folded with the two most likely periods 18.2 h (top) and 13.2 h (bottom). The dashed line corresponds to second-order Fourier series which aim to reproduce an asymmetric double-peaked lightcurve. The lightcurve phased with 13.2 h shows less scatter, but the data are not sufficient to discriminate between the two periods.

likely to be inactive.

5.5 94P/Russell

In the analysis described here, I attempted to determine the rotation rate of 94P/Russell after combining three datasets from 2005, 2007 and 2009. The observations were taken before and after the same aphelion passage in 2007.

The dataset from 2005 was previously used to determine a period of $\sim$ 33 h (Snodgrass et al., 2008b). I re-processed the data and used the method for absolute calibration to combine the observations from the four observing nights in 2005.

The surface brightness profile presented in Snodgrass et al. (2008b) suggested

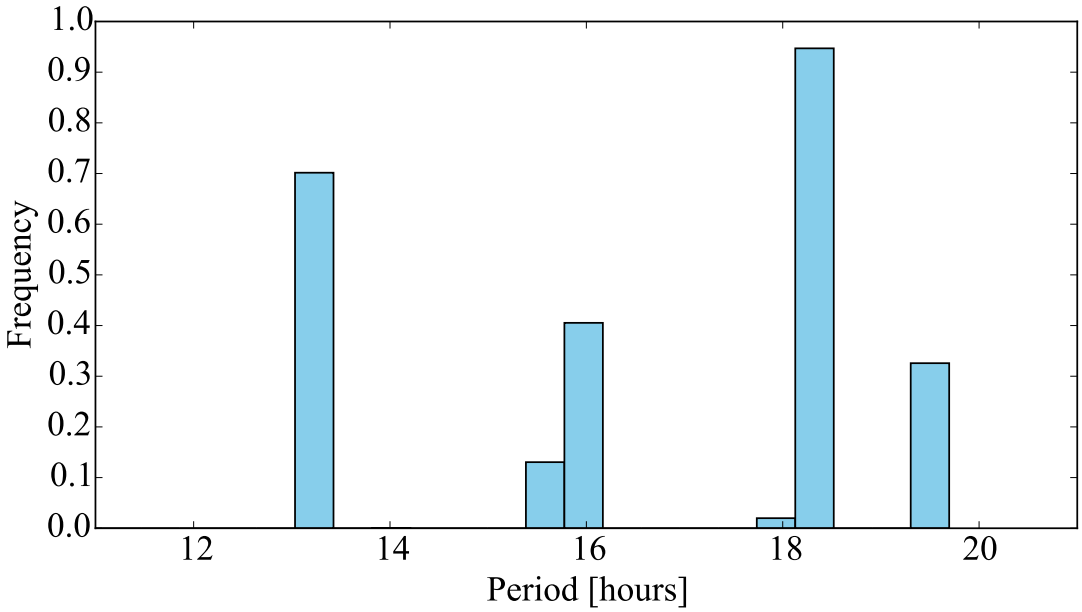

Figure 5.23: Monte Carlo simulation results for the rotation period of 93P. The most frequently preferred rotation period is 18.2 h, but the large range of possible periods does not allow a unique determination of the rotation rate of the comet.

that the comet could have been weakly active at the time of the observations. I performed a careful background subtraction of the comet composite images for each night, and concluded that 94P appeared stellar on each night of the run (see Fig. 5.24).

The Lomb-Scargle periodogram of the data taken in 2005 has two strong peaks corresponding to 20.43 and 14.31 h (Fig. 5.25). The lightcurves phased with these periods are plotted in Fig. 5.26. It is not possible to reject the second-best period based on the appearance of the lightcurve. However, in all iterations of the MC simulation the larger period was preferred and therefore the period was determined to be $P_{\rm rot} = 20.43 \pm 0.05$ h.

The resulting lightcurve had a brightness variation $\Delta m_{\rm r} = 0.7 \pm 0.1$ mag. This corresponds to an axis ratio $a/b \geq 1.9 \pm 0.2$ and density $D_{\rm N} \geq 0.05 \pm 0.01$ g cm^{-3} .

The data taken during the SEPPCoN runs in 2007 and 2009 were also checked for the presence of activity (Fig. 5.27 and 5.28). Due to the faintness of the comet, in both cases its surface brightness profiles levelled out within 5 arcseconds

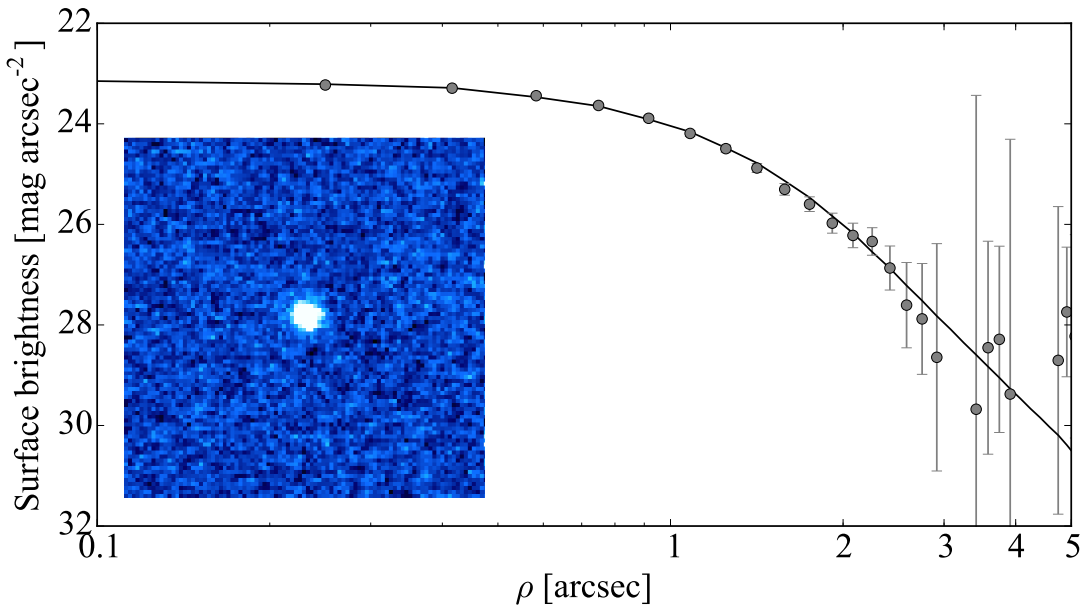

Figure 5.24: Same as Fig. 5.1, for the observations of 94P in 2005. The co-added composite image is made up of 15 × 75 s exposures taken on 7 July 2005.

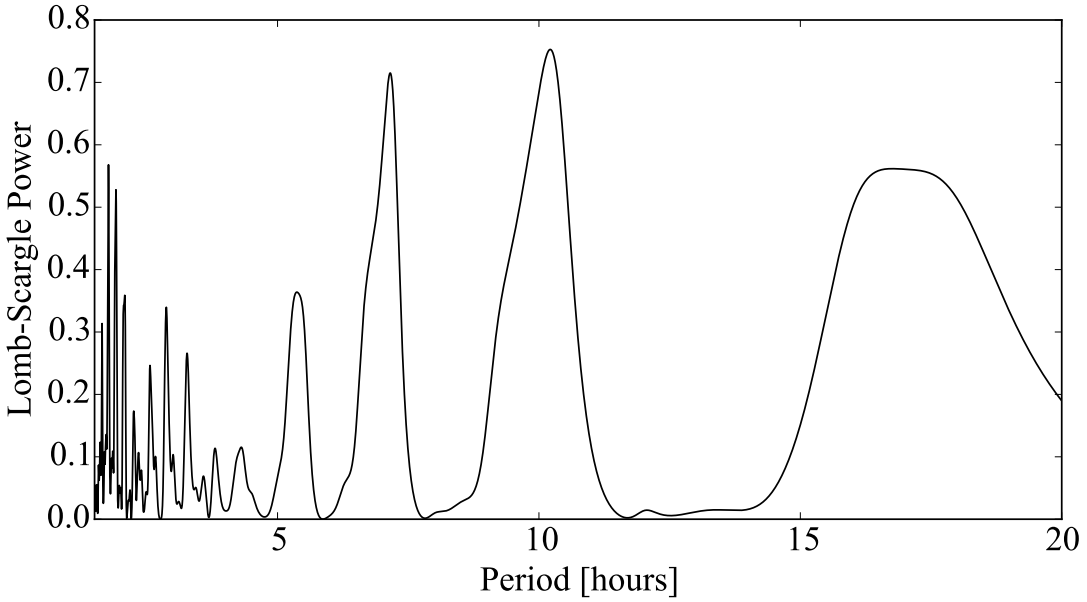

Figure 5.25: Lomb-Scargle periodogram of 94P from the dataset taken in 2005. The highest peaks correspond to the most likely periods $P_{\mathrm{rot},1}$ = 20.43 h and $P_{\mathrm{rot},2}$ = 14.31 h.

from the nucleus. However, I concluded that 94P was inactive in both epochs based on the good matches with the stellar PSF close to the centre, as well as the appearance of the composite images.

Neither of the two datasets from 2007 and 2009 were sufficient to derive

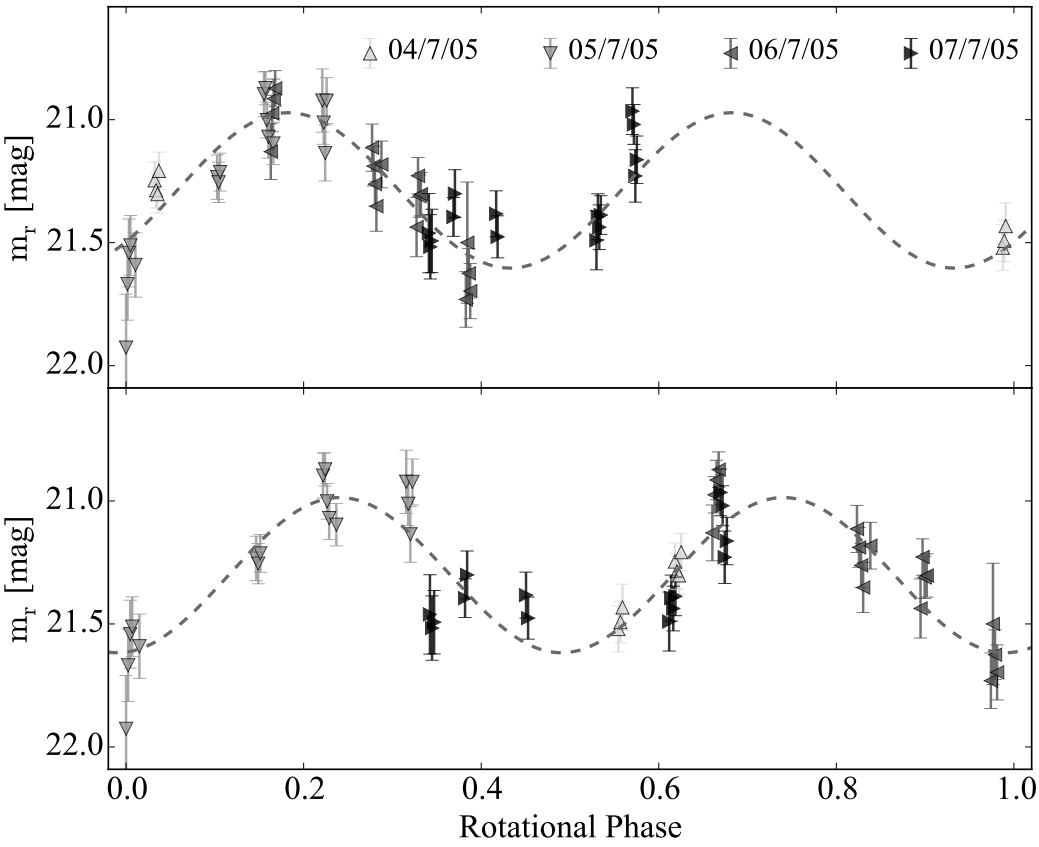

Figure 5.26: Rotational lightcurve of 94P from the data obtained in 2005. The lightcurve is folded with $P_{\rm rot,1}$ = 20.43 h (top) and $P_{\rm rot,2}$ = 14.31 h (bottom). I cannot choose between the two periods based on the appearance of the two lightcurves. However, $P_{\rm rot,1}$ = 20.43 h is preferred by the MC method, and is therefore considered as more likely.

the rotation rate of 94P independently. I therefore only used them to estimate the nucleus magnitude and the minimum brightness variation at each epoch. I measured $m_{\rm r}$ = 22.6 ± 0.2 and $\Delta m_{\rm r}$ = 1.0 ± 0.2 mag for 2007, and $m_{\rm r}$ = 21.30 ± 0.05 and $\Delta m_{\rm r}$ = 0.80 ± 0.05 mag for 2009.

I combined all three datasets to determine the precise rotation rate of the comet. The analysis of the joined datasets was done under the following assumptions: 1) the comet was inactive during all observations and the measured magnitudes had no coma contributions; 2) the rotation period remained constant during the entire aphelion passage, and 3) the changing viewing geometry between the different observations did not affect the lightcurve shape significantly.

With these assumptions in mind, I used the MC method to derive a phase

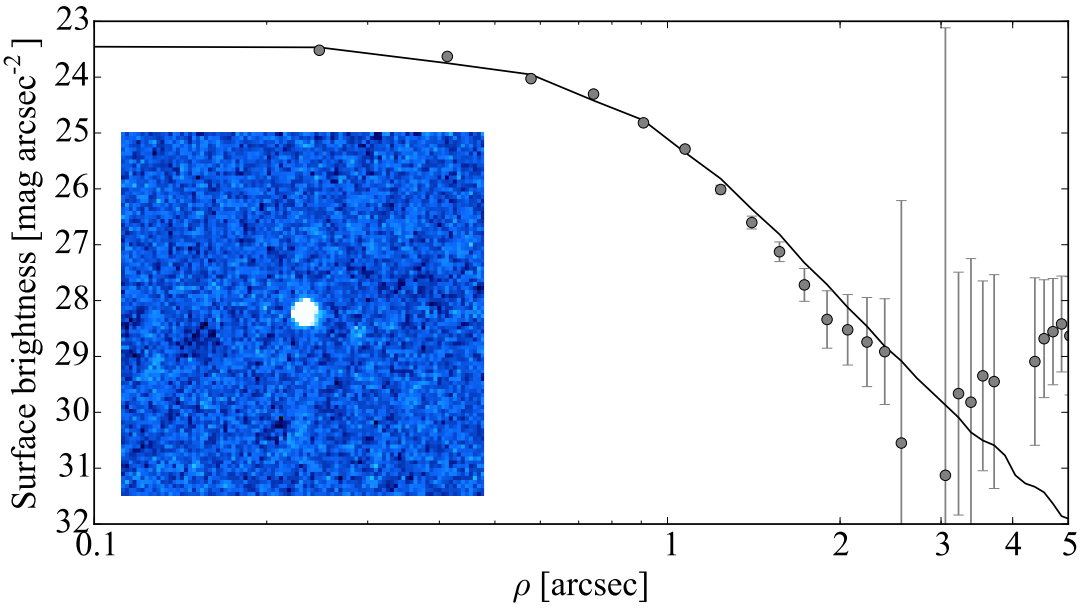

Figure 5.27: Same as Fig. 5.1, for the observations of 94P in 2007. The co-added composite image is made up of 8 × 400 s exposures taken on 20 July 2007.

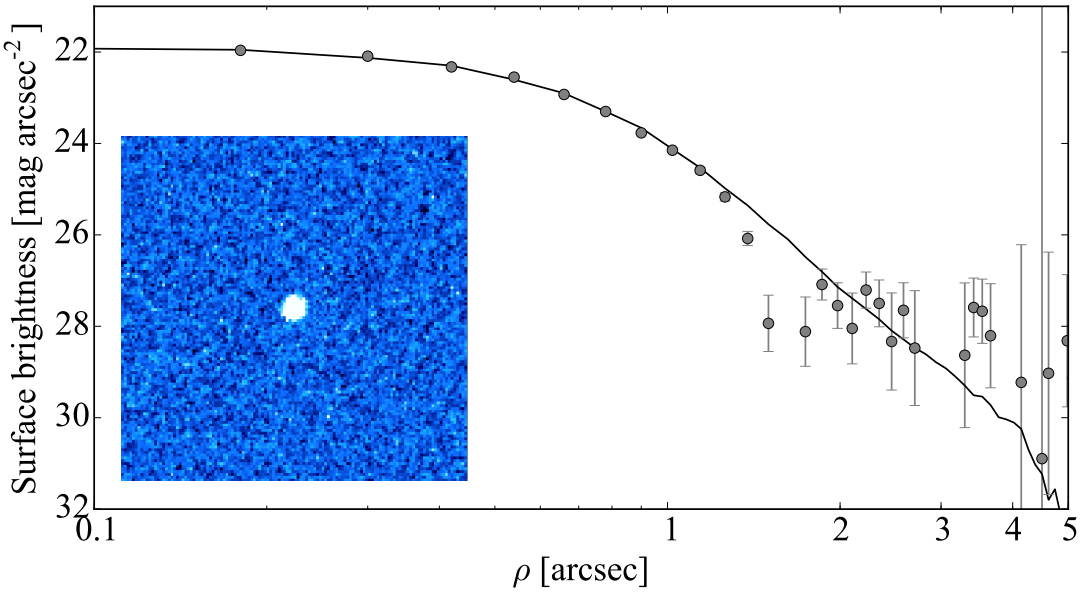

Figure 5.28: Same as Fig. 5.1, for the observations of 94P in 2009. The co-added composite image is made up of 8 × 100 s exposures taken on 28 January 2009.

function with a slope $\beta = 0.039 \pm 0.002$ mag/deg (Fig. 5.29). The LS periodogram of the combined dataset on Fig. 5.30 peaks at $P_{\rm rot} = 20.70$ h. The period $P_{\rm rot} = 20.70$ h was also suggested by PDM and SLM. The other two peaks of the LS periodogram close to 38 and 40 h were also inspected but their lightcurves were significantly noisier.

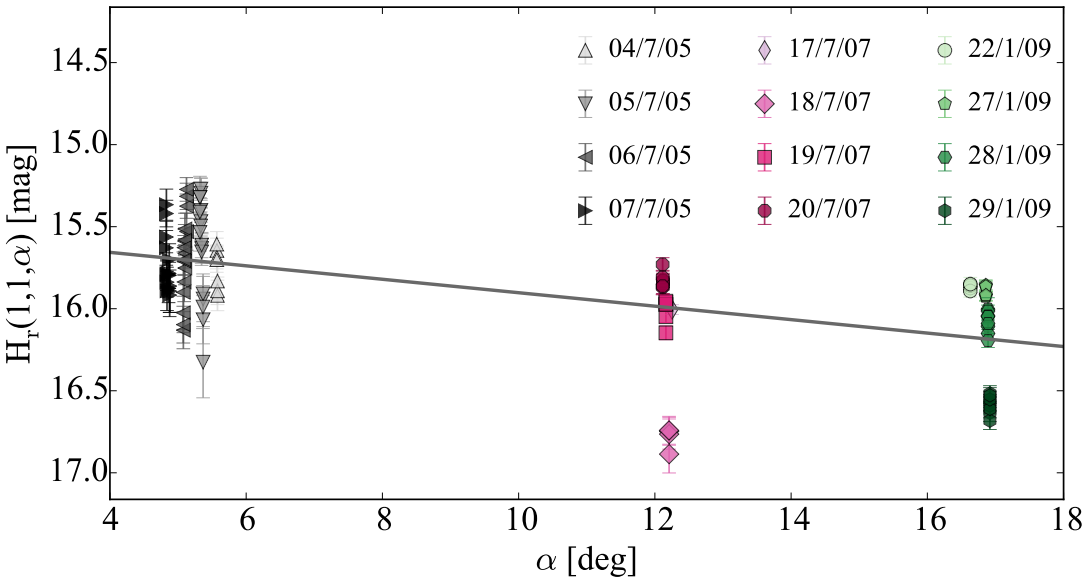

Figure 5.29: Phase function of comet 94P combining the datasets from 2005, 2007, and 2009. The linear phase function coefficient derived with the Monte Carlo method is $\beta = 0.039 \pm 0.002$ mag/deg.

The period of 20.70 h was preferred in 86% of the MC iterations, which allowed me to set the rotation rate of 94P to $P_{\rm rot} = 20.70 \pm 0.07$ h. The corresponding lightcurve plotted in Fig. 5.31 shows a very good agreement between the separate datasets.

The absolute magnitude of 94P from the combined dataset was $H_{\rm r}(1,1,0) = 15.50 \pm 0.09$ mag. The albedo of 94P was determined with Eq.3.10 to be $A_{\rm r} = 4.7 \pm 0.7$ %.

The only datasets which deviate from the first-order Fourier series in Fig. 5.31 are the ones from July 2007. These points are fainter than the comet magnitude from the rest of the nights. There were no indications of problems with the images or the photometric calibration during these nights. I therefore concluded that the lightcurve must be asymmetric, with one of the minima being sharper and deeper than the other one. Such a lightcurve would have $\Delta m_{\rm r} = 1.11 \pm 0.09$ mag which corresponds to $a/b \geq 2.8 \pm 0.2$ and density $D_{\rm N} \geq 0.07 \pm 0.02$ g cm^{-3}.

Another effect which could produce the observed lightcurve is the change of viewing geometry. Comet 94P moved approximately 120° along its orbit between

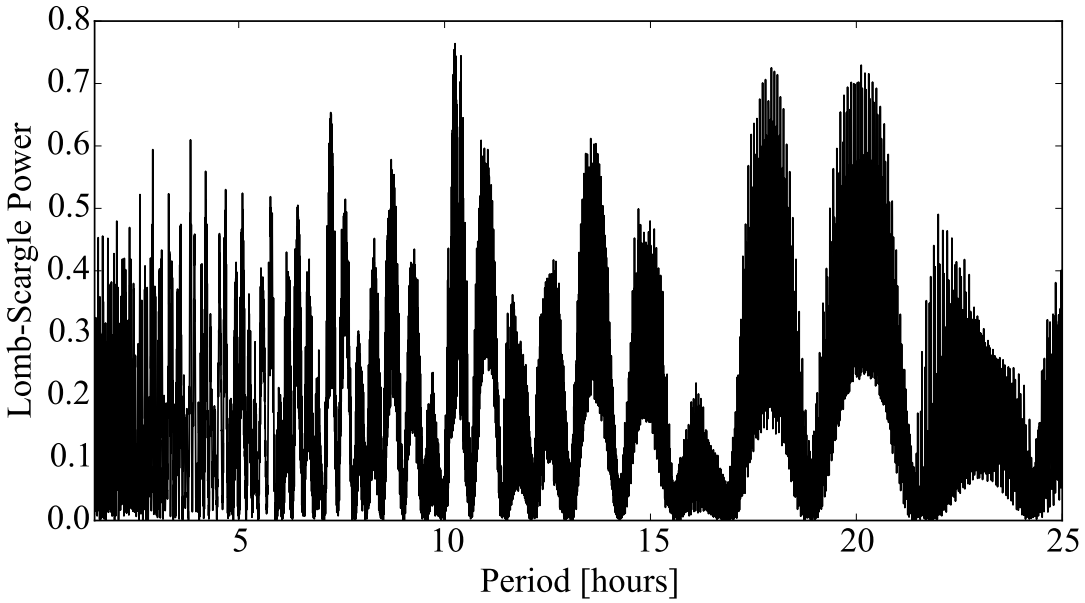

Figure 5.30: Lomb-Scargle periodogram of 94P with the datasets from 2005, 2007, and 2009 combined. The highest peak corresponds to the most likely period $P_{\rm rot}$ = 20.70 h.

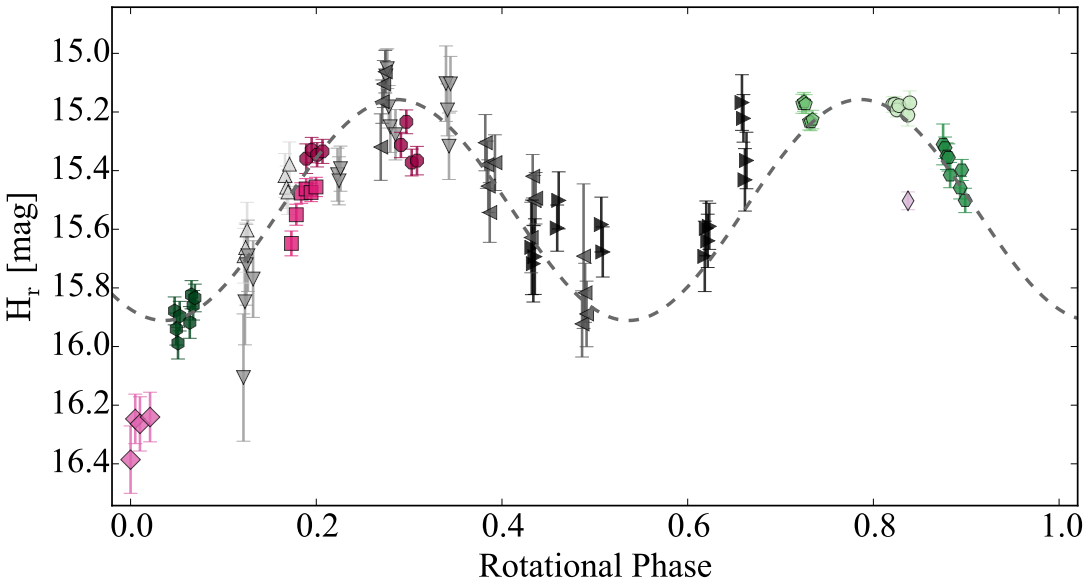

Figure 5.31: Rotational lightcurve of 94P with the combined datasets from 2005, 2007 and 2009. The symbols of each dataset correspond to those used on Fig. 5.29. The lightcurve is folded with the best-fitting period $P_{\rm rot}$ = 20.70 h. The fitted first-order Fourier series (dashed line) agree with all points except for the ones from 18 July 2007. These fainter points could be interpreted as signatures of an asymmetric lightcurve with one deep minimum, or alternatively as a result from the changing viewing geometry between the three epochs.

2005 and 2009, which could be sufficient to produce a noticeable variation in the total surface area of the nucleus for an observer on Earth. Alternatively, the shift in brightness might be caused by weak activity in the 2005 and 2009 data when the comet was closer to the Sun. Such activity is not evident in the profiles on Figs. 5.24, 5.27 and 5.28 but it is possible for some weak activity to be hidden within the seeing disc of distant comets (e.g. Snodgrass et al., 2016). With the limited data here, I cannot determine whether the deep minimum in the lightcurve is a feature of the nucleus or if it is caused by other effects.

5.6 110P/Hartley 3

Comet 110P/Hartley 3 was observed with VLT-FORS2 and NTT-EFOSC2 during 8 nights between June and August 2011. The aim of the observations was to sample the comet's phase function in the phase angle range between 1° and 10°. The method for precise absolute photometric calibration with PS1 allowed me to combine these datasets and to derive the comet's phase function as well as to study its rotational lightcurve.

I looked for signatures of activity on comet composite images for each individual night, and on Fig. 5.32 I have presented an example for the middle of the observing period. The comet did not show any indication of coma presence throughout the observing period, and I assume that the derived photometry from each night contains only signal from the nucleus.

I used the MC method to derive a phase function for 110P. The determined phase function with linear slope $\beta = 0.069 \pm 0.002$ mag/deg is in excellent agreement with all individual datasets (Fig. 5.33).

All datasets were used to derive the comet's lightcurve under the same assumptions as those described earlier for 14P, 47P and 94P. The LS periodogram in Fig. 5.34 has three pronounced peaks at $P_{\rm rot,1} = 10.153$ h, $P_{\rm rot,2} = 8.375$ h and $P_{\rm rot,3} = 6.779$ h. The MC method outlines $P_{\rm rot,1} = 10.153 \pm 0.001$ h (75%

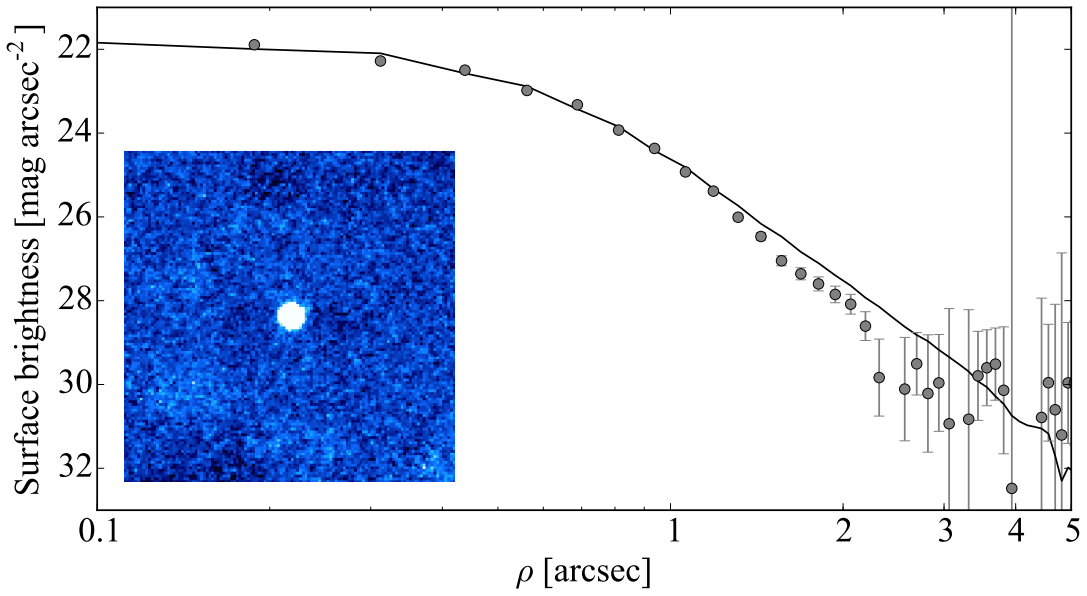

Figure 5.32: Same as Fig. 5.1, for 110P on 15 July 2012. The co-added composite image is made up of 18 × 70 s exposures. The comet appears inactive and its surface brightness profile follows that of the comparison star.

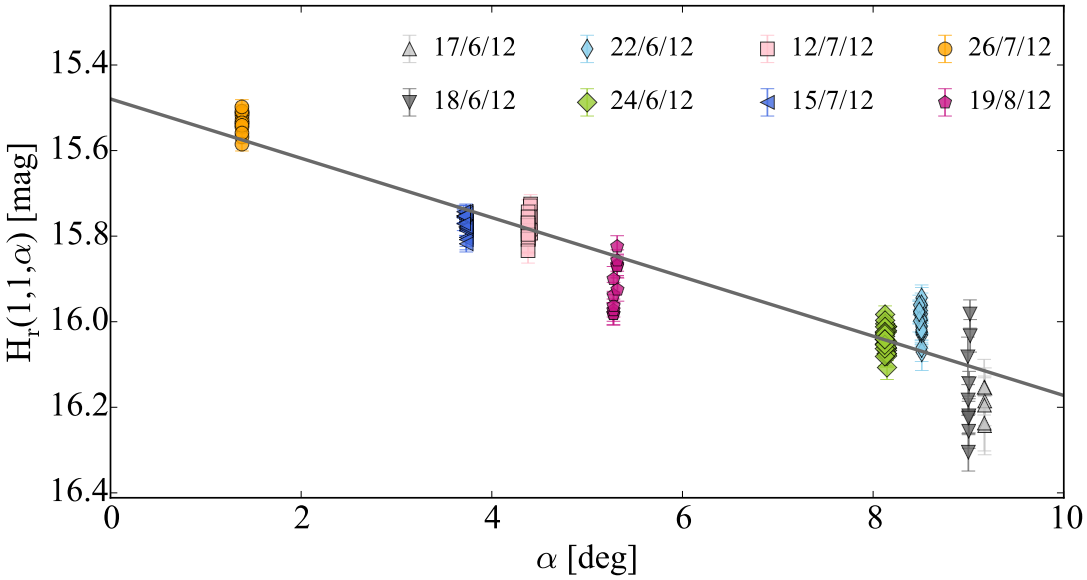

Figure 5.33: Phase function of comet 110P. The linear slope β derived with the Monte Carlo method is 0.069 ± 0.002 mag/deg. The NTT-EFOSC2 points from 17 and 18 June 2012 were binned since the S/N of the individual points was low due to bad observing conditions.

of the iterations) and $P_{\rm rot,2}$ = 8.375 ± 0.001 h (17% of the iterations) as most likely solutions (Fig. 5.35). Qualitatively, the lightcurve phased with $P_{\rm rot,1}$ = 10.153 ± 0.001 h presents less scatter of the points and agrees with the trends in

the individual observing blocks better. Since $P_{\mathrm{rot},1}$ is also preferred by the MC method, I report 10.153 ± 0.001 h as the most likely period of 110P.

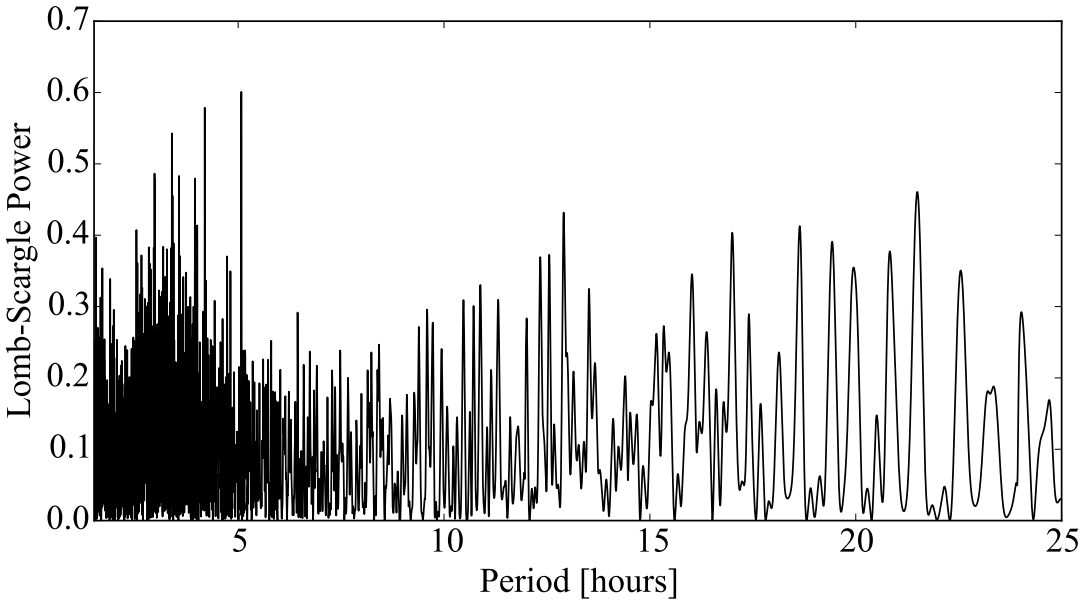

Figure 5.34: Lomb-Scargle periodogram of 110P for the combined dataset with all observations from 2012. The three highest peaks correspond to $P_{\mathrm{rot},1}$ = 10.153 h, $P_{\mathrm{rot},2}$ = 8.375 h and $P_{\mathrm{rot},3}$ = 6.779 h.

The brightness variation of the resulting lightcurve is $\Delta m_{\mathrm{r}} = 0.20 \pm 0.03$ mag which puts a lower limit on the comet axis ratio $a/b \geq 1.20 \pm 0.03$. Using $P_{\mathrm{rot},1}$, I estimated the nucleus density $D_{\mathrm{N}} \geq 0.13 \pm 0.02$ g cm^{-3}. The mean absolute magnitude of the comet was $H_{\mathrm{r}}(1,1,0) = 15.47 \pm 0.03$ mag, which corresponds to a nucleus radius $R_{\mathrm{N}} = 2.50 \pm 0.04$ km, assuming an albedo of 4%.

Our results are in good agreement with those of Lamy et al. (2011) (see Section 4.2.5). This validates the results and confirms that it is possible to constrain both the phase function and the lightcurve of the comet from sparse observations spread over months. Although the two observations were taken at different apparitions and a small period change could have occurred during the active phase of the comet, due to the large uncertainty in the period from Lamy et al. (2011), it is impossible to search for period changes between the two epochs.

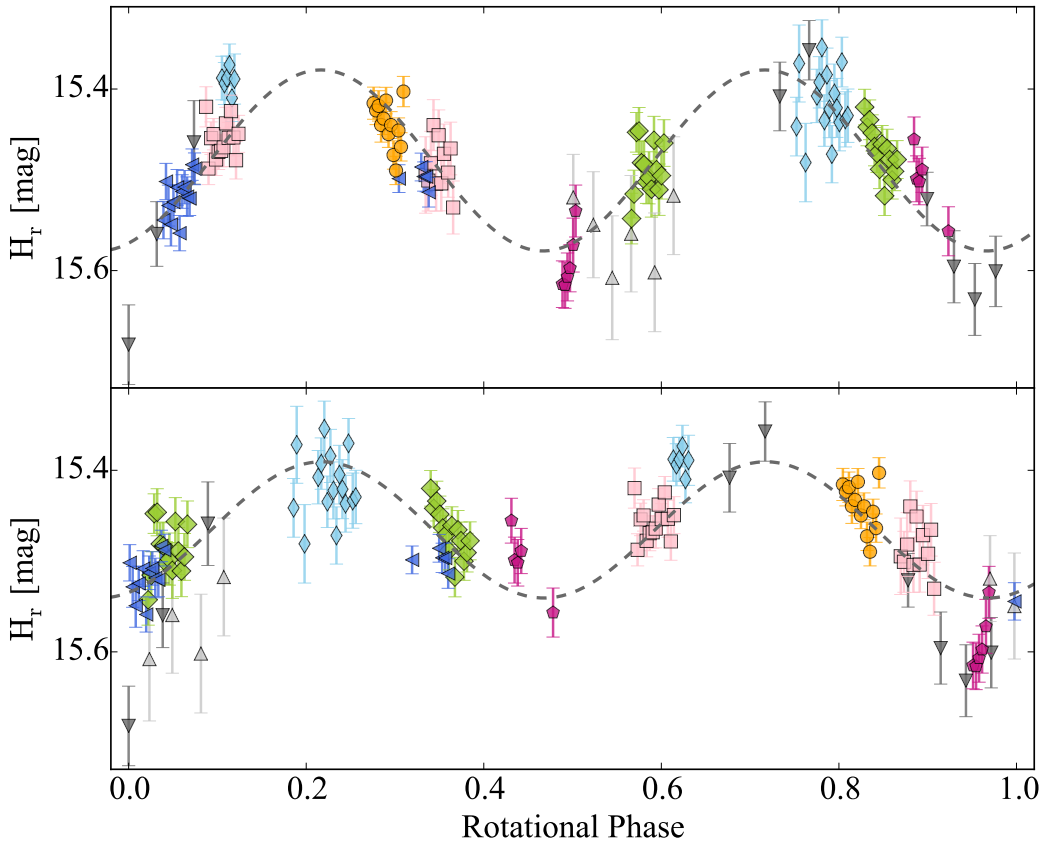

Figure 5.35: Rotational lightcurve of 110P with all of the data from 2012. The lightcurve is folded with the two most-likely periods 10.153 h (top) and 8.375 h (bottom) derived from the MC method. The lightcurve with $P_{\mathrm{rot},1} = 10.153$ h is preferred by the MC method (in 75% of the iterations) and it is in better agreement with the brightness variation within the individual nights. The symbols are the same as in Fig. 5.33. The NTT-EFOSC2 points from 17 and 18 June 2012 were binned since the S/N of the individual points was low due to bad observing conditions.

5.7 123P/West-Hartley

This SEPPCoN target was observed on three consecutive nights in July 2007 while it was at heliocentric distance of 5.6 au. A careful examination of the images indicated that despite the large heliocentric distance at the time of the observations, 123P was weakly active (Fig. 5.36).

The observations from the individual nights clearly indicated a brightness variation of the nucleus. However, the LS periodogram of the data did not reveal any pronounced peaks with significant power (Fig. 5.37). The two highest peaks

correspond to 3.7 and 10.3 h. Those two periods were also preferred by the MC simulation, which picked $P_{\rm rot} = 3.70 \pm 0.02$ h in 66% of the iterations and $P_{\rm rot} = 10.27 \pm 0.05$ h (34%).

The lightcurves resulting from these two periods are plotted in Fig. 5.38. Both periods appear to be in agreement with the data, and it is not possible to choose between them. Moreover, the data phased with other periods selected by the periodogram produce lightcurves with similar quality. Therefore, I conclude that the collected data are not sufficient to determine the spin rate of 123P.

I estimated a brightness variation $\Delta m_{\rm r} = 0.5 \pm 0.1$ mag which corresponds to an axis ratio $a/b \geq 1.6 \pm 0.1$. The mean measured magnitude of 123P was $m_{\rm r} = 23.3 \pm 0.1$ mag which converts to $H_{\rm r}(1,1,0) = 15.7 \pm 0.1$ mag if a phase function with $\beta = 0.04$ mag/deg is used. The absolute magnitude and the radius measured by Fernández et al. (2013) convert to an albedo $A_{\rm r} = 4.2 \pm 1.0\%$ (Eq. 3.10). It is however important to note that the surface brightness profile of 123P indicated a weak activity, which implies that the absolute magnitude $H_{\rm r}(1,1,0)$ of the nucleus could be fainter and the determined albedo must be treated as an upper limit.

5.8 137P/Shoemaker-Levy 2

Comet 137P was observed during one night in 2005 and two nights in 2007 as part of SEPPCoN. It appeared inactive during both observing epochs (Figs. 5.39 and 5.40).

I applied the MC method on the combined dataset from all three nights to determine the comet's phase function (Fig. 5.41). The derived phase function slope was $\beta = 0.035 \pm 0.004$ mag/deg.

Next, I attempted to determine the lightcurve period from the data taken in 2005. The highest peak of the periodogram in Fig. 5.42 corresponds to a rotation period of 7.7 h. However, all peaks on the periodogram have low powers which are not sufficient to determine the rotation rate of 137P.

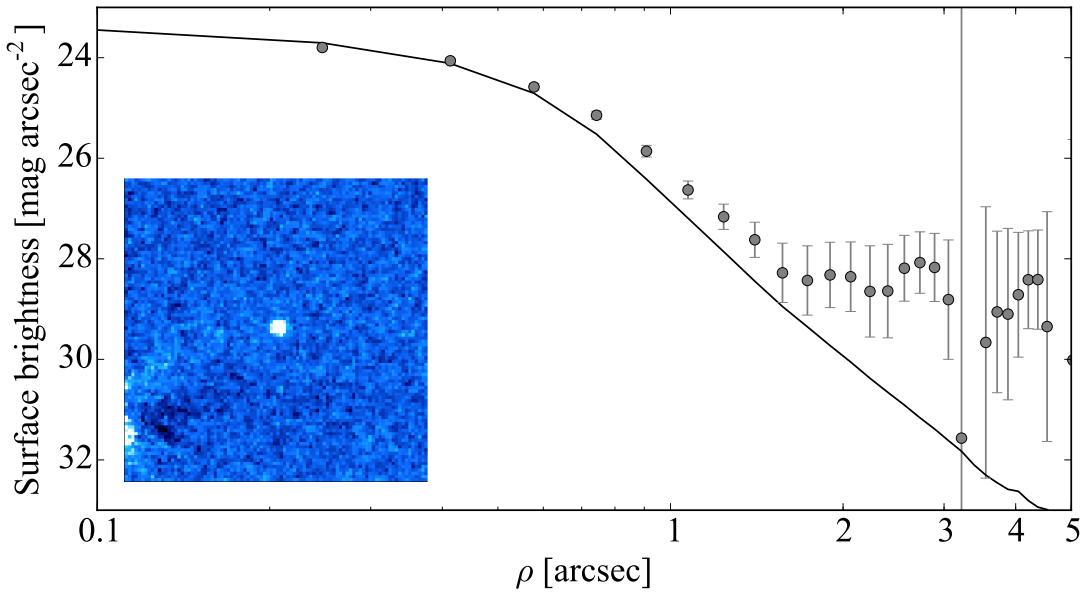

Figure 5.36: Same as Fig. 5.1, for 123P on 18 July 2007. The co-added composite image is made up of 23 × 110 s exposures. The comet appears stellar on the composite image, although its surface brightness profile deviates from that of the comparison star, which indicates that the comet was weakly active during the time of the observations.

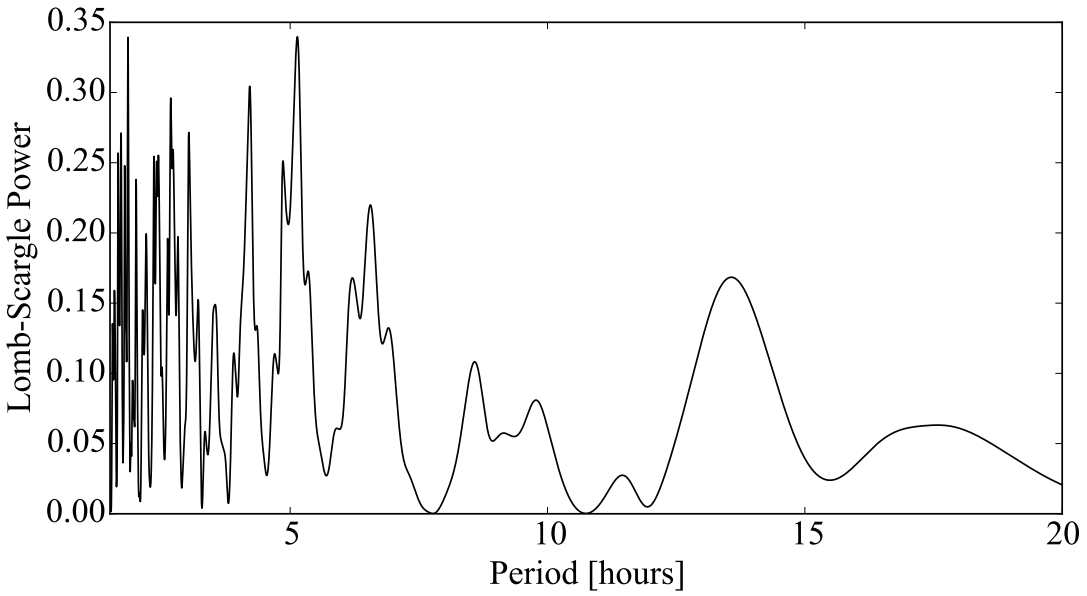

Figure 5.37: Lomb-Scargle periodogram of 123P. The two highest peaks correspond to $P_{\mathrm{rot},1}$ = 3.7 h and $P_{\mathrm{rot},2}$ = 10.7 h.

The lightcurve phased with a period of 7.7 h is plotted in Fig. 5.43. Its brightness variation is $\Delta m_{\mathrm{r}} = 0.18 \pm 0.05$ mag, which converts to $a/b \geq 1.18 \pm 0.05$. The uncertainties of the individual points are large in comparison with

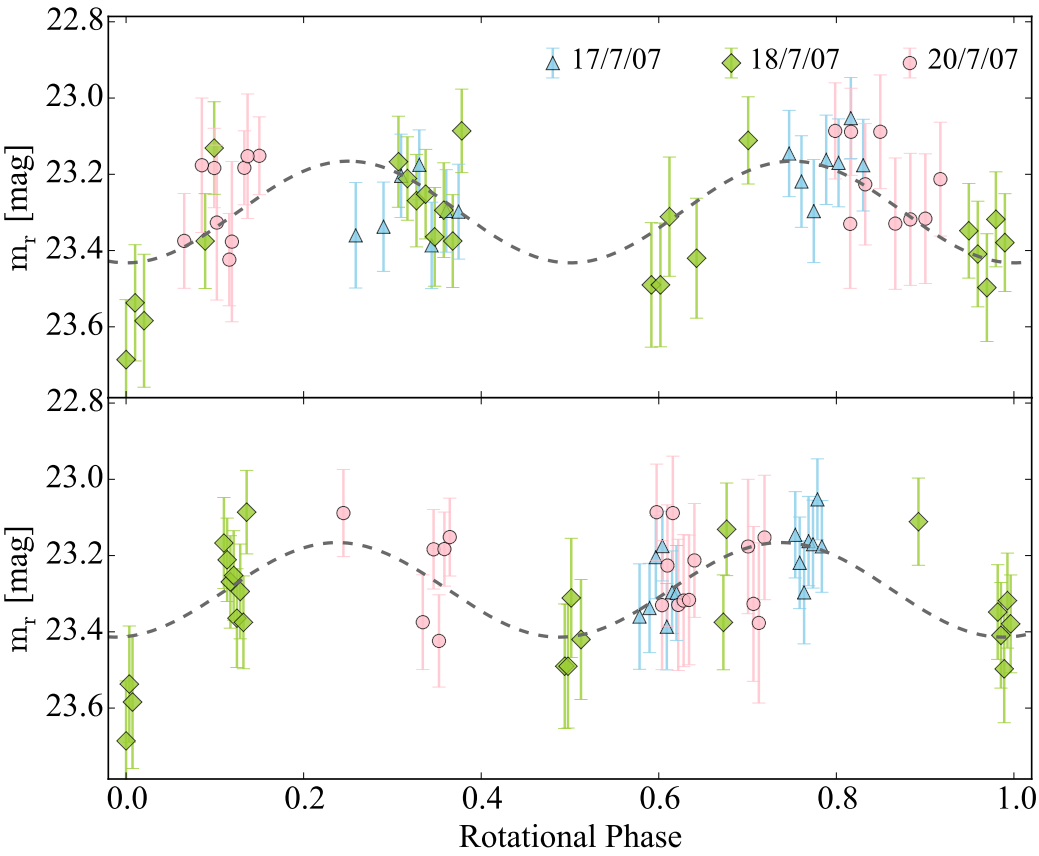

Figure 5.38: Rotational lightcurve of 123P with all of the data from 2007. The lightcurve is folded with the most-likely periods 3.7 h (top) and 10.7 h (bottom).

the detected brightness variation. Therefore, it is not possible to derive a precise rotation rate for the comet from this dataset. I attempted to improve the period determination by combining all data from 2005 and 2007. However, the photometry from 2007 has even larger photometric uncertainties and does not lead to improvement of the period estimation.

The absolute magnitude of 137P is $H_r(1,1,0) = 14.63 \pm 0.05$ mag. Using Eq. 3.10 and the SEPPCoN radius from Fernández et al. (2013), I estimated an albedo $A_r = 3.3 \pm 0.5\%$.

5.9 149P/Mueller 4

Comet 149P was observed using NTT, WHT and VLT during 7 nights at the end of January 2009. The surface brightness profiles of the comet for each night

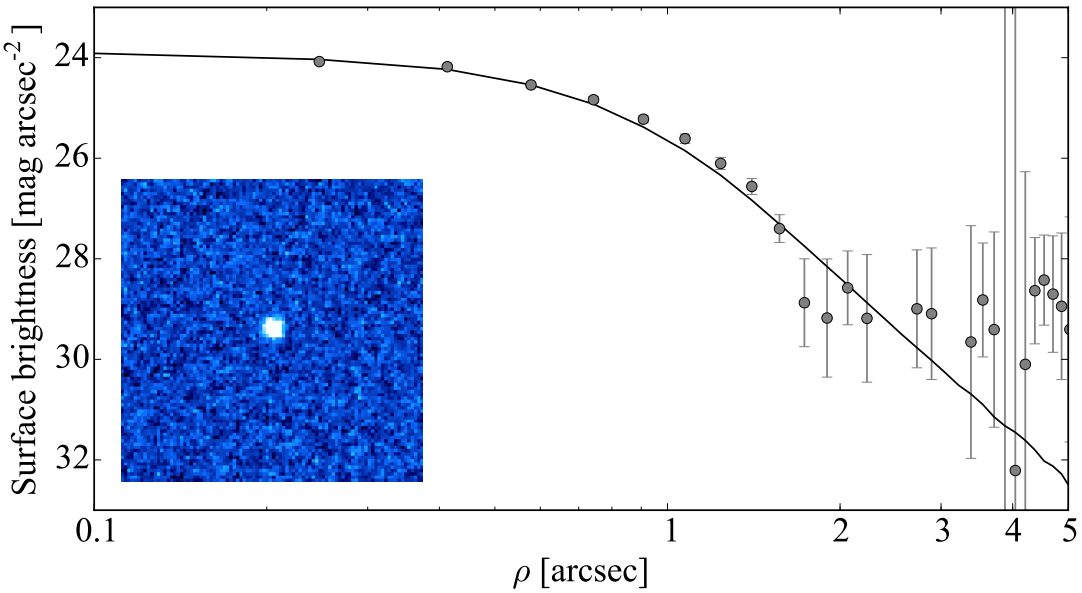

Figure 5.39: Same as Fig. 5.1 for 137P on 6 March 2005. The co-added composite image is made up of 23 × 110 s exposures. The comet appears inactive and its surface brightness profile follows that of the comparison star close to the centre before it levels out at the background noise level.

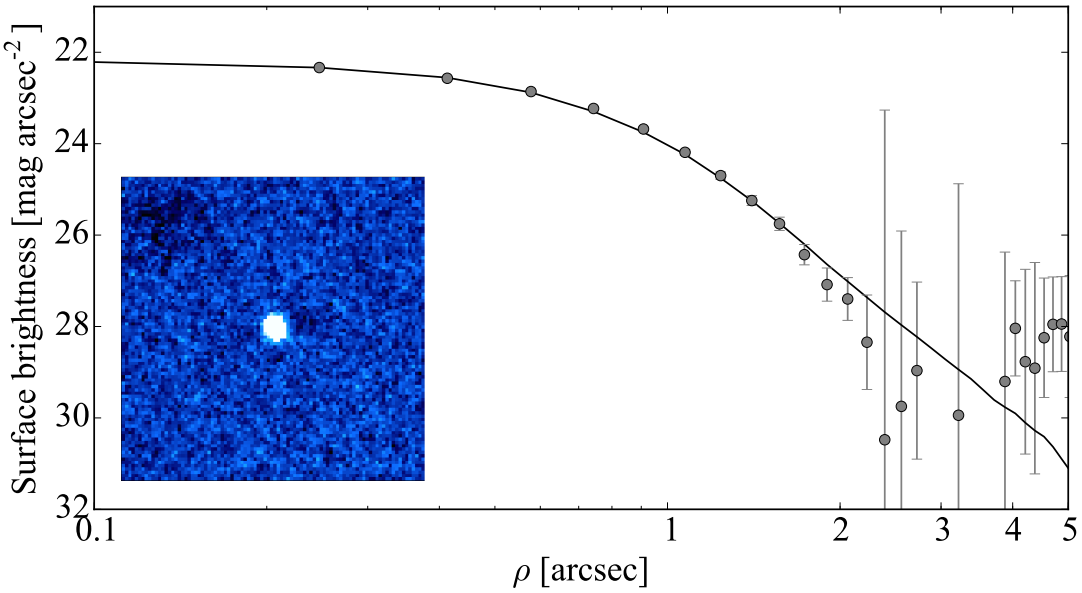

Figure 5.40: Same as Fig. 5.1 for 137P on 13 July 2007. The co-added composite image is made up of 20 × 75 s exposures. The comet appears inactive and its surface brightness profile matches that of the comparison star.

indicated that it was not active at the time of the observations (see Fig. 5.44).

The phase angle of 149P changed between 8.5 and 10 degrees between the first and the last observing night. I used the MC method to constrain the phase

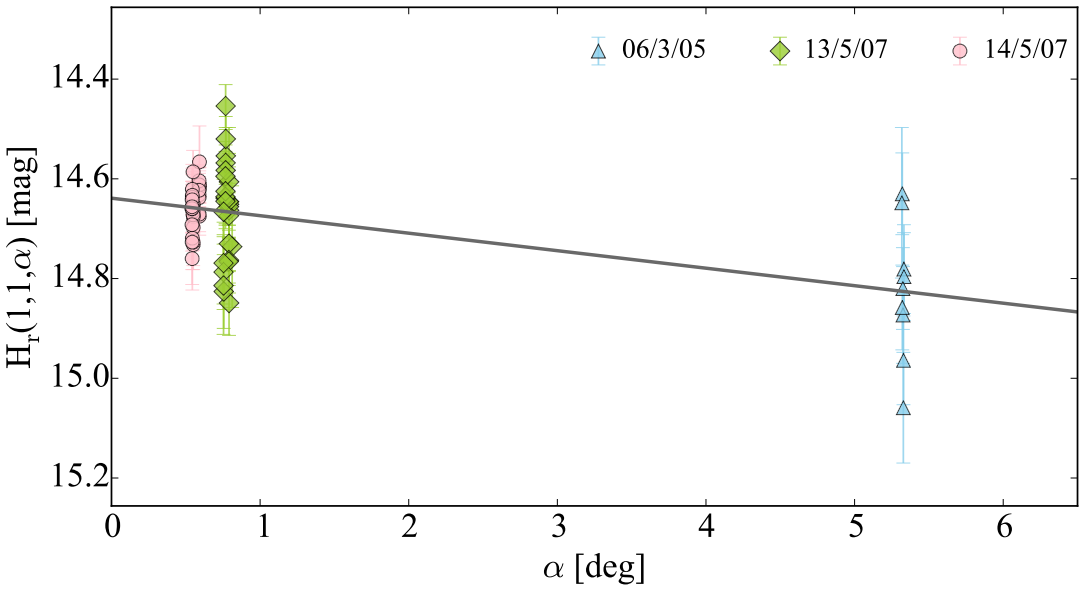

Figure 5.41: Phase function of comet 137P. The linear phase function coefficient derived from the Monte Carlo simulations is $\beta = 0.035 \pm 0.004$ mag/deg.

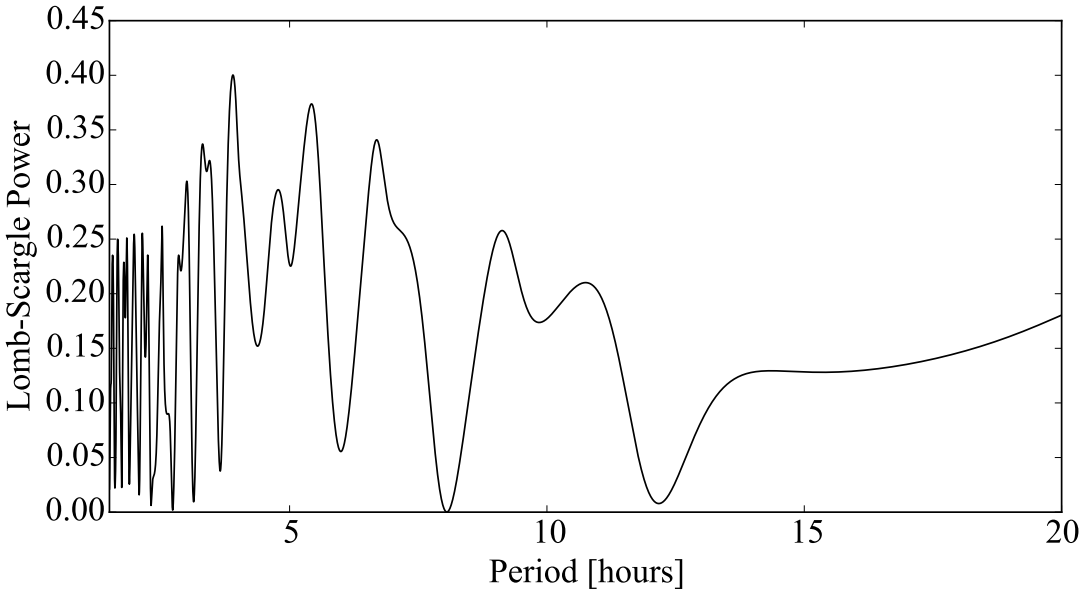

Figure 5.42: Lomb-Scargle periodogram of 137P from the 2007 dataset. The highest peak corresponds to a period of $P_{\rm rot} = 7.7$ h.

function slope of the comet as $\beta = 0.03 \pm 0.02$ mag/deg.

The periodogram of the time series corrected for geometric effects peaks at $P_{\rm rot} = 11.9$ h. The period of 11.9 ± 0.1 is preferred by the MC simulation in 84% of the iterations. However, the power of the peaks on the periodogram is too small and I cannot select the best period unambiguously. A rotation period near

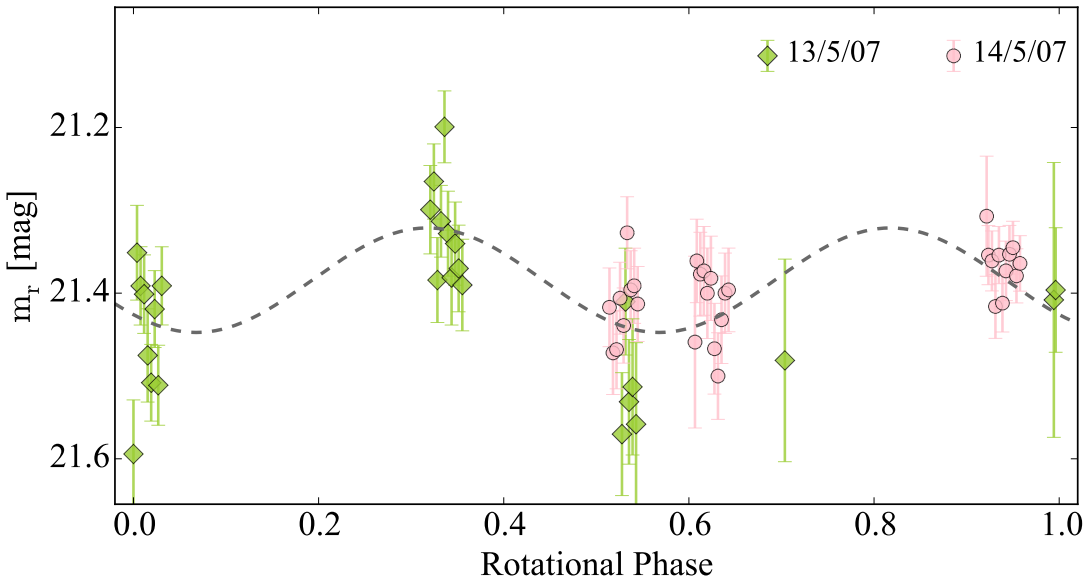

Figure 5.43: Rotational lightcurve of 137P with all of the data from 2007 folded with one of the possible periods, 7.7 h. The uncertainty of the points is large in comparison to the brightness variation of the comet, which obstructs the period determination.

12 h would make this measurement for 149P difficult, and a clear determination of such a period using an Earth-based facility would require a longer photometric time sequence.

Figure 5.47 shows the lightcurve of 149P with the best fit from the MC method. The photometric uncertainty of the individual points is large with respect to the total brightness variation of the lightcurve, which confirms that the derived lightcurve is uncertain.

The brightness variation of the comet is $\Delta m_{\rm r} = 0.11 \pm 0.04$ mag which converts to $a/b \geq 1.11 \pm 0.04$. The observed mean magnitude of 149P was $m_{\rm r} = 22.14 \pm 0.04$ mag which corresponds to $H_{\rm r}(1,1,0) = 16.93 \pm 0.04$ if the derived phase function with $\beta = 0.03 \pm 0.02$ mag/deg is used. Using Eq. 3.10, I calculated that the albedo of 149P is $A_{\rm r} = 3.2 \pm 0.5\%$.

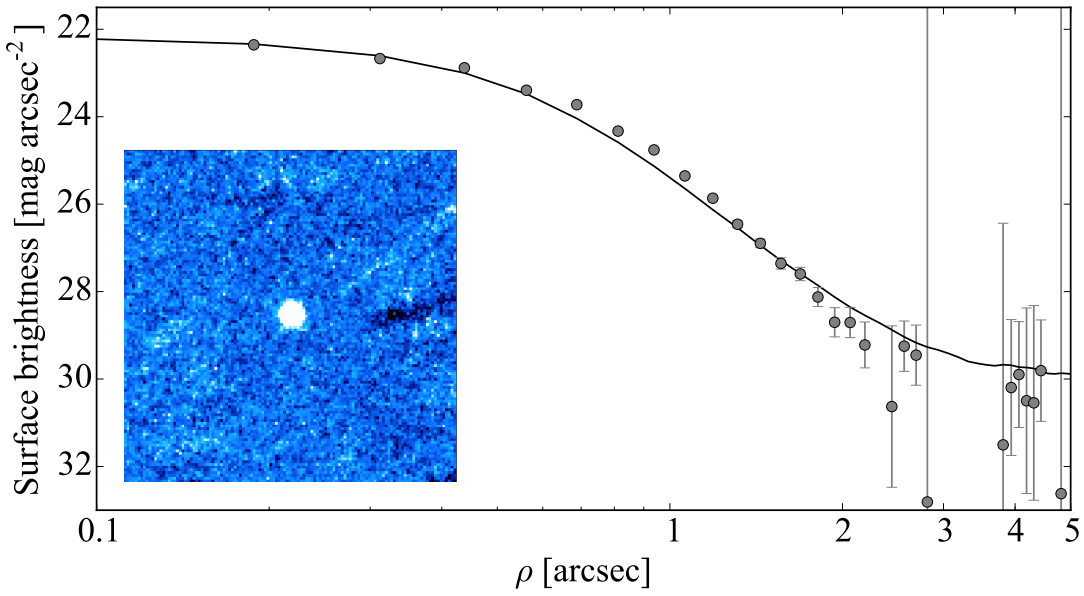

Figure 5.44: Same as Fig. 5.1 for 149P on 23 January 2009. The co-added composite image is made up of 15 × 80 s exposures. The comet appears inactive and its surface brightness profile matches that of the comparison star.

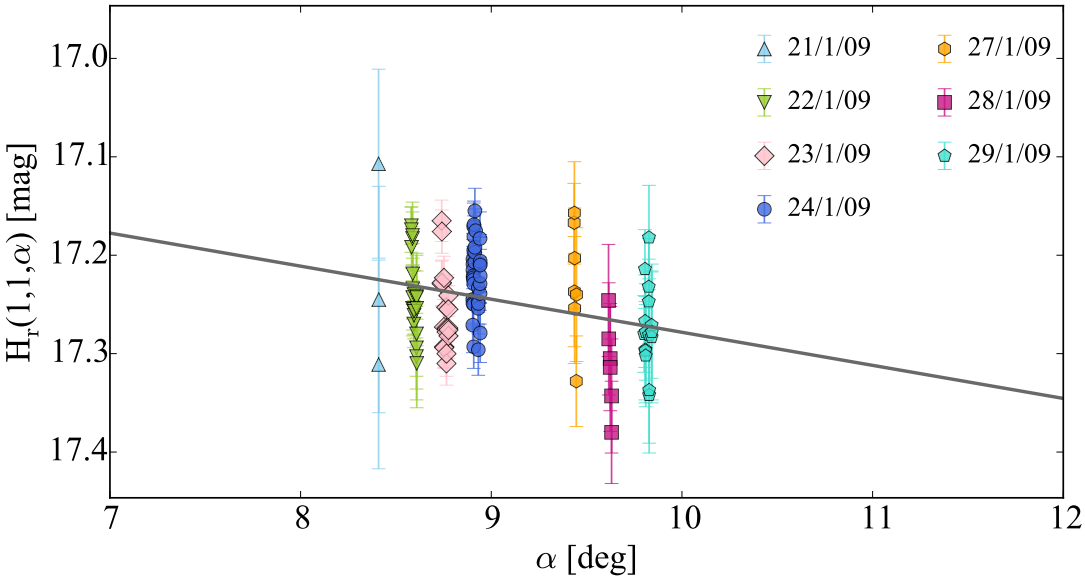

Figure 5.45: Phase function of comet 149P. The linear phase function coefficient derived from the Monte Carlo simulations is $\beta = 0.03 \pm 0.02$ mag/deg.

5.10 162P/Siding Spring

Comet 162P was observed in 2007 around its aphelion, and again in 2012 close to its next aphelion passage. The first set of observations aimed to determine the comet's lightcurve, while the second dataset focused on its phase function.

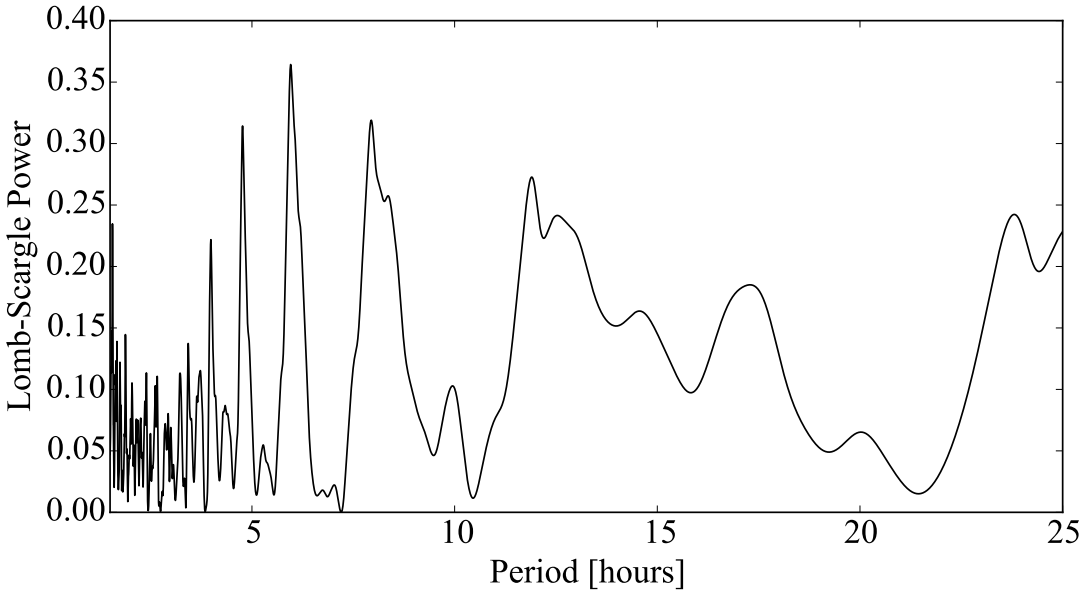

Figure 5.46: Lomb-Scargle periodogram of the combined datasets for 149P showing the LS power versus period. The highest peak corresponds to the most likely period $P_{\rm rot}$ = 11.88 h. Since all peaks have low power, the spin period of the comet cannot be determined unambiguously.

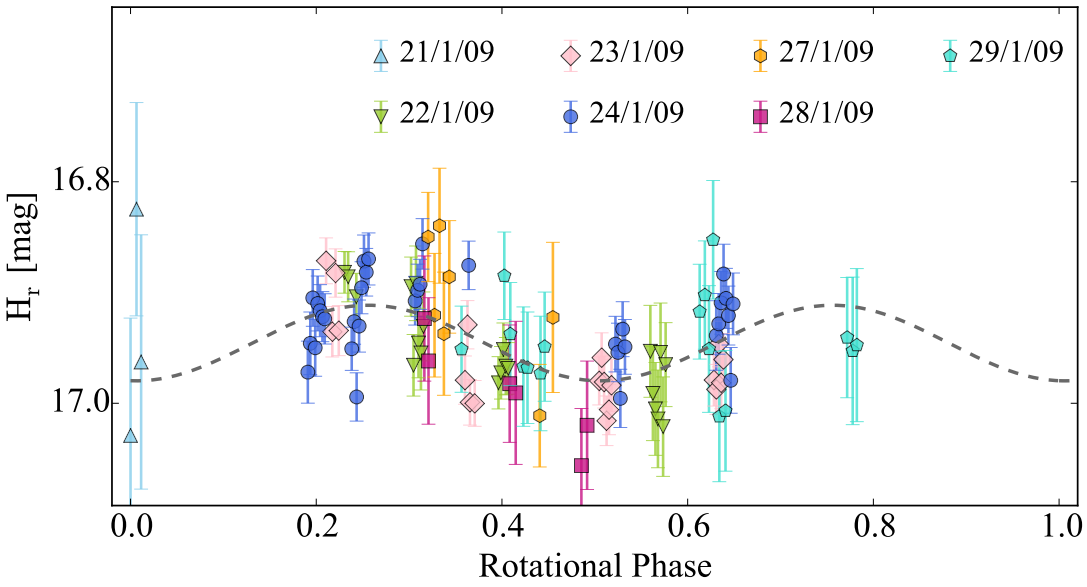

Figure 5.47: Rotational lightcurve of 149P with all of the data from 2009. The points from WHT and NTT were binned. The lightcurve is folded with the most-likely period of 11.88 h.

The comet had a stellar profile and appeared to be inactive in 2007 (Fig. 5.48). The LS periodogram of the data from the three observing nights in 2007 is shown in Fig. 5.49. The most pronounced peak in the periodogram corresponds to $P_{\rm rot}$ =

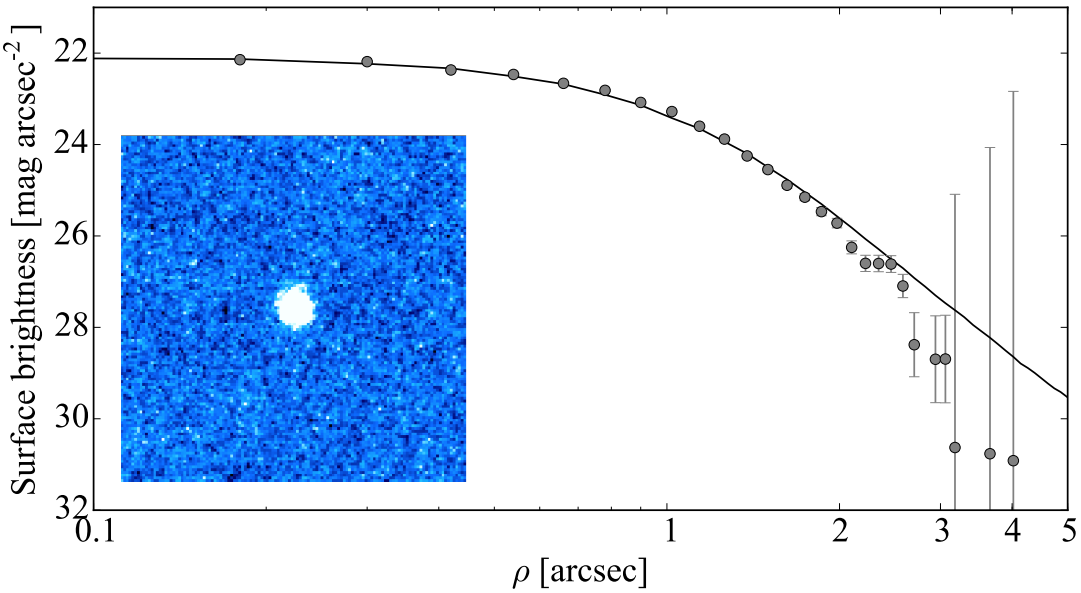

Figure 5.48: Same as Fig. 5.1, for 162P on 18 May 2007. The co-added composite image is made up of 10 × 110 s exposures. The comet appears inactive and its surface brightness profile agrees with that of the comparison star.

32.6 h, and the lightcurve phased with that period can be seen in Fig. 5.50. Using the MC method without phase function correction, I determined the rotation period of the comet to be $P_{\rm rot}$ = 32.6 ± 1 h. This period is in good agreement with the value of ∼ 33 h determined by the team of La Cañada observatory (see Section 4.2.10).

From the observations in 2007, I measured the mean magnitude of 162P to be $m_{\rm r}$ = 20.63 ± 0.05 mag. The brightness variation of the comet was $\Delta m_{\rm r}$ = 0.45 ± 0.05 mag, which corresponds to $a/b \geq 1.51 \pm 0.07$.

Comet 162P was also inactive during all observations in 2012, which is demonstrated by the surface brightness plot in Fig. 5.51. Since the observations were taken at a large phase angle range (4-12°), I could only combine the data after deriving the comet's phase function. The MC method determined a phase function coefficient β = 0.039 ± 0.002 mag/deg.

The LS periodogram of the combined dataset from 2012 suggested multiple possible rotation periods for 162P (Fig. 5.52). The MC method preferred $P_{\rm rot,1}$ = 33.237 ± 0.008 h in 62% of the iterations and $P_{\rm rot,2}$ = 32.852 ± 0.003 h in

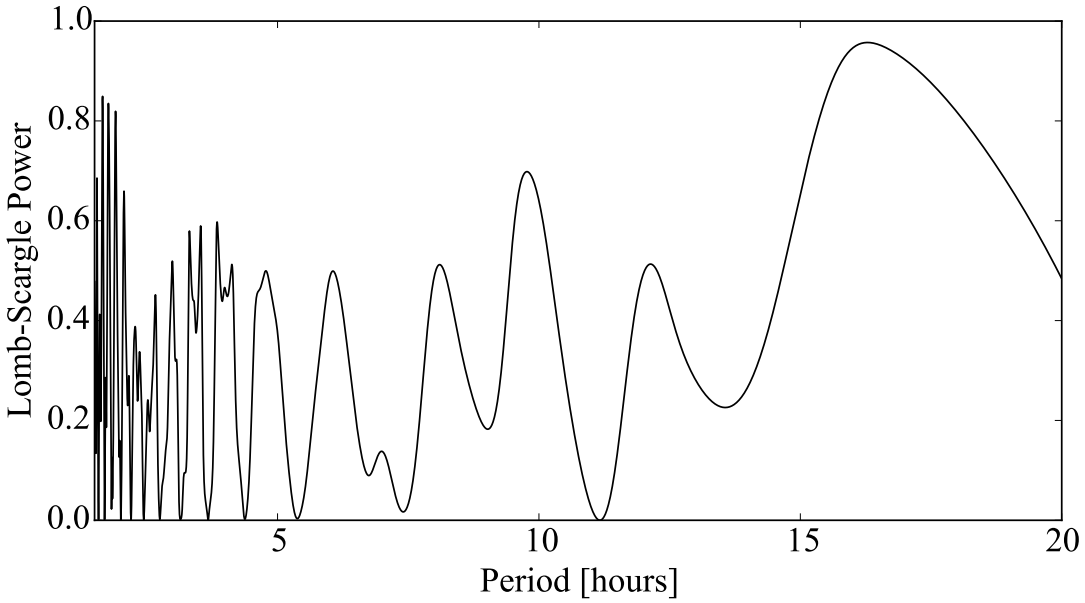

Figure 5.49: Lomb-Scargle periodogram of the 2007 dataset for 162P showing the LS power versus period. The highest peak corresponds to the most likely period $P_{\rm rot} = 32.6$ h.

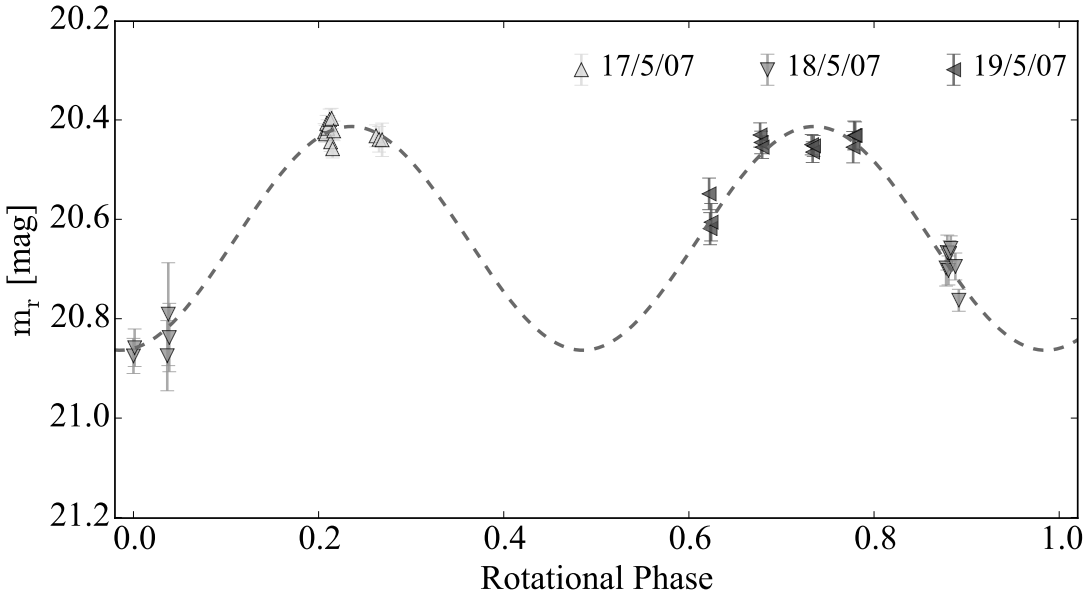

Figure 5.50: Rotational lightcurve of 162P with the data from 2007. The lightcurve is folded with period 32.6 h.

35% of the iterations. The lightcurves in Fig. 5.53 confirm that due to the limited sampling of the lightcurve, it is impossible to choose between these two possibilities, although it is worth noting that the points from 24 May 2012 agree better with $P_{\rm rot,2} = 32.852$.

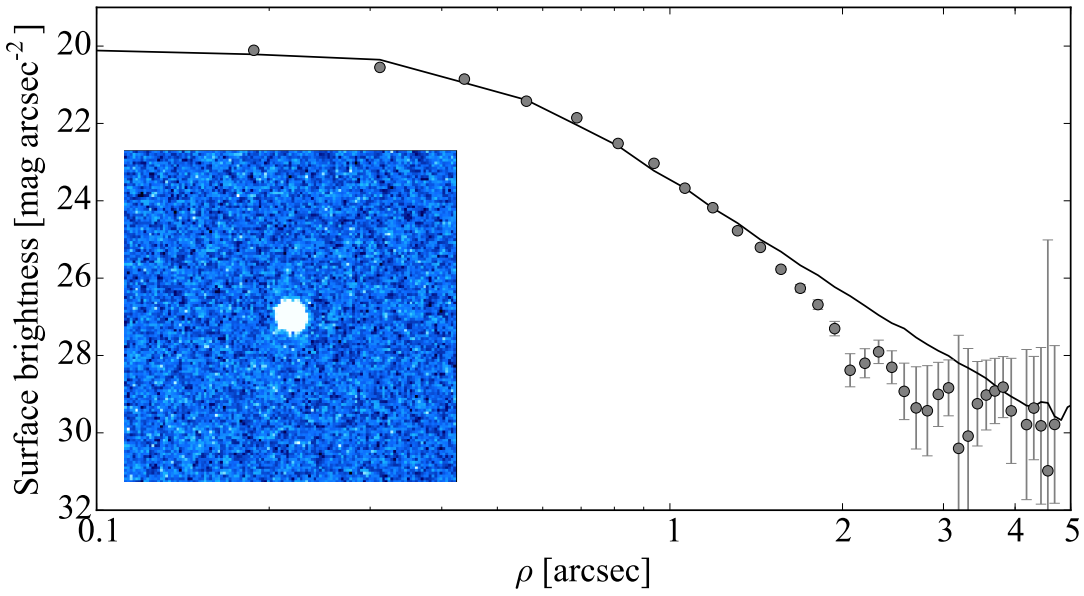

Figure 5.51: Same as Fig. 5.1, for 162P on 23 April 2012. The co-added composite image is made up of 5 × 60 s exposures. The comet appears inactive and its surface brightness profile generally agrees with that of the comparison star. The narrower profile of the comet is most likely an artefact of the position uncertainty of the comet on the frames.

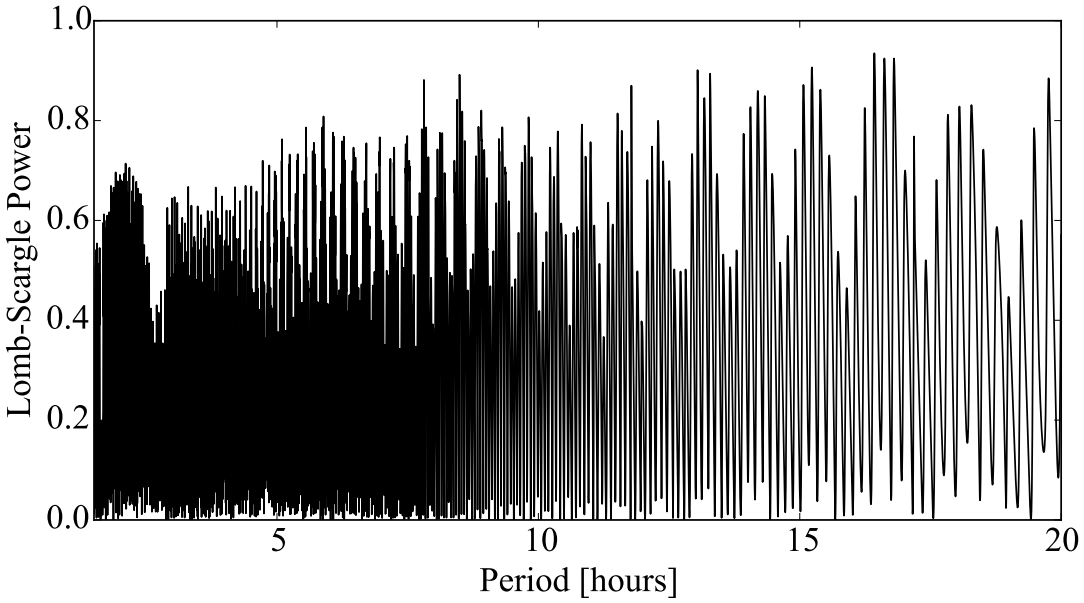

Figure 5.52: Lomb-Scargle periodogram of the 2012 dataset for 162P showing the LS power versus period. There are a number of possible periods as well as secondary peaks caused by aliasing. The highest peaks correspond to rotation periods of 32.852 h and 33.237 h.

The brightness variation in the 2012 observations was $\Delta m_{\rm r} = 0.59 \pm 0.04$ mag, which corresponds to $a/b \geq 1.72 \pm 0.06$. The absolute magnitude of 162P from

the 2012 dataset was $H_r(1,1,0) = 13.91 \pm 0.04$ mag. If I use Eq. 3.10, I estimate the albedo of 162P to be $A_r = 2.1 \pm 0.3\%$. This result makes comet 162P the JFC with the lowest known albedo (see Section 9.3).

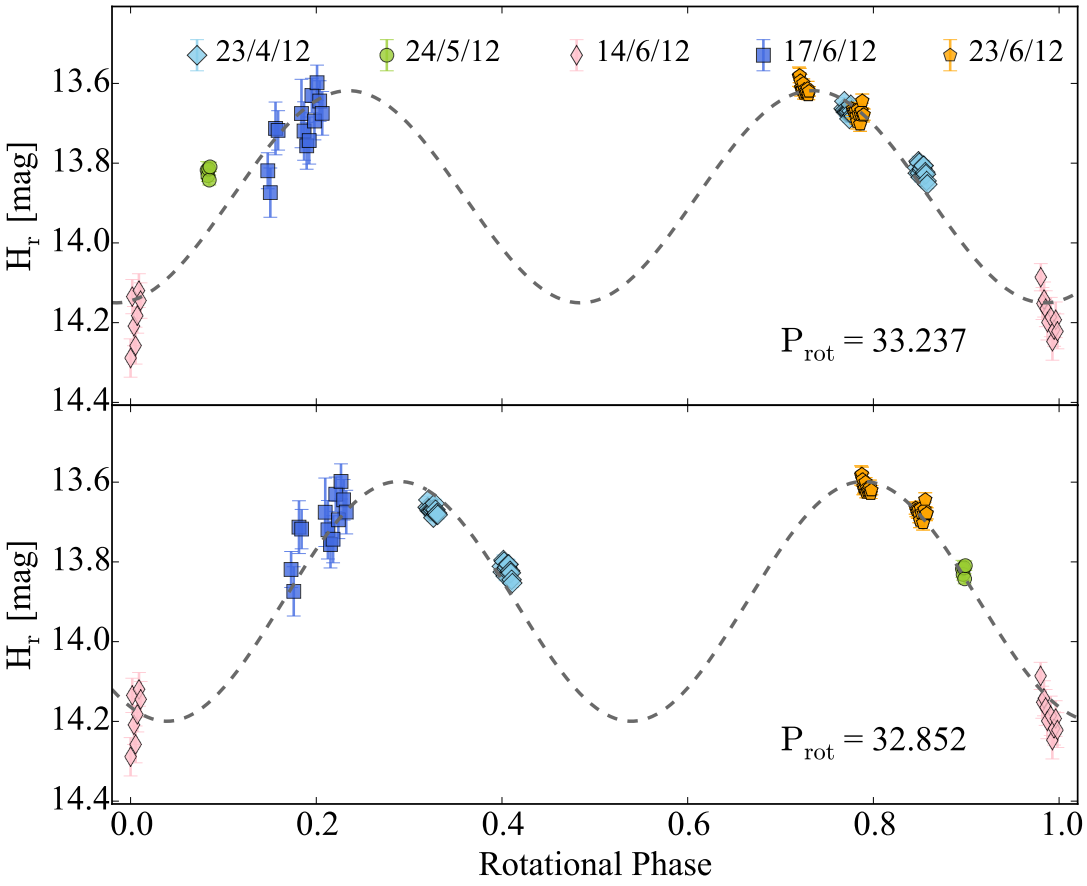

Figure 5.53: Rotational lightcurve of 162P with the data from 2012. The lightcurve is folded with $P_{\mathrm{rot},1} = 33.237$ h (top) and $P_{\mathrm{rot},2} = 32.852$ h (bottom). It is not possible to choose between the two periods from the dataset collected in 2012.

As a final step in the analysis of the data for 162P, I combined the two datasets from 2007 and 2012 in order to attempt constraining the comet's lightcurve and phase function better. It is possible that the period of 162P slightly changed between 2007 and 2012 while the comet was active close to perihelion. Besides, it is not excluded that since the two observations were done at different geometries, the resulting lightcurves can appear different. Nevertheless, it is worth attempting to combine the two datasets as the increased number of observations can provide a better understanding of the nucleus' properties.

With these caveats in mind, I proceeded to analyse the combined data from

2007 and 2012. The MC method suggested a phase function with a slope $\beta = 0.038 \pm 0.002$ mag/deg and a lightcurve with period $P_{\rm rot} = 32.853 \pm 0.002$ h. This period corresponds to the highest peak of the LS periodogram in Fig. 5.55.

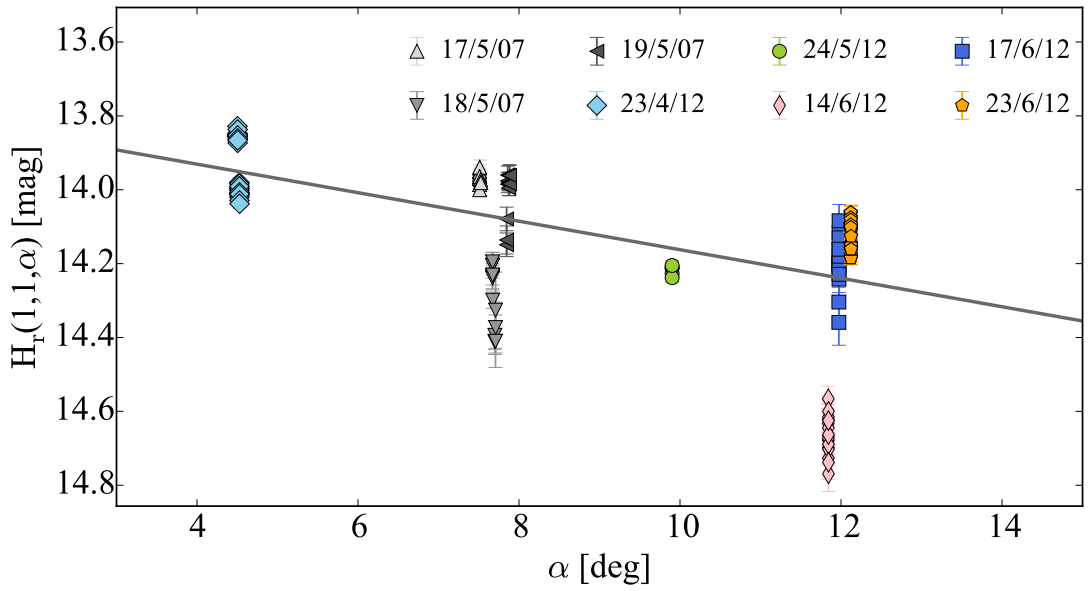

Figure 5.54: Phase function of comet 162P. The linear phase function slope derived from the Monte Carlo simulations is $\beta = 0.038 \pm 0.002$ mag/deg.

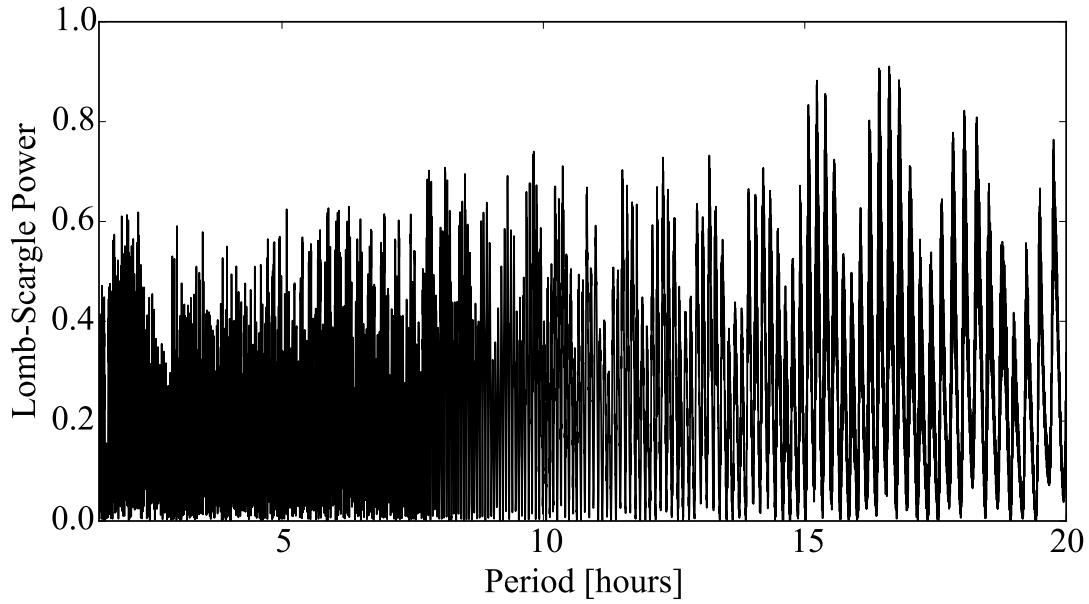

Figure 5.55: Lomb-Scargle periodogram of the combined datasets of 162P from 2007 and 2012 showing the LS power versus period. The highest peak corresponds to $P_{\rm rot} = 32.853$ h.

The derived parameters from the combined dataset are very close to those

of the 2012 dataset alone (See. Table 5.2). However since they were derived using data from two different apparitions, I consider the values from just the 2012 dataset to be less uncertain.

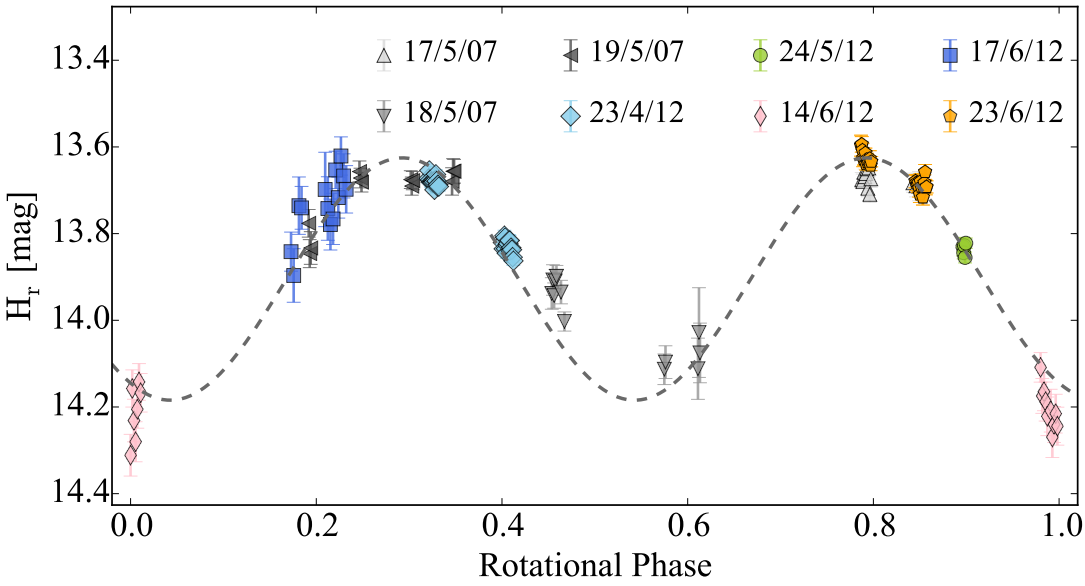

Figure 5.56: Rotational lightcurve of 162P with the data from 2007 and 2012. The lightcurve is folded with the most likely period of 32.853 h.

5.11 Summary of the derived properties

In this chapter I presented the analysis of new data for nine JFCs. The absolute photometric calibration method using stellar magnitudes from Pan-STARRS DR1 catalogue allowed me to successfully combine the sparsely sampled photometric time series for each comet. As a result I constrained the rotation rates of six of the comets, found the phase-function slopes of seven comets and derived the albedos of eight of the JFCs in the sample. A summary of the results for each comet can be found in Table 5.2.

Table 5.2: Derived physical parameters for all observed comets in this chapter.

Comet	Epoch	m_r [1]	$H_r(1,1,0)$ [1]	P_{rot} [h] [2]	β [mag/deg] [3]	R_N [km] [4]	A_r [%] [5]	Δm_r	a/b
14P	2004	22.58±0.05	-	8.93±0.04	-	-	-	0.36±0.05	1.39±0.06
	2007	21.06±0.05	-	9.02±0.04	-	-	-	0.39±0.05	1.43±0.07
	Combined	-	14.87±0.05	9.02±0.01	0.060±0.005	-	5.0±0.7	0.37±0.05	1.41±0.06
47P	2005*	21.83±0.06	-	10.8/14.1	-	-	-	0.33±0.06	1.36±0.07
	2006*	21.55±0.04	-	-	-	-	-	-	-
	2015*	21.11±0.06	14.58±0.06[a]	15.6±0.1	-	-	-	0.24±0.06	1.25±0.07
	2005 + 2015**	-	14.59±0.06	-	0.096±0.004	-	5.8±0.9[c]	-	-
93P	2009*	21.09±0.05	15.17±0.05[b]	$18.2^{+1.5}_{-15}$	-	-	4.9±1.0[c]	0.21±0.05	1.21±0.06
94P	2005	21.3±0.1	-	20.43±0.05	-	-	-	0.7±0.1	1.9±0.2
	2007	22.6±0.2	-	-	-	-	-	1±0.2	2.5±0.5
	2009	21.30±0.05	-	-	-	-	-	0.80±0.05	2.09±0.10
	Combined	-	15.50±0.09	20.70±0.07	0.039±0.002	-	4.7±0.7	1.11±0.09	2.8±0.2
110P	2012	-	15.47±0.03	10.153±0.001	0.069±0.002	2.50±0.04	-	0.20±0.03	1.20±0.03
123P	2007*	23.3±0.1	15.7±0.1[b]	-	-	-	4.2±1.0[c]	0.5±0.1	1.6±0.1
137P	2007	21.39±0.05	-	-	-	-	-	0.18±0.05	1.18±0.05

Table 5.2 continued

Comet	Epoch	m_r [1]	$H_r(1,1,0)$ [1]	P_{rot} [h] [2]	β [mag/deg] [3]	R_N [km] [4]	A_r [%] [5]	Δm_r	a/b
	2005 + 2007	-	14.63±0.05	-	0.035±0.004	-	3.3±0.5	-	-
149P	2009	22.14±0.04	16.93±0.04	-	0.03±0.02	-	3.2±0.5	0.11±0.04	1.11±0.04
162P	2007	20.63±0.05	-	32.6±1	-	-	-	0.45±0.05	1.51±0.07
	2012	-	13.91±0.04	33.237/32.852	0.039±0.002	-	2.1±0.3	0.59±0.04	1.72±0.06
	Combined**	-	13.90±0.05	32.853±0.002	0.038±0.002	-	2.1±0.3	0.62±0.05	1.77±0.08

[1] Magnitudes in PS1 system. [2] The synodic rotation periods and their uncertainties were derived from the mean and standard deviation from the MC method (see Section 3.6.2). [3] The linear phase function coefficients and their uncertainties were derived from the mean and standard deviation from the MC method (see Section 3.6.2). [4] Calculated from $H_r(1,1,0)$ assuming an albedo A=4%. [5] Calculated using Eq. 3.10 from $H_r(1,1,0)$ and the effective radius R_{eff} from Fernández et al. (2013) (see Tab. 4.1). * The comet was weakly active. The results do not include corrections for the presence of a near-nucleus coma. ** The data are from different apparitions. [a] The β value for the $H_r(1,1,0)$ was taken from the phase function fit of the combined 2005 and 2015 datasets. [b] Calculated for $\beta = 0.04$ mag/deg. [c] The comet was weakly active at the time of the observation. The albedo estimates are therefore upper limits.

Chapter 6

Ensemble properties of JFCs

In Table 4.1, I summarised the physical characteristics of all JFCs with known rotation rates. With the newly analysed lightcurves in Chapter 5, I have added six additional lightcurves, seven phase functions and eight albedo estimates. Here, I compare the newly obtained results with the overall JFC characteristics and use the expanded sample to draw conclusions about the collective population properties.

6.1 Spin rate distribution

The distribution of the rotation rates of comets can be used to study their collisional history. Fig. 6.1 displays a histogram of all known spin rates of JFCs. I have plotted the rotation frequency $f = 1/P_{\rm rot}$ which was normalised using the geometric mean $\langle f \rangle$ of the whole sample. Similar plots for asteroids have shown that the distribution of asteroid spin rates is Maxwellian which has suggested that asteroids are a collisionally evolved population (Harris, 1996; Pravec et al., 2002).

The best-fitting Maxwell distribution in Fig. 6.1 does not show good agreement with the measured spin rates. I performed Kolmogorov-Smirnov tests comparing the normalised frequency distribution in Fig. 6.1 to Maxwell distribution and flat distribution with the same mean and standard deviation. The resulting D

statistics were 0.20 ($p = 0.09$) and 0.13 ($p = 0.44$) for the uniform and Maxwell distributions respectively. The null hypothesis cannot be rejected in either of the cases, and therefore both distributions can possibly describe the data.

The cumulative size distribution (CSD) of JFCs was found to be very close to the one expected for a collisionally relaxed population of strengthless bodies (Lamy et al., 2004; Snodgrass et al., 2011; Fernández et al., 2013, and references therein). However, this result has a large uncertainty and cannot be used as a proof that JFCs originate from disrupted larger bodies (e.g KBOs). In turn, it suggests that due to the continuous mass loss of JFCs their size distribution can be shaped by a complex combination of collisional processes in the past and activity in the present epoch (Snodgrass et al., 2011).

Similarly, the results for the spin distribution of comets suggest that their rotation can be determined by the ongoing activity. The mass lost through activity jets is able to exert a torque on the nucleus, which in turn changes the spin rate of the comet on orbital timescales (e.g. Samarasinha et al., 2004). This mechanism can be responsible for reshaping the original distribution of the spin rates, and could explain the current spin rate distribution of JFC. However, it is important to know that Fig. 6.1 includes data from just 37 comets, many of which have lightcurve periods with large uncertainties. This highlights the need to increase the sample of JFCs with known rotational properties in order to enable the understanding of the population history.

It is worth noting that evidence from Rosetta, such as the low density/high porosity, and presence of hypervolatiles like O_2 and N_2, suggests that 67P is not a collisional fragment (see Davidsson et al., 2016, and references therein). The apparent coincidence of sizes and spin rates of JFC nuclei being consistent with collisional evolution, while in situ measurements of their bulk properties suggest otherwise, is surprising. This may instead support the hypothesis by Jutzi et al. (2017) that JFCs have undergone significant collisional evolution, but the distributions presented here do not yet allow a definitive conclusion.

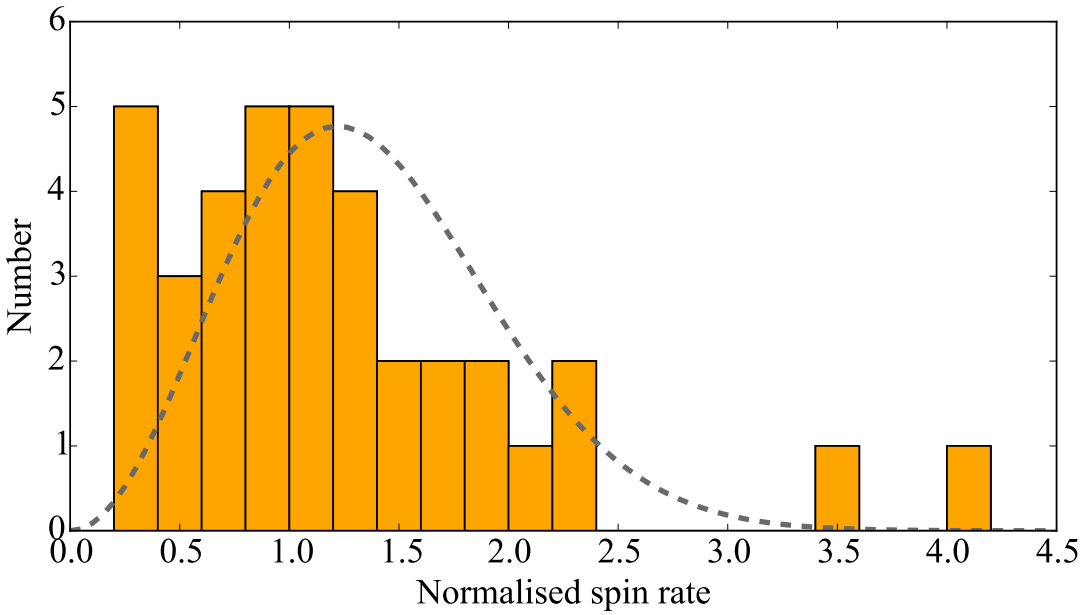

Figure 6.1: Histogram of the normalised rotation rates of 37 JFCs. The normalised spin rate is calculated as $f/\langle f \rangle$ where $f = 1 \ / \ P_{\rm rot}$ and $\langle f \rangle$ is the geometric mean of f. The dashed line corresponds to the best-fitting Maxwellian distribution.

6.2 Shapes

Fig. 6.2 shows the distribution of the axis ratios of all comets. Most a/b values are smaller than $a/b = 2$ and the median of the distribution is at $a/b = 1.5$. However, all comets with shape models obtained from in situ observations (9P, 19P, 67P, 81P, 103P) have significantly higher axis ratios (see Table 4.1). For all other objects the axis ratio is a lower limit since it was calculated from the lightcurve brightness variation. It is therefore possible that the typical elongation of JFCs is higher than the one estimated from the current distribution, suggesting that bilobate shapes (like those seen by spacecraft at 67P and 103P) may be common, in agreement with recent formation models (Davidsson et al., 2016).

6.3 Bulk density

I attempted to use the expanded sample of JFCs with estimated rotation rates and elongations to constrain the comet density and tensile strength. As I discussed in

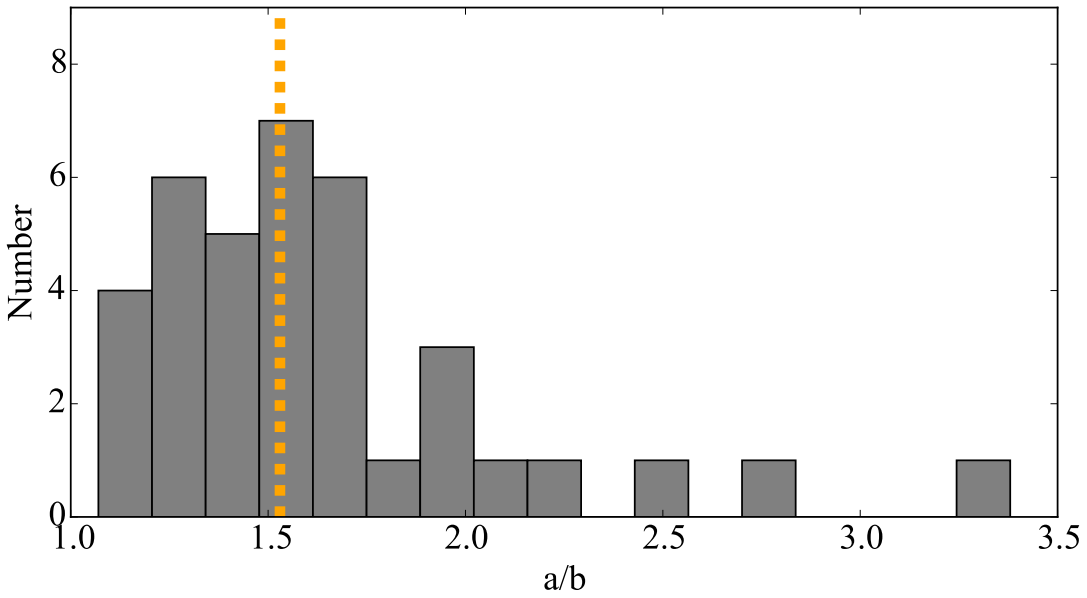

Figure 6.2: Distribution of the axis ratios a/b of JFCs. The vertical line corresponds to the median value of $a/b = 1.5$. For all comets (except 9P, 19P, 67P, 81P, 103P), the given axis ratio is obtained from ground- and space-based telescopes and is therefore just a lower limit of the elongation.

Section 3.6.3, it is commonly assumed that comets have negligible tensile strengths. Under this assumption, it is possible to set a lower limit on the density necessary to keep JFCs stable against rotational instabilities (Eq. 3.12; Pravec et al., 2002).

In Fig. 6.3 I plotted the rotation versus projected axis ratio for all comets in the expanded sample. Using a similar plot, but with fewer comets, Lowry & Weissman (2003) discovered that comets do not require densities higher than approximately 0.6 g cm^{-3} in order to be stable against rotational instabilities. Here I confirm this result for all objects except for 322P, 73P-C and 147P.

As I discussed in section 4.1.17, according to Knight et al. (2016) it is not clear whether 322P has asteroidal or cometary origin. Therefore, the fact that it requires higher density can be interpreted as evidence in favour of the hypothesis that it is an asteroid. Comet 147P lies very close to the limit of 0.6 g cm^{-3} and has a large period uncertainty. Therefore, I do not consider it as an outlier. Additionally, 147P belongs to the class of quasi-Hilda comets and might have asteroidal origin (Ohtsuka et al., 2008). Comet 73P-C on the other hand clearly has a JFC origin

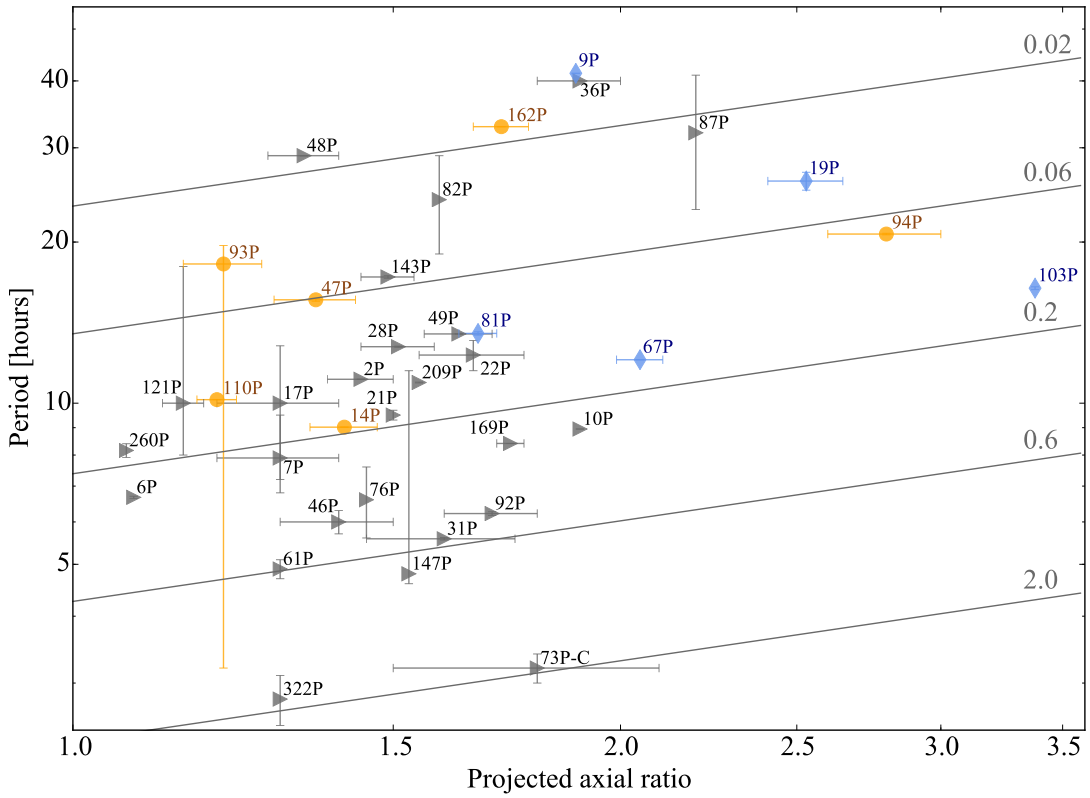

Figure 6.3: Rotation period against projected axis ratio for JFC nuclei. The grey triangles denote comets with parameters determined from lightcurve or radar measurements. The orange circles are the comets from this work. For these points, the axis ratio is a lower limit and the uncertainties are plotted when they were stated by the authors. The blue diamonds correspond to comets visited by spacecraft with precise shape models. The diagonal lines indicate the minimum density (denoted in g cm^{-3} to the right), which a strengthless body of the given axis ratio and spin period requires to remain intact. Apart from the unusual cases of 323P and 73P, which are discussed in the text, no comet requires a density greater than $\sim$ 0.6 g cm^{-3} to remain stable against rotational splitting.

and therefore should be similar to the other objects in the sample. However, since it seems to be continuously disintegrating (see section 4.1.7), it cannot be used to study the stability criterion. It is also possible that the breakup of the comet exposed the innermost part of the pre-breakup nucleus which could have a larger tensile strength (see Gundlach et al., 2016, and references therein).

If I exclude these three comets, the expanded sample confirms the density limit of 0.6 g cm^{-3} discovered by Lowry & Weissman (2003). By analogy with the clear cut-off in rotation rates of asteroids at 2.2 g cm^{-3} (Pravec et al., 2002), I interpret the cut-off for comets as an indication that 0.6 g cm^{-3} is a typical

density for JFCs. This agrees with the density estimates from recent spacecraft measurements (Richardson et al., 2007; Jorda et al., 2016).

6.4 Tensile strength

Further insights into the material properties of JFCs can be determined from comparing their rotation rates and sizes. In previous studies, Davidsson (1999, 2001) and Toth & Lisse (2006) already explored the location of comets and other primitive minor bodies in the radius-rotation period plane. In Fig. 6.4 I plot the distribution of rotation rates with radius for all comets. A key feature of the distribution of comets in the plot is that the domain in the lower right corner is not populated.

In order to interpret this observation, I employ recent discoveries from the Rosetta mission. The in-situ measurements of comet 67P provide precise estimates of the nucleus bulk parameters. It has density of 0.532 ± 0.007 g cm^{-3} (Jorda et al., 2016), axis ratio $a/b = 2.05 \pm 0.06$ (calculated from the axis estimates in Jorda et al., 2016), and tensile strength of 3-15 Pa with an upper limit of 150 Pa (Groussin et al., 2015). If I assume that 67P is a representative example for JFCs, I can use these values to study the properties of the whole population.

In Fig. 6.4, I have plotted the asteroid spin barrier (Pravec et al., 2002) which corresponds to the minimum rotation period of a strengthless body with density ~ 3 g cm^{-3}. For a comparison, I have also plotted the rotation limit for a spherical object with density of 0.6 g cm^{-3}. The position of the limit for comets will change for different elongations and densities since less dense and more elongated objects are easier to disrupt.

So far in the analysis, I have treated comets as strengthless, however the measurements of the tensile strength of 67P allow more complicated models which take the material strength of comets into account. I have used the analytical models developed by Davidsson (1999, 2001) to determine the maximum rotation

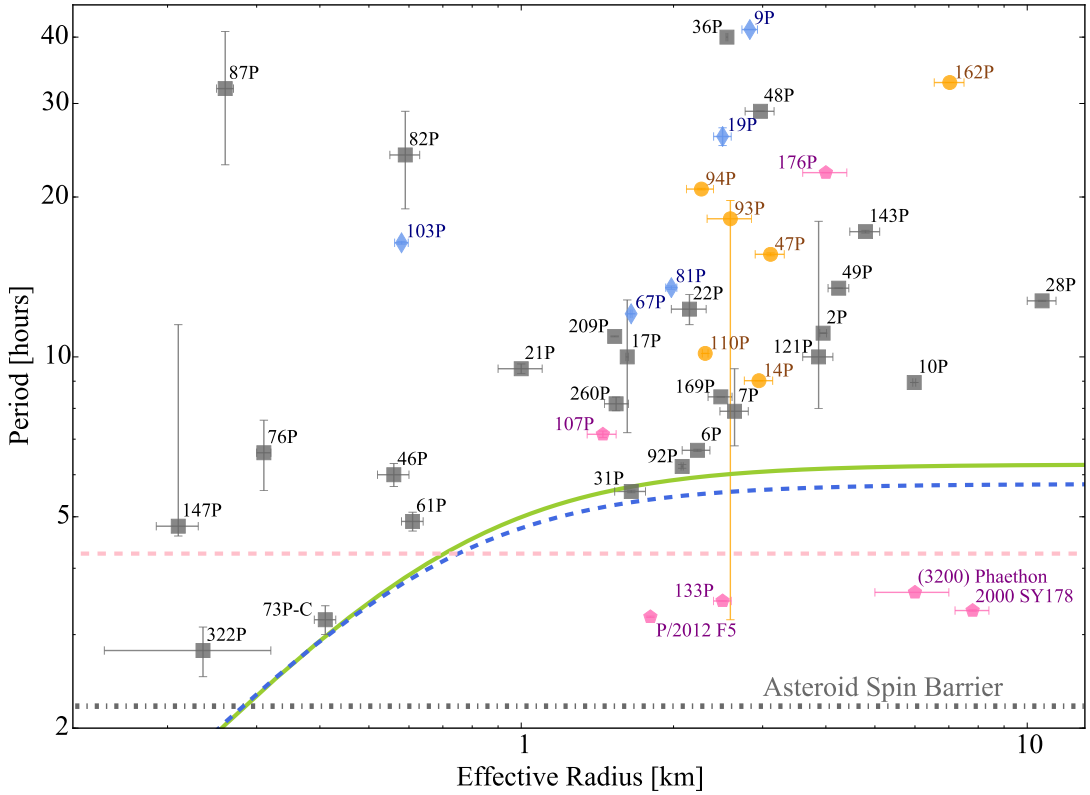

Figure 6.4: Rotation period against effective radius of the JFC nuclei. The blue diamonds are comets visited by spacecraft; the grey squares are comets observed from ground and the orange circles are the comets added in this work. For comparison I plotted active asteroids with known rotation rates (pink pentagons). The lower horizontal dotted line corresponds to the asteroid spin barrier (Harris, 1996; Pravec et al., 2002). The upper dashed pink line shows the maximum possible rotation rate for strengthless spherical bodies with density $\rho = 600$ kg m^{-3}. The curves are derived from the model for prolate ellipsoids stable against rotational instability by Davidsson (2001). The solid green line is the model for density $\rho = 532$ kg m^{-3}, axis ratio $a/b = 2$ and tensile strength $T = 15$ Pa, which corresponds to the parameters measured for 67P from Rosetta (Jorda et al., 2016; Groussin et al., 2015). The dashed blue curve is for the same density but $a/b = 1.6$ (the value for 31P) and $T = 10$ Pa. Varying the model parameters indicates that for typical densities and axis ratios ($a/b \leq 2.0$) none of the observed comets require tensile strength larger than 25 Pa to remain stable against rotational splitting.

rate of prolate ellipsoids which are stable against rotational instabilities using the density, axis ratio and tensile strength of 67P (Fig. 6.4, solid green curve). This curve agrees very well with the observed data and puts 73P-C right at the limit of stability, which agrees with its frequent fragmentation events. Although comet 31P lies below the stability line, it is known that its projected axis ratio is lower

than that of 67P (Table 4.1).

I have therefore investigated the stability limit for objects with density of 0.5 g cm^{-3} and a typical axis ratio of $a/b = 1.6$ (equal to the lower limit to the elongation of 31P). I determined that under these assumptions none of the comets require tensile strength higher than ~ 10 Pa to remain stable against rotational instabilities (Fig. 6.4, dashed blue curve). I varied the axis-ratio parameter of the model for ratios $a/b \leq 2.0$ and concluded that none of the observed comets require a tensile strength larger than 25 Pa to remain stable against rotational splitting. This confirms the low-tensile strength estimates discussed in Section 2.3.6, e.g. the small tensile strength of 67P by Groussin et al. (2015) and of Shoemaker-Levy 9 (Asphaug & Benz, 1996).

An interesting test of this model would come from future observations of the rotation rate of 31P. The comet's period was previously very well determined by Luu & Jewitt (1992). If new observations of its lightcurve show that the nucleus is spinning up, this comet would be a strong candidate for future rotational splitting.

Despite the small number of nuclei with radii larger than 3 km in the sample, it is noticeable that all of them lie far above the stability limit. The simplest explanation for this effect could be deduced from the understanding of activity-induced rotational changes. According to the relations derived in Samarasinha & Mueller (2013), the rotation changes induced by outgassing are proportional to the square of the rotation period and inversely proportional to the square of the radius. In this scenario, if a large nucleus is spinning up due to reaction torques, the faster it gets, the less it can spin up with every orbit. Therefore, it can be concluded that weakly active large nuclei which rotate with relatively short periods are not expected to exhibit large period changes.

At this stage, I cannot evaluate this hypothesis further since spin changes are poorly investigated and to this date only eight comets have confirmed period changes (see Samarasinha & Mueller, 2013, and references therein). Therefore, in order to improve the understanding of the rotation of large comets, in Chapter 7

I measured the rotation rates of three more large nuclei and increased the number of comets with period determinations at multiple apparitions.

Finally, in Fig. 6.4, I have also plotted all active asteroids with known periods and radii (Jewitt et al., 2015). Most of them lie in the lower right domain of the plot where no JFCs can be found. However, it is particularly interesting to note that 107P fulfils the stability criteria for comets too. This object has sparked a long-standing debate on whether it is a comet or an active asteroid (see Jewitt et al., 2015, and references therein) Since 107P is above the stability limit for typical JFCs, the possibility that it has a cometary origin cannot be rejected.

Chapter 7

Looking for spin changes of JFC nuclei

7.1 Overview of observations

The observations analysed in this chapter were performed between January 2016 and March 2017 using three different telescopes (Table 7.1). The data were collected during three observing runs on the 2-meter telescope at Rozhen Observatory, two runs on CAHA 3.5m telescope and one run on INT at La Palma. These observations were part of an observing campaign which I developed to look for period changes in JFCs rotation.

The three targets were chosen because of their good previous lightcurves, as well as their relative brightness during the observations. Additionally, the comets were selected to have heliocentric distances ($R_{\rm h} > 3$ au) during the observing period in order to ensure that they are inactive and that their nuclei are observed directly, free of coma contamination.

Originally, I intended to observe each comet during more than one of the observing runs. This strategy was preferred because having a relatively large timespan between the observations (of the order of a month) allows a more precise period determination. Moreover, since the data-analysis technique I have developed allows absolute photometric calibration with very low uncertainty,

having observations taken during multiple observing runs also allows for a phase-function determination. However, due to telescope time-allocation constraints and the significant number of observing nights lost to bad weather, comet 14P was observed during only one observing run. The lost nights also prevented the complete sampling of all phases of the lightcurves of comets 143P and 162P.

7.2 14P/Wolf

The rotational lightcurve of comet 14P/Wolf was previously observed in 2004 by Snodgrass et al. (2005). They determined a rotation rate $P = 7.53 \pm 0.10$ h. In Section 5.2, I revised this period by adding a dataset from 2007, in the same aphelion arc, and derived a rotation period $P = 9.02 \pm 0.01$ h. The difference between the periods determined in Snodgrass et al. (2005) and 5.2 can be explained with the better absolute photometric calibration I have adopted in this thesis. It allowed better precision when combining the datasets taken during the individual nights, and the result derived in Section 5.2 is therefore more reliable than the previous period determination.

I observed 14P again in 2016 in order to look for changes in its spin rate during the last apparition. The new observations in July 2016 were taken almost a full orbit later, while the comet was inbound, after it had passed through perihelion in 2009 and aphelion in 2013.

Comet 14P was observed during five consecutive nights in July 2016 using LAICA on the CAHA 3.5m telescope. The comet was inactive during the observations as shown by its stellar profile in the combined image (Fig. 7.1). The phase angle changed by less than 0.6 degrees during the observing run, and therefore the adopted phase function correction is expected to have a negligible effect on the derived rotational lightcurve.

In Section 5.2, I found a phase-function slope $\beta = 0.060 \pm 0.005$ mag/deg for 14P. I used this slope to correct the data, and looked for possible periods. Figure

Table 7.1: Summary of all observations analysed in this chapter.

Comet	UT date	R_h [au][a]	Δ [au][b]	α [deg.][c]	Number	Exposure time [s]	Instrument	Proposal ID
14P	2016-07-06	3.93[I]	3.15	10.57	34	24x300, 10x240	CAHA 3.5m/LAICA	H16-3.5-032
	2016-07-07	3.93[I]	3.15	10.72	24	23x300, 1x360	CAHA 3.5m/LAICA	H16-3.5-032
	2016-07-08	3.92[I]	3.15	10.87	33	17x300, 11x240, 5x180	CAHA 3.5m/LAICA	H16-3.5-032
	2016-07-09	3.92[I]	3.16	11.01	25	24x240, 1x300	CAHA 3.5m/LAICA	H16-3.5-032
	2016-07-10	3.92[I]	3.16	11.15	27	15x180, 6x150, 6x120	CAHA 3.5m/LAICA	H16-3.5-032
143P	2016-01-16	5.03[I]	4.38	9.10	29	180	CAHA 3.5m/LAICA	F16-3.5-005
	2017-02-17	3.73[I]	3.03	11.91	53	180	INT/WFC	I/2017A/05
	2017-02-18	3.73[I]	3.04	12.11	40	180	INT/WFC	I/2017A/05
	2017-02-19	3.72[I]	3.05	12.30	22	21x180, 1x60	INT/WFC	I/2017A/05
	2017-02-21	3.72[I]	3.07	12.66	26	18x300, 8x200	INT/WFC	I/2017A/05
	2017-02-26	3.70[I]	3.11	13.49	34	300	Rozhen 2m/FoReRo	-
	2017-02-27	3.69[I]	3.12	13.65	16	300	Rozhen 2m/FoReRo	-
	2017-03-23	3.61[I]	3.37	15.98	15	300	Rozhen 2m/FoReRo	-
162P	2017-02-17	4.30[O]	3.58	9.88	93	120	INT/WFC	I/2017A/05
	2017-02-18	4.31[O]	3.57	9.71	52	120	INT/WFC	I/2017A/05

Table 7.1 continued

Comet	UT date	R_h [au][a]	Δ [au][b]	α [deg.][c]	Number	Exposure time [s]	Instrument	Proposal ID
	2017-02-21	4.31^O	3.55	9.18	79	43x120, 36x150	INT/WFC	I/2017A/05
	2017-02-26	4.33^O	3.51	8.24	21	300	Rozhen 2m/FoReRo	-

[a] Heliocentric distance. Superscripts I and O indicate whether the comet was inbound (pre-perihelion) or outbound (post-perihelion).

[b] Geocentric distance.

[c] Phase angle

7.2 displays the LS periodogram with a highest peak corresponding to a double-peaked lightcurve with period 9.07 h. I inspected the lightcurves corresponding to the other two prominent peaks in the LS periodogram, at 7.6 h and 11.1 hours, but they produced lightcurves with a significantly larger scatter. The lightcurve of 14P phased with the period $P = 9.07$ h is plotted in Fig. 7.3. There are data points covering all phases of the lightcurve, and they clearly show that the lightcurve of 14P has asymmetric peaks.

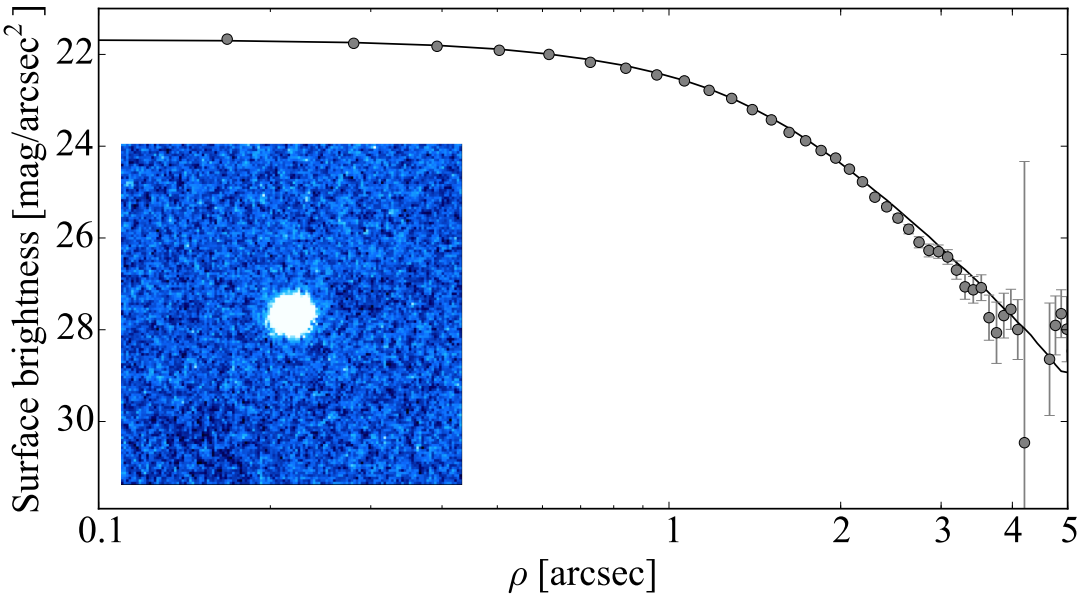

Figure 7.1: Surface brightness profile of comet 14P from 7 July 2016. The image in the lower left shows a 30 × 30 arcseconds composite image of 14P made of 12 × 300 s exposures. The frames were added using the method described in Section 3.5. The comet had a stellar-like profile and no apparent signatures of activity. The surface brightness of the comet is plotted against radius ρ from the comet centre. The agreement of the comet profile with the scaled stellar PSF (solid line), indicates that the comet was observed as a point source, and appeared as inactive during the observations.

To test the robustness of this period determination, I used the MC2 method to search for rotation periods between 3 and 30 h. For phase-function slopes in the range from 0.0 to 0.1 mag/deg, I determined that the range of possible solutions is 9.056 - 9.083 h. The top panel of Fig. 7.4 shows the distribution of all clones from the MC2 run. The derived period range appears to be largely independent of the chosen slope, although a slight trend for longer periods with increasing β can

be noticed. The colour scale in the plot indicates the goodness of the lightcurve for each clone and corresponds to the normalised string length. The bottom panel of Fig. 7.4 shows that the mean of the string length does not vary significantly. This confirms that I cannot unambiguously determine the phase-function slope from this data set, given the limited range in α of the observations in 2016. For β = 0.060 ± 0.005 mag/deg derived in Section 5.2, the range of possible periods is 9.060 - 9.079 h. I therefore conclude that in July 2016 the rotation rate of 14P was in the range 9.06 - 9.08 h.

It is possible to estimate the maximum difference between the sidereal ($P_{\rm sid}$) and synodic ($P_{\rm syn}$) rotational periods using the following expression from Pravec et al. (1996):

$$|P_{\rm sid} - P_{\rm syn}| \leq \omega_{\rm PAB} P_{\rm syn}^2, \tag{7.1}$$

where $\omega_{\rm PAB}$ is the angular velocity of the phase angle bisector (PAB, for a definition, see Harris et al., 1984). Generally, it can be concluded that for the typically large heliocentric distances necessary for the observations of bare comet nuclei, the PAB changes very slowly. For the duration of the observing run in July 2016, I estimated that the difference between the sidereal and the synodic period of comet 14P was less than 0.0001 hours, which is considerably smaller than the uncertainty of the current period determination.

The lightcurve period derived from the current data set is very close to the period P = 9.02 ± 0.01 h from Section 5.2. If the difference between the two period determinations is taken directly, then it would imply a period change of between 1.8 and 4.2 minutes per orbit. However, before this conclusion is made, it is important to point out that the uncertainty of the two periods was derived from the MC method used in Chapter 5 and the MC2 method in this work. While these procedures aim to quantify the uncertainty of the derived periods by taking into account the photometric and calibration uncertainties as well as the phase-function correction, they might not account for all possible solutions. Each of the iterations

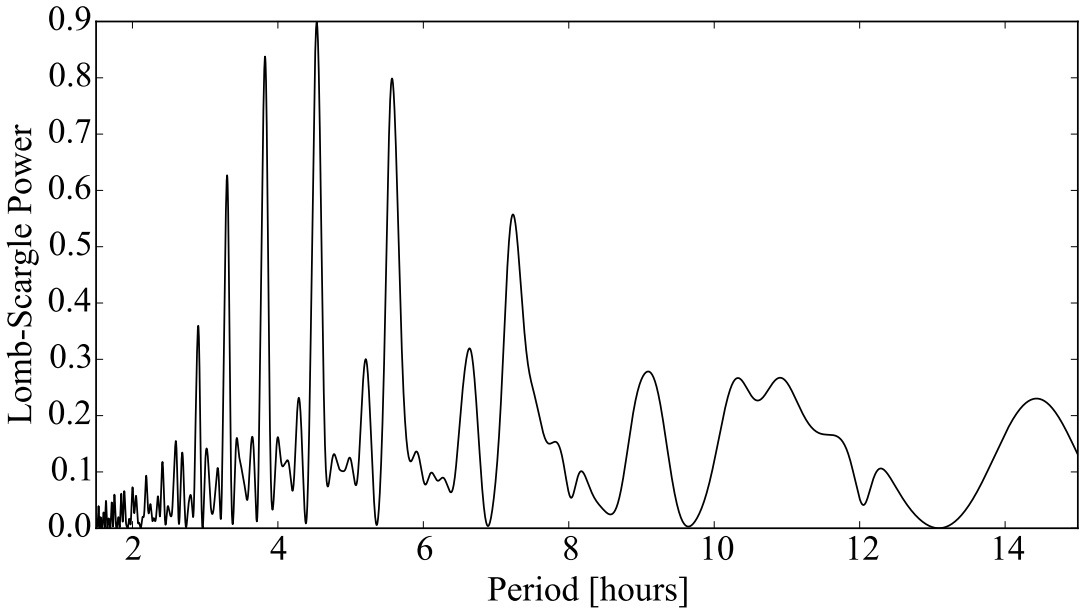

Figure 7.2: LS periodogram for 14P from the dataset collected in July 2016. The plot shows the LS power versus period. The highest peak occurs at 4.54 which corresponds to a double-peaked lightcurve with period $P = 9.07$ h.

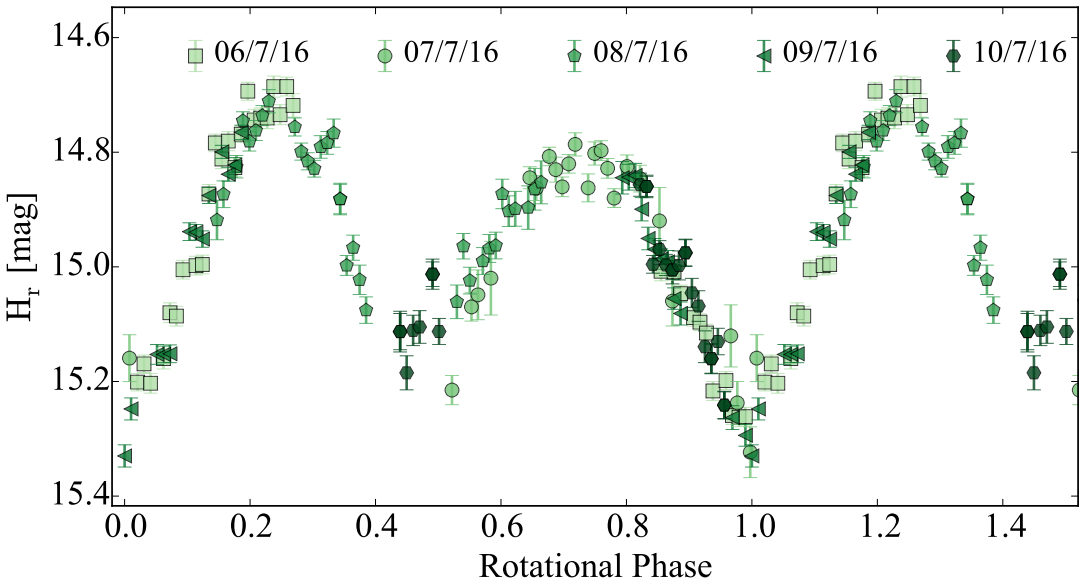

Figure 7.3: Rotational lightcurve of 14P with the data from 2016. The lightcurve is folded with the LS best period of 9.07 h h. The error bars indicate the combined 1-σ uncertainty of the differential photometry and the absolute photometric calibration.

in the Monte Carlo methods determines only the most likely period from the LS periodogram, and does not consider other less-likely but possible periods. This means that the two datasets need to be examined together in order to confirm

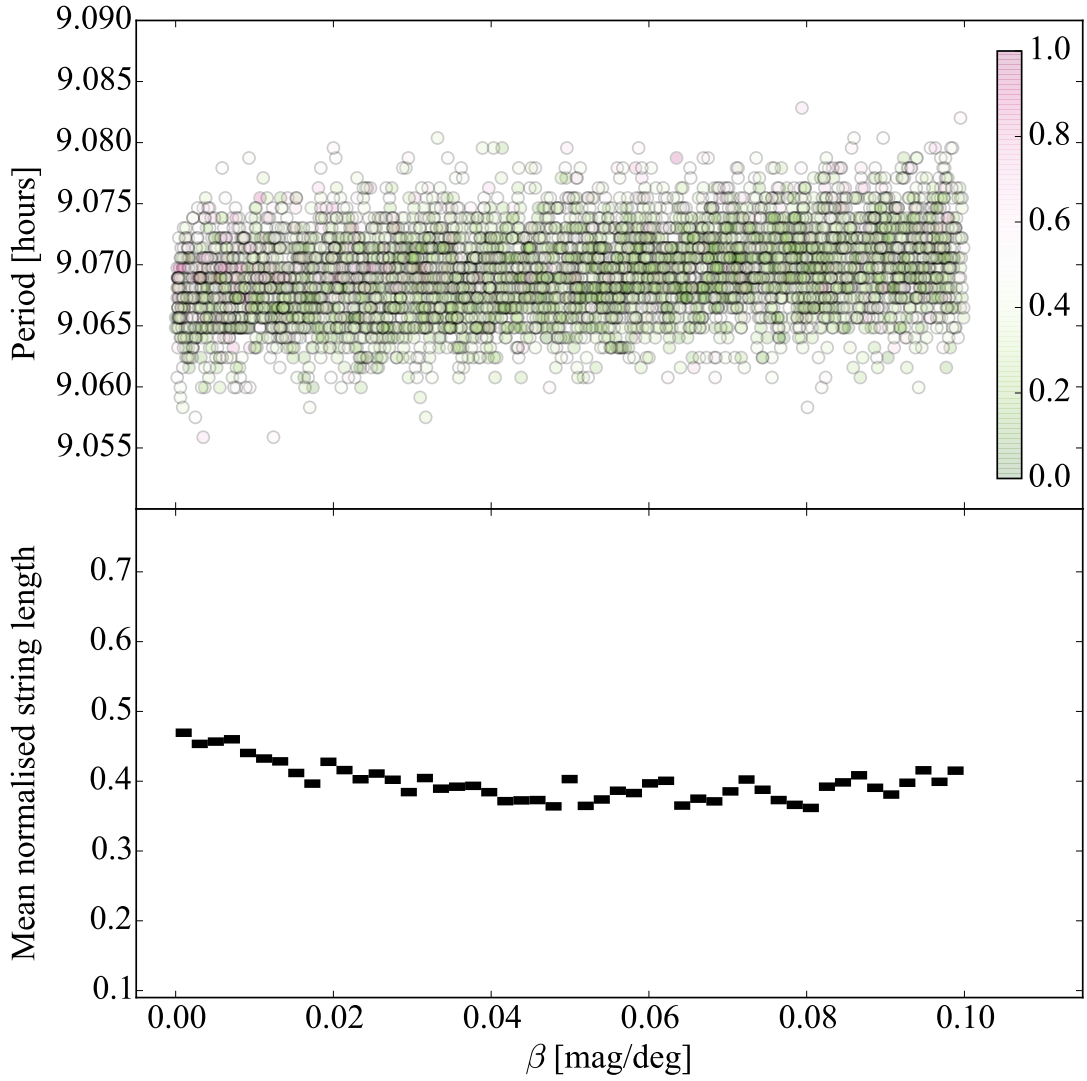

Figure 7.4: Results from the MC2 method used to determine the range of possible rotation periods of 14P using the 2016 data. The MC2 method looked for periods between 3 and 30 h using phase-function slopes in the range 0.0 - 0.1 mag/deg. The top panel contains the distribution of the rotation periods derived for each clone. The colour of the points corresponds to the normalised range of total lightcurve string length computed for each clone. The bottom panel shows the mean of the normalised string length for β bins of 0.001 mag/deg width.

the period change.

I therefore attempted to find a common period which would satisfy the data from all three epochs. I looked for possible common rotation periods by combining the old datasets from 2004 and 2007 with the new data from 2016. To correct the data, I used the slope $\beta = 0.060$ mag/deg (Fig. 7.5). The resulting LS periodogram in Fig. 7.6 has a maximum at around 9.07 hours, but a careful

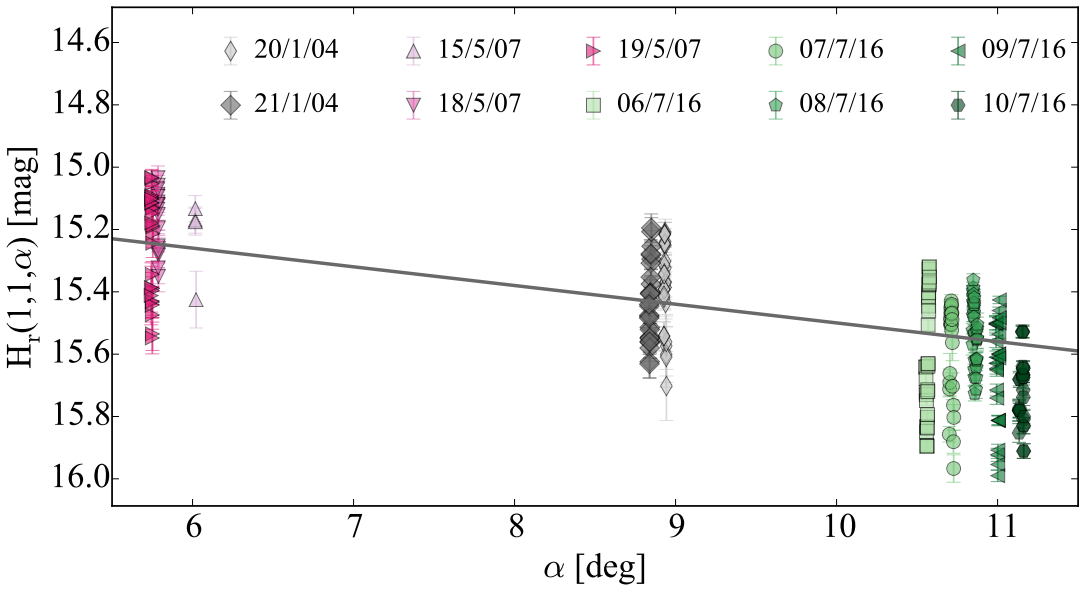

Figure 7.5: Phase function of comet 14P with the datasets taken in 2004, 2007 and 2016. The calibrated absolute magnitudes of the comet are plotted against phase angle α. Over-plotted is a linear phase function model with $\beta = 0.060$ mag/deg.

inspection shows the presence of many aliases due to the large timespan between the observations.

On Fig. 7.7, I have plotted lightcurves with two of the many possible periods suggested by the LS periodogram. These lightcurves showcase that it is possible to find common periods for the lightcurves from the two epochs. I can therefore conclude that given the current set of observations I cannot detect period changes between the two apparitions. However, the currently available data do not rule out that the period changed between the observations, and I therefore consider the maximum change derived above as an upper limit, i.e. $\Delta P < 4.2$ min, but the default conclusion given the existence of a common period to all data should be that the period did not change.

It is important to note that the match between the separate lightcurves is not perfect. There are differences in the maximum peaks and the depth of the minima between the data from 2004 and 2016 (Fig. 7.7). I interpret these differences as a result of change in the viewing geometry – a different observer latitude, based on the relative orientation of the comet rotation pole and the line of sight to Earth,

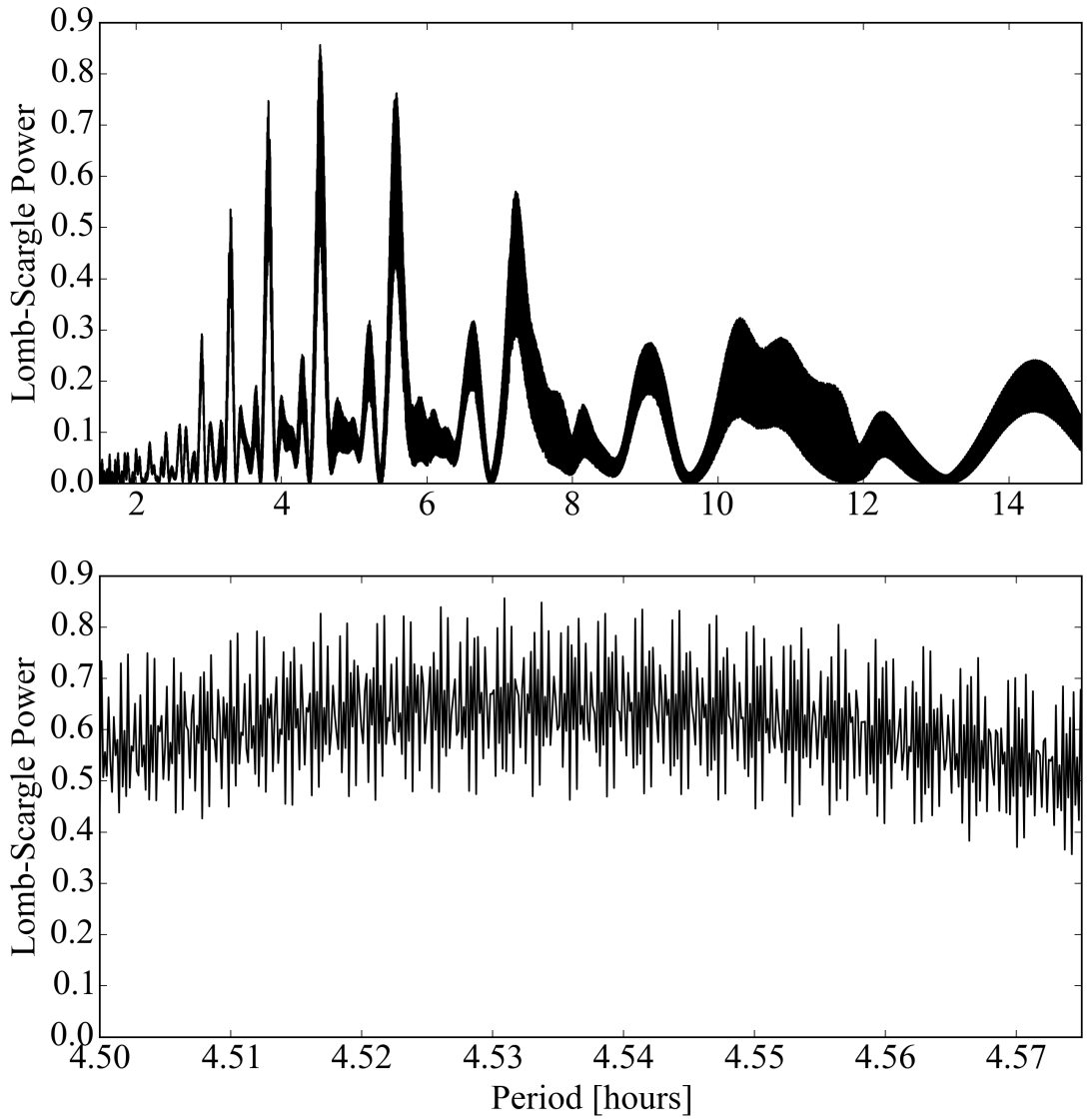

Figure 7.6: LS periodogram of the combined dataset for 14P collected in 2004, 2007 and 2016 and corrected using a phase-function slope $\beta = 0.060$ mag/deg. The highest peak corresponds to a period of 9.06748 h, but due to the large timespan between the observing epochs and the resulting aliasing, the periodogram is densely packed with other close-by maxima. The bottom panel shows an enlarged view of the highest peak.

implying a different lightcurve amplitude – rather than as evidence for a period change. This is a reasonable assumption since the solar elongation in the three epochs varied significantly, between $\sim$170° in January 2004, $\sim$ 240° in May 2007 and $\sim$ 260° in July 2016.

I applied the MC2 procedure to the combined data set for a phase function range of 0.0 - 0.1 mag/deg, and looked for periods in the range 8 - 10 h. The

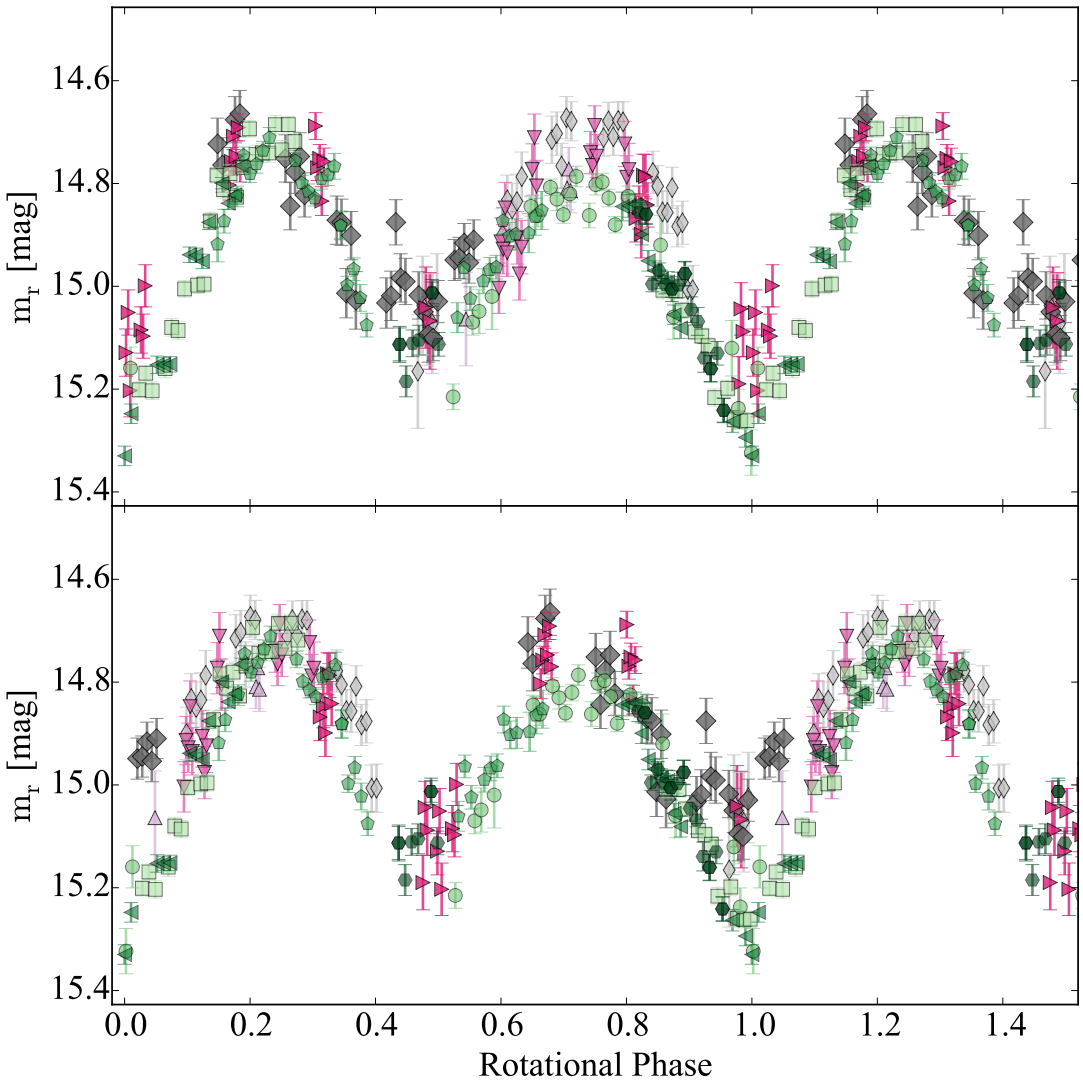

Figure 7.7: Rotational lightcurve of comet 14P with the combined dataset from 2004, 2007, 2016. The symbols correspond to these used in Fig. 7.5. The data were corrected for a phase-function slope $\beta = 0.06$ mag/deg and the lightcurves are phased with two of the possible periods according to the LS periodogram: $P_1 = 9.07313$ h (top) and $P_2 = 9.07878$ h (bottom). The good alignment of the points from the two apparitions indicates that it is possible to find rotation periods which satisfy the observations from all three epochs. In both example lightcurves the points from 2004 deviate from the 2016 data. I interpret the difference in the peak-to-peak amplitudes as a result of changes in the viewing geometry between the two epochs.

distribution of possible periods from Fig. 7.8 indicates that the total range of possible common periods for the combined data set from the two apparitions is 9.04 - 9.09 h.

According to the results from the MC2 method in Fig. 7.8, the periods with

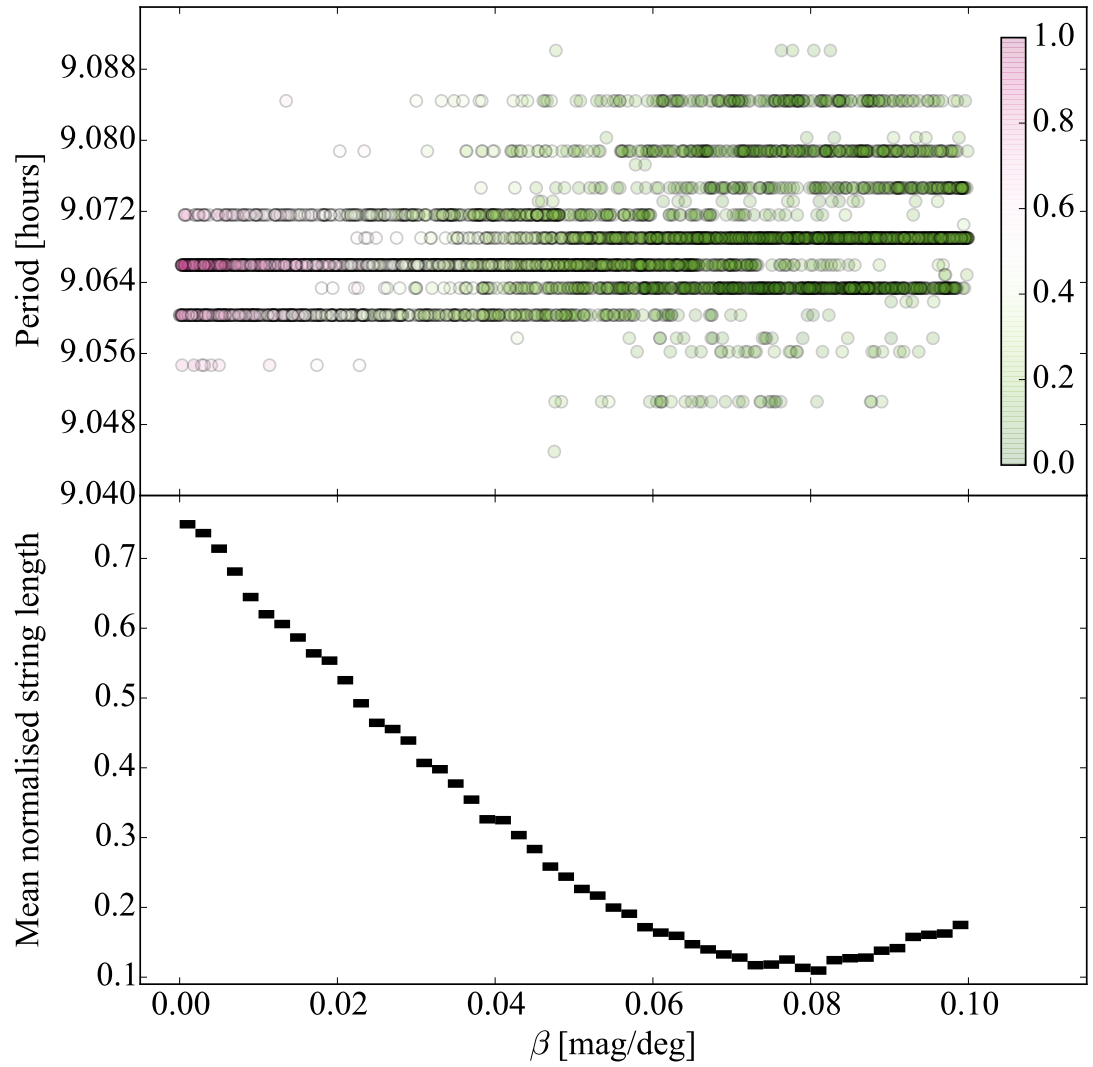

Figure 7.8: Same as Fig. 7.4 for the 14P data from the combined datasets taken in 2004, 2007 and 2016 data. I assigned a range of possible phase-function slopes of 0.00 - 0.10 mag/deg and looked for periods in the range 8 - 10 h. This diagram shows that it is possible to find common periods for all datasets in the range 9.04 - 9.09 h. The MC2 method indicates a preference for lightcurves with phase-function slopes between 0.07 and 0.08 mag/deg.

shortest string lengths are found around 9.062 h and with phase-function slopes between 0.07 and 0.08 mag/deg. This would imply that the phase-function slope of 14P is steeper than the previously determined value of $\beta = 0.060 \pm 0.005$ from Section 5.2. Looking at fig. 7.5, it can be seen that the 2016 data are taken at larger phase angle and are, on average, below the previously identified trend, which explains the steeper slope found when including these data. The best slope from the MC2 method is derived under the assumptions that the spin rate of the

comet has remained constant and that the different viewing geometry does not have a large effect on the observed lightcurve. Since both of these assumptions might be false, I consider the value of $\beta = 0.060 \pm 0.005$ mag/deg to be a better estimate of the phase-function slope since it was derived from observations taken during the same orbit around the Sun.

7.3 143P/Kowal-Mrkos

The rotation rate of comet 143P was first determined from observations in 2001 by Jewitt et al. (2003). They derived a period $P = 17.21 \pm 0.10$ h and a phase-function slope $\beta = 0.043 \pm 0.014$ mag/deg. Since then the comet has passed perihelion once, in June 2009, which motivated us to search for possible spin-rate changes that may have resulted from the comet's activity.

I attempted to observe the rotational lightcurve of 143P twice while the comet was inbound. In January 2016 I observed 143P with LAICA on the 3.5-meter telescope at Calar Alto. In February and March 2017 I used INT and the Rozhen 2-meter telescope. The comet did not show signs of activity during the observations (Figs. 7.9 and 7.10). Therefore, due to the lack of outgassing, its rotation rate most likely remained unchanged between 2016 and 2017, and I proceeded to combine the two epochs in order to derive the current rotation rate of 143P.

As a first step I corrected the new data with the phase-function slope $\beta = 0.043 \pm 0.014$ mag/deg from Jewitt et al. (2003). I then inspected the LS periodogram of the combined dataset (Fig. 7.11). The periodogram indicated a maximum corresponding to a period of ~ 17.197 h but suffered from aliasing due to the time gaps in the observations.

In order to derive a common period for the data from 2016 and 2017, I used the MC2 method for phase-function slopes in the range 0.0-0.1 mag/deg and searched for periods between 3 and 30 h. The results of the MC2 test can be seen in Fig. 7.12. The possible solutions for the full phase-function slope range between 17.145

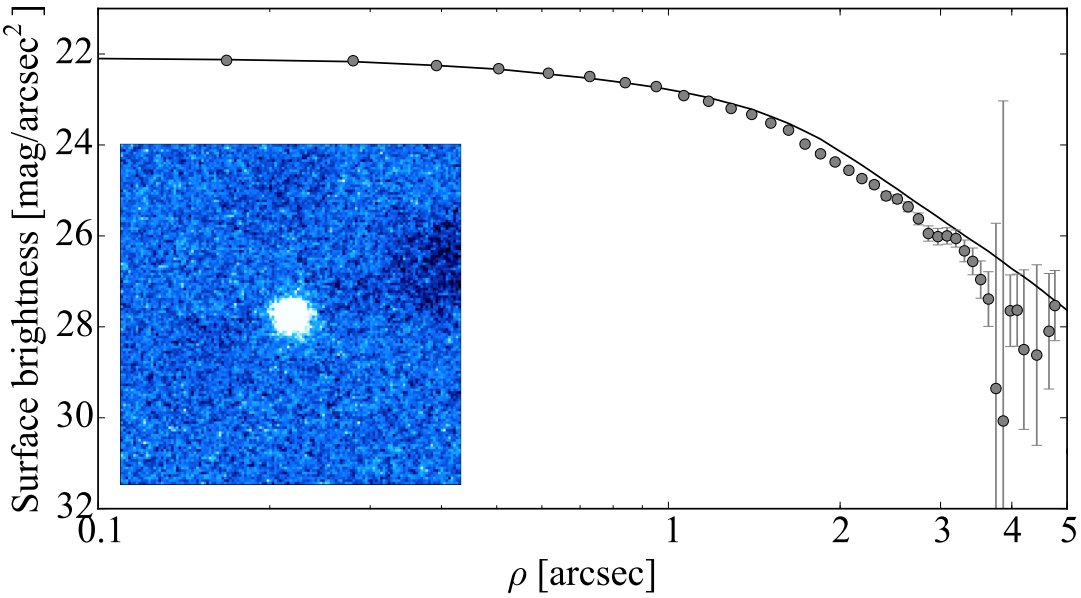

Figure 7.9: Same as Fig. 7.1, for the observations of 143P from 16 January 2016. The composite image in the lower left corner was made up of 15 × 180 s exposures. The stellar appearance in the composite image and the agreement of the surface brightness profile of the comet with the stellar PSF suggest that the comet was inactive during the observations in 2016.

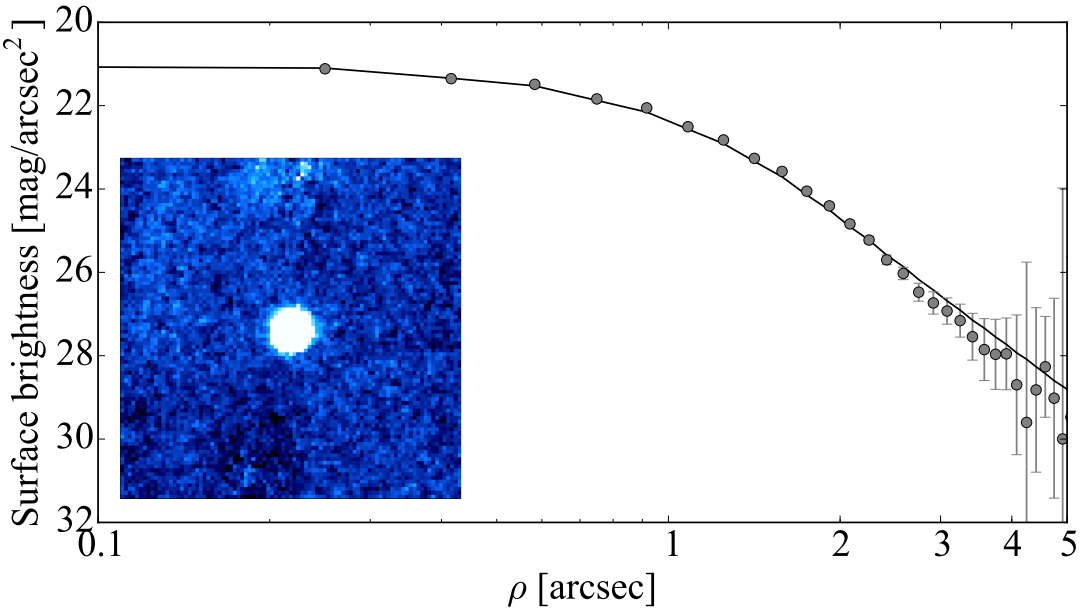

Figure 7.10: Same as Fig. 7.1, for the observations of 143P from 18 February 2017. The composite image in the lower left corner was made up of 14 × 180 s exposures.

and 17.22 h. As the lower panel in Fig. 7.12 shows, the best lightcurves are found around slope $\beta = 0.05$ mag/deg. A careful inspection of the results suggests

that the clones with phase-function slopes $\beta < 0.03$ mag/deg, $\beta > 0.07$ mag/deg and $P < 17.18$ h produce lightcurves with a large scatter. Therefore, I conclude that the rotation rate of comet 143P is between 17.18 and 17.22 hours, at one of the following distinct periods: 17.1966 ± 0.0003 hours, 17.2121 ± 0.0002 h and 17.1812 ± 0.0002 h. In Fig. 7.13 I have plotted the best lightcurve according to the MC2 test. The observations cover the whole lightcurve phase and provide very good coverage of both minima.

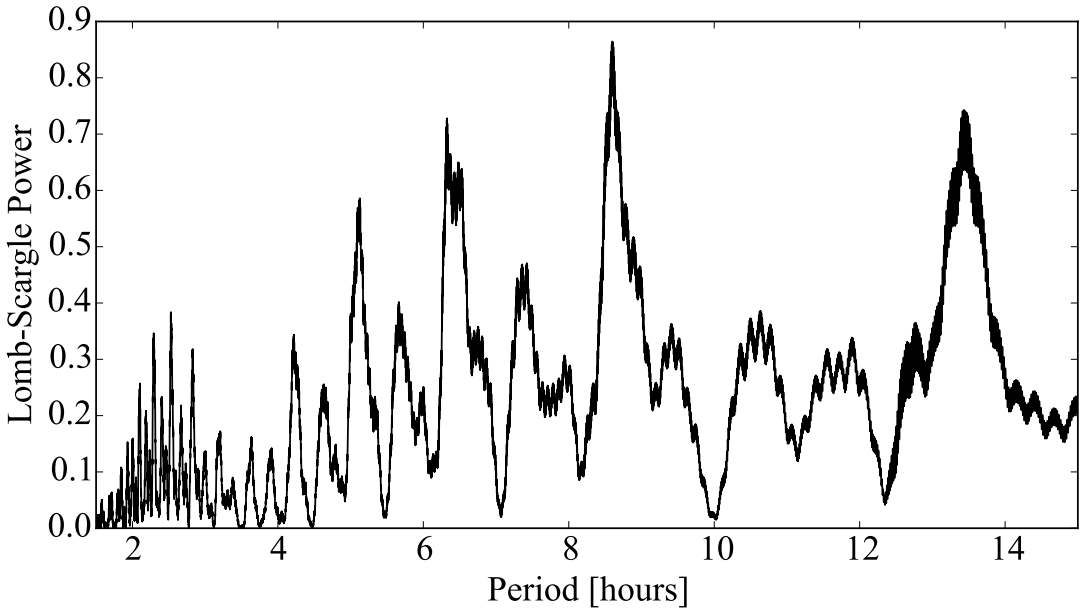

Figure 7.11: LS periodogram for 143P from the dataset collected in 2016 and 2017, and corrected for a phase-function slope $\beta = 0.043$ mag/deg. The plot shows the LS power versus period. The highest peak corresponds to a double-peaked lightcurve with period $P = 17.197$ h.

The possible period range of 17.18 - 17.22 h which I constrained for the current apparition also includes the period $P = 17.21 \pm 0.10$ h from the 2001 data (Jewitt et al., 2003). This implies that no period change was detected between the two epochs, with an upper limit of 6.6 minutes per orbit, largely due to the uncertainty quoted on the 2001 period.

To test this conclusion, I used the data points from Jewitt et al. (2003) in order to check whether the lightcurves from the two epochs are consistent, as well as to set an upper limit on a possible period change which might have remained

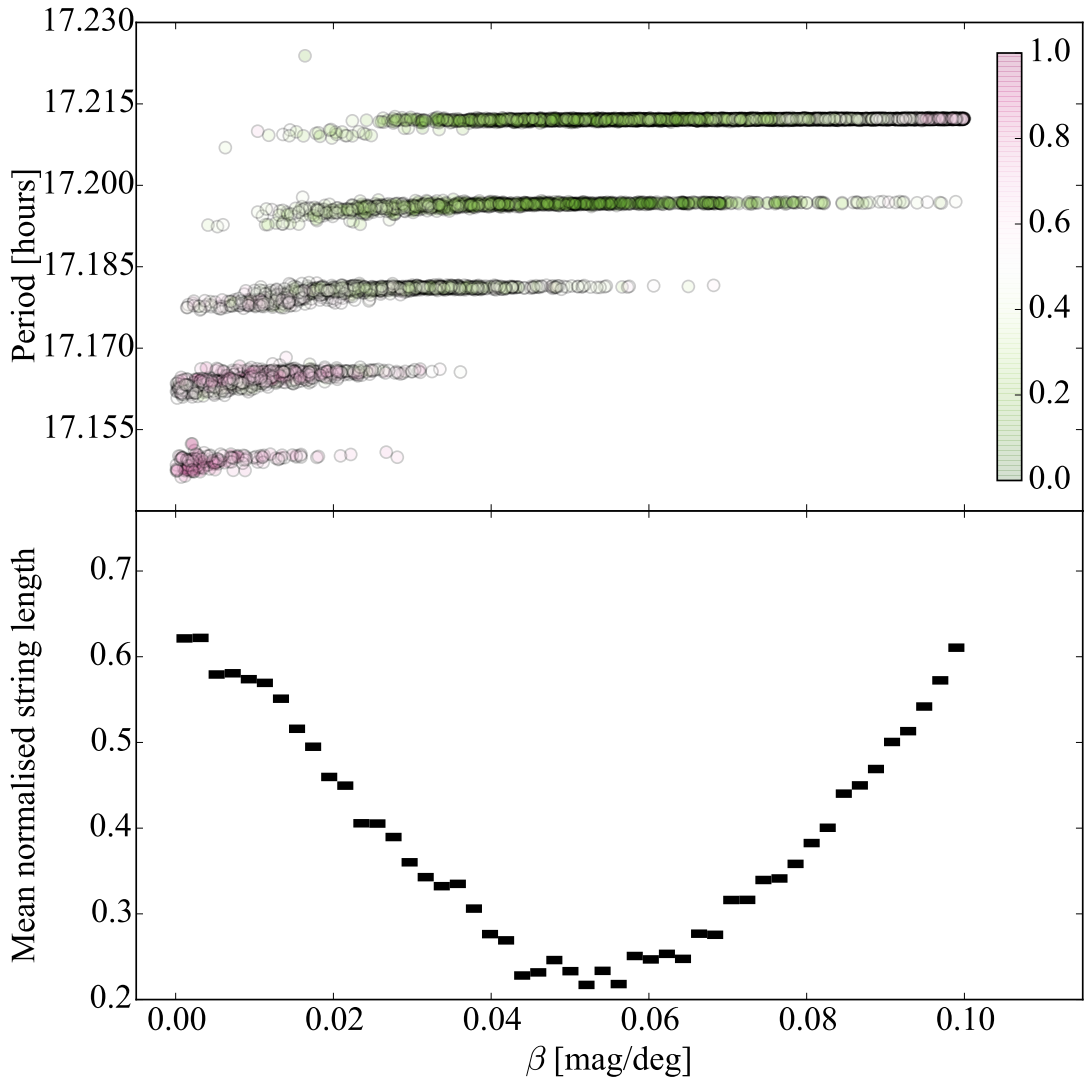

Figure 7.12: Results from the MC2 method applied to the 143P data from the combined datasets taken in 2016 and 2017. The MC2 method was run for a range of possible phase-function slopes β = 0.00 - 0.10 mag/deg and periods from 3 to 30 h.

undetected. I converted the magnitudes from Jewitt et al. (2003) to the PS1 r_{P1}-band using the nucleus colour B–V = 0.82 ± 0.02 mag from Jewitt et al. (2003) and the colour conversion terms from Tonry et al. (2012). All absolute magnitudes are plotted versus phase angle in Fig. 7.14. The data from Jewitt et al. (2003) show a very good agreement with the new points from this work, and the old phase function β = 0.043 ± 0.014 mag/deg aligns well with the extended dataset.

I next applied the MC2 method to look for common rotation periods of the combined data from 2001, 2016 and 2017. I limited the MC2 test to β between

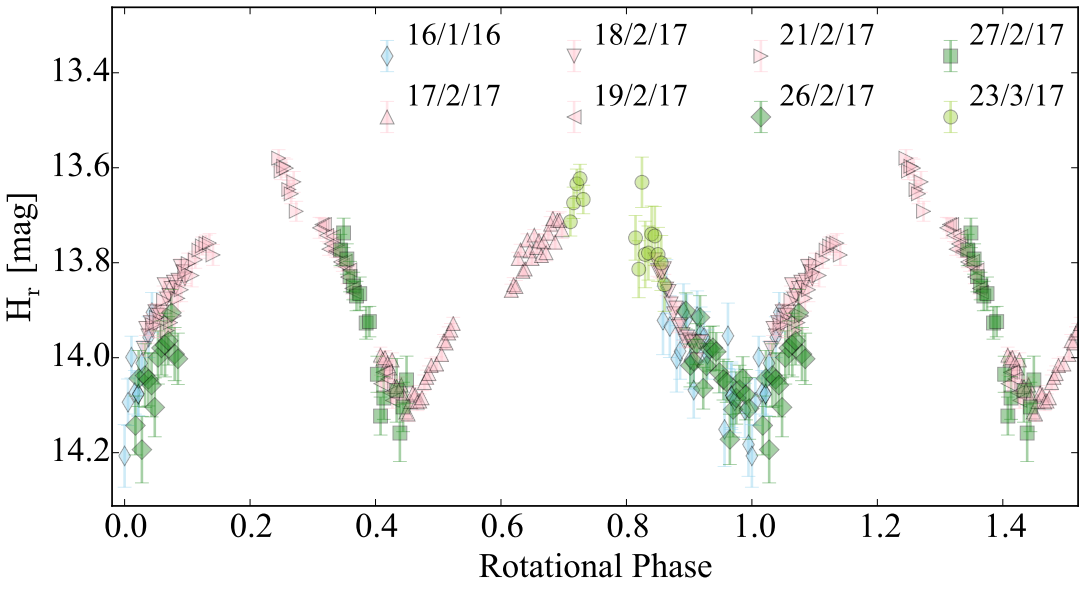

Figure 7.13: Rotational lightcurve of comet 143P from the data taken in 2016 and 2017. The magnitudes from 17-21 February and from 26-27 February were derived using the same same set of comparison stars and are therefore plotted in the same colours. This lightcurve was corrected for a phase-function slope $\beta = 0.051$ mag/deg and was phased with a period $P = 17.1966$ h. It corresponds to the best lightcurve from the MC2 test.

0.03 and 0.07 mag/deg and periods between 17.18 and 17.22 hours, derived for the new dataset above. The MC2 test in Fig. 7.15 identified that the possible common periods lie in the range 17.1945-17.200 h.

On Fig. 7.16 I have plotted the common lightcurve with the best phase-function slope and period identified by the MC2 test. This lightcurve illustrates well the remarkable match between the datasets from the two apparitions. While there might be a shift in magnitude between the two datasets due to the different absolute calibration methods used by Jewitt et al. (2003) and here, letting the phase-function slope vary removed those effects and produced a well-aligned common lightcurve. The phase-function slope derived here depends on the assumptions that 1) the absolute calibration from Jewitt et al. (2003) is very precise; 2) changes in the observing geometry (pole position) are negligible; 3) the rotation period of the comet did not change between the two epochs allowing me to derive a common lightcurve. With all of these caveats in mind, I consider the slope $\beta = 0.043 \pm$

0.014 mag/deg from Jewitt et al. (2003) to be a more reliable estimate, since it uses a broad range of phase angles and was derived from consistently calibrated magnitudes measured during the same apparition.

The radius $R_{\rm n} = 4.79^{+0.32}_{-0.33}$ km of comet 143P was determined from thermal infrared measurements in 2007 (Fernández et al., 2013). I use this size together with the absolute magnitude from the lightcurve observations to determine the albedo of the comet.

Jewitt et al. (2003) determined an absolute magnitude $H_{\rm R}(1,1,0) = 13.49 \pm 0.20$ mag and (B-V) = 0.82 ± 0.02 mag, which can be converted to $H_{\rm rp1}(1,1,0) = 13.70 \pm 0.20$ mag using the equations from Tonry et al. (2012). From this magnitude I calculate a geometric albedo $A_{\rm r} = 0.055 \pm 0.013$ using equation 3.10.

This value of the geometric albedo agrees with the conservative albedo estimate which I can derive from our observations from 2016 and 2017. For the broad range of possible β from the MC2 test in Fig. 7.12, 0.03–0.07 mag/deg, I determine an absolute magnitude $H_{\rm rp1}(1,1,0) = 13.86 \pm 0.12$. For the radius from Fernández et al. (2013), this converts to $A_{\rm r} = 0.048 \pm 0.009$. Since the new dataset was calibrated with the method for precise absolute calibration with the Pan-STARRS catalogue, and is therefore directly comparable to the other comets whose albedos were derived in Chapter 5, I adopt this value below in Chapter 9.

It is important to note that the optical observations from 2001, 2016 and 2017 were not taken simultaneously to the infrared data used to determine the size (Fernández et al., 2013). However, the low activity of 143P (e.g. Jewitt et al., 2003) suggests that the nucleus does not undergo significant mass loss and its radius has most likely remained unchanged. Additionally, the very good match between the lightcurves from 2001 and 2016-2017 suggest that the changing viewing geometry does not significantly change the estimated absolute optical magnitude of the comet. Therefore, the derived albedo is considered to be a good estimate.

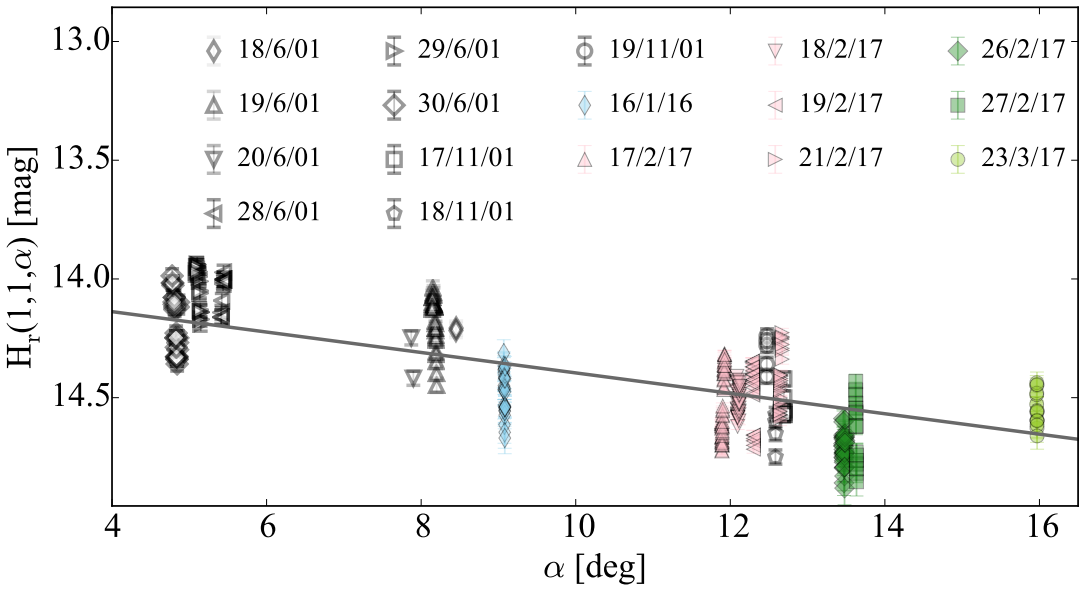

Figure 7.14: Phase function of comet 143P from the datasets taken in 2001 (Jewitt et al., 2003), 2016 and 2017. The calibrated absolute magnitudes of the comet are plotted against phase angle α. The points from 17-21 February 2018 and those from 26-27 February are plotted in the same colours since they were calibrated using the same comparison stars. The absolute magnitudes for 2001 are taken from Table 2 in Jewitt et al. (2003), and were converted to PS1 r_{P1}-band. Over-plotted is a linear phase function with slope $\beta = 0.043$ mag/deg from Jewitt et al. (2003).

7.4 162P/Siding Spring

The lightcurve of comet 162P was previously studied from two datasets taken in 2007 and 2012, during two consecutive aphelion passages (Section 5.10). The data from 2012 were collected between April and June 2012 and covered a sufficient phase angle range to allow a phase function determination with $\beta = 0.039 \pm 0.02$ mag/deg (Section 5.10). The two datasets did not show any evidence for a period change during the perihelion passage between 2007 and 2012, although this could be due to the relatively poor sampling of the lightcurve from 2007. The best period derived for 2012 was 32.852 hours, and for the combined data set, the MC method used in Section 5.10 resulted in a common period of 32.853 ± 0.002 h.

In February 2017 comet 162P was observed during three nights with WFC on INT and one night with FoReRo on the Rozhen 2-meter telescope. These observations were done before aphelion, almost a full orbit after the previous

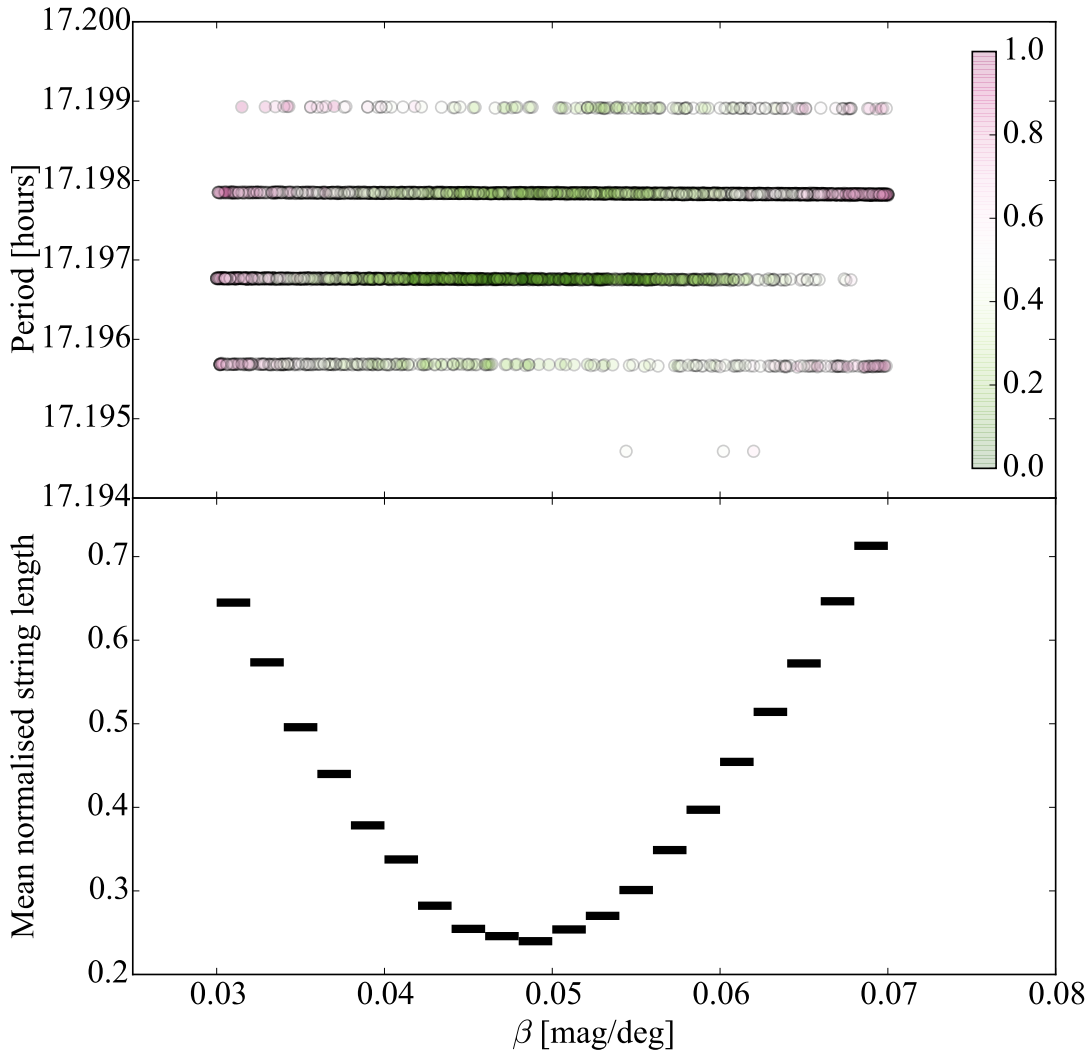

Figure 7.15: Results from the MC2 method applied to the 143P data from the combined datasets taken in 2001 (Jewitt et al., 2003), 2016 and 2017. The MC2 method was run for a range of possible phase-function slopes β = 0.03 - 0.07 mag/deg and periods from 17.18 to 17.22 h.

dataset was taken in 2012. Careful analysis of the data from each run determined that the comet was inactive during the observing period (Fig 7.17).

The data covered a phase-angle range of approximately 2 degrees, which was insufficient for an independent derivation of the phase function. Therefore, I used the slope $\beta = 0.039 \pm 0.02$ mag/deg from Section 5.10 to correct the data.

The LS periodogram in Fig. 7.18 has a maximum corresponding to a double-peaked lightcurve with P = 32.92 h. The corresponding lightcurve is plotted in Fig. 7.19. Due to the long rotation period of the comet, the observations from the

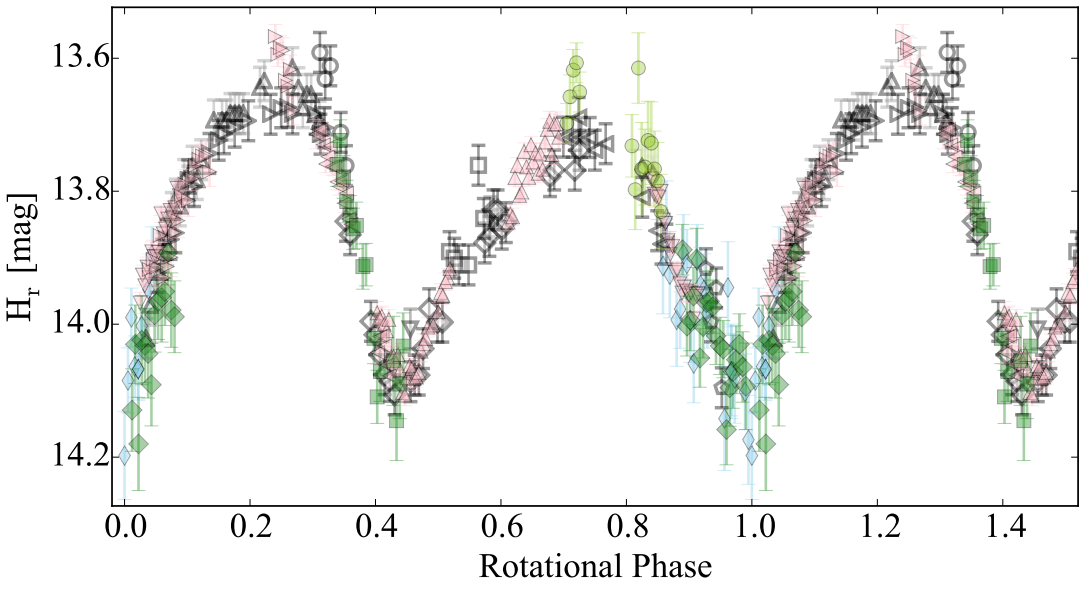

Figure 7.16: Rotational lightcurve of 143P with the datasets from 2001, 2016 and 2017. The symbols correspond to the ones in Fig. 7.14. The data were corrected with a phase-function slope $\beta = 0.052$ mag/deg and folded with a period $P = 17.19676$ h. Those values were selected from the best lightcurves in the output of the MC2 method.

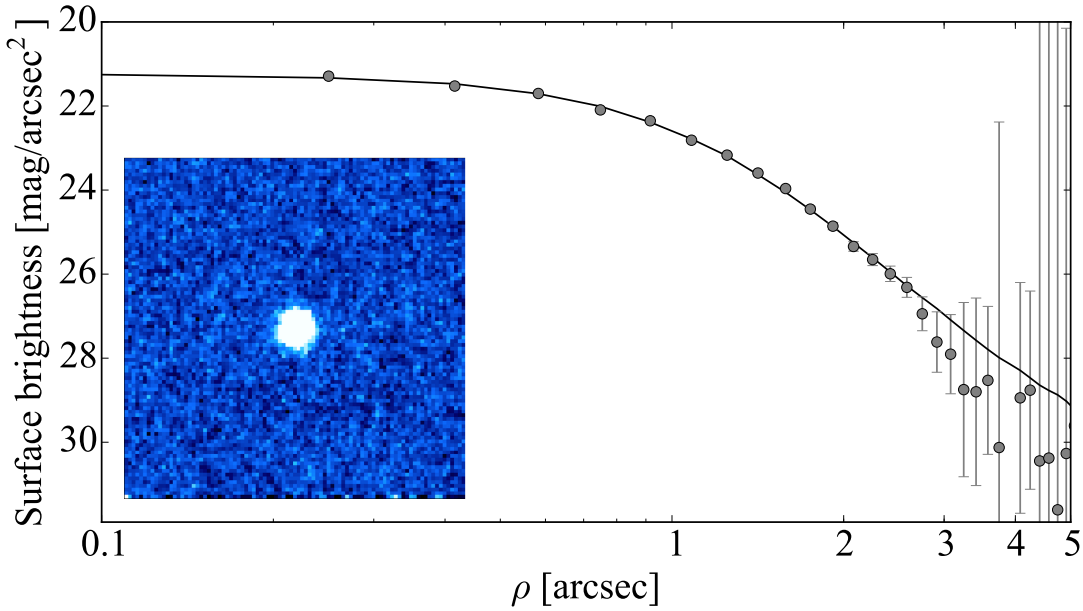

Figure 7.17: Same as Fig. 7.1, for the observations of 162P from 18 February 2017. The composite image in the lower left corner was made up of 9 × 120 s exposures.

INT only covered one of the lightcurve minima. However, due to the very dense sampling of the data close to the pronounced V-shaped minimum, a relatively narrow range of periods results in a good alignment between the points from the

different nights during the INT run.

In order to determine the uncertainty of the period, I used the MC2 method for a broad range of phase-function slopes (0.0 - 0.1 mag/deg), and looked for periods in the range 3-60 h. The results in Fig. 7.20 confirmed that the exact rotation period is dependent on the adopted phase function, and that the probed phase-angle range is too narrow and does not permit an unambiguous determination of the phase function. The possible rotation periods for the whole β-range lie between 32.72 and 33.09 h. If I take the possible periods for $\beta = 0.039 \pm 0.02$ mag/deg, then the current rotation rate of comet 162P is in the range 32.83 - 33.00 h.

The range of possible rotation periods derived for the dataset taken in 2017 also includes the rotation period $P = 32.853$ hours, which was previously derived as the best period for the combined dataset from 2007 and 2012 (Section 5.10). This implies that the current dataset does not allow a period-change detection between the three apparitions. It was possible, however, to combine all datasets from all three apparitions and to use the MC2 method to search for a common period.

In Fig. 7.21 I have plotted the phase function of the combined dataset from all three epochs. A linear fit to all points results in a phase-function slope $\beta = 0.035$ mag/deg. The phase-function slope $\beta = 0.039$ mag/deg from Section 5.10 also produces a good fit to the data. The phase function is well-sampled at phase angles between 7 and 12 degrees, but the only observations outside of this range are from a short dataset at $\alpha \sim 4.7$ degrees from April 2012. Due to the long period of the comet and the large brightness variation, even this extended dataset does not allow an unambiguous direct determination of the phase function.

Since I was unable to determine the exact value of the phase-function slope from a direct fit, I ran the MC2 method for the full range of possible phase functions - between 0.0 and 0.1 mag/deg. I looked for possible periods in the range 32.7 - 33.1 hours, which was determined above.

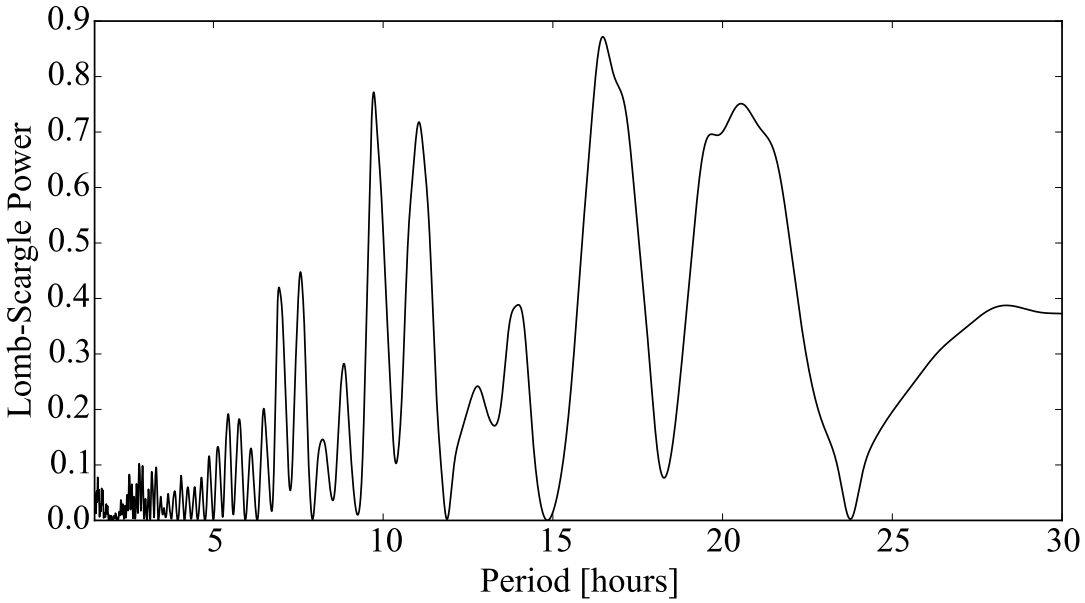

Figure 7.18: LS periodogram for 162P from the dataset collected in 2017 and corrected with a phase-function slope $\beta = 0.039 \pm 0.02$ mag/deg. The plot shows the LS power versus period. The highest peak corresponds to a double-peaked lightcurve with period $P = 32.92$ h.

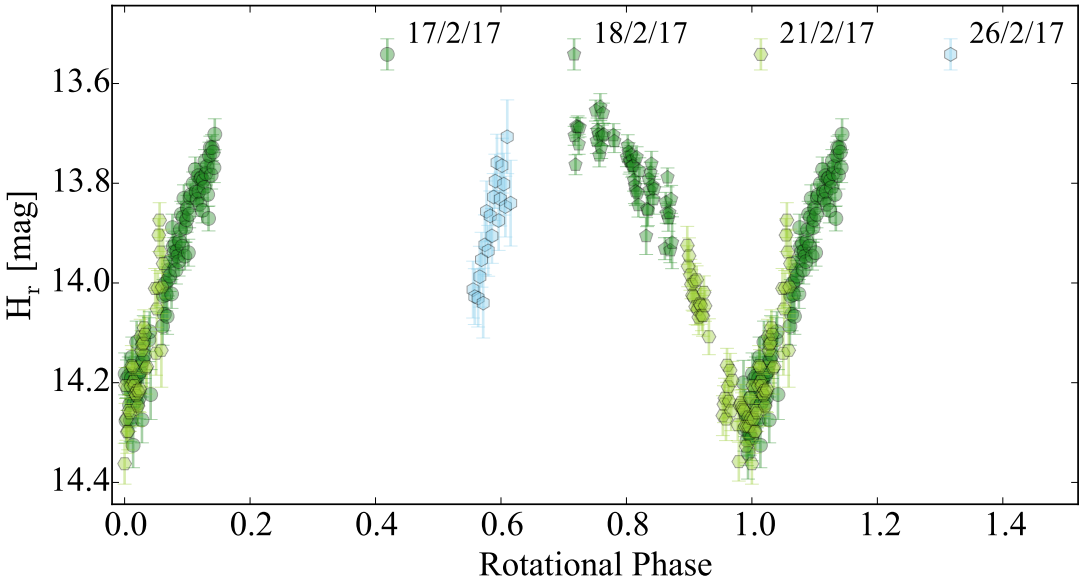

Figure 7.19: Rotational lightcurve of comet 162P from the data taken in February 2017, corrected for a phase-function slope $\beta = 0.039$ mag/deg. The lightcurve is phased with $P = 32.92$ h. The magnitudes from 17 and 18 February 2017 were calibrated using the same set of comparison stars, and are therefore plotted in the same colour.

Fig. 7.22 displays the results of the MC2 test. The best lightcurves were found for phase-function slopes of approximately 0.05 mag/deg and rotation rates of

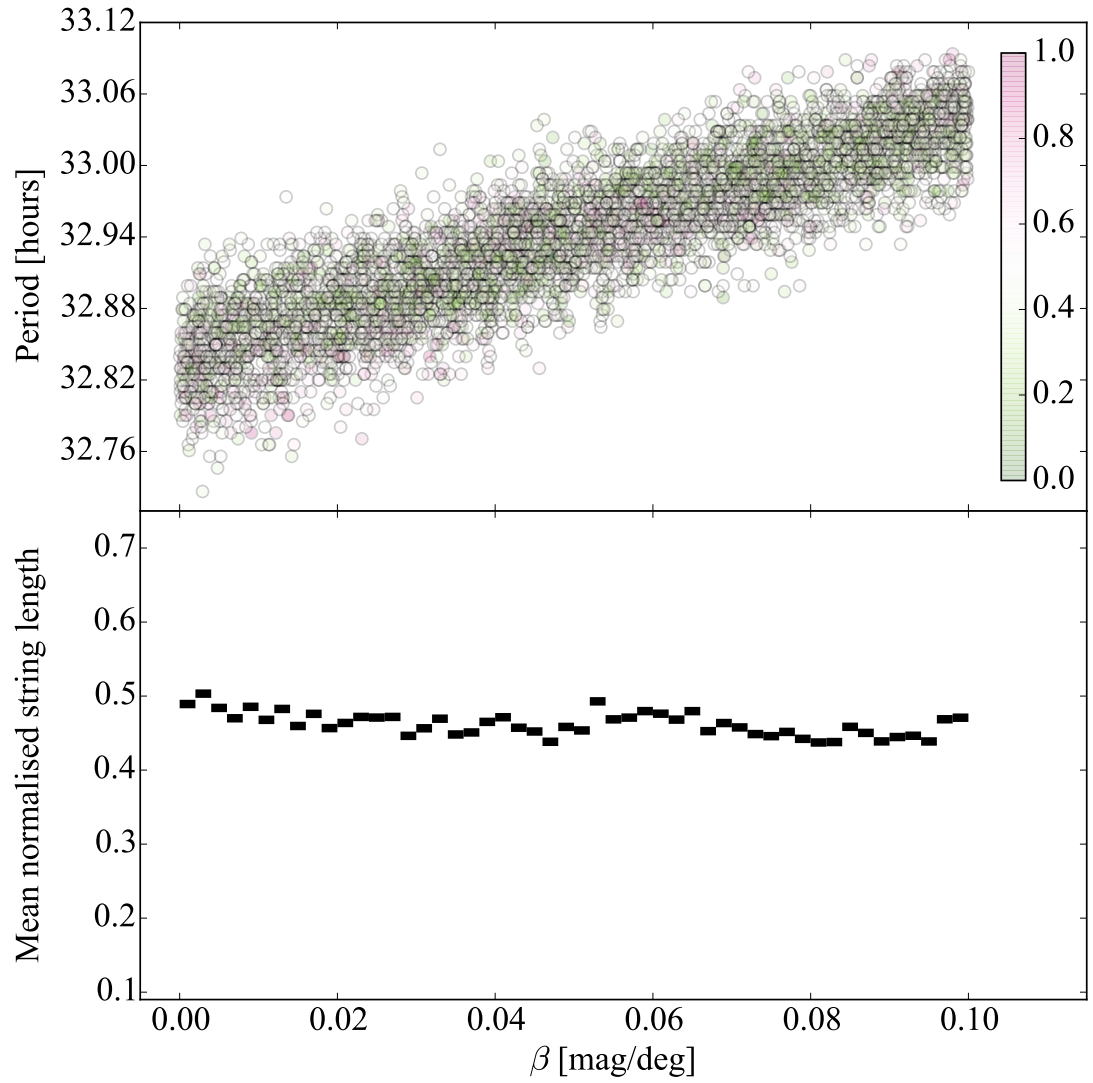

Figure 7.20: Same as Fig. 7.4 for the 162P data taken in 2017. The MC2 method was run for phase-function slopes in the range 0.00 - 0.10 mag/deg and periods from 3 to 60 h.

32.877 h. To illustrate the results, I have plotted the lightcurve of 162P from one of the combinations of β and period which produced the best lightcurves in the MC2 test (Fig. 7.23). This lightcurve is representative for the best solutions from the MC2 test and illustrates the very good alignment between the individual datasets.

I visually inspected the lightcurves of the clones with periods 32.73, 33.0–33.1 and 32.91–32.93 h and confirmed that they show poor agreement with the data. I therefore conclude that the range of possible common periods for the datasets

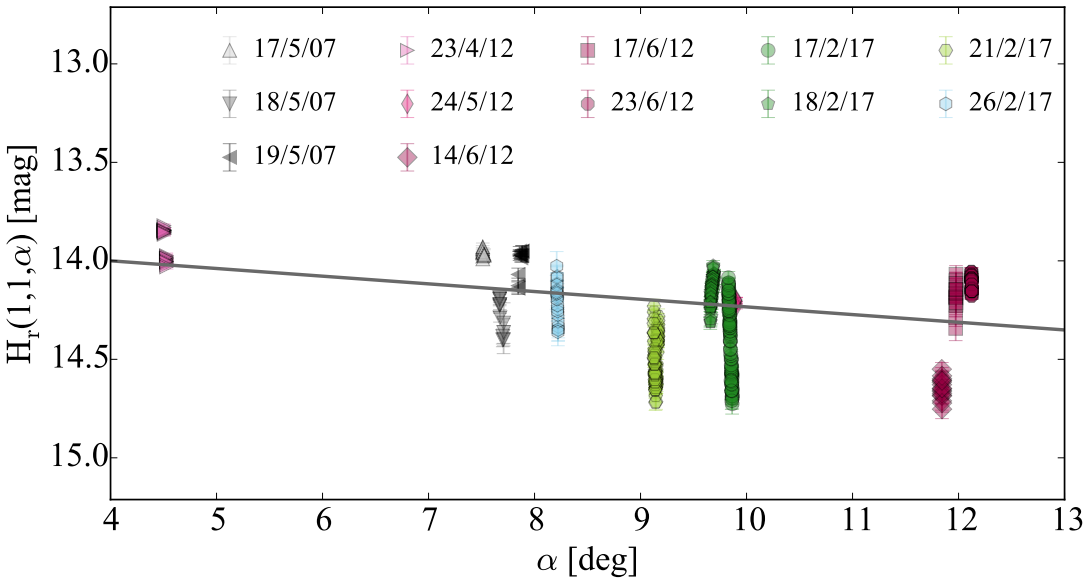

Figure 7.21: Phase function of comet 162P from the datasets taken in 2007, 2012 and 2017. The calibrated absolute magnitudes of the comet are plotted against phase angle α. The magnitudes from 17 and 18 February 2017 were calibrated using the same set of comparison stars, and are therefore plotted in the same colour. Over-plotted is a linear phase function model with 0.039 mag/deg.

from 2007, 2012 and 2017 is 32.812–32.903 h. Additional observations during the current aphelion arc may allow this to be refined further, in order to search for subtle changes in future orbits.

The common lightcurve with the data from all three apparitions shows a good match between the peak width and brightness variation of the individual datasets. There is a small offset between the points from 2007 and 2012 at rotational phase ~ 0.2. The possible differences in peak height from the different apparitions could be due to changing viewing geometry. However, the overall agreement between the three datasets implies that it is possible to find a common rotation period for all epochs. There is therefore no evidence that there was a period change between the three epochs. However, to set a formal upper limit on the spin change I take the difference between the maximum possible period for 2012 (33.237 hours; Section 5.10) and the minimum period for 2017, 32.83 to derive a conservative upper limit of 25 minutes in the past orbit.

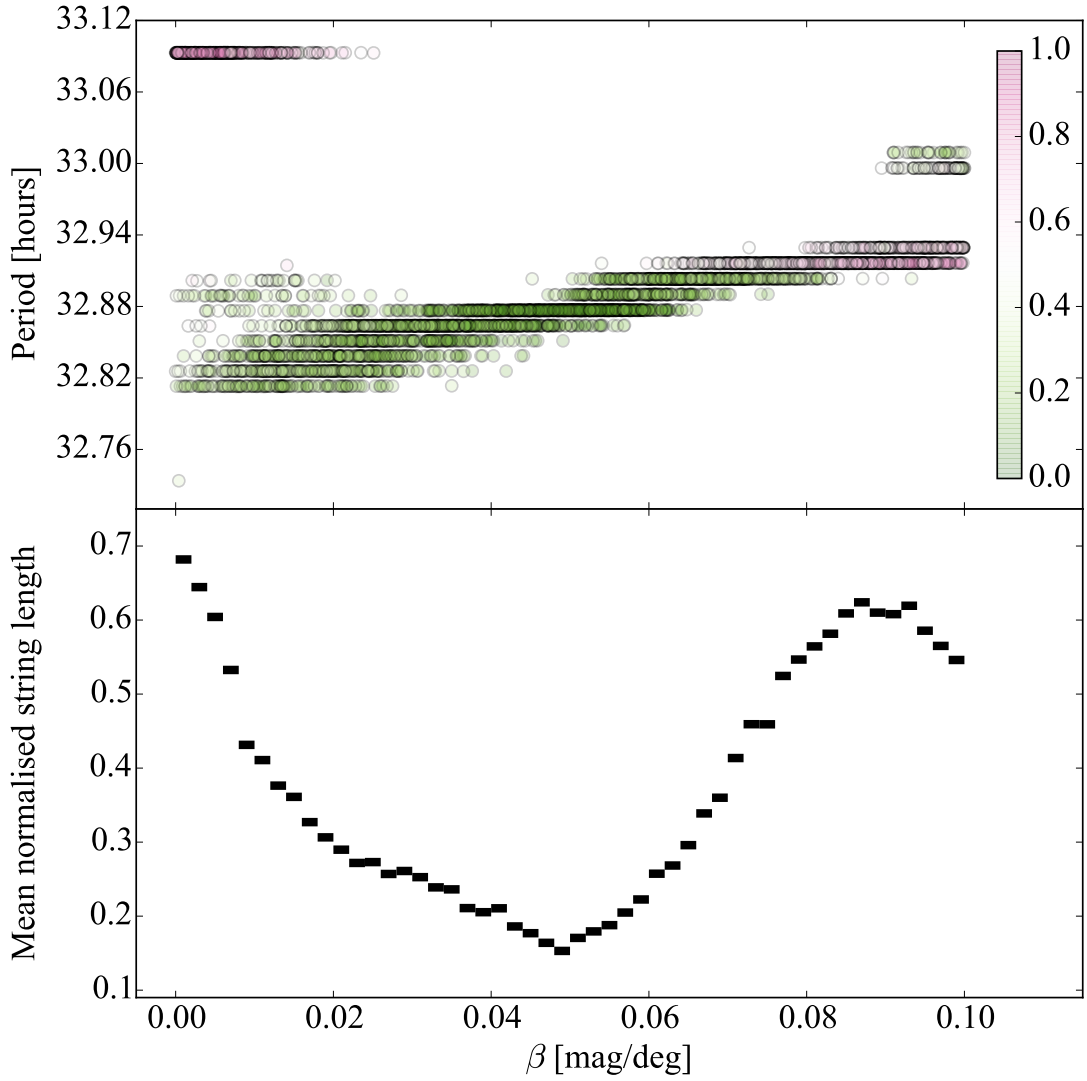

Figure 7.22: Same as Fig. 7.4 for 162P from the combined datasets taken in 2007, 2012 and 2017. The MC2 method was run for a range of possible phase-function slopes β = 0.00 - 0.10 mag/deg and periods from 32.7 to 33.1 h.

7.5 Summary of the derived properties

In this chapter I presented the search for period changes of comets 14P, 143P and 162P with respect to their lightcurves from previous orbits. I obtained the new lightcurve data within four observing programmes on three different telescopes.

I did not find evidence for period changes for any of the comets, and therefore set upper limits of 4.2, 6.6 and 25 minutes per orbit for 14P, 143P and 162P respectively. Even these conservative upper limits place the possible period changes

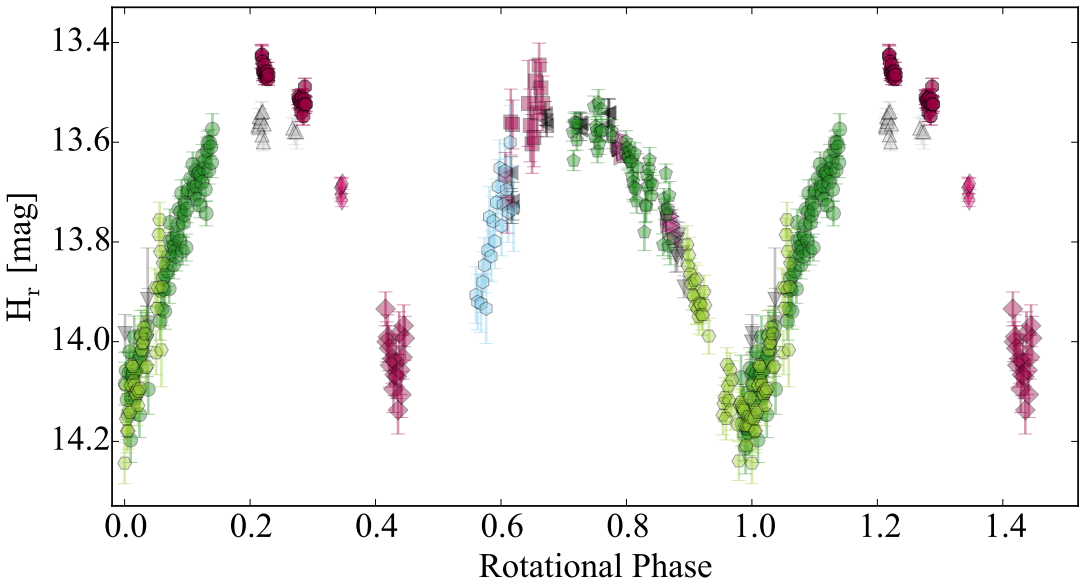

Figure 7.23: Rotational lightcurve of comet 162P with the combined dataset from 2007, 2012 and 2017. The symbols correspond to these in Fig. 7.21. The points were corrected for a phase-function slope $\beta = 0.052$ mag/deg and phased with a rotation period $P = 32.877$ h.

of these comets among the smallest measured for JFCs.

For comet 143P, I also derived a geometric albedo $A_r = 0.048 \pm 0.009$ by comparing the brightness of the nucleus from the optical observations to the size estimate from the SEPPCoN thermal observations in Fernández et al. (2013). The albedo of 143P is close to the average albedo found for JFCs (Chapter 6).

Chapter 8

Size-dependence of the survivability of JFCs

In Chapter 7, I compared newly obtained photometric observations of three large JFCs (14P, 143P and 162P) to their previous lightcurves from past orbits. For each of the three comets I was able to find a common period which describes well the combined data from the different apparitions. Even though this strongly suggests that the comets did not experience significant period changes, due to the uncertainties in the previous lightcurves and the phase functions, I have chosen to place conservative upper limits on the spin changes.

In Table 8.1 and Fig. 8.1, I compare the parameters of the three comets from this work to all other JFCs with detected spin changes. Prior to this work, spin changes were measured for eight other JFCs. It is noticeable that the two smallest nuclei, 103P and 41P, displayed the largest period changes, of ∼2 hours per orbit (Meech et al., 2011b) and >26 hours per orbit (Bodewits et al., 2018), respectively. The three comets with sizes in the range 1-3 km had period changes of the order of tens of minutes, while the three largest nuclei, 2P, 10P and 49P, had $\Delta P < 10$ min.

The three comets analysed in this work have $R \geq 3$ km and belong to the largest JFCs. Therefore the non-detection of spin changes is in agreement with the observations of the other large JFCs. For comets 14P and 143P, the conservative

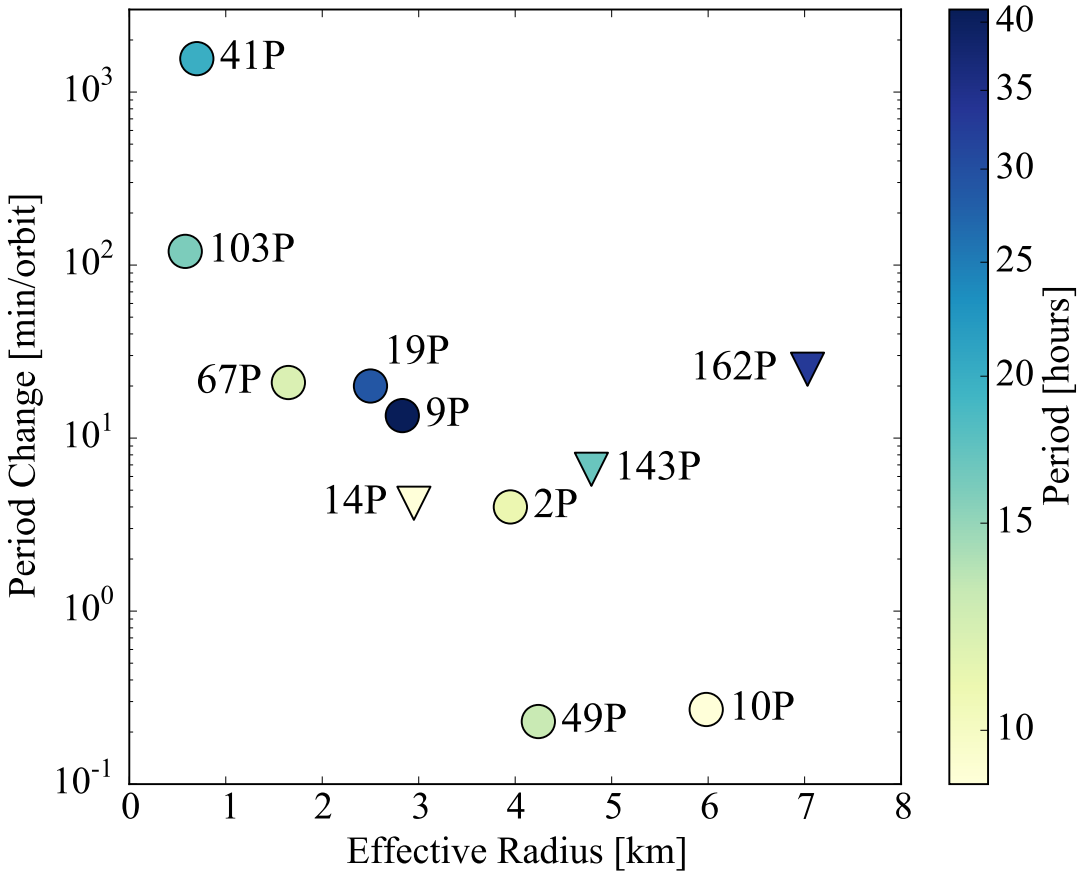

Figure 8.1: Comparison between the JFCs nuclei with known period changes. The circles show comets from the literature. The triangles correspond to the upper limits for comets from this work. The colours of the points correspond to the rotation period of the comets. The two smallest nuclei, 41P and 103P have displayed the most noticeable period changes of 26 and 2 hours respectively. On the contrary, the largest nuclei exhibit the smallest period changes.

upper limits derived in Chapter 7 also match the expected period changes $\Delta P <$ 10 minutes.

The observed trend of decreasing period change with increasing radius is predicted by simple theoretical considerations of the changing spin rate due to outgassing. For instance, according to Samarasinha & Mueller (2013), for comets with similar densities, shapes and activity distributions, the period changes decrease for increasing effective radii and decreasing rotation periods (faster rotation). It is also expected that comets with lower levels of outgassing will experience smaller period changes.

In Section 6.4 I noted that JFCs with $R \geq 3$ km lie well above the rotational-

Table 8.1: Properties of all JFCs with observed period changes.

Name	Radius [km]	Period [hours]	Spin change [min/orbit]	References
14P/Wolf	2.95 ± 0.19	9	< 4.2	(1), Ch. 5.2 , Ch. 7.2
143P/K-M	$4.79^{+0.32}_{-0.33}$	17	< 6.6	(1), (2), Ch. 7.3
162P/S-S	$7.03^{+0.47}_{-0.48}$	33	< 25	(1), Ch. 5.10, Ch. 7.4
2P/Encke	3.95 ± 0.06	11	4	(3), (4)
9P/Tempel 1	2.83 ± 0.1	41	-13.49	(5), (6), (7)
10P/Tempel 2	5.98 ± 0.04	9	0.27	(8), (9), (10), (11), (12)
19P/Borelly	2.5 ± 0.1	29	20	(13), (14), (15)
41P/T-G-K	0.7-1	20	> 1560[a]	(16), (17)
49P/A-R	4.24 ± 0.2	13	< 0.23	(18), (19), (20), (21)
67P/C-G	1.649 ± 0.007	12	-20.95	(22), ESA/Rosetta
103P/Hartley 2	0.58 ± 0.018	16	120	(23), (24), (25), (26)

[a] The period change of more than 26 hours for comet 41P was measured during the same apparition.

References: (1) Fernández et al. (2013); (2) Jewitt et al. (2003); (3) Lowry & Weissman (2007); (4) Samarasinha & Mueller (2013); (5) Thomas et al. (2013a); (6) Belton et al. (2011); (7) Chesley et al. (2013); (8) Lamy et al. (2009); (9) Mueller & Ferrin (1996); (10) Knight et al. (2011); (11) Knight et al. (2012); (12) Schleicher et al. (2013); (13) Buratti et al. (2004); (14) Mueller & Samarasinha (2002); (15) Mueller & Samarasinha (2015); (16) Tancredi et al. (2000); (17) Bodewits et al. (2018); (18) Lamy et al. (2004); (19) Millis et al. (1988); (20) Campins et al. (1995); (21) Eisner et al. (2017); (22) Jorda et al. (2016); (23) Thomas et al. (2013b); (24) Meech et al. (2009); (25) Meech et al. (2011b); (26) Jehin et al. (2010);

instability limit derived for the whole population of JFCs. I then hypothesised that this is due to the small period changes these comets are expected to undergo given their large radii. With the current work, I have added small upper limits

for the period changes of three comets in this size range. These findings confirm the prediction that large JFCs experience very small spin-rate changes, and are not expected to reach the rotational instability limit.

Out of the comets with $R \geq 3$ km in Table 8.1, 2P has a moderate activity level while all other comets can be described as very weakly active (see Jewitt et al. (2003), Samarasinha & Mueller (2013), Eisner et al. (2017), Chapter 4 and references therein). Having both large sizes and low activity levels makes these comets less likely to experience significant activity-driven period changes. They are therefore also less likely to undergo activity-induced rotational splitting, and more likely than smaller and more active comets to survive more perihelion passages without significant mass loss.

It may be possible for weakly active and dormant comets to experience an enhancement in activity without changing their orbits. If this happens, then the long-term stability of these objects might be disturbed. For example, motivated by the fly-by observations of comet 103P, Steckloff et al. (2016) suggested that a relatively fast nucleus rotation can cause avalanches which are able to expose fresh volatile-rich material and to reactivate previously dormant comets. This scenario, however, requires the comet to spin up in order to reach the minimum rotation rate necessary to trigger such an event. Considering the small period changes discovered for the large JFCs, it seems improbable that they would be affected by this reactivation mechanism. This once again suggests that if their orbits remain stable, larger nuclei will most likely remain weakly active or dormant, and will therefore survive longer than smaller comets.

I have identified three further lines of evidence which are in favour of the idea that larger JFCs have an increased survivability. Firstly, Fernández et al. (2013) noticed a bump in the cumulative size distribution (CSD) of JFCs for effective radii between 3 and 6 km. This implies an excess of large nuclei. However, since the number of comets that fall into this size range is small, this observation needs to be considered with caution. In order to confirm its validity and to verify

whether the excess is just for radii of 3-6 km, or it extends to larger nuclei, it is necessary to increase the number of JFCs with precisely measured sizes.

Secondly, recent works on the CSD of dead comets in the ACO population (Kim et al., 2014; Licandro et al., 2016) report a flatter cumulative size distribution for dormant comets than for active JFCs. Provided that the selection criteria of these two studies successfully distinguish between asteroids and dormant/dead comets, and that this finding is not a result of observational bias towards preferentially observing larger objects (see the discussion in Kim et al., 2014), the flatter CSD slope implies that the larger nuclei preferentially survive the active phase of their evolution compared to smaller comets.

Finally, dynamical studies following the orbital evolution of small bodies incoming from the Kuiper Belt fail to reproduce the observed distribution of short-period comets (Di Sisto et al., 2009; Rickman et al., 2017; Nesvorný et al., 2017). The discrepancies between the numerical models and observations, however, can be reduced significantly if a different physical lifetime for comets of different sizes is introduced. In particular Nesvorný et al. (2017) made an estimate that 10-km-class comets should survive thousands of perihelion passages while 1-km-class comets should only survive on the order of hundreds of perihelion passages, and 100-meter-sized nuclei should only live for a few perihelion passages.

In addition to the decreased likelihood for a spin-up and rotationally-driven instability, there are further mechanisms that could contribute to increase the survivability of large JFCs and can be evoked to explain these findings. Generally, ground observations have suggested that large JFC nuclei are often characterized by low levels of activity (e.g. A'Hearn et al., 1995; Tancredi et al., 2006). This tendency is explained with a variety of models that involve the formation of devolatised dust mantles which prevent the sublimation of the underlying material and can eventually make the comet dormant or dead (see Jewitt, 2002, 2004). The observations of dust deposits on comet 67P by Rosetta's OSIRIS cameras have confirmed that some large particles are unable to leave the comet's gravitational

field and get redeposited on the nucleus surface (Thomas et al., 2015b). Following this idea, the larger the comets, the stronger their gravitational potential, and therefore the more particles will get trapped in their gravitational field and will eventually return to the nucleus. Thus, larger nuclei will build insulating layers after fewer perihelion passages and will become dormant before they could undergo large mass loss.

Gundlach et al. (2016) have proposed an alternative model to explain why the CSDs of JFCs and ACOs differ for objects with radii > 2 km (Kim et al., 2014). Gundlach et al. (2016) suggest that the interiors of bigger nuclei have experienced larger hydrostatic compression and as a result have a larger tensile strength. At a certain point when the activity-driven erosion of the comet reaches deeper, more compacted layers and the sublimation is no longer able to lift off the dust particles from the surface, the activity of the comet ceases (Gundlach et al., 2016). Hence, this mechanism also implies that larger nuclei become inactive after fewer perihelion passages.

In both scenarios, since large nuclei become inactive faster than smaller ones, they are more likely to preserve their large sizes during the evolution as active comets. Provided that their average heliocentric distances remain unchanged over time, large JFCs remain shielded by their surface layers and are also less likely to undergo large mass-loss events (outbursts and splitting).

In summary, all of the outlined mechanisms imply that the combined effects of the larger size and the low activity of JFCs with effective radii larger than 2-3 km makes them more resistant to rotational splitting and other processes responsible for significant mass loss in comets. It can therefore be concluded that large JFC nuclei must have an enhanced survivability with respect to their smaller counterparts.

Chapter 9

Surface evolution of JFC nuclei

9.1 Surface Properties of JFCs

In Chapter 5, I used the precisely calibrated photometric observations of nine comets to constrain their surface properties. These data allowed me to derive the albedos of eight and the phase-function slopes of seven of the observed JFCs. In addition to this, in Chapter 7, I derived the albedo of comet 143P using new photometric observations from 2016 and 2017 in combination with the known radius of the comet from Fernández et al. (2013).

Previously, all available albedos and phase-function slopes of JFCs were collected by Snodgrass et al. (2011). I updated this sample with measurements done since then, and complemented it with the comets from this work. The extended sample of 24 JFCs with well-constrained albedos and/or phase-function coefficients is presented in Table 9.1. Where necessary, the albedos from the literature have been converted from V-band to A_{R} in R-band using the colour index of the Sun (V−R) = 0.354 ± 0.010 mag (Holmberg et al., 2006) and the comets' respective (V−R) colour indices or the average colour index of JFCs (V−R) = 0.50 ± 0.03 mag (Lamy & Toth, 2009).

The albedos $A_{\mathrm{r_{P1}}}$ from Chapters 5 and 7 are in $\mathrm{r_{P1}}$-band. In order to compare them to the albedos from the literature, I converted them to R-band using:

$$A_{\mathrm{R}} = A_{\mathrm{r_{P1}}} \times 10^{0.4\left((\mathrm{r_{P1}}-\mathrm{R})_{\mathrm{JFC}}-(\mathrm{r_{P1}}-\mathrm{R})_{\mathrm{Sun}}\right)}, \tag{9.1}$$

where the colour of the Sun $(\mathrm{r_{P1}} - \mathrm{R})_{\mathrm{Sun}} = 0.191 \pm 0.002$ mag was derived using the colour index of the Sun (B−V) = 0.642 ± 0.016 mag (Holmberg et al., 2006) and the conversion equations from Tonry et al. (2012). Similarly, the colour index of JFCs $(\mathrm{r_{P1}} - \mathrm{R})_{\mathrm{JFC}} = 0.214 \pm 0.010$ mag was derived using the average colour index of JFCs (B−V) = 0.87 ± 0.05 mag (Lamy & Toth, 2009). Substituting these values into equation 9.1, gives:

$$A_{\mathrm{R}} = A_{\mathrm{r_{P1}}} \times 1.021. \tag{9.2}$$

I use the values in Table 9.1 to derive the average albedo and phase-function slope for JFCs. The median of all 19 linear phase-function slopes is 0.046 mag/deg, the mean is 0.051 mag/deg and the standard deviation is 0.017 mag/deg. The median of all 20 albedos is 4.8%, the mean is 4.5% and the standard deviation is 1.2%. These values are slightly higher than the typically assumed values for JFCs: 4% for the albedo and 0.04 mag/deg for the phase-function coefficient. Since the sample collected in this chapter is the largest to date, the currently derived average albedo and phase-function slope values provide a better reference for future works.

There is no obvious dependence between the surface properties of the comets and their sizes. However, in Fig. 9.1 it can be seen that the largest JFCs have low albedos and small phase function coefficients. The albedo distribution with size agrees with the one presented by Fernández et al. (2016), which consisted of a larger sample of approximately 50 comets with albedos derived within the SEPPCoN program.

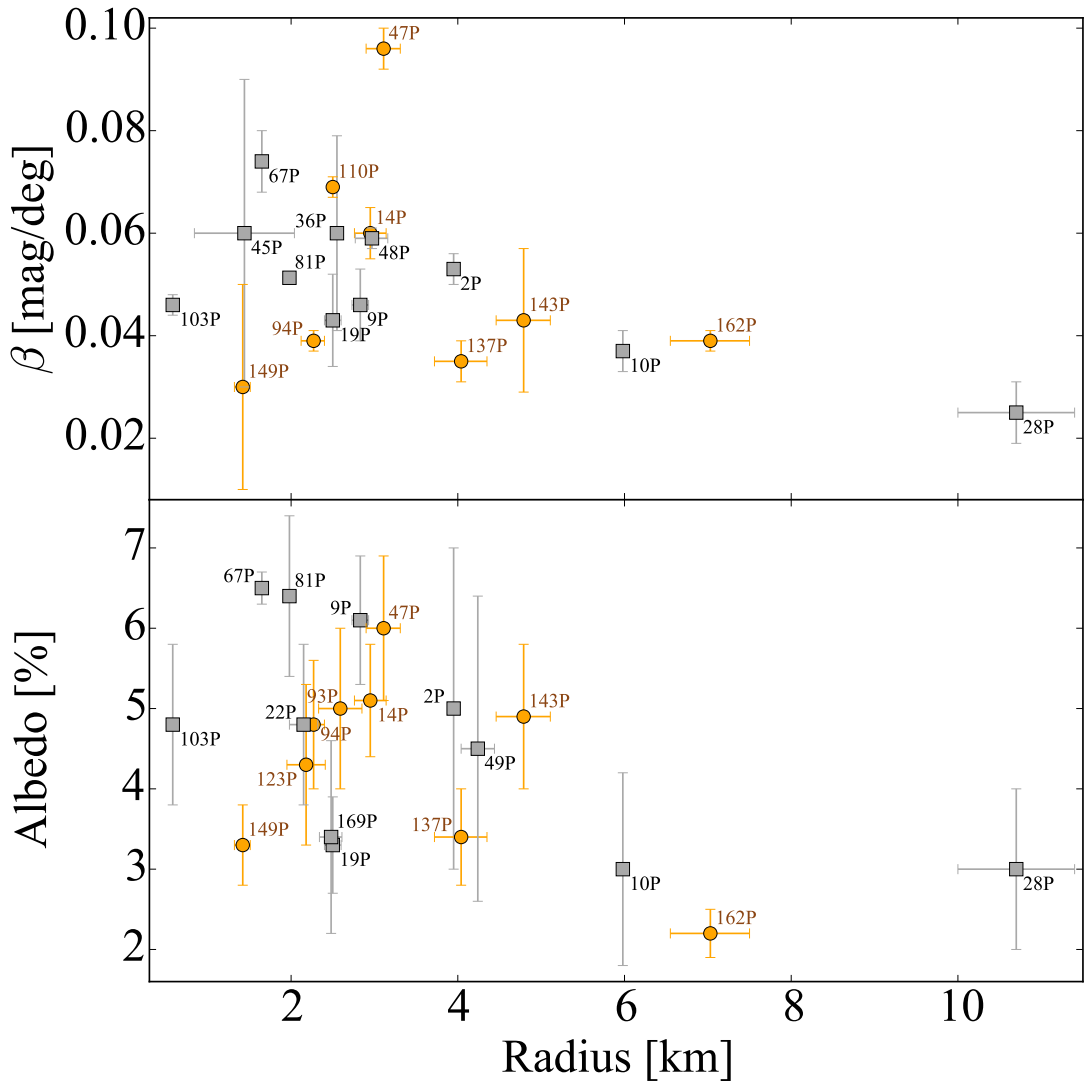

Figure 9.1: Surface properties of all JFCs with known albedos and phase-function slopes. Top: phase-function coefficient versus radius. Bottom: albedo versus radius. The orange circles correspond to comets with properties derived in this thesis. The surface properties of all comets are taken from Table 9.1, and the sizes can be found in Table 4.1. The radius $R = 1.44 \pm 0.6$ km of comet 45P is taken from Snodgrass et al. (2011) and Lowry et al. (2003). Comet 47P was active at the time of the observations, so in reality its phase-function coefficient might be smaller and its albedo might be lower.

9.2 Correlation between the phase-function coefficients and albedos

Prior to this work, there were only nine comets with reliable estimates of both the albedo and the phase-function coefficient (Snodgrass et al., 2011). I have

Table 9.1: Albedo and phase function measurements for JFCs.

Comet	A_R [%]*	Reference	β [mag/deg]	α Range [deg]	Reference.
2P	5.0 ± 2.0	Fernández et al. (2000)	0.053 ± 0.003	-	Weighted mean
”	-	-	0.060 ± 0.005	0-110	Fernández et al. (2000)
”	-	-	0.060 ± 0.005	4-28	Boehnhardt et al. (2008)
9P	6.1 ± 0.8	Weighted mean	0.046 ± 0.007	4-117	Li et al. (2007a)
”	6.4 ± 1.3	Li et al. (2007a)	-	-	-
”	4.6 ± 1.5	Lisse et al. (2005)	-	-	-
”	7.2 ± 1.6	Fernández et al. (2003)	-	-	-
10P	3.0 ± 1.2	A'Hearn et al. (1989)	0.037 ± 0.004	9-28	Sekanina & Zdenek (1991)
14P	5.1 ± 0.7	Ch. 5	0.060 ± 0.005	5-9	Ch. 5
19P	3.3 ± 0.6	Weighted mean	0.043 ± 0.009	13-80	Li et al. (2007b)
”	2.9 ± 0.6	Buratti et al. (2004)	-	-	-
”	7.2 ± 2.0	Li et al. (2007b)	-	-	-
22P	4.8 ± 1.0	Lamy et al. (2002)	-	-	-
28P	3.0 ± 1.0	Jewitt & Meech (1988)	0.025 ± 0.006	0-15	Delahodde et al. (2001)
36P	-	-	0.060 ± 0.019	1-11	Snodgrass et al. (2008b)

Table 9.1 continued

Comet	A_R [%]*	Reference	β [mag/deg]	α Range [deg]	Reference.
45P	-	-	∼0.06	88-93	Lamy et al. (2004)
47P	$\leq 6.0 \pm 0.9$	Ch. 5	0.096 ± 0.004	3-9	Ch. 5
”	-	-	0.083 ± 0.006	2-9	Snodgrass et al. (2008b)
48P	-	-	0.059 ± 0.002	5-16	Jewitt & Sheppard (2004)
49P	4.5 ± 1.9	Campins et al. (1995)	-	-	-
67P	6.5 ± 0.2	Fornasier et al. (2015)	0.074 ± 0.006	1-10	Fornasier et al. (2015)
”	5.4 ± 0.6	Kelley et al. (2009)	0.076 ± 0.003	0-11	Tubiana et al. (2008)
81P	6.4 ± 1.0	Li et al. (2009)	0.0513 ± 0.0002	0-100	Li et al. (2009)
93P	5.0 ± 1.0	Ch. 5	-	-	-
94P	4.8 ± 0.8	Ch. 5	0.039 ± 0.002	5-17	Ch. 5
103P	4.8 ± 1.0	Li et al. (2013)	0.046 ± 0.002	79-95	Li et al. (2013)
110P	-	-	0.069 ± 0.002	1-9	Ch. 5
123P	4.3 ± 1.0	Ch. 5	-	-	-
137P	3.4 ± 0.6	Ch. 5	0.035 ± 0.004	0.5-6	Ch. 5
143P	4.9 ± 0.9	Ch. 7	0.043 ± 0.014	5-13	Jewitt et al. (2003)

Table 9.1 continued

Comet	A_R [%]*	Reference	β [mag/deg]	α Range [deg]	Reference.
149P	3.3 ± 0.5	Ch. 5	0.03 ± 0.02	8-10	Ch. 5
162P	2.2 ± 0.3	Ch. 5	0.039 ± 0.002	4-12	Ch. 5
”	3.7 ± 1.4	Fernández et al. (2006)	-	-	-
169P	3.4 ± 1.2	DeMeo & Binzel (2008)	-	-	-

* Albedos are in R-band, converted from r_{P1} where necessary. The conversion was done using $A_R = A_{r_{P1}} \times 1.021$ for the mean colour index (B−V) = 0.87 ± 0.05 mag (Lamy & Toth, 2009).

increased this number to 15 by updating the values for comet 47P and adding the measurements for six additional comets from this work (Table 9.2). However, it is important to note that comet 47P was determined to be active at the time of the observations which were used to determine its albedo and phase function. Under these conditions, it is possible that these observations result in an overestimated nucleus brightness and therefore an overestimate of the albedo. Additionally, the activity possibly led to the determination of an inaccurate phase function. Due to these concerns, I exclude 47P from the further analysis.

I proceed to plot the linear phase-function slopes β versus the geometric albedos in R-band for the remaining 14 comets in Fig. 9.2. This plot shows a possible correlation between the phase-function coefficient and the albedo. It is well established that similar correlations exist between albedo or spectral type and phase functions for asteroids (e.g. Oszkiewicz et al., 2012). However, the trend for asteroids is observed to be the opposite. For instance, the albedo of asteroids increases with decreasing phase-function slope for phase angles between 5 and 25 degrees (Belskaya & Shevchenko, 2000).

I performed a Spearman rank correlation test between the phase-function coefficient and the albedo of all 14 comets (excluding 47P). The test produced rank ρ of 0.83 and p-value of 0.0003 which suggests a possible correlation between the phase-function coefficients and albedos.

Before I proceed to discuss the possible interpretation of the phase function-albedo correlation, I need to emphasise that it is based on a small set of comets. Moreover, the error bars in Fig. 9.2 clearly indicate the large uncertainties associated with each measurement. Even the measurements of comets 9P (Li et al., 2007a), 19P (Li et al., 2007b), 67P (Fornasier et al., 2015), 81P (Li et al., 2009) and 103P (Li et al., 2013) made during spacecraft visits have large uncertainties, which highlights the difficulties intrinsic to photometric studies of cometary surfaces. Since it is unlikely that observations in the near future will allow the uncertainties of the albedo and the phase-function slopes to be decreased, the best way to verify

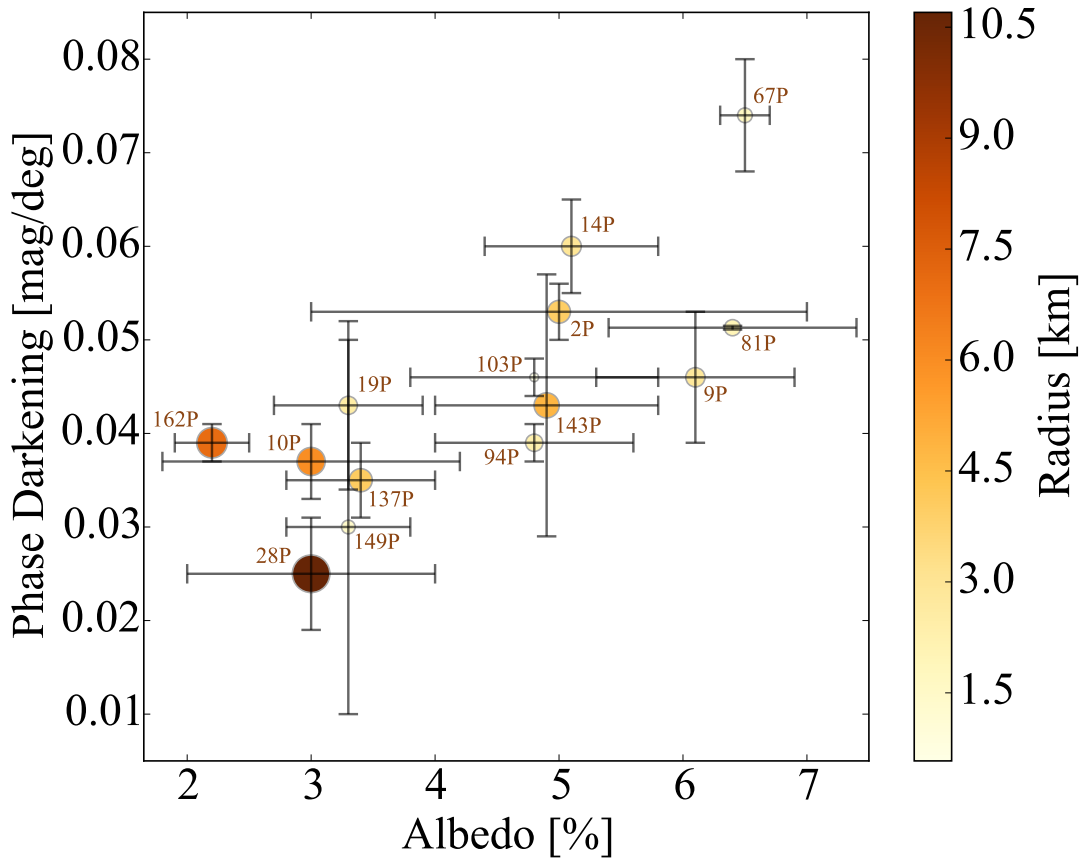

Figure 9.2: Linear phase-function slope β versus geometric albedo in R-band for all JFCs with measurements of both parameters. The size of the symbols and their colours correspond to the effective radii of the nuclei. The values of the albedos, phase-function slopes and radii are taken from Table 9.2. Despite the large uncertainties in the measurements, the distribution of the comets in this plot suggests a correlation between the phase-function slope and the albedo. The largest and least active nuclei appear to be clustered at lower β and albedo.

the validity of the correlation is to increase the number of comets in the diagram with future ground observations.

It also needs to be noted that the phase functions for the different comets were measured for different α ranges. Even though the Rosetta observations allowed the detection of an opposition surge of comet 67P (Fornasier et al., 2015; Masoumzadeh et al., 2017; Hasselmann et al., 2017), the opposition effect was not observed during the fly-bys of other comets, or in any ground-based measurement to date. This suggests that linear fits provide a good approximation to the phase functions, and hence the slopes derived from phase-function observations of

Table 9.2: Properties of all JFCs with known albedos and phase functions slopes.

Comet	A_R [%]*	Reference	β [mag/deg]	Range	Reference	Radius [km]	Reference
2P	5.0 ± 2.0	(1)	0.053 ± 0.003	0-110	WM** (1,2)	3.95 ± 0.06	(3)
9P	6.1 ± 0.8	WM (4,5,6)	0.046 ± 0.007	4-117	(4)	2.83 ± 0.1	(7)
10P	3.0 ± 1.2	(8)	0.037 ± 0.004	9-28	(9)	5.98 ± 0.04	(10)
14P	5.1 ± 0.7	Ch. 5	0.060 ± 0.005	5-9	Ch. 5	2.95 ± 0.19	(11)
19P	3.3 ± 0.6	WM (13,14)	0.043 ± 0.009	13-80	(12)	2.5 ± 0.1	(13)
28P	3.0 ± 1.0	(14)	0.025 ± 0.006	0-15	(15)	10.7 ± 0.7	(16)
67P	6.5 ± 0.2	(17)	0.074 ± 0.006	1-10	(17)	1.649 ± 0.007	(18)
81P	6.4 ± 1.0	(19)	0.0513 ± 0.0002	0-100	(19)	1.98 ± 0.05	(20)
94P	4.8 ± 0.8	Ch. 5	0.039 ± 0.002	5-17	Ch. 5	$2.27^{0.13}_{0.15}$	(11)
103P	4.8 ± 1.0	(21)	0.046 ± 0.002	79-95	(21)	0.58 ± 0.018	(22)
137P	3.4 ± 0.6	Ch. 5	0.035 ± 0.004	0.5-6	Ch. 5	$4.04^{0.31}_{0.32}$	(11)
143P	4.9 ± 0.9	Ch. 7	0.043 ± 0.014	5-13	(23)	$4.79^{0.32}_{0.33}$	(11)
149P	3.3 ± 0.5	Ch. 5	0.03 ± 0.02	8-10	Ch. 5	$1.42^{0.09}_{0.10}$	(11)
162P	2.2 ± 0.3	Ch. 5	0.039 ± 0.002	4-12	Ch. 5	$7.03^{0.47}_{0.48}$	(11)

* Albedos are in R-band, converted from r_{P1} where necessary. The conversion was done using $A_R = A_{r_{P1}} \times 1.021$ for the mean colour index (B−V) = 0.87 ± 0.05 mag (Lamy & Toth, 2009).

** Weighted mean

References: (1) Fernández et al. (2000), (2) (Boehnhardt et al., 2008), (3) Lowry & Weissman (2007), (4) Li et al. (2007a), (5) Lisse et al. (2005), (6) Fernández et al. (2003), (7) Thomas et al. (2013a), (8) A'Hearn et al. (1989), (9) Sekanina & Zdenek (1991), (10) Lamy et al. (2009), (11) Fernández et al. (2013), (12) Li et al. (2007b), (13) Buratti et al. (2004), (14) Jewitt & Meech (1988), (15) Delahodde et al. (2001), (16) Lamy et al. (2004), (17) Fornasier et al. (2015), (18) Jorda et al. (2016), (19) Li et al. (2009),(20) Sekanina et al. (2004),(21) Li et al. (2013),(22) Thomas et al. (2013b),(23) Jewitt et al. (2003)

different α ranges must be comparable.

9.3 Surface evolution of JFC nuclei

Keeping in mind the possible caveats highlighted above, I proceed to interpret the trend in Fig. 9.2 in light of the recent in-situ studies of cometary surfaces. There is now an increasing body of evidence that the surface morphology and texture of comet nuclei is governed by sublimation-driven erosion and that it reflects the degree of evolution of the comets (e.g. Basilevsky & Keller, 2006; Ip et al., 2016; Vincent et al., 2017). Moreover, the different surface morphologies are believed to produce detectable differences in the comets' optical properties (e.g. Fornasier et al., 2015; Longobardo et al., 2017).

After a comparison of the three comets visited by spacecraft at the time, Basilevsky & Keller (2006) noticed that smooth flat surfaces become more prevalent in the sequence 81P, 9P, 19P. They accounted this to progressive sublimation-induced degradation, which increases with the number of perihelion passages.

During the Rosetta visit to 67P, Ip et al. (2016) investigated whether the size frequency distribution of circular depressions of the different comets could be related to their dynamical history. They performed orbital integration simulations which showed that comets 67P, 103P and 19P could have spent more time orbiting at heliocentric distances under 2.5 au, thus being more eroded than 81P and 9P. It is however necessary to point out that such dynamical studies are complicated by the non-gravitational forces caused by outgassing and by the chaotic nature of JFC orbits which can vary greatly depending on the initial conditions of the orbital integration. Therefore, the suggested evolution sequence has to be taken with caution. In particular, it is not certain how recently 67P has entered the inner Solar System, and it is possible that it has experienced less erosion than 103P and 19P (see Ip et al., 2016; Vincent et al., 2017).

The most comprehensive evidence for the connection between the surface

morphology and the erosion levels of JFCs comes from Vincent et al. (2017). They compared the cumulative cliff-height distribution on different regions of 67P and of three other comets visited by spacecraft, 9P, 81P and 103P. They discovered that the regions on comet 67P which receive the highest insolation are lacking large cliffs. Vincent et al. (2017) hypothesised that instead of simply losing mass due to sublimation, comet nuclei, whose topography is initially dominated by steep cliffs, gradually get eroded down to flatter surfaces composed of smaller fragments (pebbles and dust).

The comparison between 67P and the other nuclei imaged during spacecraft fly-bys is in agreement with the proposed mechanism (Vincent et al., 2017). The power index of the cumulative cliff height distribution decreases in the order 81P, 67P, 9P, 103P, suggesting that the level of erosion of these comets increases in this direction (Vincent et al., 2017). This sequence is generally supported by the findings of the dynamical studies of Ip et al. (2016), once again implying that the global surface morphology can be related to the level of erosion of the nucleus.

The different surface morphologies, on the other hand, can be related to different photometric behaviour. Longobardo et al. (2017) used the VIRTIS imaging spectrometer on board Rosetta and discovered that rougher terrains on 67P produce slightly steeper phase functions. They also concluded that comets 81P and 9P, which have rougher surfaces, are photometrically similar to C-type asteroids and have phase functions steeper than those of smoother comets (103P, 19P and 67P). Using the orbital evolution studies by Ip et al. (2016), they suggested that comets which have experienced more sublimation-driven erosion have smoother surfaces and less steep phase functions.

All of these studies motivated me to look for a connection between the phase function-albedo correlation in Fig. 9.2 and the level of surface erosion of the individual comets. Comets 81P and 9P, which should have experienced less surface erosion according to Ip et al. (2016), indeed have larger albedos and phase-function slopes than 19P and 103P, which should be dynamically older

(although it is hard to distinguish 103P from 9P due to their large uncertainties).

It should be noted that comet 67P has the highest albedo and highest phase-function slope among the comets in Fig. 9.2. However, according to Ip et al. (2016) it should not be the least eroded nucleus among those visited by spacecraft. This discrepancy can be accounted for by the fact that the albedo and phase-function slope in Fig. 9.2 are taken from Fornasier et al. (2015), and were obtained before perihelion when only the northern hemisphere of the nucleus was observable. Due to the rotational axis orientation of 67P, the northern hemisphere of the nucleus receives less insolation throughout the orbit, and is therefore less eroded than the southern hemisphere (Keller et al., 2015a; Vincent et al., 2017). It is therefore very likely that the southern hemisphere would have a smaller phase-function slope and albedo. However, to my knowledge no direct comparison between the optical properties of the two hemispheres is available at the time of writing this chapter.

Finally, the bottom left corner of the plot in Fig. 9.2, at low albedos and flat phase functions, is where three of the largest JFCs (10P, 28P and 162P) can be found. Comet 10P is known to have weak activity at perihelion, while 28P and 162P have very weak and intermittent activity and have been classified as transition objects on the way to becoming dead comets (A'Hearn et al., 1995; Campins et al., 2006).

9.4 Evolution hypothesis

Considering all of the evidence presented above, I propose the following hypothesis to explain the correlation between β and geometric albedo: Dynamically young JFCs begin their lives as active comets having volatile-rich and rough surfaces characterised by tall steep cliffs. These surfaces correspond to relatively high albedos of 6-7 % and steep phase functions with slopes $\beta > 0.04$ mag/deg. As the comets orbit the Sun, their primitive topography gets increasingly eroded and gives

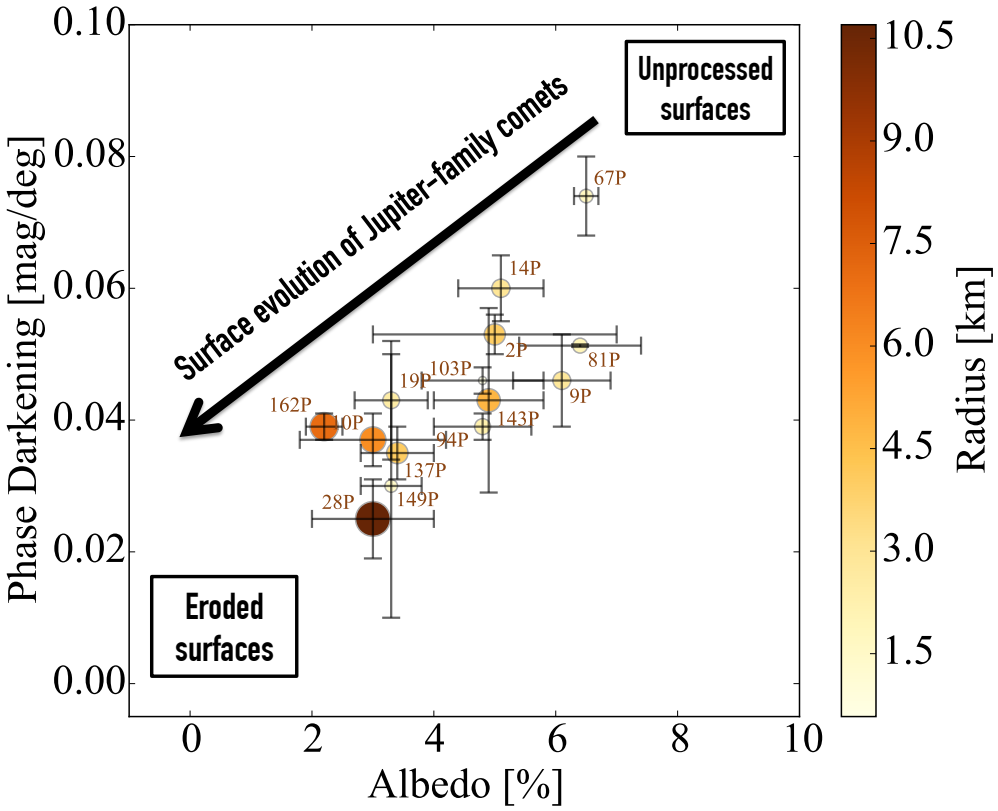

Figure 9.3: Evolution of the surface properties of JFCs according to the proposed surface evolution hypothesis.

place to smoother terrains, which correspond to flatter phase functions. Towards the end of their lives as active comets, the nuclei are covered by ever-growing dust areas which progressively quench the activity. As they transition to dormant comets, the volatiles from the surface layers gradually sublimate, which results in a further albedo decrease. The proposed evolutionary path of JFCs is illustrated in Fig. 9.3.

As I discussed in Chapter 8, the larger nuclei are less susceptible to major mass-loss mechanisms (splitting/disruption), and therefore more likely to reach a state of complete surface erosion. Hence, finding the large and almost dead comets at the bottom left corner of Fig. 9.2 supports this hypothesis.

Interestingly, some of the highest albedos and phase-function slopes are found for the comets visited by spacecraft (9P, 67P and 81P). This raises the question whether there is a discrepancy between values derived from ground observations

and from modelling disc-resolved photometry from spacecraft data. It must be considered, however, that space-mission teams aimed to select targets with well-known orbits and well-characterised behaviour. These criteria were satisfied mainly by comets which were discovered early on due to their high activity and the larger brightness corresponding to it. Therefore, it is understandable why the surfaces of more evolved and less active comets have remained unobserved by space missions. A future mission visiting a low-activity or dormant comet would be very interesting for comparison.

The majority of the comets in Fig. 9.2 were observed with ground- and space-based telescopes see Table 9.1. Therefore, the possible phase function-albedo correlation provides a compelling opportunity to study the surface characteristics and evolution of JFCs from the ground. Moreover this correlation could provide the possibility to distinguish between asteroids which have been placed on cometary orbits and dormant/dead comets. If the correlation is true, then dead comets which have undergone full erosion will have surfaces with lower albedos and flatter phase functions than those of C-type asteroids.

Chapter 10

Conclusions and Outlook

The main goal of this thesis was to study the ensemble physical properties of cometary nuclei in the light of the recent discoveries from the Rosetta Mission's rendezvous with comet 67P/Churyumov-Gerasimenko. The ground-based photometric data used to derive the properties of JFC nuclei were collected using various instruments during multiple epochs in the period 2004-2017. These new data complemented the sample of all JFCs with published rotational and surface properties, which was reviewed and collected in the current work. This extended sample was then used to characterise the bulk physical and surface properties of JFCs.

One of the most important aspects of this work is the method for precise photometric calibration especially developed for the analysis of the new data. In order to be able to combine the observations from the different programmes, I developed a technique for precise absolute calibration of photometric time series using Pan-STARRS DR1 stars. This technique achieved photometric calibration with uncertainty as low as 0.02 mag. Thus I was able to combine data from multiple observing runs and to study the rotation, the spin changes, the shapes and the surface properties of ten Jupiter family comets.

In the first part of the thesis I used time-series photometry of nine JFCs taken in the period 2004-2015 to study the comets' lightcurves. I derived the rotation

rates of six objects (14P, 47P, 93P, 94P, 110P, and 162P). For comets 123P, 137P and 149P the collected data were insufficient to derive unambiguous rotation periods. To the best of my knowledge, for comets 93P, 94P and 162P these are the first published rotation rates. Comets 14P, 47P and 110P had previous lightcurves but the results from this thesis significantly improved the period estimates. After adding the six comets from this work to the total sample of JFCs with known rotation rates, the size of the sample reached 37 comets.

This sample was then used to study the ensemble properties of JFCs. I first used the distribution of spin rates of JFCs to look for signatures of the population history. The employed Kolmogorov-Smirnov test determined that the distribution of the normalised spin rates of comets is consistent both with a Maxwell distribution and a flat distribution. Therefore, it is not possible to distinguish whether JFCs are a collisionally-dominated population like asteroids, or whether their spin rate distribution is dominated by other processes, such as activity-driven spin changes. This clearly highlights the need for obtaining lightcurves of more JFCs. Increasing the number of known rotation rates in the future would allow a better characterisation of the distribution and can potentially reveal the mechanisms responsible for shaping the current population properties.

Lower limits on the axis ratios of all observed comets have been derived from the brightness variation of the time series. The distribution of the axis ratios shows that the majority of comets have projected axis ratios smaller than 2. The median of the whole JFC sample is 1.5. However, ground observations only provide a lower limit to the axis ratio due to the unknown geometry, further reduced if the nucleus is obstructed by any present coma signal. Moreover, all five comets with shape models determined from in-situ space craft observations have axis ratios larger than 1.6. These two arguments suggest that on average comets might be more elongated than the axis-ratio distribution from ground-based observations shows.

The shapes of comet nuclei and in particular the frequency of bi-lobed nuclei

have proven to be very important for understanding the formation and evolution of JFCs. One way to possibly reveal more about the shapes of JFC nuclei with ground-based observations is to observe their lightcurves at different geometries. For many comets this would be impossible since they remain active for most of their orbits, which limits the possible geometries where they can be observed. However, for the least active nuclei, the nucleus shapes can be reconstructed from multi-epoch lightcurves. This was already attempted for comet 67P/C-G (Lowry et al., 2012), although due to the limitations of the lightcurve inversion techniques, the bi-lobed nature of the nucleus was only revealed during the Rosetta spacecraft approach (Sierks et al., 2015).

Despite the limitations of ground observations, the lower limits of cometary axis ratios have proven to be a useful source of information. Under the assumption that JFCs have negligible tensile strengths, their observed axis ratios and periods can be used to constrain the minimum bulk density required to keep the nuclei stable against rotational instability. Using this approach, I have confirmed the result from Lowry & Weissman (2003) that a density of 0.6 g cm^{-3} is sufficient to keep all of the studied nuclei stable. This lower limit of cometary density is in a very good agreement with the Rosetta result of 0.532 ± 0.007 g cm^{-3} (Jorda et al., 2016), which was the first direct measurement of a cometary density.

Alternatively, if JFCs are modelled as prolate ellipsoids with non-negligible tensile strengths using the model from Davidsson (2001), their minimum required tensile strength can be derived. Using the updated sample of JFCs rotation rates, I concluded that none of the observed comets require tensile strength higher than 10-25 Pa in order to be stable against rotational splitting. This lower limit estimate of the bulk tensile strength was found to be in excellent agreement with the growing evidence that JFCs have low strengths, proving once again that building a large sample of comets with well-constrained properties can add a great value to understanding the ensemble properties of comets. Thus, increasing the number of comets with known sizes and spin rates further in the future will be

very useful to refine the density and tensile-strength lower limits. In addition, obtaining more lightcurves will probe a greater variety of nuclei, and could be used to look for a possible size-dependence in the bulk properties, e.g. larger tensile strength for larger nuclei (as predicted by Gundlach et al., 2016).

The growing collection of well-sampled lightcurves of JFC nuclei has enabled the search for activity-driven spin changes. I have collected photometric time-series observations for three large JFCs, 14P, 143P and 162P, in order to derive their current rotation periods and to look for changes with respect to their spin rates from previous apparitions. I determined the following periods from the new lightcurves: $P = 9.07 \pm 0.01$ hours for 14P; $P_1 = 17.1966 \pm 0.0003$ hours, $P_2 = 17.2121 \pm 0.0002$ hours or $P_3 = 17.1812 \pm 0.0002$ hours for 143P; $P = 32.9 \pm 0.2$ hours for 162P. For each of the three comets I was able to find a common period which phases well all previously published lightcurves. Thus, I did not detect spin changes with respect to the last apparitions directly, and instead, set conservative upper limits for the spin changes of $\Delta P < 4.2$ min per orbit (14P), $\Delta P < 6.6$ min per orbit (143P) and $\Delta P < 25$ min per orbit (162P).

With the new observations, I have increased the number of JFCs with studied period changes from eight to eleven. This expanded sample shows clear evidence that the largest JFC nuclei with $R \geq 3$ km experience the smallest period changes (typically $\Delta P < 10$ minutes). This implies that large comets are less likely to undergo significant period changes and rotational splitting over their lifetimes. I have also reviewed other processes which can contribute to prevent large JFCs from undergoing significant mass-loss events. This led to the conclusion that the interplay of all mechanisms make large JFCs nuclei more likely to survive their evolution as active comets until they reach full surface erosion and transition to dormancy. The suggested enhanced survivability of large JFCs can explain the CSD of JFCs from Fernández et al. (2013) and of dormant comets in the ACO population from Kim et al. (2014) and Licandro et al. (2016), all of which have suggested an excess of objects with radii larger than 2.5 - 3 km.

Even after the contribution from this work, there are less than a dozen JFCs with studied spin changes. Such a small sample is insufficient to establish what characteristics play a dominant role in determining whether a comet will experience large period changes. Hence this sample needs to be increased in the future to span comets with a wide range of activity levels, sizes and elongations. This is needed in order to investigate whether more active comets tend to show larger period changes, and are therefore more likely to reach critical spin rates at which they could experience nucleus splitting, or whether shape (elongation of the nucleus) has a stronger effect on spin changes. Additionally, when looking for spin changes in JFCs, it is important to focus on objects, such as comet 31P, which have short rotation rates, close to the stability limit derived in this thesis. Following the changes of these comets over the next orbits could identify the comets most likely to break up in the future.

The photometric observations analysed in this work have allowed me to determine the linear phase function coefficients of eight of the observed comets - 14P, 47P, 94P, 110P, 137P, 143P, 149P, and 162P. To my knowledge, for all comets except 47P, this is the first phase function determination. These results have increased the number of comets with well-constrained phase function coefficients from 13 to 19. I have also been able to use these data to estimate the albedos of nine comets. The geometric albedo in R-band of comet 162P was determined to be 2.2 ± 0.3 %. This makes 162P the JFC with lowest measured geometric albedo to date.

After adding the comets from this work, the number of JFCs with known albedos and/or phase functions reached 24 JFCs. This expanded sample allowed me to update the commonly accepted values of the average albedo and phase-function coefficient of JFCs. The distribution of the linear phase function slopes has a median of 0.046 mag/deg, mean of 0.051 mag/deg and standard deviation of 0.017 mag/deg. The known albedos have a median of 4.8%, average of 4.5% and standard deviation of 1.3%.

Prior to this work, there were nine comets for which both the albedo and the phase function coefficient were known (see Snodgrass et al., 2011). In this thesis, I have updated the values for 47P and added six more comets (14P, 94P, 137P, 143P, 149P, 162P) to this sample. The increased number of comets has allowed me to look for correlations between the surface properties of JFCs. Large nuclei ($R_{\rm eff}$ $\geq$ 5 km) appear to have low albedos ($\leq$ 3 %) and low phase function coefficients ($\leq$ 0.04 mag/deg). However, since only three comets in that size range have been observed, this finding needs to be confirmed with future observations.

The 14 comets, for which both the albedo and the phase-function coefficient are known follow a trend of increasing phase-function slope with increasing albedo. In light of recent detailed studies of the surfaces of JFCs visited by spacecraft, I have hypothesised that this possibly significant correlation corresponds to an evolutionary trend for JFCs. In this scenario, dynamically young JFCs start their evolution with relatively high albedos and steeper phase functions. During their lifetime as active JFCs, sublimation-driven erosion gradually makes their surfaces smoother and their phase-function slopes decrease. As the dust-covered portions of the nuclei progressively increase, the comets become less active and the sublimation gradually decreases. Finally, the dust layers gradually lose their volatiles and therefore their albedos decrease even further as the comets transition to dormancy.

If confirmed, this trend in the photometric parameters offers a fascinating opportunity to study the evolution of cometary surfaces with ground-based observations. It could also provide a criterion to distinguish cometary bodies from asteroids on comet-like orbits. These prospects emphasise the need to validate and better understand the observed trends in the photometric properties of JFCs. This could be achieved by future work on a few possible research projects.

The first and most important step is to increase the sample of JFCs with well-constrained geometric albedos and phase functions from ground-based observations in order to confirm the possibly significant correlation. If the dependence between

albedo and phase-function slope is confirmed, then the surface properties which determine the different optical characteristics need to be identified. In particular it would be important to model the effects of large-scale topography on the observed phase functions. For instance, this can be studied by creating synthetic models of comet nuclei with representative shapes and reflectance properties. These models can then be used to test the changes of the phase-function slopes for different large-scale topographies (cliff-height distributions). Another way to identify the physical properties which determine the albedo and phase-function slopes involves laboratory comparison of the reflectance properties of analogue materials with different porosities and volatile content.

Finally, an essential test whether the phase-function-albedo correlation represents the surface evolution of JFCs is the comparison with other Solar System populations. If the surface evolution hypothesis identified in this thesis is correct, then dormant comets in the Near-Earth population should have low albedos and flat phase functions, similarly to the evolved comets. On the other hand, Centaurs and Kuiper Belt objects must have relatively large albedos and steep phase functions and must be similar to dynamically young JFCs. Due to the large geocentric distances of these objects their phase functions beyond a few degrees are unavailable to observers on Earth. However, the New Horizons mission which is currently situated in the Kuiper Belt is going to provide photometry at large phase angles of 10-20 objects.

In conclusion, this thesis has established that ground-based observations of comet nuclei remain a relevant and very important source of information that complements the results obtained by spacecraft observations. The availability of ever-larger telescopes, as well as all-sky star catalogues such as Pan-STARRS and GAIA which ensure very precise photometric calibration, allow the lightcurves of an increasing number of comets to be studied. As a consequence the number of well-characterised nuclei has enabled a significant improvement in the understanding of the bulk properties and surface characteristics of JFC nuclei. This work has

clearly highlighted the need for more lightcurve and phase-function observations of JFCs and has outlined the research questions which need to be addressed in future studies.

References

A'Hearn M. F., 2017, Philosophical Transactions of the Royal Society A: Mathematical, Physical and Engineering Sciences, 375, 20160261

A'Hearn M. F., Campins H., Schleicher D. G., Millis R. L., 1989, The Astrophysical Journal, 347, 1155

A'Hearn M. F., Millis R., Schleicher D., Osip D., Birch P., 1995, Icarus, 118, 223

A'Hearn M. F., et al., 2005, Science, 310, 258

A'Hearn M. F., et al., 2011, Science, 332, 1396

Abazajian K., et al., 2003, The Astronomical Journal, 126, 2081

Appenzeller I., et al., 1998, The Messenger, 94, 1

Asphaug E., Benz W., 1996, Icarus, 121, 225

Basilevsky A., Keller H., 2006, Planetary and Space Science, 54, 808

Batygin K., Brown M. E., Betts H., 2012, The Astrophysical Journal Letters, 744, L3

Bauer J. M., et al., 2017, The Astronomical Journal, 154, 53

Belskaya I. N., Shevchenko V. G., 2000, Icarus, 147, 94

Belton M., Samarasinha N., Fernandez Y., Meech K., 2005, Icarus, 175, 181

Belton M. J., et al., 2011, Icarus, 213, 345

Belton M. J., et al., 2013, Icarus, 222, 595

Bessell M. S., 1990, Publications of the Astronomical Society of the Pacific, 102, 1181

Bessell M. S., 2005, Annual Review of Astronomy and Astrophysics, 43, 293

Biele J., Ulamec S., Richter L., Knollenberg J., Kührt E., Möhlmann D., 2009, Acta Astronautica, 65, 1168

Blum J., Gundlach B., Mühle S., Trigo-Rodriguez J., 2014, Icarus, 235, 156

Blum J., et al., 2017, Monthly Notices of the Royal Astronomical Society, 469, S755

Bodewits D., Farnham T. L., Kelley M. S. P., Knight M. M., 2018, Nature, 553, 186

Boehnhardt H., 2004, in , Comets II, M. C. Festou, H. U. Keller, and H. A. Weaver (eds.). pp 301–316

Boehnhardt H., et al., 2002, Astronomy and Astrophysics, 387, 1107

Boehnhardt H., Tozzi G. P., Bagnulo S., Muinonen K., Nathues A., Kolokolova L., 2008, Astronomy and Astrophysics, 489, 1337

Boehnhardt H., et al., 2017, Philosophical Transactions of the Royal Society, 375, 20160248

Bohnhardt H., Kaufl H. U., Keen R., Camilleri P., Carvajal J., Hale A., 1995, IAU Circ., No. 6274, #1 (1995). Edited by Green, D. W. E., 6274

Brasser R., Morbidelli A., 2013, Icarus, 225, 40

Britt D., et al., 2004, Icarus, 167, 45

Brown A. G. A., et al., 2016, Astronomy & Astrophysics, 595, A2

Brownlee D., 2014, Annual Review of Earth and Planetary Sciences, 42, 179

Buratti B., Hicks M., Soderblom L., Britt D., Oberst J., Hillier J., 2004, Icarus, 167, 16

Buzzoni B., et al., 1984, The Messenger, 38, 9

Campins H., 1988, Icarus, 73, 508

Campins H., Osip D. J., Rieke G., Rieke M., 1995, Planetary and Space Science, 43, 733

Campins H., Ziffer J., Licandro J., Pinilla-Alonso N., Fernández Y., de León J., Mothé-Diniz T., Binzel R. P., 2006, The Astronomical Journal, 132, 1346

Capaccioni F., et al., 2015, Science, 347, aaa0628

Chambers K. C., et al., 2016, http://arxiv.org/abs/1612.05560

Chesley S., et al., 2013, Icarus, 222, 516

Cousins A. W. J., 1973, Mem. R. Astron. Soc., 77, 223

Cox A. N., 2000, Allen's astrophysical quantities, 4th ed. New York: AIP Press; Springer

Crovisier J., Biver N., Bockelee-Morvan D., Colom P., Gerard E., Jorda L., Rauer H., 1995, IAU Circ., No. 6227, #1 (1995). Edited by Green, D. W. E., 6227

Davidsson B. J. R., 1999, Icarus, 142, 525

Davidsson B. J. R., 2001, Icarus, 149, 375

Davidsson B. J. R., Sierks H., Guttler C., Marzari F., Pajola M., Rickman H., 2016, Astronomy & Astrophysics, 592, A63

Davis L. E., 1999, in Craine E. R., Tucker R. A., Barnes J. V., eds, Vol. 189, Precision CCD Photometry. ASP Conference Series, p. 35

DeMeo F., Binzel R. P., 2008, Icarus, 194, 436

Dekker H., Delabre B., D'odorioo S., 1986, in Crawford D. L., ed., Vol. 627, IN: Instrumentation in astronomy VI; Proceedings of the Meeting, Tucson, AZ, Mar. 4-8, 1986. Part 1 (A87-36376 15-35). Bellingham, WA, Society of Photo-Optical Instrumentation Engineers. pp 339–348

Delahodde C. E., Meech K. J., Hainaut O. R., Dotto E., 2001, Astronomy and Astrophysics, 376, 672

Di Sisto R. P., Fernández J. A., Brunini A., 2009, Icarus, 203, 140

Dohnanyi J. S., 1969, Journal of Geophysical Research, 74, 2531

Donn B., Hughes D., 1986, in In ESA, Proceedings of the 20th ESLAB Symposium on the Exploration of Halley's Comet. pp 523–524

Donn B., Daniels P. A., Hughes D. W., 1985, Bulletin of the American Astronomical Society, 17, 520

Drahus M., Küppers M., Jarchow C., Paganini L., Hartogh P., Villanueva G. L., 2010, Astronomy and Astrophysics, 510, A55

Drahus M., et al., 2011, The Astrophysical Journal Letters, 734, L4

Duncan M. J., Levison H. F., 1997, Science, 276, 1670

Duncan M., Levison H., Dones L., 2004, in , Comets II, M. C. Festou, H. U. Keller, and H. A. Weaver (eds.). University of Arizona Press, pp 193–204

Duxbury T. C., Newburn R. L., Brownlee D. E., 2004, Journal of Geophysical Research, 109, E12S02

Dworetsky M. M., 1983, Monthly Notices of the Royal Astronomical Society, 203, 917

Eisner N., Knight M. M., Schleicher D. G., 2017, The Astronomical Journal, 154, 196

El-Maarry M. R., et al., 2015, Astronomy & Astrophysics, 583, A26

El-Maarry M. R., et al., 2016, Astronomy & Astrophysics, 593, A110

El-Maarry M. R., et al., 2017, Science, 355, 1392

Encke J. F., 1822, Berliner Astr. Jahrbuch fuer 1823, pp 211–223

Farnham T. L., 2001, American Astronomical Society, DPS Meeting #33, id.12.10

Fernández Y. R., 2009, Planetary and Space Science, 57, 1218

Fernández Y., et al., 2000, Icarus, 147, 145

Fernández Y. R., Jewitt D. C., Sheppard S. S., 2001, The Astrophysical Journal, 553, L197

Fernández Y., Meech K., Lisse C., A'Hearn M., Pittichová J., Belton M., 2003, Icarus, 164, 481

Fernández Y. R., Jewitt D. C., Sheppard S. S., 2005a, The Astronomical Journal, 130, 308

Fernández Y., Lowry S., Weissman P., Mueller B., Samarasinha N., Belton M., Meech K., 2005b, Icarus, 175, 194

Fernández Y. R., Campins H., Kassis M., Hergenrother C. W., Binzel R. P., Licandro J., Hora J. L., Adams J. D., 2006, The Astronomical Journal, 132, 1354

Fernández Y., et al., 2013, Icarus, 226, 1138

Fernández Y. R., Weaver H. A., Lisse C. M., Meech K. J., Lowry S. C., Bauer J. M., Fitzsimmons A., Snodgrass C., 2016, American Astronomical Society, AAS Meeting #227, id.141.22

Festou M. C., Keller H. U., Weaver H. A., 2004, in , Comets II, M. C. Festou, H. U. Keller, and H. A. Weaver (eds.). University of Arizona Press, pp 3–16

Filacchione G., et al., 2016, Nature, 529, 368

Fornasier S., et al., 2015, Astronomy & Astrophysics, 583, A30

Fraser W. C., et al., 2016, The Astronomical Journal, 151, 158

Fukugita M., Ichikawa T., Gunn J. E., Doi M., Shimasaku K., Schneider D. P., 1996, The Astronomical Journal, 111, 1748

Glassmeier K.-H., Boehnhardt H., Koschny D., Kührt E., Richter I., 2007, Space Science Reviews, 128, 1

Gomes R., Levison H. F., Tsiganis K., Morbidelli A., 2005, Nature, 435, 466

Groussin O., Lamy P., Jorda L., Toth I., 2004, Astronomy and Astrophysics, 419, 375

Groussin O., et al., 2015, Astronomy & Astrophysics, 583, A32

Guilbert-Lepoutre A., Rosenberg E. D., Prialnik D., Besse S., 2016, Monthly Notices of the Royal Astronomical Society, 462, S146

Gundlach B., Blum J., Blum J., 2016, Astronomy & Astrophysics, 589, A111

Gutierrez P. J., de Leon J., Jorda L., Licandro J., Lara L. M., Lamy P., 2003, Astronomy & Astrophysics, 407, L37

Gutiérrez P. J., Jorda L., Samarasinha N. H., Lamy P., 2005, Planetary and Space Science, 53, 1135

Halley E., 1705, A synopsis of the astronomy of comets

Harmon J., Nolan M., 2005, Icarus, 176, 175

Harmon J. K., Nolan M. C., Ostro S. J., Campbell D. B., 2004, in , Comets II, M. C. Festou, H. U. Keller, and H. A. Weaver (eds.). University of Arizona Press, pp 265–279

Harmon J. K., Nolan M. C., Howell E. S., Giorgini J. D., Taylor P. A., 2011, The Astrophysical Journal, 734, L2

Harris A. W., 1996, Lunar and Planetary Science, volume 27, page 493, 27

Harris A. W., 1998, Icarus, 131, 291

Harris A., Young J., Scaltriti F., Zappalà V., 1984, Icarus, 57, 251

Hasselmann P. H., et al., 2017, Monthly Notices of the Royal Astronomical Society, 469, S550

Hergenrother C., 2014, IAU CBET, 3870

Hirabayashi M., et al., 2016, Nature, 534, 352

Hodgkin S. T., Irwin M. J., Hewett P. C., Warren S. J., 2008, Monthly Notices of the Royal Astronomical Society, 394, 675

Hoenig S. F., 2005, Astronomy & Astrophysics, 445, 759

Holmberg J., Flynn C., Portinari L., 2006, Monthly Notices of the Royal Astronomical Society, 367, 449

Howell S. B., 1989, Publications of the Astronomical Society of the Pacific, 101, 616

Howell S. B., 2006, Handbook of CCD astronomy. Cambridge University Press

Howell S. B., 2011, in , Vol. 373, Astronomical Photometry, Astrophysics and Space Science Library. pp 71–84

Howell E. S., et al., 2014, American Astronomical Society, DPS meeting #46, id.209.24, 46

Ip W.-H., et al., 2016, Astronomy & Astrophysics, 591, A132

Jansson K. W., Johansen A., 2014, Astronomy & Astrophysics, 570, A47

Jehin E., Manfroid J., Hutsemekers D., Gillon M., Magain P., 2010, Central Bureau Electronic Telegrams, 2589

Jewitt D., 1998, Earth, Moon, and Planets, 79, 35

Jewitt D. C., 2002, The Astronomical Journal, 123, 1039

Jewitt D. C., 2004, in , Comets II, M. C. Festou, H. U. Keller, and H. A. Weaver (eds.). University of Arizona Press, pp 659–676

Jewitt D., 2009, The Astronomical Journal, 137, 4296

Jewitt D., 2015, The Astronomical Journal, 150, 201

Jewitt D., Danielson G. E., 1984, Icarus, 60, 435

Jewitt D., Luu J., 1989, The Astronomical Journal, 97, 1766

Jewitt D., Meech K., 1987, The Astronomical Journal, 93, 1542

Jewitt D. C., Meech K. J., 1988, The Astrophysical Journal, 328, 974

Jewitt D., Sheppard S., 2004, The Astronomical Journal, 127, 1784

Jewitt D., Sheppard S., Fernndez Y., 2003, The Astronomical Journal, 125, 3366

Jewitt D., Hsieh H., Agarwal J., 2015, in , Asteroids IV, Patrick Michel, Francesca E. DeMeo, and William F. Bottke (eds.). University of Arizona Press, pp 221–241

Johansen A., Oishi J. S., Mac Low M.-M., Klahr H., Henning T., Youdin A., 2007, Nature, 448, 1022

Johansen A., Blum J., Tanaka H., Ormel C., Bizzarro M., Rickman H., 2014, in Protostars and Planets VI, Henrik Beuther, Ralf S. Klessen, Cornelis P. Dullemond, and Thomas Henning (eds.). University of Arizona Press, pp 547–570

Johnson H. L., Morgan W. W., 1953, The Astrophysical Journal, 117, 313

Jorda L., Lamy P., Groussin O., Toth I., A'Hearn M. F., Peschke S., 2000, ISO Beyond Point Sources: Studies of Extended Infrared Emission, September 14-17, 1999, ISO Data Centre, Villafranca del Castillo, Madrid, Spain. Edited by R. J. Laureijs, K. Leech and M. F. Kessler, 455, 61

Jorda L., et al., 2016, Icarus, 277, 257

Jutzi M., Benz W., Toliou A., Morbidelli A., Brasser R., 2017, Astronomy & Astrophysics, 597, A61

Kaiser N., et al., 2002, in Survey and Other Telescope Technologies and Discoveries. Proceedings of the SPIE. p. 154

Kaiser N., et al., 2010, in Ground-based and Airborne Telescopes III. Proceedings of the SPIE. p. 77330E

Kamoun P. G., Campbell D. B., Ostro S. J., Pettengill G. H., Shapiro I. I., 1982, Science, 216, 293

Kasuga T., Balam D. D., Wiegert P. A., 2010, The Astronomical Journal, 140, 1806

Keller H., Thomas N., 1997, Advances in Space Research, 19, 187

Keller H. U., et al., 1986, Nature, 321, 320

Keller H. U., Britt D., Buratti B. J., Thomas N., 2004, in , Comets II, M. C. Festou, H. U. Keller, and H. A. Weaver (eds.). University of Arizona Press, pp 211–222

Keller H. U., Mottola S., Skorov Y., Jorda L., 2015a, Astronomy & Astrophysics, 579, L5

Keller H. U., et al., 2015b, Astronomy & Astrophysics, 583, A34

Kelley M. S., Wooden D. H., Tubiana C., Boehnhardt H., Woodward C. E., Harker D. E., 2009, The Astronomical Journal, 137, 4633

Kim Y., Ishiguro M., Usui F., 2014, The Astrophysical Journal, 789, 151

Knapmeyer M., Fischer H.-H., Knollenberg J., Seidensticker K., Thiel K., Arnold W., Faber C., Möhlmann D., 2018, Icarus, 310, 165

Knight M. M., Farnham T. L., Schleicher D. G., Schwieterman E. W., 2011, The Astronomical Journal, 141, 2

Knight M. M., Schleicher D. G., Farnham T. L., Schwieterman E. W., Christensen S. R., 2012, The Astronomical Journal, 144, 153

Knight M. M., Mueller B. E. A., Samarasinha N. H., Schleicher D. G., 2015, The Astronomical Journal, 150, 22

Knight M. M., Fitzsimmons A., Kelley M. S. P., Snodgrass C., 2016, The Astrophysical Journal Letters, 823, L6

Kossacki K. J., Spohn T., Hagermann A., Kaufmann E., Kührt E., 2015, Icarus, 260, 464

Kron R. G., 1980, The Astrophysical Journal Supplement Series, 43, 305

Lamy P. L., Toth I., 1995, Astronomy and Astrophysics, 293L, L43

Lamy P., Toth I., 2009, Icarus, 201, 674

Lamy P. L., Toth I., Jorda L., Weaver H. A., A'Hearn M., 1998a, Astronomy and Astrophysics, 335, L25

Lamy P. L., Toth I., Weaver H. A., 1998b, Astronomy and Astrophysics, 337, 945

Lamy P., Toth I., A'Hearn M. F., Weaver H. A., Weissman P. R., 2001, Icarus, 154, 337

Lamy P., Toth I., Jorda L., Groussin O., A'Hearn M. F., Weaver H. A., 2002, Icarus, 156, 442

Lamy P. L., Toth I., Fernandez Y. R., Weaver H. A., 2004, in , Comets II, M. C. Festou, H. U. Keller, and H. A. Weaver (eds.). University of Arizona Press, pp 223–264

Lamy P. L., Toth I., Weaver H. A., Jorda L., Kaasalainen M., Gutiérrez P. J., 2006, Astronomy and Astrophysics, 458, 669

Lamy P. L., Toth I., Weaver H. A., A'Hearn M. F., Jorda L., 2009, Astronomy and Astrophysics, 508, 1045

Lamy P. L., Toth I., Weaver H. A., A'Hearn M. F., Jorda L., 2011, Monthly Notices of the Royal Astronomical Society, 412, 1573

Lamy P., Faury G., Llebaria A., Knight M., A'Hearn M., Battams K., 2013, Icarus, 226, 1350

Landolt A. U., 1992, The Astronomical Journal, 104, 340

Leibowitz E. M., Brosch N., 1986, Icarus, 68, 430

Levison H. F., 1996, in Completing the Inventory of the Solar System, Astronomical Society of the Pacific Conference Proceedings, T.W. Rettig and J.M. Hahn (Eds.). pp 173–191

Levison H., Duncan M. J., 1997, Icarus, 127, 13

Levison H. F., Terrell D., Wiegert P. A., Dones L., Duncan M. J., 2006, Icarus, 182, 161

Levison H. F., Morbidelli A., Tsiganis K., Nesvorný D., Gomes R., 2011, The Astronomical Journal, 142, 152

Li J.-Y., et al., 2007a, Icarus, 187, 41

Li J., A'Hearn M., McFadden L., Belton M., 2007b, Icarus, 188, 195

Li J.-Y., A'Hearn M. F., Farnham T. L., McFadden L. A., 2009, Icarus, 204, 209

Li J.-Y., et al., 2013, Icarus, 222, 559

Li J.-Y., Helfenstein P., Buratti B., Takir D., Clark B. E., 2015, in , Asteroids IV, Patrick Michel, Francesca E. DeMeo, and William F. Bottke (eds.). University of Arizona Press, pp 129–150

Licandro J., Tancredi G., Lindgren M., Rickman H., Hutton R. G., 2000, Icarus, 147, 161

Licandro J., Campins H., Hergenrother C., Lara L. M., 2003, Astronomy & Astrophysics, 398, L45

Licandro J., Ali-Lagoa V., Tancredi G., Fernandez Y., 2016, Astronomy & Astrophysics, 585, A9

Lisse C. M., et al., 2005, The Astrophysical Journal, 625, L139

Lisse C. M., et al., 2009, Publications of the Astronomical Society of Pacific, 121, 968

Lomb N. R., 1976, Astrophysics and Space Science, 39, 447

Longobardo A., et al., 2017, Monthly Notices of the Royal Astronomical Society, 469, S346

Lorek S., Gundlach B., Lacerda P., Blum J., 2016, Astronomy & Astrophysics, 587, A128

Lorek S., Lacerda P., Blum J., 2018, Astronomy & Astrophysics, 611, A18

Lowry S. C., Fitzsimmons A., 2001, Astronomy and Astrophysics, 365, 204

Lowry S. C., Weissman P. R., 2003, Icarus, 164, 492

Lowry S. C., Weissman P. R., 2007, Icarus, 188, 212

Lowry S. C., Fitzsimmons A., Cartwright I. M., Williams I. P., 1999, Astronomy & Astrophysics, 349, 649

Lowry S. C., Fitzsimmons A., Collander-Brown S., 2003, Astronomy and Astrophysics, 397, 329

Lowry S. C., Fitzsimmons A., Jorda L., Kaasalainen M., Lamy P., Toth I., 2006, American Astronomical Society, DPS meeting #38, p. id.08.01

Lowry S., Duddy S. R., Rozitis B., Green S. F., Fitzsimmons A., Snodgrass C., Hsieh H. H., Hainaut O., 2012, Astronomy & Astrophysics, 548, A12

Luu J. X., 1993, Icarus, 104, 138

Luu J., Jewitt D., 1990, Icarus, 86, 69

Luu J. X., Jewitt D. C., 1992, The Astronomical Journal, 104, 2243

Manzini F., Oldani V., Crippa R., Borrero J., Bryssink E., Mobberley M., Nicolas J., 2014, Astrophysics and Space Science, 351, 435

Masoumzadeh N., et al., 2017, Astronomy & Astrophysics, 599, A11

Massironi M., et al., 2015, Nature, 526, 402

Meech K., Hainaut O., Marsden B., 2004, Icarus, 170, 463

Meech et al., 2005, Science, 310, 265

Meech K. J., et al., 2009, in American Astronomical Society, DPS meeting #41, id.20.07.

Meech K., et al., 2011a, Icarus, 213, 323

Meech K. J., et al., 2011b, The Astrophysical Journal, 734, L1

Millis R. L., A'Hearn M. F., Campins H., 1988, The Astrophysical Journal, 324, 1194

Morbidelli A., Rickman H., 2015, Astronomy & Astrophysics, 583, A43

Mottola S., et al., 2014, Astronomy & Astrophysics, 569, L2

Mueller B. E. A., , Asteroids, Comets, Meteors 1991, pp 425–428

Mueller B. E., Ferrin I., 1996, Icarus, 123, 463

Mueller B. E. A., Samarasinha N. H., 2002, Earth, Moon, and Planets, 90, 463

Mueller B. E. A., Samarasinha N. H., 2015, in American Astronomical Society, DPS meeting #47 id.506.10.

Mueller B. E. A., Samarasinha N. H., Fernandez Y. R., 2008, American Astronomical Society, DPS Meeting #40, p. id.16.2

Mueller B. E. A., Farnham T. L., Samarasinha N. H., A'Hearn M. F., 2010a, American Astronomical Society, DPS meeting #42, p. id.28.31

Mueller B. E. A., Samarasinha N. H., Rauer H., Helbert J., 2010b, Icarus, 209, 745

Nesvorný D., 2011, The Astrophysical Journal Letters, 742, L22

Nesvorný D., Morbidelli A., 2012, The Astronomical Journal, 144, 117

Nesvorný D., Vokrouhlicky D., Dones L., Levison H. F., Kaib N., Morbidelli A., 2017, The Astrophysical Journal, 845, 27

Nesvorný D., Parker J., Vokrouhlicky D., 2018, The Astronomical Journal, in press

Newton I., 1687, Philosophiae Naturalis Principia Mathematica. Auctore Js. Newton

Nolan M. C., Harmon J. K., Howell E. S., Benner L. A., Giorgini J. D., Ostro S. J., Campbell D. B., Margot J. L., 2006, American Astronomical Society, DPS meeting #38, p. id.12.06

O'Brien D. P., Greenberg R., 2003, Icarus, 164, 334

Ohtsuka K., Ito T., Yoshikawa M., Asher D. J., Arakida H., 2008, Astronomy and Astrophysics, 489, 1355

Oort J. H., 1950, Bulletin of the Astronomical Institutes of the Netherlands, 11, 91

Oszkiewicz D. A., Bowell E., Wasserman L. H., Muinonen K., Penttilä A., Pieniluoma T., Trilling D. E., Thomas C. A., 2012, Icarus, 219, 283

Pajola M., et al., 2017, Nature Astronomy, 1, 0092

Pommerol A., et al., 2015, Astronomy & Astrophysics, 583, A25

Pravec P., Harris A. W., 2000, Icarus, 148, 12

Pravec P., Sarounova L., Wolf M., 1996, Icarus, 124, 471

Pravec P., Harris A. W., Michalowski T., 2002, in , Asteroids III, W. F. Bottke Jr., A. Cellino, P. Paolicchi, and R. P. Binzel (eds.). University of Arizona Press, pp 113–122

Preusker F., et al., 2015, Astronomy & Astrophysics, 583, A33

Reyniers M., Degroote P., Bodewits D., Cuypers J., Waelkens C., 2009, Astronomy and Astrophysics, 494, 379

Richardson J. E., Bowling T. J., 2014, Icarus, 234, 53

Richardson J. E., Melosh H. J., Lisse C. M., Carcich B., 2007, Icarus, 190, 357

Rickman H., et al., 2015, Astronomy & Astrophysics, 583, A44

Rickman H., Gabryszewski R., Wajer P., Wiśniowski T., Wójcikowski K., Szutowicz S., Valsecchi G. B., Morbidelli A., 2017, Astronomy & Astrophysics, 598, A110

Roll R., Witte L., 2016, Planetary and Space Science, 125, 12

Russell H. N., 1906, The Astrophysical Journal, 24, 1

Sagdeev R. Z., Blamont J., Galeev A. A., Moroz V. I., Shapiro V. D., Shevchenko V. I., SzegÅŚ K., 1986, Nature, 321, 259

Samarasinha N. H., Mueller B. E. A., 2013, The Astrophysical Journal, 775, L10

Samarasinha N. H., Mueller B. E. A., Belton M. J. S., Jorda L., 2004, in , Comets II, M. C. Festou, H. U. Keller, and H. A. Weaver (eds.). University of Arizona Press, pp 281–299

Samarasinha N. H., Mueller B. E. A., A'Hearn M. F., Farnham T. L., 2010, IAU Circ., No. 9178, #1 (2010). Edited by Green, D. W. E., 9178

Samarasinha N. H., Mueller B. E. A., A'Hearn M. F., Farnham T. L., Gersch A., 2011, The Astrophysical Journal, 734, L3

Samarasinha N. H., et al., 2012, American Astronomical Society, DPS meeting #44, p. id.506.03

Scargle J. D., 1982, The Astrophysical Journal, 263, 835

Schleicher D. G., Knight M. M., 2016, The Astronomical Journal, 152, 89

Schleicher D. G., Knight M. M., Levine S. E., 2013, The Astronomical Journal, 146, 137

Schulson E. M., Duval P., 2009, Creep and Fracture of Ice. Cambridge University Press, Cambridge

Schwartz S. R., Michel P., Jutzi M., Marchi S., Zhang Y., Richardson D. C., 2018, Nature Astronomy, 2, 379

Scotti J. V., et al., 1996, IAU Circ., No. 6301, #1 (1996). Edited by Marsden, B. G., 6301

Sekanina Z., 1987, Proceedings of the International Symposium on the Diversity and Similarity of Comets, pp 315–322

Sekanina Z., Yeomans D. K., 1985, The Astronomical Journal, 90, 2335

Sekanina Z., Zdenek 1991, The Astronomical Journal, 102, 350

Sekanina Z., Brownlee D. E., Economou T. E., Tuzzolino A. J., Green S. F., 2004, Science, 304, 1769

Sierks H., et al., 2015, Science, 347, aaa1044

Singer K. N., et al., 2016, American Astronomical Society, DPS meeting #48, p. id.213.12

Skorov Y., Blum J., 2011, Icarus, 221, 1

Snodgrass C., Carry B., 2013, The Messenger, 152, 14

Snodgrass C., Fitzsimmons A., Lowry S. C., 2005, Astronomy and Astrophysics, 444, 287

Snodgrass C., Lowry S. C., Fitzsimmons A., 2006, Monthly Notices of the Royal Astronomical Society, 373, 1590

Snodgrass C., Saviane I., Monaco L., Sinclaire P., 2008a, The Messenger, 132, 18

Snodgrass C., Lowry S. C., Fitzsimmons A., 2008b, Monthly Notices of the Royal Astronomical Society, 385, 737

Snodgrass C., Fitzsimmons A., Lowry S. C., Weissman P., 2011, Monthly Notices of the Royal Astronomical Society, 414, 458

Snodgrass C., et al., 2016, Astronomy & Astrophysics, 588, A180

Soderblom L. A., et al., 2002, Science, 296, 1087

Soderblom L., Britt D., Brown R., Buratti B., Kirk R., Owen T., Yelle R., 2004, Icarus, 167, 100

Solem J. C., 1995, Astronomy and Astrophysics, 302, 596

Sosa A., Fernández J. A., 2009, Monthly Notices of the Royal Astronomical Society, 393, 192

Steckloff J. K., Johnson B. C., Bowling T., Melosh H. J., Minton D., Lisse C. M., Battams K., 2015, Icarus, 258, 430

Steckloff J. K., Graves K., Hirabayashi T., Melosh H. J., Richardson J., 2016, Icarus, 272, 60

Stellingwerf R. F., 1978, The Astrophysical Journal, 224, 953

Storm S. P., et al., 2006, American Astronomical Society, DPS meeting #38, p. id.12.08

Sunshine J. M., et al., 2006, Science, 311, 1453

Tancredi G., Fernández J. A., Rickman H., Licandro J., 2000, Astronomy and Astrophysics Supplement Series, 146, 73

Tancredi G., Fernández J. A., Rickman H., Licandro J., 2006, Icarus, 182, 527

Taylor M. G. G. T., Alexander C., Altobelli N., Fulle M., Fulchignoni M., Grun E., Weissman P., 2015, Science, 347, 387

Thomas P., et al., 2013a, Icarus, 222, 453

Thomas P. C., et al., 2013b, Icarus, 222, 550

Thomas N., et al., 2015a, Science, 347, aaa0440

Thomas N., et al., 2015b, Astronomy & Astrophysics, 583, A17

Tody D., 1986, in Crawford D. L., ed., Vol. 0627, Instrumentation in astronomy VI; Proceedings of the Meeting, Tucson, AZ, Mar. 4-8, 1986. Part 2. p. 733

Tody D., 1993, in Astronomical Data Analysis Software and Systems II, A.S.P. Conference Series. p. 173

Tonry J. L., et al., 2012, The Astrophysical Journal, 750, 99

Toth I., Lisse C., 2006, Icarus, 181, 162

Toth I., Lamy P., Weaver H., 2005, Icarus, 178, 235

Toth I., Lamy P., Weaver H., A'Hearn M., Kaasalainen M., Lowry S., 2006, American Astronomical Society, DPS meeting #38, p. id.06.01

Tsiganis K., Gomes R., Morbidelli A., Levison H. F., 2005, Nature, 435, 459

Tubiana C., Barrera L., Drahus M., Boehnhardt H., 2008, Astronomy and Astrophysics, 490, 377

Tubiana C., Böhnhardt H., Agarwal J., Drahus M., Barrera L., Ortiz J. L., 2011, Astronomy & Astrophysics, 527, A113

Tubiana C., et al., 2015a, Astronomy & Astrophysics, 573, A62

Tubiana C., Snodgrass C., Michelsen R., Haack H., Boehnhardt H., Fitzsimmons A., Williams I. P., 2015b, Astronomy & Astrophysics, 584, id.A97,

VanderPlas J. T., 2017, eprint arXiv:1703.09824

VanderPlas J. T., Ivezic Z., 2015, The Astrophysical Journal, 812, 18

Veverka J., et al., 2013, Icarus, 222, 424

Vincent J.-B., et al., 2015a, Nature, 523, 63

Vincent J. B., et al., 2015b, Astronomy & Astrophysics, 587, id.A14

Vincent J. B., et al., 2016, Monthly Notices of the Royal Astronomical Society, 462, S184

Vincent J. B., et al., 2017, Monthly Notices of the Royal Astronomical Society, 469, S329

Warner B., 2006a, A practical guide to lightcurve photometry and analysis. Springer

Warner B. D., 2006b, The Minor Planet Bulletin, 33, 35

Warner B. D., Fitzsimmons A., 2005, IAU Circ., No. 8578, #1 (2005). Edited by Green, D. W. E., 8578

Weaver H. A., Stern S. A., Parker J. W., 2003, The Astronomical Journal, 126, 444

Weidenschilling S., Spaute D., Davis D., Marzari F., Ohtsuki K., 1997, Icarus, 128, 429

Weiler M., Rauer H., Sterken C., 2011, Icarus, 212, 351

Weissman P. R., 1986, Nature, 320, 242

Weissman P. R., Doressoundiram A., Hicks M. D., Chamberlin A., Sykes M. V., Larson S., Hergenrother C., 1999, Bulletin of the Astronomical Society, 31, 1121

Weissman P. R., Asphaug E., Lowry S. C., 2004, in , Comets II, M. C. Festou, H. U. Keller, and H. A. Weaver (eds.). University of Arizona Press, pp 337–357

Whipple F. L., 1950, The Astrophysical Journal, 111, 375

Whipple F. L., 1951, The Astrophysical Journal, 113, 464

Williams G. V., 2017, Central Bureau Electronic Telegrams, 4359, 1 (2017). Edited by Green, D. W. E., 4359

Windmark F., Birnstiel T., Güttler C., Blum J., Dullemond C. P., Henning T., 2012, Astronomy & Astrophysics, 540, A73

Youdin A. N., Goodman J., 2005, The Astrophysical Journal, 620, 459

Zsom A., Ormel C. W., Guettler C., Blum J., Dullemond C. P., 2010, Astronomy and Astrophysics, 513, A57